

PDF hosted at the Radboud Repository of the Radboud University Nijmegen

The following full text is a publisher's version.

For additional information about this publication click this link.

<http://hdl.handle.net/2066/129656>

Please be advised that this information was generated on 2018-07-07 and may be subject to change.

Antibody-based
imaging of

PROSTATE
CANCER



Susanne Lütje

Antibody-based imaging of prostate cancer

Susanne Lütje

Department of Radiology and Nuclear Medicine
Radboud university medical center

The research described in this thesis was performed at the department of Radiology and Nuclear Medicine of the Radboud university medical center and was supported by a research grant of the Dutch Cancer Society (grant no. KUN 2008-4038).

Printing of this thesis was financially supported by the Radboud University Nijmegen.

ISBN: 978-94-6259-268-1

Cover: Susanne Lütje and Esther Ris

Layout: Susanne Lütje

Printed by Ipskamp Drukkers Nijmegen

Copyright © Susanne Lütje, 2014

Antibody-based imaging of prostate cancer

Proefschrift

ter verkrijging van de graad van doctor
aan de Radboud Universiteit Nijmegen
op gezag van de rector magnificus prof. mr. S.C.J.J. Kortmann,
volgens besluit van het college van decanen
in het openbaar te verdedigen op woensdag 17 september 2014
om 10.30 uur precies

door

Susanne Lütje
geboren op 31 januari 1986
te Duisburg, Duitsland

Promotores:

Prof. Dr. O.C. Boerman

Prof. Dr. W.J.G. Oyen

Copromotores:

Dr. M. Rijpkema

Dr. W. Helfrich (UMC Groningen)

Manuscriptcommissie:

Prof. Dr. P.F.A. Mulders (voorzitter)

Prof. Dr. W.R. Gerritsen

Prof. Dr. I.J. de Jong (UMC Groningen)

Antibody-based imaging of prostate cancer

Doctoral Thesis

to obtain the degree of doctor
from Radboud University Nijmegen
on the authority of the Rector Magnificus prof. dr. S.C.J.J. Kortmann,
according to the decision of the Council of Deans
to be defended in public on Wednesday, September 17, 2014
at 10.30 hours

by

Susanne Lütje
born on January 31, 1986
in Duisburg, Germany

Supervisors:

Prof. Dr. O.C. Boerman

Prof. Dr. W.J.G. Oyen

Co-supervisors:

Dr. M. Rijpkema

Dr. W. Helfrich (UMC Groningen)

Doctoral Thesis Committee:

Prof. Dr. P.F.A. Mulders

Prof. Dr. W.R. Gerritsen

Prof. Dr. I.J. de Jong (UMC Groningen)

Für Onkel Arno

und

Oma

PRELUDE

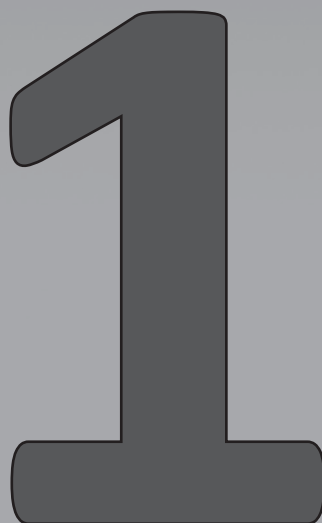
"I am among those who think that science has great beauty. A scientist in his laboratory is not only a technician: he is also a child placed before natural phenomena which impress him like a fairy tale."

Marie Curie, 1933

CONTENTS

Section 1	Scope and General Introduction	13
Section 2	Strategies to optimize antibody-based radionuclide imaging of cancer	39
	Chapter 2.1	41
	Prospects in radionuclide imaging of prostate cancer <i>The Prostate 2012; 72(11):1262-1272</i>	
	Chapter 2.2	63
	Targeting human prostate cancer with ¹¹¹ In-labeled D2B IgG, F(ab') ₂ and Fab fragments in nude mice with PSMA-expressing xenografts <i>Contrast Media and Molecular Imaging 2014 (in press)</i>	
	Chapter 2.3	81
	Pretargeted immuno-PET and radioimmunotherapy of prostate cancer with an anti-TROP-2 x anti-HSG bispecific antibody <i>Eur J Nucl Med Mol Imaging 2013; 40(9):1377-1383</i>	
	Chapter 2.4	97
	Anti-CEA antibody fragments labeled with [¹⁸ F]AIF for PET imaging of CEA-expressing tumors <i>Bioconjugate Chemistry 2014; 25(2):335-341</i>	
Section 3	Dual-modality imaging of prostate cancer	113
	Chapter 3.1	115
	Targeted dual-modality NIRF and radionuclide imaging of cancer: preclinical status and clinical applications <i>Molecular Imaging and Biology 2014 (in press)</i>	
	Chapter 3.2	135
	Dual-modality image-guided surgery of prostate cancer with a radiolabeled fluorescent anti-PSMA monoclonal antibody <i>Journal of Nuclear Medicine 2014; 55(6):995-1001</i>	
	Chapter 3.3	153
	Pretargeted dual-modality immuno-SPECT and near-infrared fluorescence imaging for image-guided surgery of prostate cancer <i>(Submitted for publication)</i>	
Section 4	Epilogue	169
	General Discussion	171
	Summary	179
	Samenvatting	185
	Zusammenfassung	191
	List of Publications	197
	Curriculum Vitae	199
	Dankwoord	201

Scope and General Introduction



SCOPE OF THIS THESIS

SCOPE OF THIS THESIS

In oncology, the search for tumor lesions in the body of a patient can be compared to the proverbial looking for the needle in a haystack. For various malignancies, the outcome of treatment mainly depends on early detection of the disease and complete removal of all tumor lesions. To achieve this, accurate and highly sensitive imaging modalities are pivotal to improve early detection of cancer and provide guidance for surgical removal of tumor lesions.

As prostate cancer is one of the most frequent cancers in men worldwide and is only curable when detected in early stages, this thesis focuses on the development and evaluation of strategies to optimize antibody-based imaging of prostate cancer to improve the detection of tumor lesions.

In the **first section** of this thesis, a general introduction to prostate cancer is provided and the basic principles of radionuclide and fluorescence imaging are described.

The **second section** focuses on strategies to optimize antibody-based radionuclide imaging of cancer, such as the use of antibody fragments (**chapter 2.2** and **2.4**) or the application of pretargeting strategies (**chapter 2.3**) to increase tumor-to-background ratios and potentially enhance the sensitivity to detect tumor lesions.

The **third section** of this thesis is devoted to preclinical advances and the current clinical status of diagnostic and therapeutic dual-modality approaches based on radionuclide and near-infrared fluorescence imaging. A dual-modality imaging strategy based on an anti-PSMA monoclonal antibody was developed and characterized in a subcutaneous as well as in a metastatic tumor model (**chapter 3.2**). Additionally, one of the optimization strategies described in the second section, a pretargeting approach, using a bispecific antibody in combination with a haptent-peptide, was applied and characterized for dual-modality imaging of prostate cancer (**chapter 3.3**). Finally, the feasibility of both dual-modality strategies for image-guided surgery was investigated.

GENERAL INTRODUCTION

PROSTATE CANCER

Malignancies of the prostate gland are one of the most significant health problems for the male population worldwide. In Europe, prostate cancer outnumbers lung and colorectal cancer, being the most common solid neoplasm with an incidence of 214 cases per 1000 men [1] and the second most common cause of death in men [2].

Several factors are known to drastically increase the risk for the development of prostate cancer, such as increasing age or heredity. Another risk factor for the development of adenocarcinoma of the prostate is ethnicity [3]. Other factors such as diet/nutrition, alcohol consumption, pattern of sexual behavior, chronic inflammation, and exposure to ultraviolet irradiation are being discussed to play a role in the development of prostate cancer and in the progression of latent prostate cancer to a clinical variant [4, 5]. At present, adenocarcinoma of the prostate are classified by the 2005 ISUP Modified Gleason scoring system.

First line diagnostic tools for prostate cancer include digital rectal examination (DRE), measurement of serum concentration of the prostate-specific antigen (PSA), and transrectal ultrasonography (TRUS) [3]. Most adenocarcinomas of the prostate are located in the peripheral zone of the gland. This fact allows the detection of lesions of a volume of 0.2 ml or larger. A suspect DRE represents a strong indication for (ultrasound-guided) biopsy of the prostate. In addition to DRE, serum levels of PSA can be measured for diagnostic purposes of prostate cancer. The kallikrein-like serine protease PSA is an organ-specific marker of the prostate gland and elevated levels of PSA are a strong indicator for disease processes in the prostate such as prostate carcinoma. However, since PSA is not cancer-specific, elevated levels of PSA are not only found in case of malignant disease, but can also be caused by benign diseases of the prostate, for instance benign prostatic hypertrophy (BPH) or prostatitis. So far, several modifications have been described to increase the specificity of PSA and to facilitate the discrimination between prostate cancer and BPH, such as the free/total PSA (f/t PSA) ratio. While the greatest amount of PSA in the blood is bound to serum proteins, a small amount circulates freely. In men with prostate cancer, the ratio between the amount of free and total PSA is decreased. However, several aspects limit the use of the f/t PSA ratio as an independent marker for prostate cancer, such as instability of free PSA especially at 4°C and room temperature, or variable assay characteristics [3]. In addition to more specific discrimination between malignant and benign diseases of the prostate, the f/t PSA ratio was found to decrease the number of unnecessary biopsies significantly [6].

Mainly based on PSA level and suspect DRE, but also taking into account the age of the patient, comorbidity and therapeutic consequences, a biopsy of the prostate can be performed. Currently, the standard method to obtain material for histopathologic examination is TRUS-guided biopsy. In case of negative biopsies, but persisting clinical suspicion for malignant involvement of the prostate, magnetic

resonance imaging (MRI) may provide information on the anterior lobe of the prostate. For the detection of metastases, pelvic CT/MRI or bone scans are recommended [11].

At present, the therapeutic management of prostate cancer is stage-specific. In low-risk prostate cancer, one approach is active surveillance. Initially, patients eligible for active surveillance are not treated, however in case of progressive disease, patients will receive curative treatment. Currently, radical prostatectomy involving removal of the entire prostate gland and resection of both seminal vesicles along with sufficient surrounding tissue to obtain a negative resection margin, is the surgical treatment option of choice for localized prostate cancer [11]. The intent of radical prostatectomy is curative in men with localized prostate cancer with a life expectancy of more than 10 years. Radical prostatectomy can be performed in open procedures, which include radical retropubic prostatectomy (RRP) and perineal prostatectomy. Currently however, robot-assisted laparoscopic radical prostatectomy (RALP) represents the gold standard surgical approach for clinically localized prostate cancer in the United States and is increasingly used in Europe. Compared to the non-laparoscopic approach, the percentage of RALP yielding negative-surgical margins seems to be equivalent. In intermediate-risk localized prostate cancer, radical prostatectomy should be accompanied by extended lymph node dissection if the estimated risk for positive lymph nodes exceeds 5%. In addition, this procedure should be performed in high-risk cases, where the estimated risk for positive lymph nodes is 15-40% [7, 11]. Among others, postoperative complications include persistent urinary incontinence, urinary fistulas, impotence, and bladder neck obstruction [11]. In case of adverse tumor characteristics such as extraprostatic involvement of the disease, presence of tumor cell containing resection margins, or seminal vesicle invasion, adjuvant radiotherapy may be used after recuperation from surgery [11]. In addition, neoadjuvant hormonal therapy can be considered prior to surgical interventions to decrease the size of hormone dependent prostate cancer lesions. While this attempt does not improve overall survival or disease-free survival, the rate of positive resection margins and lymph node invasion could be decreased significantly [8]. Another treatment option for prostate cancer is radiation therapy. Currently, intensity modulated radiotherapy (IMRT) with or without image guidance (IGRT) can be considered as the gold standard [11]. The addition of short-term androgen deprivation treatment (ADT) to external irradiation has been shown to improve overall survival in certain patient groups [11]. Another treatment option is transperitoneal brachytherapy, for which patients with low-risk prostate cancer are the most suitable candidates [11]. Alternative treatment options for patients with clinically localized prostate cancer are cryosurgical ablation of the prostate (CSAP) [9] and high-intensity ultrasound (HIFU) [10], with the latter still being considered an experimental treatment.

Treatment for advanced prostate cancer usually consists of a combination of several therapeutic options such as hormone, chemo-, or radiation therapy.

Initial treatment of men with metastatic prostate cancer is ADT with luteinizing hormone-releasing hormone (LHRH) agonists, anti-androgens, or a combined androgen blockade [11]. While the cancer lesions of most patients respond well to ADT initially, recurrence/progression of the disease after several years is common. When this occurs, the disease is considered to be castration resistant. In this case, secondary hormone therapy represents a treatment option since a portion of the cancer cells might still respond to androgen deprivation. Secondary hormone therapy includes addition or substitution of an anti-androgen by another type of androgen or prescription of another androgen blocking agent such as estrogen, steroids [11] or the antifungal medication ketoconazole [12, 13].

Other options to treat advanced disseminated prostate cancer are sipuleucel T, a dendritic cell vaccine, abiraterone, a drug blocking the production of androgens, and radium-223, a alpha-emitting radionuclide that localizes in bone and can be effective for the treatment of bone metastases. In addition, taxane chemotherapy for instance with docetaxel can be considered [11].

In follow-up after treatment with curative intent, serum PSA measurements and DRE should be performed 3, 6, and 12 months after treatment, then every 6 months until 3 years. After this, follow-up should be performed annually. For hormone therapy, patients should be evaluated at 3 and 6 months after initiation of the treatment. During the last decades, extensive research has been focused on the development of molecular imaging techniques that might improve prostate cancer detection. For diagnostic as well as therapeutic imaging purposes, specific targeting of the tumor is a prerequisite. Tumor targeting can be achieved with various strategies of which the binding of antibodies that target tumor-associated antigens is particularly promising.

TUMOR TARGETING

The term antibody (Antikörper) was first mentioned by the German scientist and Nobel Prize laureate Paul Ehrlich in 1891 [14]. In the following years, he proposed his theory for antibody and antigen interactions, hypothesizing that receptors on the cell surface could bind specifically to toxins in a lock-and-key interaction.

Several years later, tumor-associated antigens were identified and the idea emerged, that antibodies could be used to target these tumor specific cell surface molecules for diagnostic as well as therapeutic purposes. During the last decades, various tumor-associated antigens have been identified which are specific to either one single tumor entity or to multiple malignancies. Within this thesis, the targetability of several tumor-associated antigens such as PSMA (**chapter 2.2** and **3.2**), TROP-2 (**chapter 2.3** and **3.3**), or CEA (**chapter 2.4**) was evaluated.

Prostate-specific membrane antigen

The prostate-specific membrane antigen (PSMA) is a type II transmembrane protein (**figure 1**) [15]. PSMA is expressed in high levels in 95% of all prostate cancers [16]. In particular poorly differentiated, metastatic, and hormone refractory carcinomas express significantly higher levels of PSMA compared to benign prostate tissues [17]. Due to the selective overexpression of PSMA on the surface of prostate cancer cells, PSMA provides an excellent target for prostate cancer imaging [18]. Initial validation of PSMA as an *in vivo* target resulted from imaging with the monoclonal antibody capromab pendetide (7E11/CYT-356, ProstaScint), which was labeled to the radionuclide ^{111}In [19]. Capromab pendetide was FDA approved for imaging soft tissue metastatic lesions of prostate cancer for presurgical staging. Additionally, it was approved for evaluation of PSA relapse after local therapy. However, capromab binds to an intracellular domain of PSMA, which is considered a suboptimal target for imaging purposes. To overcome limitations due to intracellular localization of the target of capromab, anti-PSMA antibodies, such as J591, J415, and J533 have been developed [20], which bind to the extracellular domain of PSMA. These antibodies are considered to be more suitable for imaging approaches, since the binding site is more accessible for the targeting agent. PSMA-targeting with another monoclonal antibody (D2B) directed against the extracellular domain of PSMA is described in **chapter 2.2** and **3.2** of this thesis.

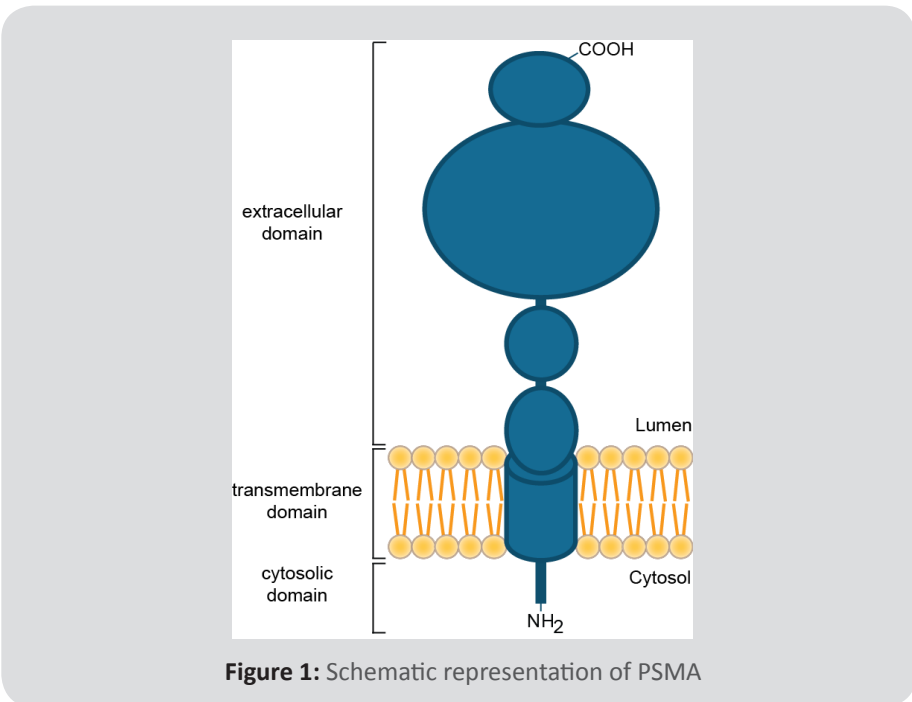


Figure 1: Schematic representation of PSMA

Epithelial glycoprotein-1

Another well described antigen is the epithelial glycoprotein-1, also known as EGP-1, TROP-2, GA733-1, gp50/T16, TACSTD2 (tumor-associated calcium signal transducer 2), which is a 46 kDa transmembrane glycoprotein expressed in carcinomas of the lung, bladder, breast, cervix, ovary, stomach and prostate [21]. While most normal human tissues do not express TROP-2, including lymph nodes, heart, connective tissues, blood vessels, stomach, jejunum and duodenum, TROP-2 is found at low levels in several normal glandular cells, including glands in the bronchus, breast, prostate and skin, and ducts and acini of the pancreas [22].

TROP-2 can be targeted by several antibodies, such as the humanized IgG1 monoclonal antibody hRS7, which was originally developed for human non-small cell carcinoma of the lung [22]. In addition, this antibody is reactive with bladder, breast, cervix, ovary, stomach and prostate carcinomas [23]. It has been shown previously, that hRS7 labeled with ^{111}In or ^{89}Zr is an excellent targeting agent to visualize TROP-2 expressing prostate cancer with SPECT or PET [23].

Carcinoembryonic antigen

The carcinoembryonic antigen (CEA) is a glycoprotein with a molecular mass of 180-200 kDa, which is attached to the cellular membrane by a glycosyl phosphatidylinositol anchor [24]. It consists for 60% of carbohydrates and has a molecular mass of 180-200 kDa. CEA is a tumor-associated antigen, that is overexpressed in 95% of colorectal cancers. CEA expression in tumors is approximately 60-fold higher compared to nonmalignant tissues [25].

So far, various antibodies have been developed which target CEA, such as the monoclonal antibodies hMN-14 [26] (labetuzumab) or T84.66 [27].

While achieving specific tumor targeting is one of the challenges for molecular imaging of cancer, another challenge is the visualization of the targeting agent, which is bound to its target. At present, multiple imaging modalities are available for these purposes, such as radionuclide imaging or fluorescence based-imaging approaches.

RADIONUCLIDE IMAGING

Radioactive decay refers to a process in which the nucleus of an unstable atom loses energy by spontaneous emission of ionizing radiation in form of photons and/or alpha/beta particles. Radionuclide imaging techniques such as positron emission tomography (PET) or single-photon emission tomography (SPECT) are based on detection of these emissions produced during radioactive decay. The use of radionuclide imaging in clinical practice is promoted by several advantages such as high sensitivity and the option to label targeting molecules with radionuclides

that allow accumulation of radionuclides in tissues of interest. Major limitations of nuclear imaging for clinical purposes are the use of ionizing radiation, the relatively low spatial resolution, and the lack of anatomical references.

PET and SPECT

In PET, image information is provided by two photons with an energy of 511 keV each, which are emitted in opposite directions, when a positron interacts with an electron in a process called annihilation. These photons are detected by a PET camera and localized by a series of opposing detectors that correspond to several rings of scintillation crystals. The acquisition of an image is based on simultaneous (coincidental) detection of the pairs of photons. Photons that are not detected pair wise, are ignored in this technique. After collection of sufficient events, a three-dimensional image can be reconstructed. An important advantage of PET is that fact that this technique is quantitative, which allows correlation between contrast agent and image intensity.

In SPECT imaging, as opposed to PET imaging, gamma emissions are measured directly using a (set of) rotating detectors, which acquire a series of two-dimensional projection images from multiple angles around the longitudinal axis of the patient/animal. Different techniques are available to reconstruct these tomographic images such as back-projection or Fourier transform reconstruction.

Radionuclides

Several factors should be considered when determining which radionuclide is most suitable for a particular medical application. First, the half-life of a radionuclide should be taken into account. For imaging with intact antibodies, radionuclides with longer half-life of days to weeks are suitable, since accumulation of intact antibodies in tumors takes several days. In addition, radionuclides with a longer half-life are useful in settings when imaging is required several times after injection. Radionuclides with a shorter physical half-life such as ^{18}F (110 min) or ^{68}Ga (68 min) are more suitable for imaging with antibody fragments or peptides owing to their fast pharmacokinetics and tumor accumulation. Due to the intermediate half-life of ^{111}In (2.8 days), this radionuclide is suitable for imaging with intact antibodies as well as antibody fragments or even peptides. ^{111}In was used as a radiotracer in several chapters of this thesis (**2.2, 2.3, 3.2, and 3.3**) in approaches using intact antibodies, antibody fragments, or pretargeting systems.

Another important consideration is the emission profile of the radionuclide. Depending on their emission profile, radionuclides can be used for SPECT or PET imaging purposes. For PET, one of the most widely used radionuclides is ^{18}F . The positron-emitter ^{18}F has ideal properties for PET due to the low energy of the positrons emitted (635 keV) that reveals optimal spatial resolution of PET images [28]. In addition, the lack of other emissions favors PET imaging. ^{68}Ga in contrast

has a higher positron energy (1899 keV), which limits the resolution of PET images. Advantage of ^{68}Ga over ^{18}F is that labeling procedures for ^{68}Ga are relatively straightforward, because ^{68}Ga can be chelated with macrocyclic chelates such as DOTA or NOTA. In contrast, the labeling of ^{18}F in general is cumbersome requiring labeling of a prosthetic group, deprotection and subsequent conjugation to a protein [29]. To benefit from the advantageous emission profile of ^{18}F , more efficient and straightforward labeling methods are desirable. In **chapter 2.4** of this thesis, a newly developed radiofluorination method is applied which allows ^{18}F -labeling to heat-sensitive molecules in a effective 2-step procedure.

For SPECT imaging, radionuclides which emit gamma rays with energies of 100 to 200 keV would be ideal [30]. For this imaging modality, radionuclides such as ^{111}In or $^{99\text{m}}\text{Tc}$ can be used.

Another important issue to be addressed is the availability of the radionuclide. ^{68}Ga for instance is generated by a $^{68}\text{Ge}/^{68}\text{Ga}$ generator, allowing ^{68}Ga generation on-demand. However, $^{68}\text{Ge}/^{68}\text{Ga}$ generators are not widely available. Radionuclides such as ^{18}F are produced in a cyclotron.

Radiolabeled targeting agents in prostate cancer

Recently, substantial progress has been made in the development of radionuclide imaging techniques for prostate cancer. The value of numerous radiolabeled tracers such as metabolite tracers, androgen receptor binding ligands, bombesin- and gastrin-releasing peptide receptor binding ligands, or antibodies, for the detection of prostate cancer has been evaluated. The recent advances and new developments in radionuclide imaging of prostate cancer are discussed in more detail in **chapter 2.1** of this thesis.

RADIOIMMUNOTHERAPY FOR PROSTATE CANCER

In radioimmunotherapy, radiolabeled antibodies or antibody fragments are used to target a certain cancer-specific antigen and deliver a therapeutic radiation dose. This approach allows delivery of radiation to tumor tissue but spares normal organs. Radioimmunotherapy can be administered either in a single dose or in multiple doses within a fractionated regimen. The effectiveness of this treatment modality depends on several factors, such as the cumulative radiation dose to the tumor, the dose-rate, and the tumor radiosensitivity [31]. Radioimmunotherapy has been studied extensively for several malignancies, mainly non-Hodgkin's lymphoma exploiting CD20-expression [31], but also solid tumors such as colorectal cancer and prostate cancer. So far, several clinical phase I trials have evaluated the role of the anti-PSMA antibody J591 for radioimmunotherapy of prostate cancer [32, 33]. In these studies, this antibody was labeled with ^{90}Y or ^{177}Lu and delivered to patients with metastatic castration-resistant prostate cancer.

These studies revealed a maximum tolerated dose (MTD) for a single administration regimen of 17.5 mCi/m² for ⁹⁰Y-J591 and 70 mCi/m² for ¹⁷⁷Lu-J591. In addition, dosimetry and pharmacokinetics were determined and preliminary evidence was provided for anti-tumor activity.

For radioimmunotherapy, it is crucial to carefully select the radionuclide to obtain an optimal balance between the therapeutic effect and unwanted side effects [24]. For therapeutic purposes, β -emitting radionuclides such as ¹⁷⁷Lu or ⁹⁰Y are suitable. Compared to ⁹⁰Y (half-life 2.7 days), the half-life of ¹⁷⁷Lu is relatively long (6.7 days). In addition, the penetration range of the beta-particles emitted by ¹⁷⁷Lu in tissue is 2.5 mm due to their low-energy (betamax 498 keV). As ⁹⁰Y emits higher energy (betamax 2.28 MeV), the penetration range in tissue is higher, resulting in a maximum of 12 mm [24]. Due to these properties, ¹⁷⁷Lu is more suitable for the treatment of small tumors and micro-metastases. In **chapter 2.3** of this thesis, the role of a pretargeting approach with the bispecific antibody TF12 and the ¹⁷⁷Lu-labeled peptide IMP288 for radioimmunotherapy of prostate cancer is evaluated.

FLUORESCENCE IMAGING

In certain settings, fluorescence imaging might be more suitable to visualize tumor-associated antigens than radionuclide imaging. In fluorescence imaging, a source of light with a specific wavelength is required to excite the fluorophore. Upon excitation, the electrons of the fluorophore remain in the excited state for approximately 10⁻⁸ seconds [34], called the lifetime of the fluorophore. This phase is followed by return of the fluorophore to its ground state, which may be accompanied by emission of a photon. The quantum yield is defined as the ratio of the number of photons emitted to the number of photons absorbed. Photons propagating to tissue, either generated by excitation light entering tissue from the outside, or generated after excitation of the fluorophore, are subject to three main parameters: light absorption, light scattering, and light reflection and refraction (**figure 2**). After excitation of the fluorophore, Stokes shift occurs, a phenomenon describing the shift from shorter wavelength (higher energetic state) to higher wavelength (lower energetic state). Absorption of photons can be caused by microscopic elements such as fatty acids, amino acids, ions, proteins, phospholipids, and water as well as larger structures such as organelles and cellular membranes. Due to limited tissue penetration depth caused by tissue absorption and scattering of light, applications for fluorescence imaging remained rather limited. This limitation can partially be overcome by adapting light to the near-infrared (NIR) regions (650 – 900 nm), as photons in the NIR range of light travel much deeper through tissue than photons in the visible light range (400 – 600 nm) [35], resulting in a tissue penetration depth in the millimeter to centimeter range [36]. In the NIR spectral region, the main absorbing elements

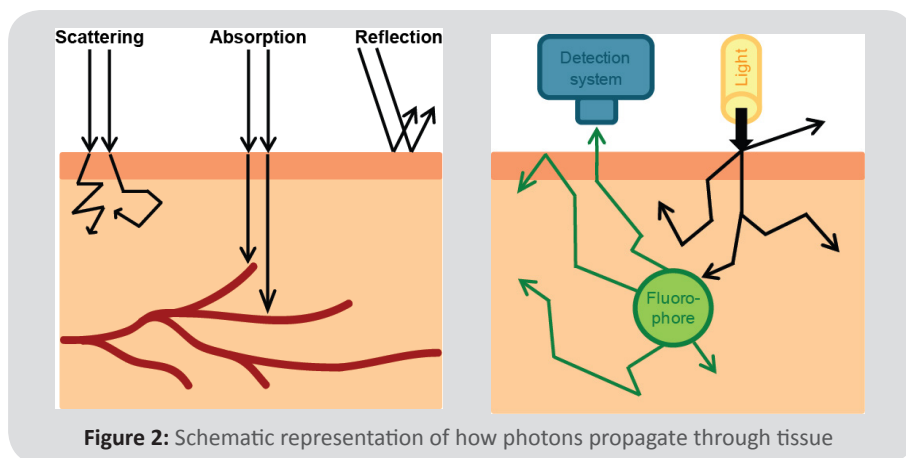


Figure 2: Schematic representation of how photons propagate through tissue

are deoxyhemoglobin, oxyhemoglobin, water, and lipids, which consequences in less absorption compared to light in the visible range, allowing deeper penetration of photons into the tissue [34].

The second phenomenon, scattering, is much more prominent than absorption of photons. The term scattering refers to a change in direction of the photons when traveling through tissue. Directional changes of the photons occur multiple times and result in a gradual randomization of the tissue penetration direction which consequences in a reduction of signal strength and accuracy. In general, after having propagated around 1 mm of tissue, photons have an equal probability of traveling in any direction. This, together with the fact that scattering occurs much more frequently than absorption, the transport of light through tissue can be regarded as an diffusive process [34].

However, scattering of photons on their way through tissue can be advantageous for near-infrared fluorescence (NIRF) imaging purposes as the path of the contorted light of photons that excite the fluorophore is similar to that of the emitted photons [34]. Consequently, highly scattering tissues cause retention of photons in that area and enhance the likelihood of induction of fluorescence [37].

The third parameter that influences photons on their way through tissue is reflection/refraction. Due to a mismatch between the refraction indices of tissue and air, photons emitted by the fluorophore will change their direction upon penetrating from tissue to air. Depending on the angle on which the photon reaches the tissue-to-air border, reflection of the fluorescent signal can occur. While the internal diffuse reflection coefficient remains negligibly small for perpendicular angles, the reflection coefficient can reach up to 50% at larger angles [34], resulting in backwards reflection of the fluorescent signal into the tissue and thereby causing an overall loss of signal intensity and an increase in diffusivity of the signal. In **chapter 3.1** of this thesis, the preclinical developments and the current clinical status of targeted fluorescence imaging combined with radionuclide imaging are reviewed.

Fluorescence imaging systems

The typical fluorescence imaging system consists of a spectrally-resolved light source which excites the fluorophores. Subsequently, the light which is emitted from the fluorophores is detected by a charge-coupled device (CCD) camera, whereas excitation light is filtered out. So far, several dedicated NIRF camera systems have been used for intra-operative optical imaging and image-guided surgery, including the Photodynamic Eye (PDE, Hamamatsu Photonics, Hamamatsu City, Japan) [38], and the Fluorescence-assisted Resection and Exploration (FLARE™) system, a self-build system from the Fragoni laboratory (Brookline, MA, USA) [39]. More recently, a smaller variant of the FLARE™ system, the Mini-FLARE™, has been developed by the same group. Another recently developed system is the Artemis imaging system (O2view, Marken, The Netherlands), a real-time imaging system combining visible light with NIRF light images.

In the studies described in this thesis (**chapter 3.2** and **3.3**), the IVIS Lumina II imaging system (Xenogen VivoVision IVIS Lumina II, Caliper Life Sciences, Lincolnshire, United Kingdom) was used. A schematic representation of this imaging system is displayed in **figure 3**.

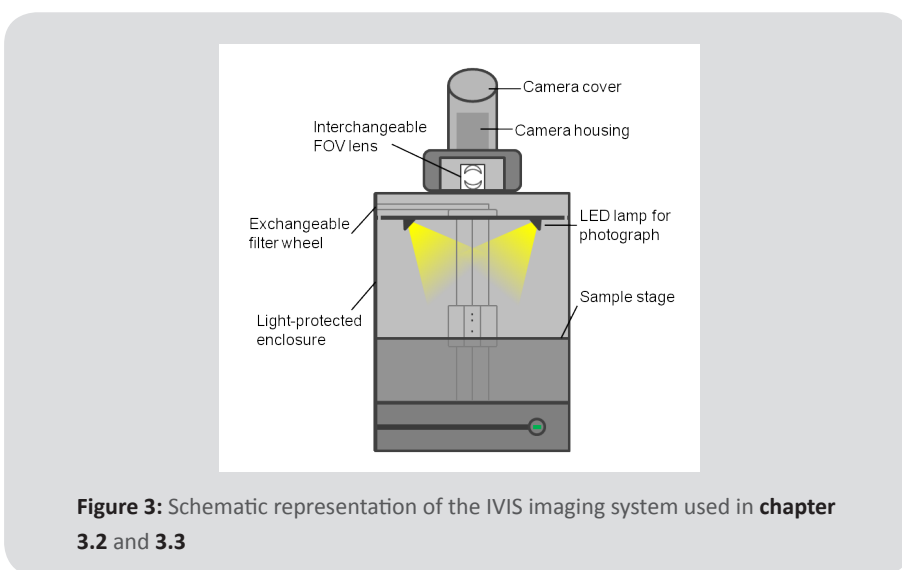


Figure 3: Schematic representation of the IVIS imaging system used in **chapter 3.2** and **3.3**

Fluorophores

For fluorescence imaging, various different fluorophores can be used, depending on the imaging purpose. For *in vivo* imaging purposes, fluorophores which emit light in the near-infrared fluorescent range are usually used since they have relatively deep tissue penetration. At present, NIR fluorophores can be categorized into two main classes, inorganic and organic NIR dyes [40]. Inorganic NIRF dyes mainly

associate with quantum dots and other nanoparticles. The use of inorganic NIRF dyes is mainly restricted by the potential cytotoxicity of nanoparticles due to heavy metal ingredients such as cadmium and selenium or surface-coatings. Major advantage of organic NIRF dyes is their feasibility for covalent conjugation with various molecules such as amino acids, nucleotides, DNA, or antibodies [40]. At present, various organic NIR fluorophores are being evaluated for biological imaging applications, such as cyanine dyes which are small organic molecules with two aromatic nitrogen-containing heterocycles linked by a polymethine bridge [40]. Another important organic fluorophore is IRDye800CW. This fluorophore possesses optimal characteristics for clinical uses. The toxicity of IRDye800CW carboxylate has been evaluated preclinically, showing no toxicity in doses up to 20mg/kg intravenously or intradermally [41]. In **chapter 3.2** and **3.3** of this thesis, targeting agents conjugated to both IRDye800CW and ^{111}In are evaluated regarding their tumor binding characteristics.

Ideal properties of NIR fluorophores are a large stokes shift, high molar absorption coefficient, and high quantum yield [40]. In addition, water solubility is a prerequisite to avoid dye aggregation in aqueous solutions. Moreover, the fluorophore should be chemically and photo-stable in solutions and biological conditions and suitable functional groups need to be present to allow bioconjugation to targeting molecules [40].

Fluorescence imaging in prostate cancer

So far, several preclinical studies have been focused on fluorescence imaging of prostate cancer. Humbert et al. developed a small molecule specific for PSMA and conjugated it to the fluorophore indocyanine green (ICG) [42]. It has been shown that this conjugate specifically binds to PSMA-expressing prostate cancer xenografts and can be visualized with NIRF imaging. Another group synthesized a PSMA NIRF imaging agent by conjugation of the PSMA inhibitor CTT-54.2 with the fluorophore Cy5.5 [43]. This probe was successfully applied for labeling of PSMA-expressing LNCaP cells in two- and three-dimensional cell cultures. Recently, Kelderhouse et al. conjugated a PSMA-targeting ligand to three different fluorophores (DyLight680, Alexa Fluor 647, and IRDye800CW) [44]. They demonstrated that this fluorescently labeled tumor-targeting probe can be used to visualize PSMA-expressing prostate tumor tissue *in vivo* and to perform image-guided resection of tumors. Jin et al. conjugated the monoclonal antibody H6-11, which recognizes a β -N-acetylglucoside group on PC3 cells, to IRDye800CW and performed optical imaging in mice with PC-3 tumors [45]. In this study, good tumor-to-muscle contrast was reported with clear visualization of the tumors on fluorescence images. Zhu et al. labeled the monoclonal anti-EpCAM antibody 7.4 to IRDye800CW and performed NIRF imaging in mice with prostate cancer lymph node metastases [46]. In this study, tumor lesions could be visualized specifically with NIRF imaging.

In addition to these preclinical studies, fluorescence imaging of prostate cancer has been evaluated clinically. Van der Poel et al. showed the applicability of sentinel lymph node imaging using multimodal ICG-^{99m}Tc-NanoColloid in prostate cancer patients [47]. They showed that this imaging agent can be used to facilitate the dissection of sentinel lymph nodes during RALP.

DUAL-MODALITY IMAGING

As described above, both radionuclide and fluorescence imaging can be used to image cancer lesions *in vivo*. While radionuclide imaging has high sensitivity and is suitable for the detection of even deeply seeded tumors, intra-operative application of this technique is limited and based on gamma probe detection. NIRF imaging in contrast, is suitable for intra-operative purposes and can provide real-time images of tumor lesions. However, fluorescence imaging is limited by a penetration depth in the millimeter range. By combination of radionuclide and fluorescence imaging, both techniques might complement each other and contribute to improvements in the detection and surgical removal of prostate cancer lesions. In **section 3** of this thesis, two dual-modality radionuclide and fluorescence imaging approaches are evaluated, one using a dual-labeled monoclonal antibody and one using pretargeting with a fluorescent ¹¹¹In-labeled peptide.

OPTIMIZATION OF ANTIBODY-BASED IMAGING

During the last decades, several strategies have been introduced to optimize tumor targeting. The main strategies for these purposes are the use of antibody fragments or pretargeting strategies.

Antibody fragments

In particular settings, visualization of tumor lesions might be required relatively early after injection of the radiolabeled antibody. For instance, when the patient's status needs to be evaluated several times within a short time interval or when imaging is required directly before and after treatment. Intact antibodies (157 kDa) clear relatively slowly from the circulation. Therefore, the optimal time for imaging with good tumor-to-background ratios is only reached several days after injection of the radiolabeled antibody.

In general, lower molecular weight agents provide higher target-to-nontarget ratios. Antibody fragments (F(ab')₂, Fab, scFv, diabodies, a.o.) represent promising candidates for radioimmunotargeting of cancer lesions (**figure 4**).

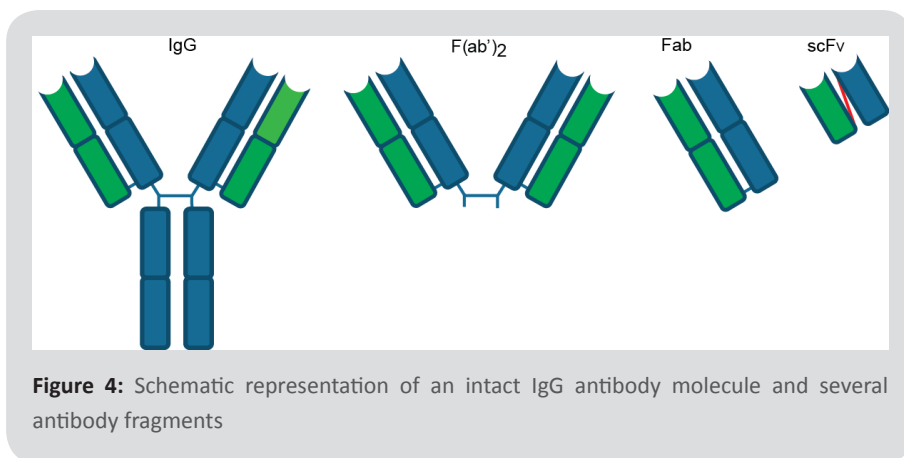


Figure 4: Schematic representation of an intact IgG antibody molecule and several antibody fragments

Thus, one strategy to optimize the targeting and clearance characteristics of antibodies against tumor-associated antigens is the development of antibody fragments. While it has been shown that the tumor uptake of antibody fragments is usually lower compared to the tumor uptake that is reached with intact antibody molecules [48, 49], antibody fragments are especially useful in settings when imaging is required early after injection. Due to the rapid clearance of antibody fragments, high tumor-to-background ratios can be reached as early as several hours after injection of the radiolabeled antibody fragment.

Most important limitation of imaging of cancer with antibody fragments is the fact that smaller sized imaging agents also tend to show high accumulation in the kidneys. In **chapter 2.2** of this thesis, antibody fragments are used to evaluate whether tumor targeting can be improved *in vivo* by the use of fragments compared to intact IgG molecules.

Pretargeting strategies

Visualization of tumors with antibodies might be hampered by slow clearance from the blood due to recycling via receptors. This results in low tumor-to-background ratios especially early after injection. In addition, it takes several days before sufficient accumulation of the antibody within the tumor is reached. As described earlier, these limitations can partially be overcome by the use of antibody fragments. Another promising approach to overcome these limitations and to improve tumor targeting and increase tumor-to-background ratios is the pretargeting approach. In pretargeting, tumor tissue is pretargeted with an unlabeled antibody construct (that is injected i.v. in the first phase). Subsequently, the construct will accumulate in the tumor via its specific binding sites. As soon as the antibody construct has been cleared from the blood, a radiolabeled peptide with affinity for the antibody construct is injected intravenously. The radioactive peptide will then distribute within the body

and bind to the antibody construct in the tumor. Unbound radioactive peptides will be cleared via the renal clearance route from the blood rapidly, due to their small size.

The concept of pretargeting has been proposed for the first time in 1984 [50]. Goodwin and colleagues proposed that tumors could be pretargeted with agents which possess specificity for both the tumor and a radiolabeled ligand. Since then, extensive research has been focused on the development of pretargeting strategies, resulting in two main approaches for pretargeting based on antibody constructs can be distinguished. First, the interaction between (strept)avidin and biotin can be exploited and secondly, bispecific antibodies (bsAb) can be used that possess both, affinity for tumor tissue as well as for the radiolabeled peptide (**figure 5**) [51].

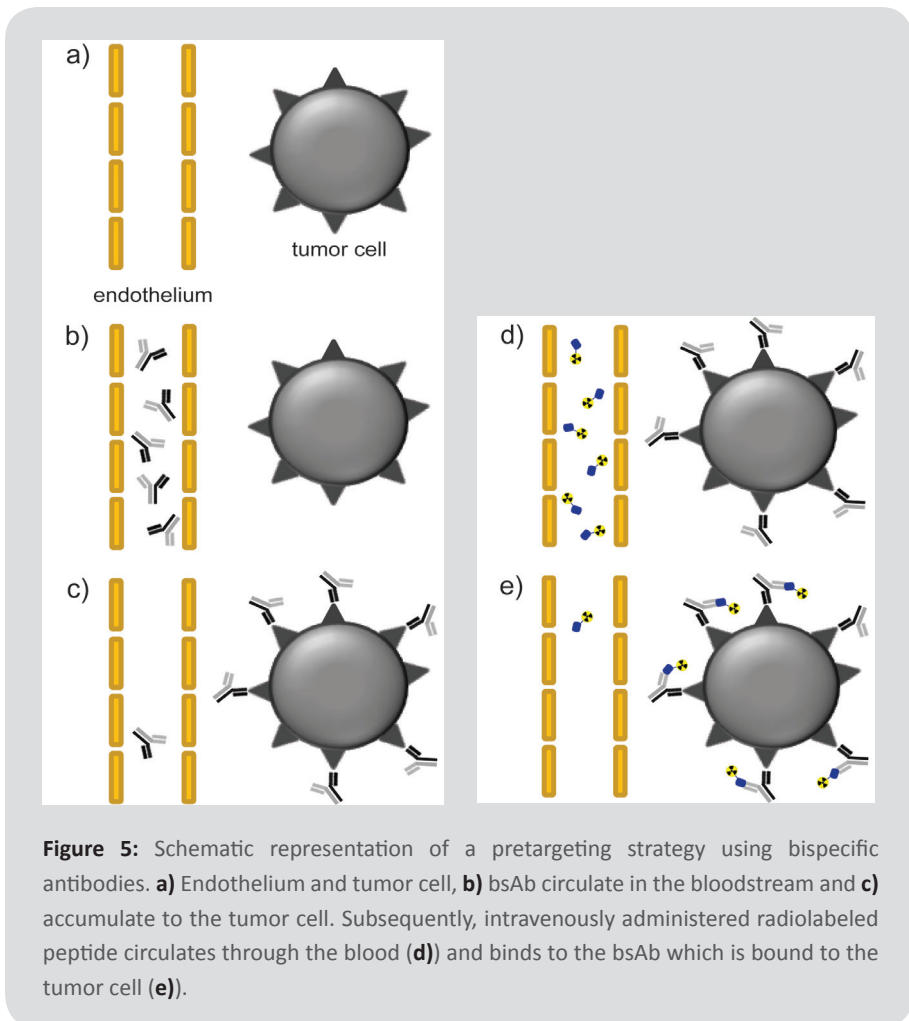


Figure 5: Schematic representation of a pretargeting strategy using bispecific antibodies. **a)** Endothelium and tumor cell, **b)** bsAb circulate in the bloodstream and **c)** accumulate to the tumor cell. Subsequently, intravenously administered radiolabeled peptide circulates through the blood (**d**) and binds to the bsAb which is bound to the tumor cell (**e**).

The first pretargeting strategy is based on the avid binding of avidin to biotin. The protein avidin is a constituent of the egg white of amphibians and birds that can bind to biotin (vitamin H) [52] with high affinity ($K_a = 10^{15} \text{ M}^{-1}$) [53, 54]. Alternatively, the bacterial analog streptavidin can be used for pretargeting purposes, since it has comparable biotin-binding characteristics. However, the retention of streptavidin in healthy tissues is lower compared to avidin [55].

These (strept)avidin – biotin pretargeting approaches have several limitations compared to pretargeting approaches using bsAb. First, due to the high affinity of (strept)avidin to biotin, both agents also complex in the circulatory system. Consequently, tumor uptake will be lower. To overcome this limitation, clearing agents could be used that remove the excess of the antibody conjugate from the circulation prior to administration of the radioactive small molecule. However, another disadvantage restricting the use of (strept)avidin – biotin pretargeting approaches is the fact that (strept)avidin is immunogenic in humans and can only be applied once to a patient.

Pretargeting with bispecific antibodies

Major advantage of the pretargeting approach using bsAb however is the fact that bsAb can be humanized which reduces the immunogenicity. In general, bsAb can be produced in three different ways: 1. Biologically by fusion of two hybridoma cell lines which produce two parental monoclonal antibodies, 2. chemically by conjugation of antibody fragments, and 3. by recombinant DNA methods producing fusion proteins of single chain antibodies of antibody fragments. Bispecific antibodies can be produced with different valencies: It has been shown that malignant tissues can be pretargeted in a more efficient ways when the bsAb is trivalent and consists of a $F(ab')_2$ and a Fab fragment compared to bivalent bsAb, consisting of two Fab fragments [56]. Trivalent bsAb have dual specificity of the tumor antigen, while they are monospecific for the radioactive peptide. Consequently, the bsAb is more effectively trapped in the tumor. To produce humanized trivalent bsAb constructs efficiently, the dock-and-lock methodology was introduced by Rossi et al. in 2006. This technology is based on the dimerization and docking domain of cAMP-dependent protein kinase A. Both anti-tumor Fab fragments form dimers. The dimer sequence of this construct has high affinity for the anti-hapten Fab (docking). Subsequently, cysteine residues are placed to form disulfide bridges which stabilize the trivalent bsAb (locking) [24]. So far, dock-and-lock conjugates have been synthesized for several malignancies, including colorectal cancer (anti-CEA x anti-HSG bsAb TF2 [57]) or prostate cancer (anti-TROP-2 x anti-HSG bsAb TF12).

Practical considerations in pretargeting

In pretargeting, the administration of both the bispecific antibody as well as the peptide need to be tuned carefully to obtain maximum tumor-to-background ratios.

Two main factors determine the tumor targeting capacity gained by this approach: (i) the interval between administration of the bispecific antibody and the peptide, and (ii) the dose of both agents. Both aspects have been evaluated in previous studies.

The interval between administration of bispecific antibody and peptide is mainly determined by the blood clearance and tumor accretion of the bispecific antibody over time. However, the interval should not be too long either, as the retention time of the antibody at the binding site at the tumor can be limited. Therefore, the best compromise between low tracer amounts in the blood and highest tracer accumulation in the tumor should be used. For TF-based antibodies, the interval between administration of antibody and peptide is approximately 16-18 hours. The same concept applies for the interval between administration of the peptide and image acquisition. Optimal images will be acquired when tracer accumulation within the circulation is low and accumulation to the tumor is high. Usually, this interval is approximately 1-2 hours.

The second aspect to be considered is the dosing of both bispecific antibody and peptide. While increasing the dose of the bispecific antibody can improve tumor targeting, the dose should not be too high to prevent saturation of the antigens expressed in the tumor. In addition, the dose of the peptide needs to be taken into account. For imaging purposes, this dose is mainly determined by the radiolabeling procedure and the minimum amount of peptide that is required to label the desirable amount of radioactivity [24]. In general, a low dose of the peptide leads to a higher ratio between bispecific antibody and peptide in the circulation. As a consequence, a relatively higher amount of circulating peptide could be captured by the remaining bsAb in the circulation. This would increase the circulatory half-life of the peptide. In addition, less peptide would be available to accumulate to the tumor.

Pretargeting agents for prostate cancer

The monoclonal antibody hRS7 is a humanized IgG1 monoclonal antibody, which is directed against TROP-2. Previous studies in nude mice with prostate cancer xenografts have shown excellent *in vivo* targeting of the TROP-2 expressing tumors [23].

However, as hRS7, like all intact monoclonal antibodies, clears slowly from the circulatory system, tumor-to-background ratios, especially at early time points after injection, were poor. To improve this, the bsAb TF12 (molecular weight 157 kDa) was developed for pretargeting of TROP-2 expressing tumors. TF12 is a trivalent bispecific antibody consisting of two anti-TROP-2 Fab fragments and one anti-HSG (histamine-succinyl-glycine) Fab fragment. Via the latter Fab fragment, TF12 has a high affinity for the DOTA (7,10-tetra-azacyclododecane-N,N',N'',N''')-tetraacetic acid conjugated D-Tyr-D-Lys-D-Glu-D-Lys tetrapeptide IMP288 (molecular weight 1456 Da), in which both NH₂ groups of the lysine residues are substituted with a HSG-moiety, forming DOTA-D-Tyr-D-Lys(HSG)-D-Glu-D-Lys(HSG)-NH₂. In **chapter 2.3**

of this thesis, the feasibility of TF12 and IMP288 for pretargeting prostate cancer is evaluated. In addition, in **chapter 3.3** of this thesis, the fluorescent peptide RDC018 which is derived from IMP288 and contains a IRDye800CW moiety, is used for dual-modality imaging in TF12-pretargeted prostate cancer. A schematic representation of TF12, IMP288 and RDC018 is provided in **figure 6**.

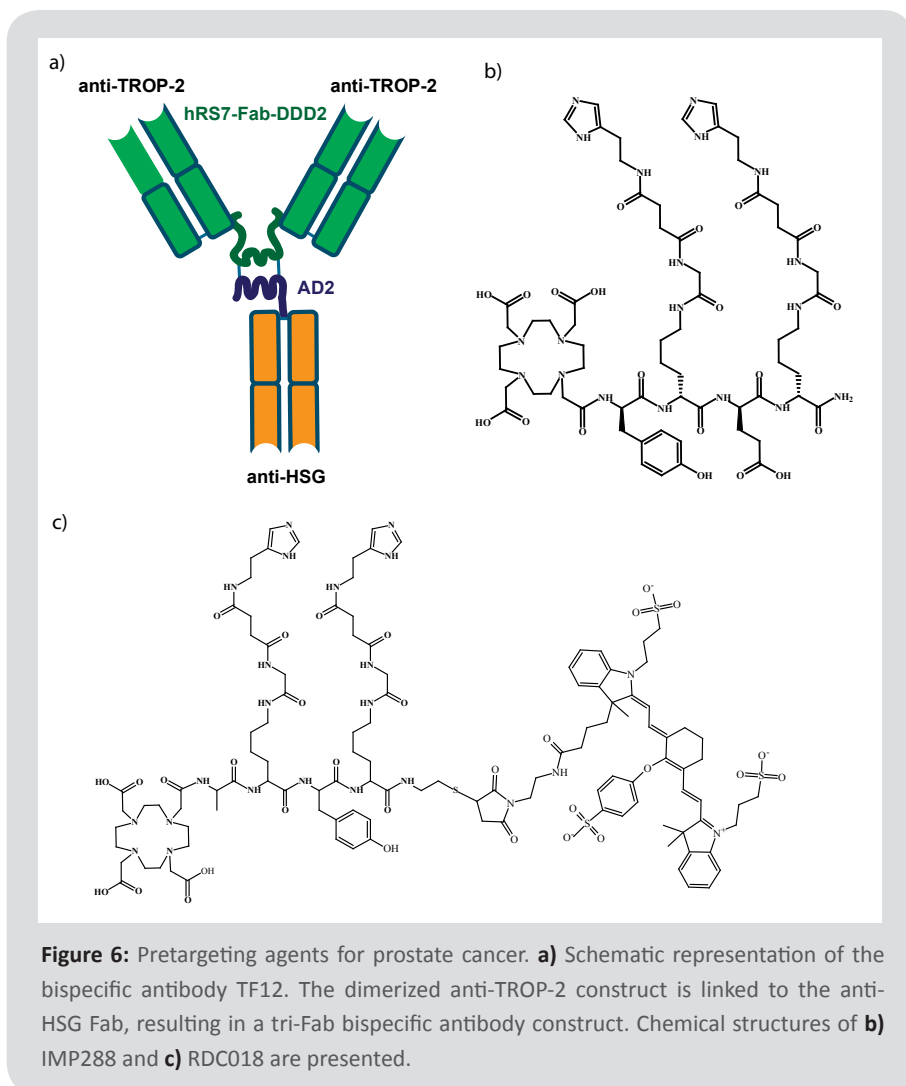


Figure 6: Pretargeting agents for prostate cancer. **a)** Schematic representation of the bispecific antibody TF12. The dimerized anti-TROP-2 construct is linked to the anti-HSG Fab, resulting in a tri-Fab bispecific antibody construct. Chemical structures of **b)** IMP288 and **c)** RDC018 are presented.

REFERENCES

- (1) Boyle P, Ferlay J. Cancer incidence and mortality in Europe, 2004. *Ann Oncol.* 2005; 16(3):481-488
- (2) Jemal A, Siegel R, Ward E, Hao Y, Xu J, Murray T, Thun MJ. Cancer statistics. 2008. *CA Cancer J Clin.* 2008; 58(2):71-96
- (3) Heidenreich A, Bellmunt J, Bolla M, Joniau S, Mason M, Matveev V, Mottet N, Schmid HP, van der Kwast T, Wiegel T, Zattoni F; European Association of Urology. EAU guidelines on prostate cancer. Part 1: screening, diagnosis, and treatment of clinically localised disease. *Eur Urol.* 2011; 59(1):61-71
- (4) Leitzmann MF, Rohrmann S. Risk factors for the onset of prostatic cancer: age, location, and behavioral correlates. *Clin Epidemiol.* 2012; 4:1-11
- (5) Nelson WG, De Marzo AM, Isaacs WB. Prostate cancer. *N Engl J Med.* 2003; 349(4):366-381
- (6) Kobori Y, Kitagawa Y, Mizokami A, Komatsu K, Namiki M. Free-to-total prostate-specific antigen (PSA) ratio contributes to an increased rate of prostate cancer detection in a Japanese population screened using a PSA level of 2.1-10.0 ng/ml as a criterion. *Int J Clin Oncol.* 2008; 13(3):229-232
- (7) Briganti A, Larcher A, Abdollah F, Capitanio U, Gallina A, Suardi N, Bianchi M, Sun M, Freschi M, Salonia A, Karakiewicz PI, Rigatti P, Montorsi F. Updated nomogram predicting lymph node invasion in patients with prostate cancer undergoing extended pelvic lymph node dissection: the essential importance of percentage of positive cores. *Eur Urol.* 2012; 61(3):480-487
- (8) Shelley MD, Kumar S, Wilt T, Staffurth J, Coles B, Mason MD. A systematic review and meta-analysis of randomised trials of neo-adjuvant hormone therapy for localised and locally advanced prostate carcinoma. *Cancer Treat Rev.* 2009; 35(1):9-17
- (9) Fahmy WE, Bissada NK. Cryosurgery for prostate cancer. *Arch Androl.* 2003; 49(5):397-407
- (10) Aus G. Current status of HIFU and cryotherapy in prostate cancer--a review. *Eur Urol.* 2006; 50(5):927-934
- (11) Heidenreich A, Bastian PJ, Bellmunt J, Bolla M4, Joniau S, van der Kwast T, Mason M, Matveev V, Wiegel T, Zattoni F, Mottet N. EAU Guidelines on Prostate Cancer. Part II: Treatment of Advanced, Relapsing, and Castration-Resistant Prostate Cancer. *Eur Urol.* 2014; 65(2):467-479
- (12) Eichenberger T, Trachtenberg J, Toor P, Keating A. Ketoconazole: a possible direct cytotoxic effect on prostate carcinoma cells. *J Urol.* 1989; 141(1):190-191
- (13) Small EJ, Halabi S, Dawson NA, Stadler WM, Rini BI, Picus J, Gable P, Torti FM, Kaplan E, Vogelzang NJ. Antiandrogen withdrawal alone or in combination with ketoconazole in androgen-independent prostate cancer patients: a phase III trial (CALGB 9583). *J Clin Oncol.* 2004; 22(6):1025-1033
- (14) Paul Ehrlich, *Experimental Studies on Immunity*, 1891
- (15) Israeli RS, Powell CT, Fair WR, Heston WDW. Molecular cloning of a complementary DNA encoding a prostate specific membrane antigen. *Cancer Res.* 1993; 53(2): 227-230

- (16) Yao V, Bacich DJ. Prostate specific membrane antigen (PSMA) expression gives prostate cancer cells a growth advantage in a physiologically relevant folate environment in vitro. *Prostate*. 2006; 66(8):867-875
- (17) Wright GL Jr, Grob BM, Haley C, Grossman K, Newhall K, Petrylak D, Troyer J, Konchuba A, Schellhammer PF, Moriarty R. Upregulation of prostate-specific membrane antigen after androgen-deprivation therapy. *Urology*. 1996; 48(2):326-334
- (18) Ross JS, Sheehan CE, Fisher HA, Kaufman RP, Jr, Kaur P, Gray K, Webb I, Gray GS, Mosher R, Kallakury BV. Correlation of primary tumor prostate-specific membrane antigen expression with disease recurrence in prostate cancer. *Clin Cancer Res*. 2003; 9(17):6357-6362
- (19) Horoszewicz JS, Kawinski E, Murphy GP. Monoclonal antibodies to a new antigenic marker in epithelial prostatic cells and serum of prostatic cancer patients. *Anticancer Res*. 1987; 7(5B):927-935
- (20) Smith-Jones PM, Vallabhajosula S, Navarro V, Bastidas D, Goldsmith SJ, Bander NH. Radiolabeled monoclonal antibodies specific to the extracellular domain of prostate-specific membrane antigen: Preclinical studies in nude mice bearing LNCaP human prostate tumor. *J Nucl Med*. 2003; 44(4):610-617
- (21) Basu A, Goldenberg DM, Stein R. The epithelial/carcinoma antigen EGP-1, recognized by monoclonal antibody RS7-3G11, is phosphorylated on serine 303. *Int J Cancer*. 1995; 62(4):472-479
- (22) Stein R, Basu A, Chen S, Shih LB, Goldenberg DM. Specificity and properties of MAb RS7-3G11 and the antigen defined by this pancarcinoma monoclonal antibody. *Int J Cancer*. 1993; 55(6):938-946
- (23) van Rij CM, Sharkey RM, Goldenberg DM, Frielink C, Molkenboer JD, Franssen GM, van Weerden WM, Oyen WJ, Boerman OC. Imaging of prostate cancer with immuno-PET and immuno-SPECT using a radiolabeled anti-EGP-1 monoclonal antibody. *J Nucl Med*. 2011; 52(10):1601-1607
- (24) Schoffelen R. Pretargeted Radioimmunodetection and -therapy in colorectal cancer. Doctoral Thesis.
- (25) Boucher D, Cournoyer D, Stanners CP, Fuks A. Studies on the control of gene expression of the carcinoembryonic antigen family in human tissue. *Cancer Res*. 1989; 49(4):847-852
- (26) Sharkey RM, Juweid M, Shevitz J, Behr T, Dunn R, Swayne LC, Wong GY, Blumenthal RD, Griffiths GL, Siegel JA, et al. Evaluation of a complementarity-determining region-grafted (humanized) anti-carcinoembryonic antigen monoclonal antibody in preclinical and clinical studies. *Cancer Res*. 1995; 55(23 Suppl):5935s-5945s
- (27) Wagener C, Clark BR, Rickard KJ, Shively JE. Monoclonal antibodies for carcinoembryonic antigen and related antigens as a model system: determination of affinities and specificities of monoclonal antibodies by using biotin-labeled antibodies and avidin as precipitating agent in a solution phase immunoassay. *J Immunol*. 1983; 130(5):2302-2307
- (28) Visser EP, Disselhorst JA, Brom M, Laverman P, Gotthardt M, Oyen WJ, Boerman OC. Spatial resolution and sensitivity of the Inveon small-animal PET scanner. *J Nucl Med*. 2009; 50(1):139-147

- (29) Miller PW, Long NJ, Vilar R, Gee AD. Synthesis of ^{11}C , ^{18}F , ^{15}O , and ^{13}N radiolabels for positron emission tomography. *Angew Chem Int Ed Engl*. 2008; 47(47):8998-9033
- (30) Zanzonico P. Principles of nuclear medicine imaging: planar, SPECT, PET, multi-modality, and autoradiography systems. *Radiat Res*. 2012; 177(4):349-364
- (31) Bouchelouche K, Tagawa ST, Goldsmith SJ, Turkbey B, Capala J, Choyke P. PET/CT Imaging and Radioimmunotherapy of Prostate Cancer. *Semin Nucl Med*. 2011; 41(1):29-44
- (32) Milowsky MI, Nanus DM, Kostakoglu L, Vallabhajosula S, Goldsmith SJ, Bander NH. Phase I trial of yttrium-90-labeled anti-prostate-specific membrane antigen monoclonal antibody J591 for androgen-independent prostate cancer. *J Clin Oncol*. 2004; 22(13):2522-2531
- (33) Bander NH, Milowsky MI, Nanus DM, Kostakoglu L, Vallabhajosula S, Goldsmith SJ. Phase I trial of ^{177}Lu -labeled J591, a monoclonal antibody to prostate-specific membrane antigen, in patients with androgen-independent prostate cancer. *J Clin Oncol*. 2005; 23(21):4591-4601
- (34) Keereweer S, Van Driel PB, Snoeks TJ, Kerrebijn JD, Baatenburg de Jong RJ, Vahrmeijer AL, Sterenborg HJ, Löwik CW. Optical image-guided cancer surgery: challenges and limitations. *Clin Cancer Res*. 2013; 19(14):3745-3754
- (35) Patterson MS, Chance B, Wilson BC. Time resolved reflectance and transmittance for the non-invasive measurement of tissue optical properties. *Appl Opt*. 1989; 28(12):2331-2336
- (36) Fomina N, McFearin CL, Sermsakdi M, Morachis JM, Almutairi A. Low power, biologically benign NIR light triggers polymer disassembly. *Macromolecules*. 2011; 44(21):8590-8597
- (37) Star WM. Light dosimetry in vivo. *Phys Med Biol*. 1997; 42(5):763-787
- (38) Keereweer S, Kerrebijn JD, van Driel PB, Xie B, Kaijzel EL, Snoeks TJ, Que I, Hutteman M, van der Vorst JR, Mieog JS, Vahrmeijer AL, van de Velde CJ, Baatenburg de Jong RJ, Löwik CW. Optical image-guided surgery - where do we stand? *Mol Imaging Biol*. 2011; 13(2):199-207
- (39) De Grand AM, Frangioni JV. An operational near-infrared fluorescence imaging system prototype for large animal surgery. *Technol Cancer Res Treat*. 2003; 2(6):553-562
- (40) Luo S, Zhang E, Su Y, Cheng T, Shi C. A review of NIR dyes in cancer targeting and imaging. *Biomaterials*. 2011; 32(29):7127-7138
- (41) Marshall MV, Draney D, Sevick-Muraca EM, Olive DM. Single-dose intravenous toxicity study of IRDye 800CW in Sprague-Dawley rats. *Mol Imaging Biol*. 2010; 12(6):583-594
- (42) Humblet V, Lapidus R, Williams LR, Tsukamoto T, Rojas C, Majer P, Hin B, Ohnishi S, De Grand AM, Zaheer A, Renze JT, Nakayama A, Slusher BS, Frangioni JV. High-affinity near-infrared fluorescent small-molecule contrast agents for in vivo imaging of prostate-specific membrane antigen. *Mol Imaging*. 2005; 4(4):448-462
- (43) Liu T, Wu LY, Hopkins MR, Choi JK, Berkman CE. A targeted low molecular weight near-infrared fluorescent probe for prostate cancer. *Bioorg Med Chem Lett*. 2010; 20(23):7124-7126

- (44) Kelderhouse LE, Chelvam V, Wayua C, Mahalingam S, Poh S, Kularatne SA, Low PS. Development of tumor-targeted near infrared probes for fluorescence guided surgery. *Bioconjug Chem*. 2013; 24(6):1075-1080
- (45) Jin H, Xu M, Padakanti PK, Liu Y, Lapi S, Tu Z. Preclinical evaluation of the novel monoclonal antibody H6-11 for prostate cancer imaging. *Mol Pharm*. 2013; 10(10):3655-3664
- (46) Zhu B, Wu G, Robinson H, Wilganowski N, Hall MA, Ghosh SC, Pinkston KL, Azhdarinia A, Harvey BR, Sevic-Muraca EM. Tumor margin detection using quantitative NIRF molecular imaging targeting EpCAM validated by far red gene reporter iRFP. *Mol Imaging Biol*. 2013; 15(5):560-568
- (47) van der Poel HG, Buckle T, Brouwer OR, Valdés Olmos RA, van Leeuwen FW. Intraoperative laparoscopic fluorescence guidance to the sentinel lymph node in prostate cancer patients: clinical proof of concept of an integrated functional imaging approach using a multimodal tracer. *Eur Urol*. 2011; 60(4):826-833
- (48) Heskamp S, van Laarhoven HW, Molkenboer-Kuenen JD, Bouwman WH, van der Graaf WT, Oyen WJ, Boerman OC. Optimization of IGF-1R SPECT/CT Imaging Using (¹¹¹In)-Labeled F(ab')₂ and Fab Fragments of the Monoclonal Antibody R1507. *Mol Pharm*. 2012; 9(8):2314-2321
- (49) Fleuren ED, Versleijen-Jonkers YM, Heskamp S, Roeffen MH, Bouwman WH, Molkenboer-Kuenen JD, van Laarhoven HW, Oyen WJ, Boerman OC, van der Graaf WT. The strength of small: improved targeting of insulin-like growth factor-1 receptor (IGF-1R) with F(ab')₂-R1507 fragments in Ewing sarcomas. *Eur J Cancer*. 2013; 49(13):2851-2858
- (50) Goodwin D, Meares C, Diamanti C, McCall M, Lai C, Torti F, McTigue M, Martin B. Use of specific antibody for rapid clearance of circulating blood background from radiolabeled tumor imaging proteins. *Eur J Nucl Med*. 1984; 9(5):209-215
- (51) Boerman OC, van Schaijk FG, Oyen WJ, Corstens FH. Pretargeted radioimmunotherapy of cancer: progress step by step. *J Nucl Med*. 2003; 44(3):400-411
- (52) Lindqvist Y, Schneider G. Protein-biotin interactions. *Curr Opin Struct Biol*. 1996; 6(6):798-803
- (53) Hnatowich DJ, Virzi F, Rusckowski M. Investigations of avidin and biotin for imaging applications. *J Nucl Med*. 1987; 28(8):1294-1302
- (54) Paganelli G, Magnani P, Fazio F. Pretargeting of carcinomas with the avidin-biotin system. *Int J Biol Markers*. 1993; 8(3):155-159
- (55) Schechter B, Silberman R, Arnon R, Wilchek M. Tissue distribution of avidin and streptavidin injected to mice. Effect of avidin carbohydrate, streptavidin truncation and exogenous biotin. *Eur J Biochem*. 1990; 189(2):327-331
- (56) Karacay H, Sharkey RM, McBride WJ, Griffiths GL, Qu Z, Chang K, Hansen HJ, Goldenberg DM. Pretargeting for cancer radioimmunotherapy with bispecific antibodies: role of the bispecific antibody's valency for the tumor target antigen. *Bioconjug Chem*. 2002; 13(5):1054-1070
- (57) Schoffelen R, Sharkey RM, Goldenberg DM, Franssen G, McBride WJ, Rossi EA, Chang CH, Laverman P, Disselhorst JA, Eek A, van der Graaf WT, Oyen WJ, Boerman OC. Pretargeted immuno-positron emission tomography imaging of carcinoembryonic antigen-expressing tumors with a bispecific antibody and a ⁶⁸Ga- and ¹⁸F-labeled hapten peptide in mice with human tumor xenografts. *Mol Cancer Ther*. 2010; 9(4):1019-1027

Chapter 2.1

Prospects in radionuclide imaging of prostate cancer

Chapter 2.2

Targeting human prostate cancer with ^{111}In -labeled D2B IgG, F(ab')_2 and Fab fragments in nude mice with PSMA-expressing xenografts

Chapter 2.3

Pretargeted immuno-PET and radioimmunotherapy of prostate cancer with an anti-TROP-2 x anti-HSG bispecific antibody

Chapter 2.4

Anti-CEA fragments labeled with ^{18}F AIF for PET imaging of CEA-expressing tumors

Strategies to optimize antibody-based imaging of cancer

2

2.1

Prospects in radionuclide imaging of prostate cancer

Susanne Lütje¹

Otto C. Boerman¹

Catharina M. van Rij¹

Michiel Sedelaar²

Wijnand Helfrich³

Wim J.G. Oyen¹

Peter F.A. Mulders²

¹ Department of Radiology and Nuclear Medicine,
Radboud University Medical Center, Nijmegen, The Netherlands

² Department of Urology, Radboud University Medical Center,
Nijmegen, The Netherlands

³ Department of Surgery, University Medical Centre Groningen,
Groningen, The Netherlands

ABSTRACT

Prostate cancer is the most common malignancy in men in the Western world and represents a major health problem with substantial morbidity and mortality. Sensitivity and specificity of digital rectal examination (DRE) and evaluation of the prostate-specific antigen (PSA) are suitable for diagnosis of prostate cancer, but have limited value for staging. Imaging of prostate cancer has become increasingly important to improve staging and management of prostate cancer patients. Conventional imaging modalities, such as transrectal ultrasound and computed tomography show limited accuracy for a reliable assessment of prostate cancer. The diagnostic value of magnetic resonance imaging has improved by dynamic contrast enhancement (DCI-MRI) and diffusion-weighted magnetic resonance imaging (DWI). Recently, substantial progress has been made in the development of functional and molecular imaging modalities, such as positron emission tomography using radiolabeled metabolic tracers, receptor-binding ligands, amino acids, peptides, or antibodies. Here, we review the value of these novel radionuclide imaging techniques in the assessment of prostate cancer.

INTRODUCTION

Prostate cancer remains the most common malignancy in men in Europe, with an incidence of 382,000 cases and a mortality rate of 89,000 in 2008 [1]. In early stages of the disease, neoplastically transformed prostate cells are confined to the prostate gland. In later stages, malignant cells metastasize to other parts of the body, typically including bones and lymph nodes. Currently, metastatic prostate cancer is essentially incurable. Therefore, early diagnosis represents the most effective strategy with a change for curative treatment options and consequently minimizes prostate cancer-related mortality [2].

At present, in the US, screening for prostate cancer is advisable for men above 40 years of age by evaluation of the prostate-specific antigen levels (PSA) and by digital rectal examination (DRE). When abnormalities are suspected or have been found, further evaluation is commenced, typically by taking transrectal ultrasound (TRUS)-guided biopsy [3]. The most commonly used histopathological grading system for prostate cancer is the Gleason score. Together with other patient parameters like age, health state, PSA levels, and biopsy pathology, the Gleason grading system predicts prognosis and helps to guide therapeutic management. Patients with a low Gleason score have well to moderately differentiated prostate cancer histology and usually have localized disease. These early-stage patients can have a very indolent course of the disease with low mortality rates and can be monitored by watchful waiting to prevent overtreatment and treatment-related morbidity.

Curative treatment of confined prostate cancer includes radical prostatectomy performed either as an open conventional procedure or by (robot-assisted) laparoscopic surgery and may be combined with various forms of radiation therapy (RT), including 3-dimensional conformal RT, intensity-modulated RT, or proton beam RT [4]. Other curative treatment options include brachytherapy combined with external-beam RT, high-intensity focused ultrasound, and cryosurgery. However, in a substantial proportion of prostate cancer patients, primary curative treatment fails, as becomes evident by frequent recurrences of the disease. In general, the first sign indicating treatment failure is a shorter doubling time of PSA serum levels that may occur months or even years before development of clinical symptoms or radiographic indications for recurrent disease. However, the diagnostic use of PSA levels has several important drawbacks. Due to low sensitivity and specificity, the diagnostic value of PSA levels is limited and may yield both false-negative and false-positive results, leading to under- and overtreatment, respectively. Most notably, evaluation of PSA levels fails to differentiate between local and metastatic disease, which is in fact a prerequisite for appropriate management of the disease [5]. Therefore, new highly sensitive and specific imaging modalities for accurate visualization of prostate cancer and reliable monitoring of therapy response are urgently needed. Radionuclide imaging techniques such as PET and SPECT are very sensitive imaging

modalities as picomolar amounts of tracers can be detected. Depending on the radiotracer used, these techniques can visualize specific molecular processes.

Here, we review conventional and novel imaging modalities in prostate cancer and discuss the new developments in radionuclide imaging of prostate cancer in more detail.

CONVENTIONAL IMAGING METHODS

Transrectal Ultrasound

Today, transrectal ultrasound (TRUS) is the most commonly used technique for further clinical evaluation of size and anatomy of the prostate gland. TRUS has several advantages including high level of safety, favorable portability, relatively low costs, ease of use, and the possibility to perform real-time imaging. However, several disadvantages like low resolution, sensitivity, and specificity limit the reliability of TRUS. In particular, TRUS has a limited ability to delineate small cancer foci which usually are isoechoic and therefore cannot be detected. Moreover, the majority of hypoechoic foci detected by TRUS are not malignant, but rather represent conditions such as benign prostatic hyperplasia (BPH), atrophy, or inflammatory processes in the prostate gland [6].

Currently, several modulations of TRUS are clinically available, including Doppler TRUS and contrast-enhanced TRUS with microbubbles. Using Doppler TRUS, regions of tumors with hypervascularity can be detected. However, since many small tumors are not angiogenic, the sensitivity of Doppler TRUS is not significantly increased compared to TRUS [7]. In contrast-enhanced TRUS with microbubbles, the sensitivity to detect tumor foci is higher than in conventional TRUS, still, imaging does not reliably discriminate between inflammatory and malignant processes in the prostate [8].

Computed Tomography

Due to its soft-tissue type tissue architecture, the prostate gland can only poorly be visualized by computed tomography (CT). An accurate distinction between neoplastic and healthy tissue by CT is currently not feasible. Therefore, the use of CT in prostate cancer is limited to providing an anatomic reference for functional imaging modalities and for the detection of metastatic bone involvement.

Magnetic Resonance Imaging

The soft-tissue resolution of Magnetic Resonance Imaging (MRI) is superior to CT. MRI accurately visualizes the anatomy of the prostate, which allows a more reliable detection of prostate cancer. Moreover, with innovative techniques such as diffusion-weighted MRI (DWI), MR spectroscopy (MRS), and dynamic contrast-enhanced MRI

(DCI-MRI), functional assessment of the disease is also possible, resulting in a more precise staging and follow-up of prostate cancer.

In malignant tumors with high cellular density, diffusion of water molecules is restricted, a process that can be visualized by DWI [9]. Typically, prostate cancers have relatively tight glandular elements with increased cellular density and decreased extracellular space, producing high-signal-intensity foci on DWI [8]. Unfortunately, the specificity of this modality is relatively low since benign hyperplastic changes can also show low water diffusion [8].

MRS is a technique that provides information on aberrant levels of cellular metabolites. Prostate cancer is associated with locally elevated levels of choline and polyamine and decreased levels of citrate that can be evaluated by MRS. Recent reports indicate that MRS appears to be a promising functional imaging modality for the detection of prostate cancer [10–12]. Unfortunately, to obtain increased tumor detection rate MRS needs to be combined with MRI, which is technically challenging and therefore currently not widely available [13].

With DCE-MRI, tumor vascularization can be visualized by quantitative kinetic parameters that reflect blood flow and the vascular permeability [8]. DCE-MRI has higher specificity than MRI alone [14]. However, small low-grade tumors might be missed due to lack of angiogenesis. Furthermore, there is a concern regarding gadolinium-based contrast agents due to the risk for induction of nephrogenic systemic fibrosis in patients with renal failure [8].

More advanced imaging techniques include high-resolution MRI combined with lymphotropic superparamagnetic (ultra) small particles of iron oxide, (U) SPIO. Administered intravenously, (U)SPIO penetrate the vascular endothelium and enter the interstitial space and lymph vessels, finally reaching the lymph nodes. In the lymph nodes, the particles are phagocytised by macrophages which produces signal variations. In case of malignant involvement of the lymph node, absence of macrophage activity leads to signal modification. Consequently, affected lymph nodes will appear hyperintense on T2-weighted MRIs [15]. It has been found that USPIO-MRI has a significantly higher sensitivity than conventional MRI [16]. However, several disadvantages may limit the clinical use of USPIO-MRI, such as the requirement for particular expertise, its timeconsuming nature, and the limited sensitivity of USPIO-MRI in small lymph nodes (<5 mm). Recently, the uptake of bombesin-functionalized iron oxide nanoparticles in PC3 prostate cancer cells has been evaluated and preclinical data indicate that this approach may yield a prostate cancer-selective imaging probe [17].

RADIONUCLIDE IMAGING

Positron Emission Tomography

Radiolabeled metabolite tracers.

Today, positron emission tomography (PET) is emerging as an important functional imaging modality in various malignancies. Using PET, specific cellular and molecular processes, such as glucose metabolism and cell proliferation can be functionally visualized. The most commonly used tracer for PET imaging is ^{18}F -fluorodeoxyglucose (^{18}F -FDG). Tumor cells can be depicted by this technique by exploiting their enhanced glucose demand that is mainly due to increased aerobic glycolysis in malignant cells, allowing them to be distinguished from normal cells [18]. ^{18}F -FDG is taken up via glucose transporters. Intracellularly, ^{18}F -FDG is rapidly phosphorylated after which it cannot be metabolized any further. Consequently, ^{18}F -FDG is trapped inside metabolically active cells and can be visualized with PET. For anatomic reference for the functional PET images, integrated PET/CT has become the standard technology. Unfortunately, in primary prostate cancer ^{18}F -FDG-PET with or without integration of CT has limited sensitivity. A large fraction of prostate cancers expresses only low numbers of glucose transporters such as Glut-1, which limits ^{18}F -FDG uptake [19]. In addition, sensitivity of ^{18}F -FDG-PET is also limited since ^{18}F -FDG is excreted mainly via the urinary tract, obscuring the prostate gland, and restricting the identification of pelvic lymph node metastases [20].

3-Deoxy-3-fluorothymidine (FLT) radiolabeled with ^{18}F is another potential tracer for monitoring early effects of treatment of hormone-refractory prostate cancer. FLT has been introduced as a radiopharmaceutical for assessing tumor proliferation with PET imaging. Oyama et al. [21] demonstrated a significant decrease of FLT uptake in tumors after administration of docetaxel, while the changes of FDG uptake were minimal. Immunohistochemical analysis revealed that the changes of FLT uptake were correlated with those of proliferation activity.

Currently, choline radiolabeled with ^{11}C (**figure 1**) or ^{18}F (**figure 2**) is routinely used as PET tracer to image prostate cancer [22]. The use of choline is based on the fact that it is a key precursor in the biosynthesis of phosphatidylcholine, a major component of the cell membrane. An explanation for increased choline uptake in prostate cancer might be the increased proliferation rate in tumors [23]. Another possible explanation is upregulation of choline kinase in cancer cells [24].

The major advantage of ^{11}C -choline PET is the limited excretion rate via the urinary system, which minimizes obscuring of the prostate and therefore enables imaging of the pelvis without confounding bladder activity [25]. Rinnab and coworkers [26] evaluated ^{11}C -choline PET/CT in 50 patients with biochemical recurrence and reported a sensitivity of 91% at PSA concentrations below 2.5 ng/ml and a specificity of 50%. Besides low specificity, the use of the tracer ^{11}C -choline is limited by the short half-life of ^{11}C ($t_{1/2} = 20$ min), which requires the availability of

an on-site cyclotron [22]. With a half-life of 110 min, ^{18}F -labeled choline (^{18}F -FCH) overcomes this limitation. However, urinary excretion of ^{18}F -FCH is higher than that of ^{11}C -choline and might confound image interpretation. Eschmann et al. [27] compared ^{11}C -choline PET/CT with conventional whole-body MRI and reported a better overall diagnostic performance with ^{11}C -choline PET/CT due to higher detection rate of lymph node metastases and other local disease related alterations. However, for detection of bone metastases, the authors recommend a combination of both techniques to improve diagnostic accuracy.

Acetate is another commonly used tracer for PET imaging of prostate cancer. Intracellularly, acetate is converted into acetyl-CoA and incorporated into cholesterol and fatty acids, which finally form the cellular membrane. Recently, fatty acid synthesis was shown to be increased in prostate cancer with fatty-acid synthase being overexpressed [28]. Since acetate is excreted mainly via the pancreas [8], confounding bias through bladder activity is prevented which enables accurate imaging of the pelvis. Therefore, ^{11}C -acetate PET has been clinically evaluated for detection and follow-up of prostate cancer. A clinical trial by Albrecht et al. [29] suggested that ^{11}C -acetate PET might be useful for the detection of recurrent prostate cancer, especially in very early work-up of postoperative patients presenting with very low PSA values. Those data confirmed previous PET studies by Oyama et al. [30], who showed that ^{11}C -acetate uptake in the prostate bed as well as in lymph nodes was superior to that of ^{18}F -FDG.

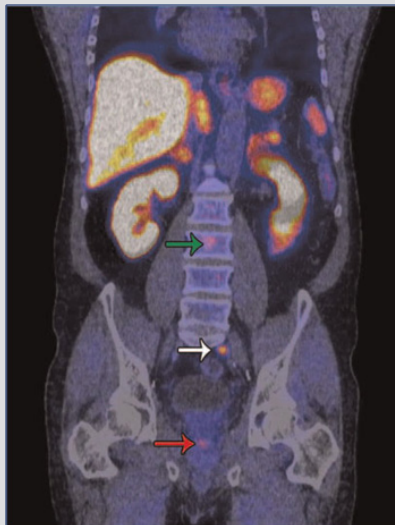


Figure 1: PET/CT image acquired after injection of ^{11}C -choline in a patient with prostate cancer. This image shows metastatic involvement of a lymph node (white arrow) and vertebrae (green and red arrow).

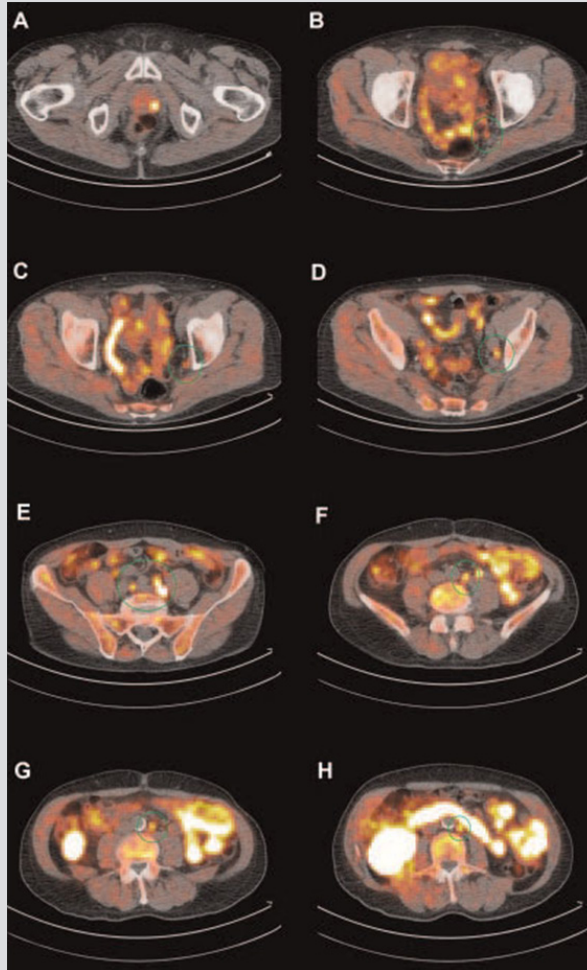


Figure 2: Transaxial slices of ^{18}F -choline PET/CT images of a patient with metastasized prostate cancer. Panel **A** shows local recurrence of prostate cancer in the left retrovesical area. Panels **(B-H)** show metastatic involvement of lymph nodes.

^{18}F -fluoroacetate, an ^{18}F -labeled analogue of acetate, has also been developed for PET. Similar to acetate, ^{18}F -fluoroacetate is substrate for acetyl coenzyme A synthase, but with lower specificity. ^{18}F -fluoroacetate represents a new alternative for ^{11}C -acetate in PET imaging of prostate cancer with the benefit of using a positron emitter with a longer half-life [31]. Small-animal PET series with ^{18}F -fluoroacetate in CWR22 tumor-bearing mice showed clear delineation of tumor tissue compared to reference organs, suggesting that it might be a useful PET tracer for imaging of

malignancies [31]. Matthies et al. [32] provided preliminary clinical data of a prostate cancer patient with rising PSA and progressive bone metastases. They showed that, compared to ^{11}C -acetate, ^{18}F -fluoroacetate PET offers the possibility of delayed imaging with the potential to further increase tumor to-background ratios.

For detection of malignant bone metastases, ^{18}F -sodium fluoride PET (**figure 3**) has shown high sensitivity and specificity [33]. The uptake in malignant lesions represents the increase in local blood flow and osteoblast activity. ^{18}F -fluoride PET has been found to be more sensitive than $^{99\text{m}}\text{Tc}$ -methylene diphosphonate ($^{99\text{m}}\text{Tc}$ -MDP) planar bone scintigraphy, especially in the early detection of metastases [33]. ^{18}F -fluoride PET is characterized by a two-fold higher bone uptake than $^{99\text{m}}\text{Tc}$ -MDP, faster clearance from the blood pool and a higher target-to-background ratio [33]. Unfortunately, like $^{99\text{m}}\text{Tc}$ -MDP, ^{18}F -fluoride PET is not tumor-selective and false-positive rates may be high [34]. However, this limitation can be overcome by integration of ^{18}F -fluoride PET with CT, which provides higher specificity and sensitivity [35]. More recent data indicate ^{18}F -FCH PET/CT to be more specific than ^{18}F -fluoride PET/CT in the early detection of bone metastases [36].



Figure 3: Coronal and sagittal slices of a Na-F-18 PET scan of a patient with bone metastases in clavicle (black arrow), lumbar spine (white arrow), and left femur (gray arrow).

Another potential tracer for PET imaging of prostate cancer is ^{18}F -fluoropropionic acid (^{18}F -FPA). It is hypothesized that, as discussed above for fluoroacetate, ^{18}F -FPA mimics acetate and therefore accumulates in tumor tissue [37]. Compared to ^{18}F -FDG, ^{18}F -FPA showed more accurate delineation of CWR22 prostate cancer xenografts in mice. However, further research is necessary to evaluate if ^{18}F -FPA offers further advantages over existing tracers for prostate cancer.

Radiolabeled androgen receptor binding ligands.

Recently, the imaging agent ^{18}F -fluoro-5- α -dihydrotestosterone (^{18}F -FDHT) that binds to androgen receptors, has been developed. Functional androgen receptor expression is a key factor in anti-androgen-based treatment of prostate cancer. Consequently ^{18}F -FDHT PET/CT may be exploited to monitor viable and androgen-sensitive tumor tissue and for the evaluation of anti-androgen therapy response [38]. The major advantage of this modality is that androgen-sensitive tumors can be detected whereas androgen-resistant tumors cannot, predicting if anti-androgen-based approaches represent a therapeutic option for individual patients. ^{18}F -FDHT PET/CT seems to be more likely to be of use in advanced disease with metastatic bone involvement rather than in localized prostate cancer, since background uptake can be high [39]. However, so far, experience with ^{18}F -FDHT PET/CT is limited and more studies evaluating its role in prostate cancer are needed.

Radiolabeled bombesin and gastrin-releasing peptide receptor binding ligands.

Since bombesin and gastrin-releasing peptide receptors (GRPR) are overexpressed in prostate cancer, they represent a potential target for molecular imaging. The first radiolabeled bombesin analog (Cu-64-DOTA-8-amino-octanoic acid-bombesin) was introduced by Rogers et al. [39]. In this study, specific tumor localization of ^{64}Cu -DOTA-Aoc-bombesin in mice with PC3 xenografts was demonstrated by microPET imaging and was confirmed by biodistribution studies. However, the high uptake of ^{64}Cu -labeled bombesin in normal tissues prevented its clinical implementation.

In a very recent study, the values of the ^{111}In -labeled bombesin agonists PESIN, AMBA, MP2346, and MP2653 and the $^{99\text{m}}\text{Tc}$ -labeled antagonist Demobesin-1 for SPECT/CT imaging of prostate cancer were evaluated in SCID mice xenografted with human GRPR-overexpressing PC3 tumors [40]. Schroeder et al. showed that Demobesin-1 was superior to the other agents with respect to *in vivo* stability, tumor uptake, and retention. Typically, renal and pancreatic clearance for Demobesin-1 was fast. The best GRPR agonists in this study were PESIN and AMBA with sufficient *in vivo* stabilities and relatively high tumor uptake and retention. However, further studies are needed to evaluate the clinical use of these agents in patients with prostate cancer.

In another study, novel series of [^{64}Cu -NO2A-(X)-BBN(7–14)NH₂] agonists for the specific targeting of GRPR on human PC3 cells and tumor tissue have been

evaluated [41]. The [^{64}Cu -NO2A-(AMBA)-BBN(7–14)NH $_2$] conjugate exhibited the highest accumulation in tumor tissue and the most efficient whole-body clearance via the renal–urinary excretion pathway.

One of the first clinical studies for imaging androgen-dependent prostate cancer using $^{99\text{m}}\text{Tc}$ -[Leu13]BN has been performed by Scopinaro and colleagues in eight patients with primary prostate cancer. They were able to visualize eight cancers in the prostate fossa with SPECT. Moreover, they reported uptake in obturator nodes which were proven to be cancer-specific by histopathology in three patients that were negative on MRI and CT [42]. In another study, Vincentis et al. [43] reported detection of prostate cancer by $^{99\text{m}}\text{Tc}$ -BN SPECT in 12 out of 12 patients with androgen-dependent prostate cancer and visualization of loco-regional lymph nodes in 4 out of 12 patients. These preliminary data suggest that $^{99\text{m}}\text{Tc}$ BN SPECT could be useful to detect primary prostate cancer and to evaluate locoregional lymph node involvement.

Other strategies focus on imaging of the heterodimeric transmembrane glycoprotein $\alpha\beta_3$ integrin that plays an important role in angiogenesis, metastasis, and the development of bone metastases in prostate cancer [44]. To image expression of $\alpha\beta_3$, the PET tracer ^{18}F -galacto-RGD was developed. Compared to conventional bone scans, the detection rate of bone metastases was higher using tracer ^{18}F -galacto-RGD PET. However, uptake of ^{18}F -galacto-RGD was heterogeneous, which suggests a variation in $\alpha\beta_3$ expression in prostate cancer metastases [45].

During invasion, angiogenesis, and metastasis of GRPR-positive tumors, the endothelial cells around the tumor tissue are activated and express high levels of integrin $\alpha\beta_3$. Thus, many GRPR-positive tumors are also positive for integrin $\alpha\beta_3$ [45]. Due to this, dual-receptor targeting of $\alpha\beta_3$ and GRPR represents another potential approach for detection of prostate cancer. Therefore, a BBN-RGD peptide heterodimer has been developed, that recognizes GRPR through the BBN motif and integrin through the RGD motif. In prostate cancer xenograft models, the BBNRGD heterodimer labeled with ^{18}F exhibited excellent tumor uptake and favorable *in vivo* kinetics superior to the BBN and RGD analogues [46].

In a subsequent study, 1,4,7-triazacyclononane-1,4,7-triacetic acid (NOTA) has been used as a chelator and the potential advantages of ^{64}Cu -labeled NOTA-RGD bombesin heterodimer above the monomeric analogues NOTA-RGD and NOTA-bombesin for imaging GRPR-positive tumors were demonstrated [47].

Radiolabeled antibody imaging.

Currently, extensive research is focused on both imaging and therapy of several types of malignancies using radiolabeled monoclonal antibodies (mAbs) directed towards relevant tumor-associated cell surface antigens.

Recently, several anti-PSMA antibodies have been developed that target the prostate-specific membrane antigen (PSMA). The first antibody used to target

PSMA in prostate cancer is capromab pendetide (7E11-C5). Capromab pendetide (Prostascint®) is a monoclonal antibody labeled with ¹¹¹Indium that specifically targets an intracellular epitope of PSMA. Capromab pendetide was approved by the FDA for imaging of soft tissue sites in metastatic prostate cancer for presurgical staging. In addition, it was approved for the evaluation of PSA relapse after local therapy. In a low number of presurgical patients with high-risk disease that show no lesions on CT or MRI scans, capromab pendetide detected positive nodes, thereby sparing these patients unnecessary surgical procedures [48]. However, as indicated above, capromab pendetide binds to the intracellular domain of PSMA. Therefore, binding to viable tumor cells requires internalization. Alternatively, capromab pendetide may only bind to dead cells with disrupted cellular membranes. In addition, localization of capromab uptake is limited by nonspecific binding and relatively high activity in the blood [8]. However, due to the relatively long half-life of ¹¹¹Indium (2.8 days), SPECT images can be obtained several days after injection, allowing washout of background activity from blood and bowel. Using capromab pendetide, detection of recurrence of disease, lymph node metastases, and other metastatic involvement is possible and combination with CT to improve anatomical resolution increases its specificity. One of the major limitations of imaging with radiolabeled capromab is the poor penetration in bone, limiting the detection of metastatic bone involvement [49].

To overcome limitations due to intracellular binding of capromab, antibodies binding to the epitopes on the extracellular domain of PSMA, such as J591, J415, and J533, have been developed that show high affinity binding to viable PSMA-expressing LNCaP cells [50]. In a preclinical study, mice were treated with J591 radiolabeled with ¹³¹Iodine, ¹⁷⁷Lutetium, and ⁹⁰Yttrium. ¹⁷⁷Lu and ⁹⁰Y provide better dosimetry due to their longer biological half-lives [51]. However, due to development of human-anti-mouse antibody (HAMA) responses, repetitive dosing was restricted. Meanwhile, a humanized form of J591 has been developed, which was well-tolerated and showed high tumor targeting capacity [52]. The first clinical studies with ¹¹¹In-, ⁹⁰Y, and ¹⁷⁷Lu-radiolabeled humanized mAb J591 have been performed by Bander et al. [53]. Tumor targeting results of 53 patients that received radiolabeled humanized J591 in phase 1 trials have been analyzed. In 43 evaluable patients, J591 accurately targeted bone lesions in 94% and soft tissue lesions in 72% of the patients, respectively. They also showed that the humanized antibody is less immunogenic and can be administered several times to the same patient with persistently accurate tumor targeting activity.

More recently, a phase-II clinical trial with ¹⁷⁷Lu-J591 for metastatic castration-resistant prostate cancer has been completed with excellent targeting of CT or MRI proven sites of prostate cancer metastases in 94% of the patients [54]. During this study, thrombocytopenia was the most commonly seen hematologic toxicity and limited the dose of ¹⁷⁷Lu-J591. Also, ⁹⁰Y-J591 is known for its hematologic toxicity causing significant myelosuppression.

Recently, three other antibodies were identified that are directed against alternative epitopes on PSMA that appear to have diagnostic potential for prostate cancer [55]. Wolf et al. characterized the monoclonal antibodies 3/A12, 3/E7, and 3/F11 *in vitro* and demonstrated a high affinity binding to PSMA-positive C4-2 cells for all three antibodies. A subsequent study focused on *in vivo* behavior, biodistribution, and tumor uptake of the ^{64}Cu -DOTA labeled antibodies 3/F11 and 3/E7 and fragments of 3/A12 [52]. PET imaging demonstrated specific tumor uptake of these monoclonal antibodies in PSMA-positive C4-2 tumors in SCID mouse xenografts models, which further confirmed possible use of those antibodies in imaging of prostate cancer. Very recently, the potential targeting ability of the humanized IgG1 mAb hRS7 which is also directed against the epithelial glycoprotein-1 (EGP-1) was evaluated [67]. They evaluated the biodistribution of ^{111}In -, ^{125}I -, and ^{89}Zr -labeled hRS7 and performed immuno-PET and immuno-SPECT with ^{111}In -hRS7 and ^{89}Zr -hRS7 in mice with s.c. and intraprostatic PC3 xenografts. They showed that specific tumor uptake of hRS7 is high with high tumor-to-blood ratios, which allowed excellent immuno-PET/CT and immuno-SPECT imaging of the PC3 xenografts [67].

In another recent study performed by the same group, a pretargeting approach for localizing advanced prostate cancer based on an anti-EGP-1 antibody in subcutaneous and orthotopic PC3 mouse models was developed [57]. EGP-1 is a pancarcinoma marker that is expressed at high levels on virtually all-prostate carcinomas. The pretargeting approach resulted in high uptake in the tumor, rapid blood clearance, and excellent tumor-to-blood ratios for ^{111}In -IMP-288 in the PC-3 tumors. As early as 1 h after injection of the radiolabeled peptide, pretargeted immuno-PET images clearly visualized the subcutaneous and orthotopic tumors with minimal activity in the kidneys. Van Rij et al. showed that pretargeting with the bispecific antibody TF12 in combination with radiolabeled IMP-288 is an excellent approach for specific, fast, high-contrast imaging of prostate cancer.

Another important cell surface target for molecular imaging of prostate cancer is the prostate stem cell antigen (PSCA), which is overexpressed in a majority of prostate cancers and has low levels of expression in a very limited number of normal tissues. PSCA has been detected in approximately 60% of lymph node and liver metastases [58] and strong PSCA staining has been observed in 87–100% of bone metastases [56]. Elevated PSCA expression has also been shown to correlate with increased tumor stage, grade, and progression to androgen independence. Olafsen et al. studied a humanized anti-PSCA monoclonal antibody 1G8 (hu1G8) in preclinical models [59] and showed that PET evaluation in LAPC-9-xenografted mice following radioiodination with the positron emitter ^{124}I provided high contrast PET images. Due to the slow clearance kinetics of the antibody, enhanced target-to-background images were not obtained until 1 week after administration of ^{124}I -hu1G8. To facilitate and accelerate clearance from blood, antibody fragments of various sizes were used in subsequent studies. Leyton et al. evaluated the role of the from hu1G8

antibody derived minibody 2B3 labeled with ^{131}I or ^{124}I for imaging prostate cancer xenograft-bearing mice. The 2B3 minibody showed fast blood clearance in comparison to the intact hu1G8 monoclonal antibody, which resulted in the ability to image prostate cancer xenografts within 21 h in contrast to 168 h with the intact antibody [60]. Remarkably, the 2B3 minibody mimicked the tumor uptake of the intact hu1G8 monoclonal antibody in the LAPC-9 model despite its rapid elimination from the circulation. Due to the ability of the 2B3 antibody to image androgen-independent as well as androgen-dependent xenografts, 2B3 has promising potential as a rapid imaging agent for high-risk prostate cancer patients [60].

Another recent study evaluated the tumor targeting activity of an internalizing human single-chain antibody fragment (scFv) UA20 that is directed against a still unknown antigen. UA20 was labeled with $^{99\text{m}}\text{Tc}$ to target human prostate carcinoma in DU145 xenograft mouse models [61]. In this study, UA20 scFv showed rapid and specific internalization in prostate tumor cells *in vitro* and accumulation in prostate tumor xenografts *in vivo*. SPECT/CT showed significant tumor uptake as early as 1 h after injection and at 3 h after injection, tumor uptake was 4.4% ID/g. In contrast, the control antibody N3M2 showed a tumor uptake of only 0.26% ID/g that was similar to nonspecific uptake in muscle and fat. These data indicated the potential of UA20 scFv for future development for prostate cancer imaging.

Radiolabeled amino acid imaging.

Radiolabeled amino acids may be alternative tracers for imaging of prostate cancer, since their uptake is frequently increased in rapidly proliferating cells [28].

A potential tracer for PET imaging of prostate cancer is the radiolabeled amino acid methionine. Since accumulation of ^{11}C -methionine in tumor cells reflects transport of amino acids and protein synthesis, enhanced metabolism of tumors can be visualized with ^{11}C -methionine. Methionine is mainly metabolized in liver and pancreas, without excretion via the urinary tract [3].

The few studies available that investigated the role of ^{11}C -methionine PET in prostate cancer indicate superiority of ^{11}C -methionine PET over ^{18}F -FDG PET in the detection of metastatic bone and soft tissue lesions [62]. Nunez et al. obtained a relatively high sensitivity (72.1%) of ^{11}C -methionine PET for the detection of bone and soft-tissue metastases, which compared favorably with the sensitivity of 48% for ^{18}F -FDG PET. A possible explanation for this difference in sensitivity of detection of metastatic lesions might be the relatively high activity of ^{18}F -FDG in the bladder, interfering with the evaluation of the prostate and nearby tissues. In contrast, only a minimal amount of ^{11}C -methionine is excreted via the urinary system allowing more reliable evaluation of pelvic structures. As a consequence ^{18}F -FDG may have limited ability to detect abdominal retroperitoneal metastases [37].

In a pilot study, the L-leucine analogue anti-1-amino-3- ^{18}F -fluorocyclobutyl-1-carboxylic acid (anti- ^{18}F -FACBC) showed uptake in primary and metastatic prostate

cancer. Bladder excretion of anti- ^{18}F -FACBC was found to be low and data indicate a potential role for anti- ^{18}F -FACBC in the differentiation between BPH and malignant transformation of the prostate gland [63]. However, anti- ^{18}F -FACBC needs to be further evaluated in clinical studies.

Since tumors express specific antigens, radiolabeled antibodies can target the antigens and can be of diagnostic value. However, due to the long circulatory half-life of radiolabeled antibodies, high target to background ratios are obtained several days after injection. Therefore, peptides that target those antigens represent alternatives for imaging of prostate cancer [64]. PET imaging of xenografted tumors overexpressing PSMA was achieved with a PSMA inhibitor labeled with ^{11}C . This ^{11}C -DCMC compound specifically binds with high affinity to the extracellular domain of PSMA [65]. ^{11}C -DCMC showed clear delineation of the tumor at 30 min after injection. This PSMA inhibitor was also labeled with ^{18}F . High uptake of ^{18}F -DCFBC was observed in the PSMA-positive tumors whereas uptake in PSMA-negative tumors remained low [66].

CONCLUSION AND FUTURE PERSPECTIVES

Since conventional approaches have limited value in the early detection, staging, and follow-up of prostate cancer, extensive research currently focuses on the development of highly sensitive and specific imaging modalities for accurate visualization of prostate cancer.

Improvements on conventional MR imaging have yielded promising new approaches such as DWI, MRS, or DCI-MRI, which allow for more accurate disease staging and follow-up of prostate cancer.

Substantial progress has been made in the development of radionuclide imaging techniques and the value of numerous radioactive tracers for the detection of prostate cancer has been evaluated. Since sensitivity of ^{18}F -FDG-PET for imaging of prostate cancer is limited, tracers like ^{11}C -choline, ^{18}F -FCH, ^{11}C -acetate, and ^{11}C -methionine represent more appropriate alternatives for prostate cancer imaging. ^{11}C -methionine PET is superior to ^{18}F -FDG-PET in both the detection of soft tissue lesions and the early detection of bone metastases. For evaluation of tumor bed and lymph nodes, ^{11}C -acetate PET was superior to ^{18}F -FDG-PET. However, in progressive disease and detection of bone metastases, ^{18}F -fluoroacetate might be superior to ^{11}C -acetate. For this purpose, ^{18}F -fluoride PET represents another appropriate tracer for detection of bone involvement with high sensitivity and specificity. The relatively novel tracer ^{18}F -FPA appears to be superior to ^{18}F -FDG in the detection of prostate cancer; however, more preclinical and clinical data are needed for further evaluation. Receptor binding ligands like ^{18}F -FDHT may have a value in the detection of androgen-sensitivity of the tumor, which would direct therapeutic strategies

towards anti-androgen-based approaches. During the last decade, a wide range of antibodies and antibody fragments, such as capromab pendetide, 3/A12, 3/E7, 3/F11, 2B3, and UA20 have been developed which show promising potential for targeted imaging of prostate cancer.

More studies are necessary to accurately compare novel imaging modalities and their tracers for optimal suitability in the early detection of (recurrent) prostate cancer, metastatic manifestations, and response to therapy.

REFERENCES

- (1) Ferlay J, Parkin DM, Steliarova-Foucher E. Estimates of cancer incidence and mortality in Europe in 2008. *Eur J Cancer*. 2010; 46(4):765–781
- (2) Kularatne SA, Wang K, Santhapuram HKR, Low PS. Prostatespecific membrane antigen targeted imaging and therapy of prostate cancer using a PSMA inhibitor as a homing ligand. *Mol Pharm*. 2009; 6(3):780–789
- (3) Turkbey B, Albert PS, Kurdziel K, Choyke PL. Imaging localized prostate cancer: Current approaches and new developments. *Am J Roentgenol*. 2009;192(6):1471–1480
- (4) Choi M, Hung AY. Technological advances in radiation therapy for prostate cancer. *Curr Urol Rep*. 2010; 11(3):172–179
- (5) Beer AJ, Eiber M, Souvatzoglou M, Schwaiger M, Krause BJ. Radionuclide and hybrid imaging of recurrent prostate cancer. *Lancet Oncol*. 2011; 12(2):181–191
- (6) Hricak H, Choyke PL, Eberhardt SC, Leibel SA, Scardino PT. Imaging prostate cancer: A multidisciplinary perspective. *Radiology*. 2007; 243(1):28–53
- (7) Cornud F, Hamida K, Flam T, Helenon O, Chretien Y, Thiounn N, Correas JM, Casanova JM, Moreau JF. Endorectal color Doppler sonography and endorectal MR imaging features of nonpalpable prostate cancer: Correlation with radical prostatectomy findings. *Am J Roentgenol*. 2000; 175(4):1161–1168
- (8) Turkbey B, Pinto PA, Choyke PL. Imaging techniques for prostate cancer: Implications for focal therapy. *Nat Rev Urol*. 2009; 6(4):191–203
- (9) Kwee TC, Takahara T, Ochiai R, Niewelstein RAJ, Luijten PR. Diffusion-weighted whole-body imaging with background body signal suppression (DWIBS): Features and potential applications in oncology. *Eur J Radiol*. 2008; 18(9):1937–1952
- (10) Costello LC, Franklin RB, Feng P. Mitochondrial function, zinc, and intermediary metabolism relationships in normal prostate and prostate cancer. *Mitochondrion*. 2005; 5(3):143–153
- (11) Ramirez de Molina A, Rodriguez-Gonzalez A, Gutierrez R, Martinez-Pineiro L, Sanchez J, Bonilla F, Rosell R, Lacal J. Overexpression of choline kinase is a frequent feature in human tumor-derived cell lines and in lung, prostate, and colorectal human cancers. *Biochem Biophys Res Commun*. 2002; 296(3):580–583
- (12) Shukla-Dave A, Hricak H, Moskowitz C, Ishill N, Akin O, Kuroiwa K, Spector J, Kumar M, Reuter VE, Koutcher JA, Zakian KL. Detection of prostate cancer with MR spectroscopic imaging: An expanded paradigm incorporating polyamines. *Radiology*. 2007; 245(2):499–506
- (13) Casciani E, Poletini E, Bertini L, Masselli G, Emiliozzi P, Amini M, Pansadoro V, Gualdi GF. Contribution of the MR spectroscopic imaging in the diagnosis of prostate cancer in the peripheral zone. *Abdom Imaging*. 2007; 32(6):796–802
- (14) Ocak I, Bernardo M, Metzger G, Barrett T, Pinto P, Albert PS, Choyke PL. Dynamic contrast-enhanced MRI of prostate cancer at 3T: A study of pharmacokinetic parameters. *Am J Roentgenol*. 2007; 189(4):849
- (15) Heesakkers RA, Hovels AM, Jager GJ, van den Bosch HC, Witjes JA, Raat HP, Severens JL, Adang EM, van der Kaa CH, Fütterer JJ, Barentsz J. MRI with a lymph node-specific contrast agent as an alternative to CT scan and lymph-node dissection in patients

- with prostate cancer: A prospective multicohort study. *Lancet Oncol.* 2008; 9(9):850–856
- (16) Harisinghani MG, Barentsz J, Hahn PF, Deserno WM, Tabatabaei S, van de Kaa CH, de la Rosette J, Weissleder R. Noninvasive detection of clinically occult lymph-node metastases in prostate cancer. *N Engl J Med.* 2003; 349(10):1010
- (17) Martin AL, Hickey JL, Ablack A, Lewis JD, Leonard GL, Gillies ER. Synthesis of bombesin-functionalized iron oxide nanoparticles and their specific uptake in prostate cancer cells. *J Nanoparticle Res.* 2010; 12(5):1599–1608
- (18) Van der Heiden MG, Cantley LC, Thompson CB. Understanding the Warburg effect: The metabolic requirements of cell proliferation. *Science.* 2009; 324(5930):1029–1033
- (19) Jana S, Blaurock MD. Nuclear medicine studies of the prostate, testes, and bladder. *Semin Nucl Med.* 2006; 36(1):51–72
- (20) Liu JJ, Zafar MB, Lai YH, Segall GM, Terris MK. Fluorodeoxyglucose positron emission tomography studies in diagnosis and staging of clinically organ-confined prostate cancer. *Urology.* 2001; 57(1):108–111
- (21) Oyama N, Hasegawa Y, Kiyono Y, Kobayashi M, Fujibayashi Y, Ponde DE, Dence C, Welch MJ, Yokoyama O. Early response assessment in prostate carcinoma by ^{18}F -fluorothymidine following anticancer therapy with docetaxel using preclinical tumour models. *Eur J Nucl Med Mol Imaging.* 2011; 38(1):81–89
- (22) Bouchelouche K, Tagawa ST, Goldsmith SJ, Turkbey B, Capala J, Choyke P. PET/CT imaging and radioimmunotherapy of prostate cancer. *Semin Nucl Med.* 2011; 41(1):29–44
- (23) Breeuwsma AJ, Pruijm J, Jongen MM, Suurmeijer AJ, Vaalburg W, Nijman RJ, de Jong IJ. In vivo uptake of ^{11}C -choline does not correlate with cell proliferation in human prostate cancer. *Eur J Nucl Med Mol Imaging.* 2005; 32(6):668–673
- (24) Zheng QH, Gardener TA, Raikwar S, Kao C, Stone KL, Martinez TD, Mock BH, Fei X, Wang JQ, Hutchins GD. ^{11}C -choline as a PET biomarker for assessment of prostate cancer tumor models. *Bioorg Med Chem.* 2004; 12(11):2887–2893
- (25) de Jong IJ, Pruijm J, Elsinga PH, Vaalburg W, Mensink HJ. Visualization of prostate cancer with ^{11}C -choline positron emission tomography. *Eur Urol.* 2002; 42(1):18–23
- (26) Rinnab L, Mottaghy FM, Blumstein NM, Reske SN, Hautmann RE, Hohl K, Moller P, Wiegel T, Kuefer R, Gschwend JE. Evaluation of ^{11}C -choline positron-emission/computed tomography in patients with increasing prostate-specific antigen levels after primary treatment for prostate cancer. *Br J Urol Int.* 2007; 100(4):786–793
- (27) Eschmann SM, Pfannenberger AC, Rieger A, Aschoff P, Müller M, Paulsen F, Anastasiadis A, Claussen CD, Bares R, Schlemmer HP. Comparison of ^{11}C -choline-PET/CT and whole body-MRI for staging of prostate cancer. *Nuklearmedizin.* 2007; 46(5):161–168
- (28) Apolo AB, Pandit-Taskar N, Morris MJ. Novel tracers and their development for the imaging of metastatic prostate cancer. *J Nucl Med.* 2008; 49(12):2031–2041
- (29) Albrecht S, Buchegger F, Soloviev D, Zaidi H, Veas H, Khan HG, Keller A, Bischof F, Delaloye A, Ratib O, Miralbell R. ^{11}C -acetate PET in the early evaluation of prostate cancer recurrence. *Eur J Nucl Med Mol Imaging.* 2007; 34(2):185–196
- (30) Oyama N, Miller TR, Dehdashti F, Siegel BA, Fischer KC, Michalski JM, Kibel AS, Andriole GL, Picus J, Welch MJ. ^{11}C -acetate PET imaging of prostate cancer: Detection

- of recurrent disease at PSA relapse. *J Nucl Med.* 2003; 44(4):549–555
- (31) Ponde DE, Dence CS, Oyama N, Kim J, Tai YC, Laforest R, Siegel BA, Welch MJ. ^{18}F -fluoroacetate: A potential acetate analog for prostate tumor imaging—In vivo evaluation of ^{18}F -fluoroacetate versus ^{11}C -acetate. *J Nucl Med.* 2007; 48(3):420–428
- (32) Matthies A, Ezziddin S, Ulrich EM, Palmedo H, Biersack HJ, Bender H, Gohlke S. Imaging of prostate cancer metastases with ^{18}F -fluoroacetate using PET/CT. *Eur J Nucl Med Mol Imaging.* 2004; 31(5):797
- (33) Even-Sapir E, Metser U, Mishani E, Lievshitz G, Lerman H, Leibovitch I. The detection of bone metastases in patients with high-risk prostate cancer: $^{99\text{m}}\text{Tc}$ -MDP planar bone scintigraphy, single- and multi-field-of-view SPECT, ^{18}F -fluoride PET, and ^{18}F -fluoride PET/CT. *J Nucl Med.* 2006; 47(2):287–297
- (34) Fogelman I, Cook G, Israel O, Van der Wall H. Positron emission tomography and bone metastases. *Semin Nucl Med.* 2005; 35(2):135–142
- (35) Even-Sapir E, Metser U, Flusser G, Zuriel L, Kollender Y, Lerman H, Lievshitz G, Ron I, Mishani E. Assessment of malignant skeletal disease: Initial experience with ^{18}F -fluoride PET/CT and comparison between ^{18}F -fluoride PET and ^{18}F -fluoride PET/CT. *J Nucl Med.* 2004; 45(2):272–278
- (36) Beheshti M, Vali R, Waldenberger P, Fitz F, Nader M, Loidl W, Broinger G, Stoiber F, Fogelman I, Langsteiger W. Detection of bone metastases in patients with prostate cancer by ^{18}F -fluorocholine and ^{18}F -fluoride PET-CT: A comparative study. *Eur J Nucl Med Mol Imaging.* 2008; 35(10):1766–1774
- (37) Pillarsetty N, Punzalan B, Larson SM. 2- ^{18}F -Fluoropropionic acid as a PET imaging agent for prostate cancer. *J Nucl Med.* 2009; 50(10):1709–1714
- (38) Dehdashti F, Picus J, Michalski JM, Dence CS, Siegel BA, Katzenellenbogen JA, Welch MJ. Positron tomographic assessment of androgen receptors in prostatic carcinoma. *Eur J Nucl Med Mol Imaging.* 2005; 32(3):344–350
- (39) Rogers BE, Bigott HM, McCarthy DW, Della Manna D, Kim J, Sharp TL, Welch MJ. MicroPET imaging of a gastrin-releasing peptide receptor-positive tumor in a mouse model of human prostate cancer using a ^{64}Cu -labeled bombesin analogue. *Bioconjug Chem.* 2003; 14(4):756–763
- (40) Schroeder RP, Müller C, Reneman S, Melis ML, Breeman WA, de Blois E, Bangma CH, Krenning EP, van Weerden WM, de Jong M. A standardised study to compare prostate cancer targeting efficacy of five radiolabelled bombesin analogues. *Eur J Nucl Med Mol Imaging.* 2010; 37(7):1386–1396
- (41) Lane SR, Nanda P, Rolde TL, Sieckman GL, Figueroa SD, Hoffman TJ, Jurisson SS, Smith CJ. Optimization, biological evaluation and microPET imaging of copper-64-labeled bombesin agonists, [^{64}Cu -NO₂A-(X)-BBN(7–14)NH₂], in a prostate tumor xenografted mouse model. *Nucl Med Biol.* 2010; 37(7):751–761
- (42) Scopinaro F, De Vincentis G, Varvarigou AD, Laurenti C, Iori F, Remediani S, Chiarini S, Stella S. $^{99\text{m}}\text{Tc}$ -bombesin detects prostate cancer and invasion of pelvic lymph nodes. *Eur J Nucl Med Mol Imaging.* 2003; 30(10):1378–1382
- (43) De Vincentis G, Remediani S, Varvarigou AD, Di Santo G, Iori F, Laurenti C, Scopinaro F. Role of $^{99\text{m}}\text{Tc}$ -bombesin scan in diagnosis and staging of prostate cancer. *Cancer Biother Radiopharm.* 2004; 19(1):81–84

- (44) Cooper CR, Chay CH, Pienta KJ. The role of alpha(v)beta(3) in prostate cancer progression. *Neoplasia*. 2002;4(3):191–194
- (45) Haubner R, Weber WA, Beer AJ, Vabuliene E, Reim D, Sarbia M, Becker KF, Goebel M, Hein R, Wester HJ, Kessler H, Schwaiger M. Noninvasive visualization of the activated alphavbeta3 integrin in cancer patients by positron emission tomography and [¹⁸F] Galacto-RGD. *PLoS Med*. 2005; 2(3):e70
- (46) Li ZB, Wu Z, Chen K, Ryu EK, Chen X. ¹⁸F-labeled BBN-RGD heterodimer for prostate cancer imaging. *J Nucl Med*. 2008; 49(3):453–461
- (47) Liu Z, Li ZB, Cao Q, Liu S, Wang F, Chen X. Small-animal PET of tumors with ⁶⁴Cu-labeled RGD-bombesin heterodimer. *J Nucl Med*. 2009; 50(7):1168–1177
- (48) Bander NH. Technology insight: Monoclonal antibody imaging of prostate cancer. *Nat Clin Pract Urol*. 2006; 3(4):216–225
- (49) Schettino CJ, Kramer EL, Noz ME, Taneja S, Padmanabhan P, Lepor H. Impact of fusion of indium-111 capromab pendetide volume data sets with those from MRI or CT in patients with recurrent prostate cancer. *Am J Roentgenol*. 2004; 183(2):519–524
- (50) Liu H, Rajasekaran AK, Moy P, Xia Y, Kim S, Navarro V, Rahmati R, Bander NH. Constitutive and antibody-induced internalization of prostate-specific membrane antigen. *Cancer Res*. 1998; 58(18):4055–4060
- (51) Smith-Jones PM, Vallabhajosula S, Navarro V, Bastidas D, Goldsmith SJ, Bander NH. Radiolabeled monoclonal antibodies specific to the extracellular domain of prostate-specific membrane antigen: Preclinical studies in nude mice bearing LNCaP human prostate tumor. *J Nucl Med*. 2003; 44(4):610–617
- (52) Alt K, Wiehr S, Ehrlichmann W, Reischl G, Wolf P, Pichler BJ, Elsasser-Beile U, Bühler P. High-resolution animal PET imaging of prostate cancer xenografts with three different ⁶⁴Cu-labeled antibodies against native cell-adherent PSMA. *Prostate*. 2010; 70(13):1413–1421
- (53) Bander NH, Trabulsi EJ, Kostakoglu L, Yao D, Vallabhajosula S, Smith-Jones P, Joyce MA, Milowsky M, Nanus DM, Goldsmith SJ. Targeting metastatic prostate cancer with radiolabeled monoclonal antibody J591 to the extracellular domain of prostate specific membrane antigen. *J Urol*. 2003; 170(5):1717–1721
- (54) Tagawa ST, Milowsky MI, Morris MJ, Vallabhajosula S, Goldsmith S, Matulich D, Kaplan J, Berger F, Scher HI, Bander NH, Nanus DM. Phase II trial of ¹⁷⁷Lutetium radiolabeled anti-prostate-specific membrane antigen (PSMA) monoclonal antibody J591 (¹⁷⁷Lu-J591) in patients with metastatic castrate-resistant prostate cancer. *J Clin Oncol*. 2008; 26(15S): 5140
- (55) Wolf P, Freudenberg N, Bühler P, Alt K, Schultze-Seemann W, Wetterauer U, Elsasser-Beile U. Three conformational antibodies specific for different PSMA epitopes are promising diagnostic and therapeutic tools for prostate cancer. *Prostate*. 2010; 70(5):562–569
- (56) Gu Z, Thomas G, Yamashiro J, Shintaku IP, Dorey F, Raitano A, Witte ON, Said JW, Loda M, Reiter RE. Prostate stem cell antigen (PSCA) expression increases with high gleason score, advanced stage and bone metastasis in prostate cancer. *Oncogene*. 2000; 19(10):1288–1296
- (57) van Rij C, Franssen G, Sharkey R, Frielink C, McBride B, Oyen W, Goldenberg D, Boerman O. Pretargeted immunoPET imaging and radioimmunotherapy (RIT) of

- prostate cancer with an anti-EGP1 x anti-HSG bispecific antibody (bsMAb). *J Nucl Med.* 2010; 51(Supplement 2):501
- (58) Lam JS, Yamashiro J, Shintaku IP, Vessella RL, Jenkins RB, Horvath S, Said JW, Reiter RE. Prostate stem cell antigen is overexpressed in prostate cancer metastases. *Clin Cancer Res.* 2005; 11(7):2591–2596
- (59) Olafsen T, Gu Z, Sherman MA, Leyton JV, Witkosky ME, Shively JE, Raubitschek AA, Morrison SL, Wu AM, Reiter RE. Targeting, imaging, and therapy using a humanized antiprostate stem cell antigen (PSCA) antibody. *J Immunother.* 2007; 30(4):396–405
- (60) Leyton JV, Olafsen T, Lepin EJ, Hahm S, Bauer KB, Reiter RE, Wu AM. Humanized radioiodinated minibody for imaging of prostate stem cell antigen-expressing tumors. *Clin Cancer Res.* 2008; 14(22):7488–7496
- (61) He J, Wang Y, Feng J, Zhu X, Lan X, Iyer AK, Zhang N, Seo Y, VanBrocklin HF, Liu B. Targeting prostate cancer cells in vivo using a rapidly internalizing novel human single-chain antibody fragment. *J Nucl Med.* 2010; 51(3):427–432
- (62) Nunez R, Macapinlac HA, Yeung HW, Akhurst T, Cai S, Osman I, Gonen M, Riedel E, Scher HI, Larson SM. Combined ^{18}F -FDG and ^{11}C -methionine PET scans in patients with newly progressive metastatic prostate cancer. *J Nucl Med.* 2002; 43(1):46–55
- (63) Schuster DM, Votaw JR, Nieh PT, Yu W, Nye JA, Master V, Bowman FD, Issa MM, Goodman MM. Initial experience with the radiotracer anti-1-amino-3- ^{18}F -fluorocyclobutane-1-carboxylic acid with PET/CT in prostate carcinoma. *J Nucl Med.* 2007; 48(1):56–63
- (64) Hong H, Zhang Y, Sun J, Cai W. Positron emission tomography imaging of prostate cancer. *Amino Acids.* 2010; 39(1):11–27
- (65) Foss CA, Mease RC, Fan H, Wang Y, Ravert HT, Dannals RF, Olszewski RT, Heston WD, Kozikowski AP, Pomper MG. Radiolabeled small-molecule ligands for prostate-specific membrane antigen: In vivo imaging in experimental models of prostate cancer. *Clin Cancer Res.* 2005; 11(11):4022–4028
- (66) Mease RC, Dusich CL, Foss CA, Ravert HT, Dannals RF, Seidel J, Prideaux A, Fox JJ, Sgouros G, Kozikowski AP, Pomper MG. N-[N-[(S)-1,3-Dicarboxypropyl]carbonyl]-4- ^{18}F fluorobenzyl-L-cysteine, [^{18}F]DCFBC: A new imaging probe for prostate cancer. *Clin Cancer Res.* 2008; 14(10):3036–3043
- (67) van Rij CM, Sharkey RM, Goldenberg DM, Frielink C, Molkenboer JD, Franssen GM, van Weerden WM, Oyen WJ, Boerman OC. Imaging of prostate cancer with immuno-PET and immuno-SPECT using a radiolabeled anti-EGP-1 monoclonal antibody. *J Nucl Med.* 2011; 52(10):1601-1607

2.2

Targeting human prostate cancer with ^{111}In -labeled D2B IgG, $\text{F(ab}')_2$ and Fab fragments in nude mice with PSMA-expressing xenografts

Susanne Lütje¹
Catharina M. van Rij¹
Gerben M. Franssen¹
Giulio Fracasso²
Wijnand Helfrich³
Annemarie Eek¹
Wim J.G. Oyen¹
Marco Colombatti²
Otto C. Boerman¹

¹ Department of Radiology and Nuclear Medicine,

Radboud University Medical Center, Nijmegen, The Netherlands

² Department of Pathology and Diagnostics, University of Verona, Italy

³ Department of Surgery, University Medical Centre Groningen,
Groningen, The Netherlands

ABSTRACT

Background

D2B is a new monoclonal antibody directed against an extracellular domain of prostate-specific membrane antigen (PSMA), which is overexpressed in prostate cancer. The potential of D2B IgG, and F(ab')₂ and Fab fragments of this antibody for targeting prostate cancer was determined in mice bearing subcutaneous prostate cancer xenografts.

Methods

The optimal time point for imaging was determined in biodistribution and microSPECT imaging studies with ¹¹¹In-D2B IgG, ¹¹¹In-capromab pentetide, ¹¹¹In-D2B F(ab')₂ and ¹¹¹In-D2B Fab fragments in mice with PSMA-expressing LNCaP and PSMA-negative PC3 tumors at several time points after injection.

Results

All ¹¹¹In-labeled antibody formats specifically accumulated in the LNCaP tumors, with highest uptake of ¹¹¹In-D2B IgG and ¹¹¹In-capromab pentetide at 168 h p.i. (94.8 ± 19.2% ID/g and 16.7 ± 2.2% ID/g, respectively), whereas uptake of ¹¹¹In-D2B F(ab')₂ and ¹¹¹In-Fab fragments peaked at 24 h p.i. (12.1 ± 3.0% ID/g and 15.1 ± 2.9% ID/g, respectively). Maximum LNCaP tumor-to-blood ratios were 13.0 ± 2.3 (168 h p.i.), 6.2 ± 0.7 (24 h p.i.), 23.0 ± 4.0 (24 h p.i.), and 4.5 ± 0.6 (168 h p.i.) for ¹¹¹In-D2B IgG, ¹¹¹In-F(ab')₂, ¹¹¹In-Fab, and ¹¹¹In-capromab pentetide, respectively. LNCaP tumors were clearly visualized with microSPECT with all antibody formats.

Conclusion

This study demonstrates feasibility of D2B IgG, F(ab')₂ and Fab fragments for targeting PSMA-expressing prostate cancer xenografts.

INTRODUCTION

Prostate cancer is the second leading cause of cancer-related deaths in men in the Western world and since metastatic prostate cancer is incurable, early diagnosis represents the most effective strategy with a change towards curative treatment options. Additionally, differentiation between malignant and nonmalignant prostate tissue is essential for the initiation of adequate treatment and the evaluation of response to therapy and relapse.

At present, prostate cancer is usually diagnosed by transrectal ultrasound (TRUS)-guided biopsy. However, the ability of TRUS to delineate small cancer foci and differentiate between benign prostatic hyperplasia (BPH), atrophy, inflammatory processes and malignancies is limited. Magnetic Resonance Imaging (MRI) is used in many centers for primary diagnostic purposes of prostate cancer, while MRI is less suitable to determine metastatic spread. Positron Emission Tomography (PET) imaging is a useful imaging modality to detect metastatic disease in several cancers. However, ^{18}F -FDG-PET is not suited for staging patients with prostate cancer, due to the relatively low avidity of prostate cancer for ^{18}F -FDG. Therefore, the most commonly used approach to identify metastases or tumor cell-containing lymph nodes in prostate cancer patients is multi-detector computed tomography (MDCT). However, the sensitivity and specificity of this modality are still limited. Imaging with radiolabeled monoclonal antibodies (mAb) as tracers for SPECT or PET imaging could have additional diagnostic value.

The prostate-specific membrane antigen (PSMA) is a type II membrane glycoprotein [1] which provides an excellent target for prostate cancer imaging due to its selective overexpression on the surface of prostate cancer cells [2]. Initial validation of PSMA as an *in vivo* target resulted from imaging with the ^{111}In -labeled mAb capromab pendetide (7E11/CYT-356, ProstaScint[®]) [3] which is FDA approved for diagnostic imaging in patients with biopsy-proven prostate cancer, who are at high risk for pelvic lymph node metastases [4]. However, capromab pendetide is directed against an epitope on an intracellular domain of PSMA [5]. Therefore, binding of this antibody to tumor cells requires uptake of the antibody into the cells. It has been postulated that capromab pendetide may only bind to dying or necrotic cells with cellular membranes that are permeable for IgG. The mAb J591 which is directed against an extracellular epitope of PSMA has shown great potential for radionuclide imaging and therapy in prostate cancer patients [6, 7].

In the present study, we use the new mAb D2B IgG, a murine IgG1 mAb directed against an epitope on the extracellular domain of PSMA [8]. We characterized the tumor targeting capacity of D2B IgG and compared it to those of F(ab')_2 and Fab fragments of D2B IgG to evaluate possible limitations such as low tumor-to-blood ratios that can occur due to relatively slow clearance of intact antibodies compared to fragments [9]. In these experiments capromab pendetide was used as a reference.

MATERIALS AND METHODS

Production and purification of antibodies and fragments

The monoclonal antibody D2B (IgG1) was derived from mice that were immunized three times with a cell lysate of membranes of LNCaP cells. Mice were boosted with a recombinant form of PSMA produced in bacteria.

D2B IgG was purified from hybridoma culture supernatant by Protein A affinity chromatography. F(ab')₂ fragments were produced by pepsin digestion essentially as described earlier [10]. Briefly, after incubation of D2B IgG for 3 h at 37 °C with pepsin in 0.15 M sodium citrate (pH 3.8), digestion was stopped by adjusting the pH of the solution to pH 7.0 with 1.0 M Tris. F(ab')₂ fragments were purified using a cation exchange column (Mono-S H/R 5/5, Pharmacia, Uppsala, Sweden) that was eluted with 40 mM sodium acetate buffer (pH 6.0) with a 0 to 400 mM lithium chloride gradient. The F(ab')₂ fragment containing fractions were identified by sodium dodecyl sulfate–polyacrylamide gel electrophoresis (SDS–PAGE) and pooled.

Fab fragments were generated by papain digestion (6 h at 37°C) of D2B IgG using papain immobilized on agarose resin according to the protocol of the manufacturer (Thermo Scientific, Pierce Fab Preparation Kit) followed by purification using protein A affinity chromatography and dialysis.

Cell culture

The human prostate cancer cell lines PC3 (PSMA⁻) and LNCaP (PSMA⁺) derived from a bone metastasis and a supraclavicular lymph node, respectively, were used. Both cell lines were obtained from the ATCC and grown in RPMI 1640 medium, supplemented with 10% fetal calf serum (Life technologies, Bleiswijk, The Netherlands) and glutamine 2mM.

Mouse models

Male BALB/c nude mice (Janvier, Le Genest Saint Isle, France), 8-9 weeks old, housed in filter-topped cages (5 mice per cage) under nonsterile standard conditions with free access to standard animal chow and water, were adapted to laboratory conditions for 1 week before experimental use. Mice were subcutaneously inoculated with 3 x 10⁶ LNCaP cells (right flank) suspended in 200 µL of 33% complete RPMI 1640 medium with 67% Matrigel (BD Biosciences) and with 3 x 10⁶ PC3 cells (left flank) suspended in 200 µL of 67% complete RPMI 1640 medium with 33% Matrigel. LNCaP cells were inoculated 7 days prior to PC3 cells and grew to approximately 0.1 g in 14 and 7 days after tumor cell inoculation respectively.

All experiments have been approved by the institutional Animal Welfare Committee of the Radboud University Medical Center Nijmegen and were conducted in accordance to the principles set forth by the Revised Dutch Act on Animal Experimentation.

Radiolabeling of D2B

The murine mAb D2B IgG and all fragments were conjugated with p-isothiocyanatobenzyl-diethylenetriaminepentaacetic acid (ITC-DTPA) (Macrocyclics) in 0.1 M NaHCO₃, pH 9.5, with a 10-fold molar excess of ITC-DTPA (2.5 mg D2B IgG with 110 µg ITC-DTPA, 4.5 mg F(ab')₂ with 250 µg ITC-DTPA and 0.75 mg Fab with 100 µg ITC-DTPA). After incubation of 1 h at room temperature, the reaction mixture was dialyzed for 3 days in a Slide-A-Lyzer (20-kDa cutoff, Pierce) against 0.25 M NH₄Ac, pH 5.4.

For biodistribution studies, D2B IgG-DTPA (28 µg), F(ab')₂-DTPA (22 µg), Fab-DTPA (20 µg) and capromab pendetide (30 µg) were radiolabeled with 3.7 MBq ¹¹¹In-chloride (Covidien, Petten, Netherlands) in 0.1 M MES buffer at pH 5.4 (three times the volume of ¹¹¹In-chloride) and incubated during 30 min at room temperature under metal-free conditions. For SPECT/CT studies, D2B IgG-DTPA, F(ab')₂-DTPA, Fab-DTPA and capromab pendetide-DTPA were incubated with 160 MBq, 152 MBq, 150 MBq or 340 MBq of ¹¹¹In in 0.1 M MES buffer pH 5.4, respectively. Following incubation, 50 mM EDTA was added to the final concentration of 5 mM to chelate unincorporated ¹¹¹In.

The labeling efficiency was determined by instant thin layer chromatography on silicagel strips (ITLC-SG; Gelman Sciences, Ann Arbor, MI, USA) using 15 mM citrate buffer, pH 6.0, as the mobile phase. For biodistribution, it was 95%, 58% 90% and 95%, for ¹¹¹In-labeled D2B IgG-DTPA, F(ab')₂-DTPA, Fab-DTPA and capromab-DTPA, respectively. For SPECT imaging, it was 70%, 79%, 97% and 95%, respectively.

¹¹¹In-labeled D2B IgG-DTPA, F(ab')₂-DTPA, Fab-DTPA, and capromab-DTPA were purified by gel filtration on a PD-10 column. The radiochemical purity was determined by ITLC and exceeded 97% for all preparations used in the studies.

Immunoreactivity

The immunoreactive fractions of the radiolabeled antibody/fragment preparations were determined using freshly trypsinized LNCaP cells, essentially as described by Lindmo et al. [11, 12]. The activity in the vials and in the cell pellet after washing with 500 µL binding buffer was determined in the γ-counter (Wizard 3" 1480, LKB-Wallac, Oy, Finland) after incubation of 1 h at 37°C. Immunoreactive fractions of all radiolabeled preparations used in the experiments exceeded 80%. For ¹¹¹In-capromab pendetide, the assay was carried out on live and permeabilized LNCaP cells using the Fix & Perm Cell Fixation and Permeabilization Kit (Invitrogen) to permeabilize the cells.

Competitive binding assay

The IC₅₀ of D2B IgG, F(ab')₂ and Fab fragments was determined in a competitive binding assay on LNCaP cells using ¹¹¹In-labeled D2B as a tracer. LNCaP cells were grown to confluency in six-well plates, and incubated on ice for 2 h in 1 mL of binding buffer with 1.85 kBq of ¹¹¹In-labeled D2B IgG and increasing concentrations (0.005

-300 nM) of unlabeled D2B IgG, F(ab')₂ and Fab fragments. Cells were washed with binding buffer after incubation and the cell-associated activity was measured in a γ -counter. IC₅₀ values were calculated using GraphPad Prism software, version 5.03 (GraphPad, La Jolla, USA).

Flow cytometric analysis

For cell surface staining, LNCaP cells were incubated with either the mAbs D2B IgG, capromab pendetide or an isotype control murine IgG (Jackson ImmunoResearch) in phosphate buffered saline (PBS) with 2% of bovine serum albumin (BSA) and 2% human serum (HS) for 30 minutes on ice. Part of the cells were fixed in 2% paraformaldehyde and incubated in PBS, 2% HS, 0.1% saponin to permeabilize the cells. After the incubation, samples were washed three times in PBS or PBS and 0.1% saponin and incubated for 20 minutes on ice with the secondary anti-mouse-alexa 488 antibody for staining. Cells were analyzed in a FACSCalibur flow cytometer equipped with CellQuest software (BD Biosciences).

Biodistribution studies

The effect of mAb protein dose on the biodistribution of ¹¹¹In-D2B in nude mice with subcutaneous LNCaP tumors was determined in groups of 5 mice that received different protein doses of ¹¹¹In-D2B IgG (0.1, 1, 3, 10, 30 or 100 μ g of D2B IgG per mouse, 0.4 MBq). Mice were euthanized with CO₂/O₂ asphyxiation 3 days after injection of ¹¹¹In-D2B IgG. Blood samples were obtained by heart puncture and tissues (LNCaP tumor, muscle, lung, spleen, kidney, liver, pancreas, stomach, duodenum, and prostate) were dissected, weighed, and the radioactivity was measured in a γ -counter. For calculation of the uptake of radioactivity in each tissue as a fraction of the injected dose, an aliquot of the injection dose was counted simultaneously.

In a subsequent study, ¹¹¹In-D2B IgG (0.4 MBq, 3.0 μ g/mouse), ¹¹¹In-F(ab')₂ (0.4 MBq, 2.2 μ g/mouse), ¹¹¹In-Fab fragments (0.4 MBq, 1 μ g/mouse) or ¹¹¹In-capromab pendetide (0.4 MBq, 5 μ g/mouse) were injected i.v. into groups of 5 mice with subcutaneous PC3 tumors (left flank) and LNCaP tumors (right flank). In addition, for Fab and F(ab')₂, five mice per antibody format received an excess of unlabeled D2B IgG (300 μ g/mouse) two days before injection of the ¹¹¹In-labeled fragments into the mice. For D2B IgG and capromab pendetide, the excess of unlabeled D2B IgG or capromab was injected on the same day as the ¹¹¹In-labeled antibodies. Mice were euthanized by CO₂/O₂ asphyxiation and the biodistribution of ¹¹¹In-D2B IgG was determined at 1, 2, 4, 24, 72 and 168 hours after injection. Because of their more rapid clearance, biodistribution of the ¹¹¹In-F(ab')₂ and ¹¹¹In-Fab fragments was determined at 1, 2, 4 and 24 hours after injection. Activity concentrations in the tissues (percentage injected dose per gram, % ID/g) were determined as described above.

MicroSPECT/CT imaging

Four groups of 5 mice with subcutaneous LNCaP (right flank) and PC3 (left flank) tumors were injected with 37 MBq of ^{111}In -D2B IgG (3.0 $\mu\text{g}/\text{mouse}$), ^{111}In -F(ab')₂ (1.5 $\mu\text{g}/\text{mouse}$), ^{111}In -Fab (1 $\mu\text{g}/\text{mouse}$), and ^{111}In -capromab pendetide (5 $\mu\text{g}/\text{mouse}$), respectively. The mice that received ^{111}In -labeled D2B IgG and capromab pendetide, SPECT/CT scans were imaged 0, 1, 3, and 7 days after injection using a small animal SPECT/CT scanner (U-SPECT II, MILabs, Utrecht, Netherlands) (acquisition time: 30-90 minutes, depending on the time point) with a 1.0 mm diameter pinhole collimator tube. Mice injected with ^{111}In -F(ab')₂ and ^{111}In -Fab fragments underwent SPECT/CT at 0, 1, and 2 days after injection. For Fab and F(ab')₂, two additional mice were injected with an excess of unlabeled D2B IgG 2 days before injection of the ^{111}In -labeled antibody fragments. For D2B IgG, the excess of unlabeled antibody formats was coadministered on the same day as ^{111}In -D2B.

After the last scan, mice were euthanized and biodistribution of the ^{111}In -D2B, ^{111}In -F(ab')₂, ^{111}In -Fab, or ^{111}In -capromab pendetide was determined as described above. Scans were reconstructed with MILabs reconstruction software (MILabs, Utrecht, Netherlands), which uses an ordered-subset expectation maximization algorithm.

Statistical analysis

Statistical analyses were performed with Graphpad Prism, version 5.03 (GraphPad, La Jolla, USA). Results are presented as mean \pm standard deviation (SD). Differences in tumor uptake of the antibody formats were tested for significance using the Two-tailed *t*-test. A *p*-value below 0.05 was considered significant.

RESULTS

In vitro characterization

FACS analysis with live and permeabilized LNCaP cells revealed high binding of D2B IgG to live (95.9% \pm 2.2) as well as to permeabilized cells (96.9% \pm 1.7). In contrast, for capromab pendetide, binding to live cells was low (7.6% \pm 0.7), while binding to permeabilized cells was high (96.1% \pm 1.1), showing that D2B recognizes an epitope on the cell surface and capromab is directed against an intracellular epitope (**figure 1**).

For ^{111}In -D2B IgG the immunoreactive fraction on live LNCaP cells was 84.1%, and the immunoreactive fractions of ^{111}In -capromab pendetide on permeabilized LNCaP cells was 93.6%, indicating that the immunoreactivity of both antibodies was preserved during the labeling procedure.

The IC₅₀ of D2B IgG and F(ab')₂ fragments was 3.7 nM (95% confidence interval (CI): 2.8 – 4.8 nM) and 1.9 nM (CI: 1.6 – 2.3 nM), respectively, whereas it was slightly

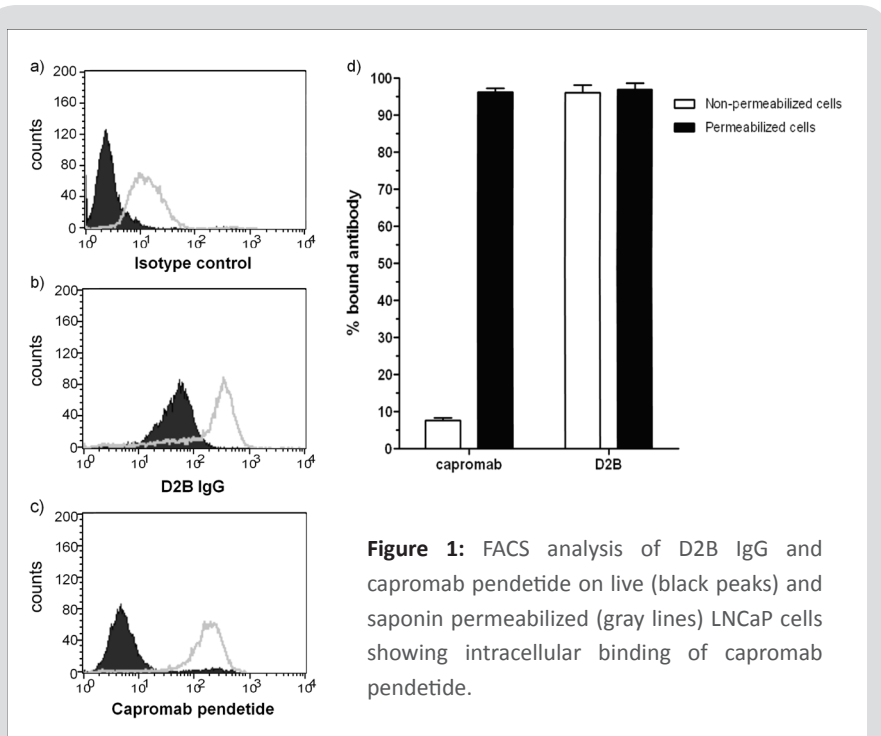


Figure 1: FACS analysis of D2B IgG and capromab pentetide on live (black peaks) and saponin permeabilized (gray lines) LNCaP cells showing intracellular binding of capromab pentetide.

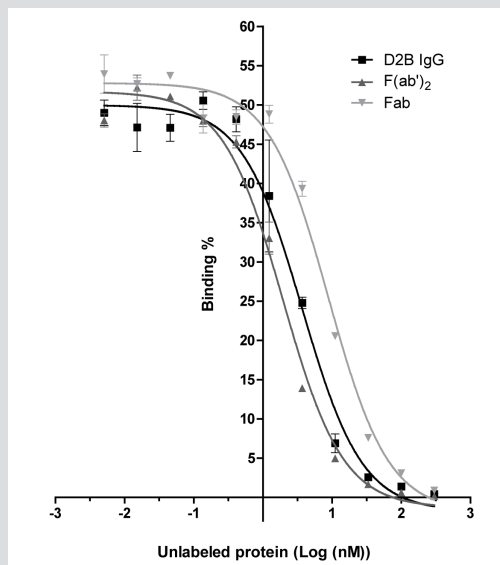


Figure 2: Competitive binding curves of IC₅₀ determination of D2B IgG, F(ab')₂ and Fab fragments on PSMA-positive LNCaP cells.

lower for Fab fragments (8.9 nM (CI: 7.1 – 11.0 nM) (**figure 2**), which could be due to the monovalency of Fab fragments.

Biodistribution studies

In the dose escalation study an inverse correlation between the D2B antibody protein dose and the uptake in the LNCaP tumor was observed: LNCaP tumor uptake of ^{111}In -D2B IgG decreased from $52 \pm 5\%$ ID/g at $0.1 \mu\text{g}/\text{mouse}$ to $26 \pm 1.5\%$ ID/g at $100 \mu\text{g}/\text{mouse}$. Highest tumor uptake ($54 \pm 4\%$ ID/g) was observed at D2B doses $\leq 3 \mu\text{g}/\text{mouse}$ at 3 days p.i. (**figure 3**). At that time point, tumor-to-blood ratios ranged from 4.3 (at $0.1 \mu\text{g}/\text{mouse}$) to 1.8 (at $100 \mu\text{g}/\text{mouse}$). Tumor weight was $0.04 \text{ g} \pm 0.02 \text{ g}$ (D2B IgG group), $0.08 \text{ g} \pm 0.03 \text{ g}$ (F(ab')₂ group), $0.07 \text{ g} \pm 0.02 \text{ g}$ (Fab group), and $0.10 \text{ g} \pm 0.02 \text{ g}$ (capromab group).

For biodistribution studies, ^{111}In -D2B IgG (0.4 MBq , $3.0 \mu\text{g}/\text{mouse}$), ^{111}In -F(ab')₂ (0.4 MBq , $2.2 \mu\text{g}/\text{mouse}$), ^{111}In -Fab fragments (0.4 MBq , $1 \mu\text{g}/\text{mouse}$) or ^{111}In -capromab pentetide (0.4 MBq , $5 \mu\text{g}/\text{mouse}$) were injected intravenously. All three ^{111}In -labeled D2B antibody formats specifically accumulated in the s.c. PSMA⁺ LNCaP tumors (right flank), while uptake in PSMA⁻ PC3 xenografts (left flank) remained low.

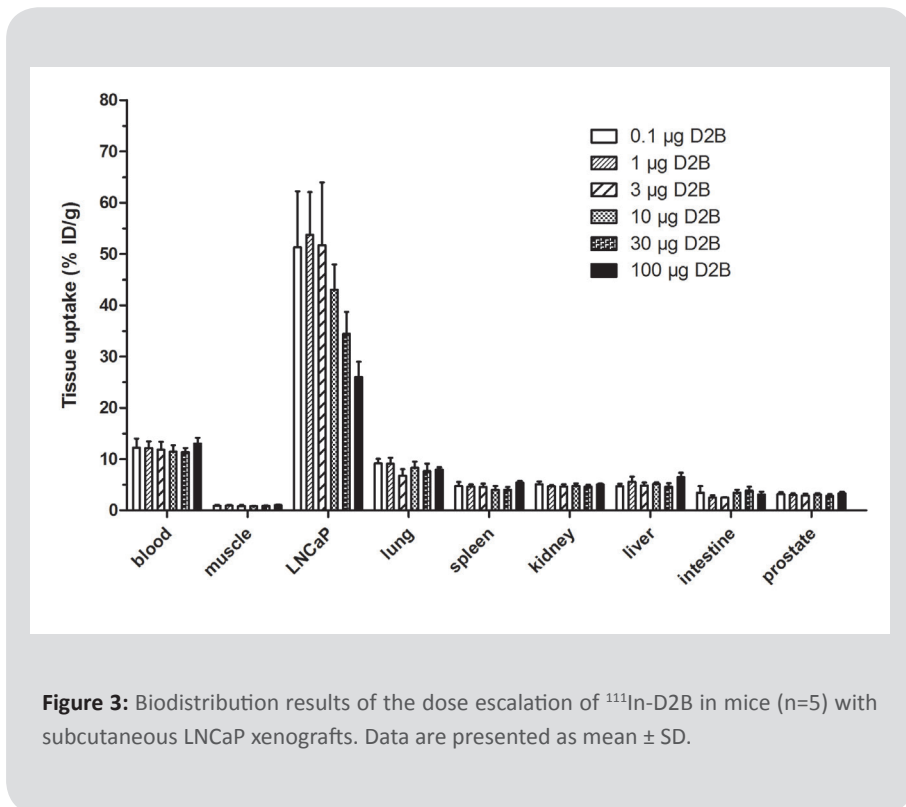


Figure 3: Biodistribution results of the dose escalation of ^{111}In -D2B in mice (n=5) with subcutaneous LNCaP xenografts. Data are presented as mean \pm SD.

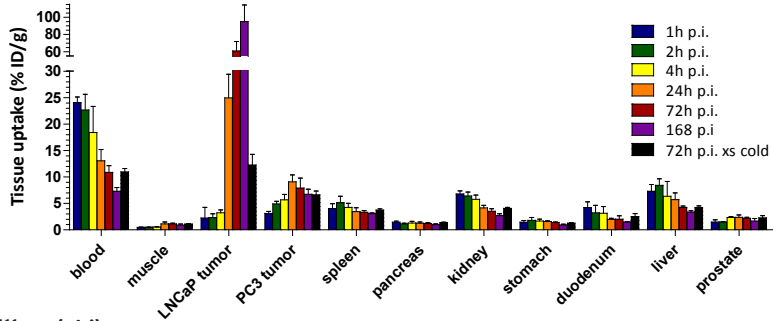
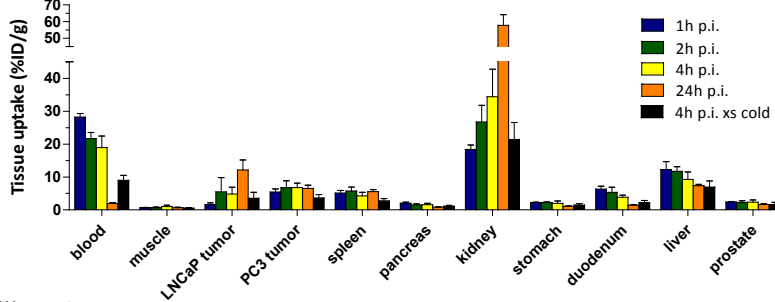
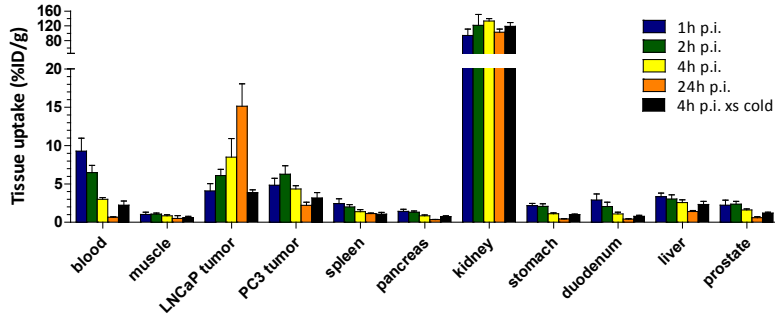
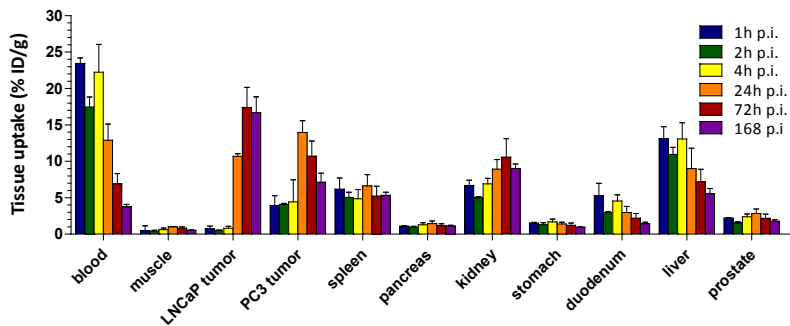
a) $^{111}\text{In-D2B IgG}$ b) $^{111}\text{In-F(ab')}_2$ c) $^{111}\text{In-Fab}$ d) $^{111}\text{In-capromab pentetide}$ 

Figure 4: *Ex vivo* biodistribution of nude mice bearing subcutaneous PSMA-negative PC3 and PSMA-positive LNCaP xenografts at several time points after intravenous injection of a) ^{111}In -D2B IgG, b) ^{111}In -F(ab')₂, c) ^{111}In -Fab fragments and d) ^{111}In -capromab pentetide. Data are presented as mean \pm SD.

LNCaP tumor uptake increased for ^{111}In -D2B IgG from $2.2 \pm 2.0\%$ ID/g at 1 h p.i. to $94.8 \pm 19.2\%$ ID/g at 168 h after injection, the latter representing the highest tumor uptake observed in these studies (**figure 4**). For ^{111}In -F(ab')₂ and ^{111}In -Fab, LNCaP tumor uptake ranged from $1.6 \pm 0.6\%$ ID/g and $4.1 \pm 0.9\%$ ID/g at 1 h p.i. to $12.1 \pm 3.0\%$ ID/g and $15.1 \pm 2.9\%$ ID/g at 24 h after injection, respectively. For ^{111}In -labeled capromab pentetide, LNCaP tumor uptake ranged from $0.7 \pm 0.4\%$ ID/g at 1 h p.i. to $16.7 \pm 2.2\%$ ID/g at 168 h after injection, reaching a maximum of $17.4 \pm 2.8\%$ ID/g three days after injection.

Tumor uptake of the three D2B formats could be blocked by coinjection of an excess of unlabeled mAb. The uptake of ^{111}In -D2B IgG decreased from $60.9 \pm 11.0\%$ ID/g to $12.3 \pm 7.1\%$ ID/g at 72 h p.i.. The LNCaP uptake of ^{111}In -F(ab')₂ decreased from $4.8 \pm 2.1\%$ ID/g to $3.5 \pm 1.8\%$ ID/g (4 h p.i.), while the LNCaP uptake of ^{111}In -Fab decreased from $8.5 \pm 2.4\%$ ID/g to $3.9 \pm 0.4\%$ ID/g, respectively at 4 h p.i.. Maximum uptake in the PSMA⁻ PC3 tumor was 9.1 ± 1.3 (24 h p.i.), 6.8 ± 1.3 (4 h p.i.) and $6.3 \pm 1.1\%$ ID/g (2 h p.i.) for ^{111}In -labeled IgG, F(ab')₂ and Fab, further confirming the specific uptake of the D2B antibody formats in the PSMA⁺ tumor.

Maximum LNCaP tumor-to-blood ratio for ^{111}In -D2B IgG was 13.0 ± 2.3 (168 h p.i.). For D2B Fab and F(ab')₂ fragments, high tumor-to-blood ratios were reached faster compared to tumor-to-blood ratios of D2B IgG, with a maximum of 23.0 ± 4.0 and 6.2 ± 0.7 , respectively 24 h after injection (**table 1**).

Table 1. *Ex vivo* biodistribution (tissue uptake % ID/g) and LNCaP tumor-to-organ ratios of ^{111}In -capromab pentetide, ^{111}In -D2B IgG, ^{111}In -F(ab')₂ and ^{111}In -Fab fragments in nude mice with subcutaneous prostate-specific membrane antigen (PSMA)-negative PC3 xenografts and PSMA-positive LNCaP xenografts

	^{111}In -capromab (168 h p.i.) (% ID/g tissue uptake)	LNCaP tumor- to-organ ratio (^{111}In -capromab)	^{111}In -D2B IgG (168 h p.i.) (% ID/g tissue uptake)	LNCaP tumor- to-organ ratio (^{111}In -D2B IgG)	^{111}In -F(ab') ₂ (24 h p.i.) (% ID/g tissue uptake)	LNCaP tumor- to-organ ratio (^{111}In -F(ab') ₂)	^{111}In -Fab (24 h p.i.) (% ID/g tissue uptake)	LNCaP tumor-to- organ ratio (^{111}In -Fab)
Blood	3.7 \pm 0.3	4.5 \pm 0.6	7.3 \pm 0.7	13.0 \pm 2.3	2.0 \pm 0.3	6.2 \pm 0.7	0.7 \pm 0.0	23.1 \pm 4.0
Muscle	0.5 \pm 0.1	31.9 \pm 6.5	0.9 \pm 0.2	110.4 \pm 41.1	0.7 \pm 0.2	18.4 \pm 3.4	0.5 \pm 0.4	38.2 \pm 19.8
Lung	3.0 \pm 0.4	5.5 \pm 0.7	4.3 \pm 0.8	22.8 \pm 6.3	2.1 \pm 0.1	5.7 \pm 1.2	0.9 \pm 0.1	20.0 \pm 4.2
Spleen	5.3 \pm 0.4	3.5 \pm 0.6	3.1 \pm 0.13	30.9 \pm 6.4	5.5 \pm 0.7	2.8 \pm 0.4	1.1 \pm 0.1	13.2 \pm 2.4
Pancreas	1.1 \pm 0.1	14.9 \pm 1.0	1.0 \pm 0.2	98.9 \pm 18.6	0.9 \pm 0.0	14.1 \pm 3.4	0.3 \pm 0.0	45.8 \pm 12.1
Kidney	9.0 \pm 0.6	1.9 \pm 0.3	2.7 \pm 0.4	35.5 \pm 7.5	57.8 \pm 6.4	0.2 \pm 0.0	102.8 \pm 8.5	0.2 \pm 0.0
Stomach	1.00 \pm 0.1	17.6 \pm 2.5	0.9 \pm 0.2	104.0 \pm 31.0	1.1 \pm 0.1	11.4 \pm 1.5	0.4 \pm 0.0	35.5 \pm 8.8
Duodenum	1.4 \pm 0.2	11.9 \pm 2.4	1.5 \pm 0.1	64.3 \pm 14.3	1.4 \pm 0.2	8.5 \pm 2.5	0.4 \pm 0.0	37.3 \pm 9.7
Liver	5.5 \pm 0.7	3.1 \pm 0.7	3.4 \pm 0.3	28.2 \pm 4.6	7.3 \pm 0.4	1.7 \pm 0.3	1.4 \pm 0.1	10.8 \pm 2.3
Prostate	1.8 \pm 0.2	9.5 \pm 1.8	1.7 \pm 0.5	59.2 \pm 14.4	1.6 \pm 0.3	8.0 \pm 3.2	0.6 \pm 0.1	25.7 \pm 5.8
PC3 tumor	7.1 \pm 1.2	2.4 \pm 0.4	6.7 \pm 0.9	14.0 \pm 1.2	6.5 \pm 1.0	1.9 \pm 0.2	2.2 \pm 0.4	7.1 \pm 2.0
LNCaP tumor	16.7 \pm 2.2		94.8 \pm 19.2		12.1 \pm 3.0		15.1 \pm 2.9	

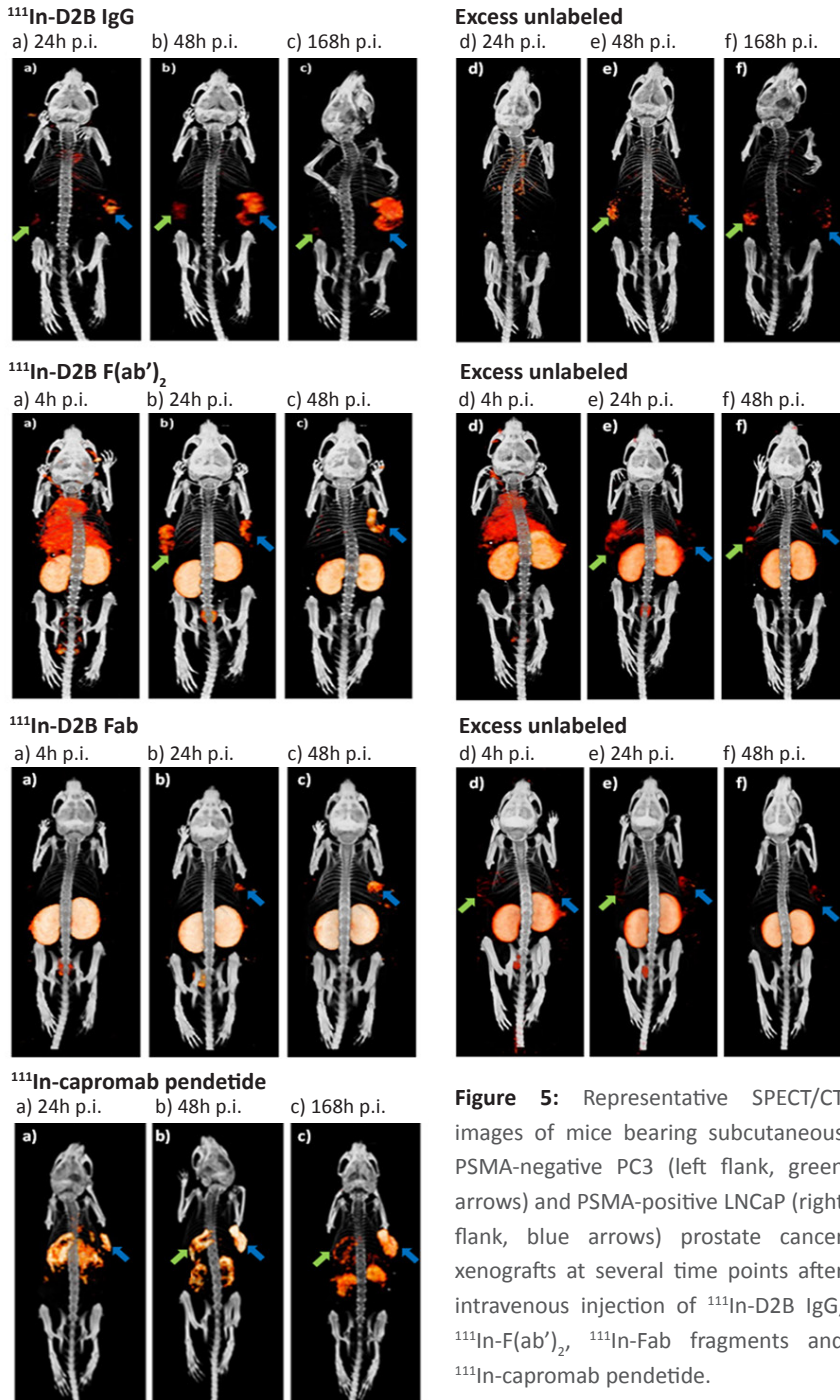


Figure 5: Representative SPECT/CT images of mice bearing subcutaneous PSMA-negative PC3 (left flank, green arrows) and PSMA-positive LNCaP (right flank, blue arrows) prostate cancer xenografts at several time points after intravenous injection of ^{111}In -D2B IgG, ^{111}In -F(ab')₂, ^{111}In -Fab fragments and ^{111}In -capromab pendetide.

The highest LNCaP tumor-to-blood ratio of ^{111}In -labeled capromab pentetide was 4.5 ± 0.6 , reached seven days after injection. LNCaP tumor-to-muscle ratio for ^{111}In -D2B IgG (168 h p.i.), ^{111}In -F(ab')₂ (24 h p.i.), ^{111}In -Fab (24 h p.i.), and ^{111}In -capromab pentetide (168 h p.i.) were 94.8 ± 19.2 , 12.1 ± 3.0 , 15.1 ± 2.9 , and 16.7 ± 2.2 , respectively.

MicroSPECT/CT imaging

SPECT/CT images of all ^{111}In -labeled antibody formats in mice in prone position with subcutaneous PSMA⁺ LNCaP and PSMA⁻ PC3 tumors are displayed in **figure 5**. At 24 h p.i., LNCaP tumors were clearly visualized with all formats. The optimal time point for imaging with ^{111}In -D2B IgG and ^{111}In -capromab pentetide was 168 h p.i. and for ^{111}In -F(ab')₂ and ^{111}In -Fab this was 48 h p.i.. Tumor uptake was specific for ^{111}In -D2B IgG, ^{111}In -F(ab')₂ and ^{111}In -Fab since tumor uptake was markedly lower in mice coinjected with an excess of unlabeled D2B IgG (**figure 5**). Uptake in the PSMA⁻ PC3 tumors remained low for all antibody formats at all time points.

For D2B F(ab')₂ and Fab fragments, high accumulation of ^{111}In in the kidneys, especially the renal cortex, was observed, indicating that these antibody preparations were cleared via the kidneys apparently with tubular reabsorption of the ^{111}In -labeled metabolites.

DISCUSSION

In the present study, the *in vivo* tumor targeting characteristics of ^{111}In -D2B IgG, ^{111}In -F(ab')₂, and ^{111}In -Fab fragments for targeting of prostate cancer were examined in mice with human prostate cancer xenografts using ^{111}In -labeled capromab pentetide as a reference.

Since intact antibodies clear slowly from the circulation and maximum tumor uptake is reached at 3 - 7 days after injection, we included F(ab')₂ and Fab fragments of D2B in our studies to investigate whether further improvements in prostate cancer targeting would be possible by using D2B antibody fragments. The slow accumulation of intact antibodies has been attributed to the slow blood clearance of intact IgG in combination with the presence of various physiological barriers between the circulation and the tumor cell surface [18]. It has been pointed out that the vascular endothelium, the relatively large transport distances in the tissue and the enhanced interstitial fluid pressure in the tumor tissue hamper the penetration of antibodies into the tumor tissue to bind to their target antigen. Antibody fragments such as F(ab')₂ and Fab fragments are cleared more rapidly from the blood, mainly because they lack the CH2 domain, which causes IgG molecules to recycle into the bloodstream via the FcRn receptor [19]. On the other hand, the sustained blood levels of intact IgG molecules are the driving force for their accumulation in tumors. Therefore, the

uptake of antibody fragments in tumors is lower than that of intact IgGs as was also observed in the present study. Because the diffusion rate of a molecule is linearly correlated to its molecular size [20], antibody fragments diffuse more rapidly in the interstitial fluid. Due to the more rapid blood clearance, higher tumor-to-blood ratios are obtained. With the antibody fragments, tumors can be visualized more rapidly: optimal images can be acquired within 24 h p.i., whereas intact IgG can be used when high concentrations of the antibody in the tumor are required (e.g. in therapeutic applications when high payloads of toxic agents should be targeted to the tumor).

Here, we observed that the tumor uptake of ^{111}In -D2B IgG was higher than that of ^{111}In -F(ab')₂ and ^{111}In -Fab at all time points, even as early as 24 h after injection. However, at early time points after injection, tumor-nontumor ratios of ^{111}In -F(ab')₂ and ^{111}In -Fab were higher than those of ^{111}In -D2B IgG indicating that the antibody fragments are preferred for imaging purposes. For the evaluation of response to therapy, when imaging early after tracer injection is required, and to determine tracer uptake before and shortly after intervention, antibody fragments should be used.

In contrast to ^{111}In -D2B IgG, the renal clearance of ^{111}In -F(ab')₂ and ^{111}In -Fab resulted in high accumulation in the kidneys, most likely due to tubular reabsorption after glomerular filtration of these antibody preparations. Usually, the threshold for glomerular filtration is approximately 60 kDa, suggesting that the antibody fragments are catabolized into smaller molecules in the kidneys [21]. Renal clearance and accumulation of F(ab')₂ and Fab fragments might be a disadvantage, since it might interfere with visualization of malignant tissue located in the vicinity of the kidneys and the urinary bladder.

For the characterization of the tumor targeting capacities of ^{111}In -D2B IgG, ^{111}In -F(ab')₂ and ^{111}In -Fab fragments, ^{111}In -labeled capromab pendetide was used as a reference in this study. Since capromab pendetide targets an intracellular epitope of PSMA, internalization or uptake into the cell by another process is required to bind to PSMA. It has been postulated that capromab pendetide may only bind dying or necrotic cells with cellular membranes that are permeable for IgG [22]. Therefore, ^{111}In -capromab pendetide has low sensitivity for viable tumor lesions which makes it a suboptimal agent for diagnostic imaging of prostate cancer. Still, specific tumor targeting of the PSMA⁺ LNCaP tumors was observed with ^{111}In -labeled capromab pendetide, although at a much lower level than ^{111}In -D2B IgG.

Overall, the new mAb D2B IgG has excellent *in vivo* tumor targeting characteristics. In addition, ^{111}In -F(ab')₂ and ^{111}In -Fab fragments of D2B IgG are feasible for SPECT or PET imaging of PSMA-expressing prostate cancer. The preparations based on antibody fragments allow imaging at early time points after injection, while the preparation based on intact D2B IgG has a higher absolute uptake in the tumor.

CONCLUSION

^{111}In -labeled D2B IgG can be used for imaging of PSMA-expressing cancer, as shown in mice with s.c. PSMA-expressing tumors. The xenografts were clearly visualized in SPECT/CT with specific differentiation between PSMA⁻ and PSMA⁺ tumors. Compared to ^{111}In -capromab pentetide, higher tumor-to-blood ratios were obtained. Due to renal accumulation of F(ab')₂ and Fab fragments visualization of malignant tissue located in the vicinity of the kidneys might be hampered. However, especially in settings where multiple images within a short time interval are required, ^{111}In -D2B F(ab')₂ and Fab fragments can be used.

REFERENCES

- (1) Heidenreich A, Bastian PJ, Bellmunt J, Bolla M, Joniau S, van der Kwast T, Mason M, Matveev V, Wiegel T, Zattoni F, Mottet N. EAU Guidelines on Prostate Cancer. Part 1: Screening, Diagnosis, and Local Treatment with Curative Intent-Update 2013. *Eur Urol.* 2014; 65(1):124-37
- (2) Fletcher JW, Djulbegovic B, Soares HP, Siegel BA, Lowe VJ, Lyman GH, Coleman RE, Wahl R, Paschold JC, Avril N, Einhorn LH, Suh WW, Samson D, Delbeke D, Gorman M, Shields AF. Recommendations on the use of ¹⁸F-FDG PET in oncology. *J Nucl Med.* 2008; 49(3):480-508
- (3) Jana S, Blaufox MD. Nuclear medicine studies of the prostate, testes, and bladder. *Semin Nucl Med.* 2006; 36(1):51-72
- (4) Israeli RS, Powell CT, Fair WR, Heston WDW. Molecular cloning of a complementary DNA encoding a prostate specific membrane antigen. *Cancer Res.* 1993; 53(2):227-230
- (5) Ross JS, Sheehan CE, Fisher HA, Kaufman RP, Jr, Kaur P, Gray K, Webb I, Gray GS, Mosher R, Kallakury BV. Correlation of primary tumor prostate-specific membrane antigen expression with disease recurrence in prostate cancer. *Clin Cancer Res.* 2003; 9(17):6357-6362
- (6) Horoszewicz JS, Kawinski E, Murphy GP. Monoclonal antibodies to a new antigenic marker in epithelial prostatic cells and serum of prostatic cancer patients. *Anticancer Res.* 1987; 7(5B):927-935
- (7) FDA Capromab Pendetide Product Approval Information; <http://www.fda.gov/Drugs/DevelopmentApprovalProcess/HowDrugsareDevelopedandApproved/ApprovalApplications/TherapeuticBiologicApplications/ucm080734.htm>
- (8) Barren RJ 3rd, Holmes EH, Boynton AL, Misrock SL, Murphy GP. Monoclonal antibody 7E11.C5 staining of viable LNCaP cells. *Prostate.* 1997; 30(1):65-68
- (9) Smith-Jones PM, Vallabhajosula S, Goldsmith SJ, Navarro V, Hunter CJ, Bastidas D, Bander NH. In vitro characterization of radiolabeled monoclonal antibodies specific for the extracellular domain of prostate-specific membrane antigen. *Cancer Res.* 2000; 60(18):5237-5243
- (10) Milowsky MI, Nanus DM, Kostakoglu L, Vallabhajosula S, Goldsmith SJ, Bander NH. Phase I trial of yttrium-90-labeled anti-prostate-specific membrane antigen monoclonal antibody J591 for androgen-independent prostate cancer. *J Clin Oncol.* 2004; 22(13):2522-2531
- (11) Bander NH, Trabulsi EJ, Kostakoglu L, Yao D, Vallabhajosula S, Smith-Jones P, Joyce MA, Milowsky M, Nanus DM, Goldsmith SJ. Targeting metastatic prostate cancer with radiolabeled monoclonal antibody J591 to the extracellular domain of prostate specific membrane antigen. *J Urol.* 2003; 170(5):1717-21
- (12) Bander NH, Milowsky MI, Nanus DM, Kostakoglu L, Vallabhajosula S, Goldsmith SJ. Phase I trial of ¹⁷⁷lutetium-labeled J591, a monoclonal antibody to prostate-specific membrane antigen, in patients with androgen-independent prostate cancer. *J Clin Oncol.* 2005; 23(21):4591-601

- (13) Colombatti M. Isolated monoclonal antibody or fragment thereof binding Prostate Specific Membrane Antigen, conjugates and uses thereof. WO 2009/130575 A2 International Patent Application (PCT/IB2009/005326)
- (14) Steiner M, Neri D. Antibody-radionuclide conjugates for cancer therapy: historical considerations and new trends. *Clin Cancer Res.* 2011; 17(20):6406-6416
- (15) Parham P, Androlewicz MJ, Brodsky FM, Holmes NJ, Ways JP. Monoclonal antibodies: purification, fragmentation and application to structural and functional studies of class I MHC antigens. *J Immunol Methods.* 1982; 53(2):133-173
- (16) Lindmo T, Boven E, Cuttitta F, Fedorko J, Bunn PA Jr., Determination of the immunoreactive fraction of radiolabeled monoclonal antibodies by linear extrapolation to binding at infinite antigen excess. *J Immunol Methods.* 1984; 72(1):77-89
- (17) Heskamp S, van Laarhoven HW, Molkenboer-Kuening JD, Franssen GM, Versleijen-Jonkers YM, Oyen WJ, van der Graaf WT, Boerman OC. ImmunoSPECT and immunoPET of IGF-1R expression with the radiolabeled antibody R1507 in a triple-negative breast cancer model. *J Nucl Med.* 2010; 51(10):1565-1572
- (18) Jain RK. Physiological Barriers to Delivery of Monoclonal Antibodies and Other Macromolecules in Tumors. *Cancer Res.* 1990; 50(3 Suppl):814s-819s
- (19) Gehlsen K, Gong R, Bramhill D, Wiersma D, Kirkpatrick S, Wang Y, Feng Y, Dimitrov DS. Pharmacokinetics of engineered human monomeric and dimeric CH2 domains. *MAbs.* 2012; 4(4):466-474
- (20) Pluen A, Boucher Y, Ramanujan S, McKee TD, Gohongi T, di Tomaso E, Brown EB, Izumi Y, Campbell RB, Berk DA, Jain RK. Role of tumor-host interactions in interstitial diffusion of macromolecules: cranial vs. subcutaneous tumors. *Proc Natl Acad Sci U S A.* 2001; 98(8):4628-4633
- (21) Heskamp S, van Laarhoven HW, Molkenboer-Kuening JD, Bouwman WH, van der Graaf WT, Oyen WJ, Boerman OC. Optimization of IGF-1R SPECT/CT Imaging Using ¹¹¹In-Labeled F(ab')₂ and Fab Fragments of the Monoclonal Antibody R1507. *Mol Pharm.* 2012; 9(8):2314-2321
- (22) Troyer JK, Feng Q, Beckett ML, Wright GL Jr. Biochemical characterization and mapping of the 7E11-C5.3 epitope of the prostate-specific membrane antigen. *Urol Oncol.* 1995; 1(1):29-37

2.3

Pretargeted immuno-PET and radioimmunotherapy of prostate cancer with an anti-TROP-2 x anti-HSG bispecific antibody

Catharina M. van Rij^{1,2}

Susanne Lütje¹

Cathelijne Frielink¹

Robert M. Sharkey³

David M. Goldenberg³

Gerben M. Franssen¹

William J. McBride³

Edmund A. Rossi³

Wim J.G. Oyen¹

Otto C. Boerman¹

¹ Department of Radiology and Nuclear Medicine,
Radboud University Medical Center, Nijmegen, Netherlands

² Department of Clinical Pharmacy, Radboud University Medical
Center, Nijmegen, Netherlands

³ Immunomedics, Inc., Morris Plains, New Jersey, United States

ABSTRACT

Background

TF12 is a trivalent bispecific antibody that consists of two anti-TROP-2 Fab fragments and one anti-histaminesuccinyl-glycine (HSG) Fab fragment. The TROP-2 antigen is found in many epithelial cancers, including prostate cancer (PC), and therefore this bispecific antibody could be suitable for pretargeting in this cancer. In this study, the characteristics and the potential for pretargeted radioimmunoimaging and radioimmunotherapy with TF12 and the radiolabeled di-HSG peptide IMP288 in mice with human PC were investigated.

Methods

The optimal TF12 protein dose, IMP288 peptide dose, and dose interval for PC targeting were assessed in nude mice with s.c. PC3 xenografts. Immuno-positron emission tomography (PET)/CT was performed using TF12/⁶⁸Ga-IMP288 at optimized conditions. The potential of pretargeted radioimmunotherapy (PRIT) using the TF12 and ¹⁷⁷Lu-IMP288 was determined.

Results

TF12 and ¹¹¹In-IMP288 showed high and fast accumulation in the tumor ($20.4 \pm 0.6\%$ ID/g at 1 h postinjection (p.i.)) at optimized conditions, despite the internalizing properties of TF12. The potential for PRIT was shown by retention of 50 % of the ¹¹¹In-IMP288 in the tumor at 48 h p.i.. One cycle of treatment with TF12 and ¹⁷⁷Lu-IMP288 showed significant improvement of survival compared to treatment with ¹⁷⁷Lu-IMP288 alone (90 vs. 67 days, $p < 0.0001$) with no renal or hematological toxicity.

Conclusion

TROP-2-expressing PC can be pretargeted efficiently with TF12, with very rapid uptake of the radiolabeled hapten-peptide, IMP288, sensitive immuno-PET, and effective therapy.

INTRODUCTION

Prostate cancer (PC) causes significant morbidity and still is the second leading cause of cancer-related deaths in men in the Western world. Approximately 17 % of American men will be diagnosed with PC during their lifetime, and 20 % of them will die of the disease. While curable when diagnosed in an early stage and treatable in the hormone-dependent stage, PC treatment options are limited in advanced stages. In view of this, it is essential to differentiate between metastatic and non-metastatic disease to predict disease outcome and to determine treatment options. Furthermore, an accurate imaging method for determining the location, extent, and biological potential of PC could improve patient outcome by directing therapy more accurately both in surgery and radiation therapy. Transrectal ultrasound (TRUS) and conventional magnetic resonance imaging (MRI) can be used for the diagnosis of the primary tumor, but adequate detection of metastatic spread leaves room for further improvement. Positron emission tomography (PET) imaging is a widely used imaging modality to detect metastatic disease in several cancers. However, ^{18}F -fluorodeoxyglucose (FDG) PET is not suited for staging patients with PC, since sensitivity is low due to artifacts related to its renal excretion and due to the relatively low avidity of differentiated PC for ^{18}F -FDG [1, 2]. Several other radiotracers have been developed for imaging metastasized PC, but all of them have disadvantages, such as low sensitivity or practical considerations, such as the need for an on-site cyclotron for the ^{11}C tracers. Antibody imaging in humans has been reported with several radiolabeled monoclonal antibodies, such as 7E11-C53 (ProstaScint[®], capromab pendetide) and J591 [2]. Due to the long circulatory half-lives of imaging agents based on intact antibody molecules, lesions can only be depicted several days after injection.

hRS7 is a humanized IgG1 monoclonal antibody directed against TROP-2, also known as epithelial glycoprotein-1 (EGP-1), GA733-1, gp50/T16, and tumor-associated calcium signal transducer 2 (TACSTD2). TROP-2 is a 46 kDa transmembrane glycoprotein expressed in carcinomas of the lung, bladder, breast, cervix, ovary, stomach, and prostate [3]. Most normal human tissues do not express TROP-2, but it is found at low levels in several normal glandular cells, including glands in the bronchus, breast, prostate and skin, and ducts and acini of the pancreas [4]. Given its expression in PC, we studied the potential targeting ability of hRS7 IgG in a nude mouse-human PC model [5], showing excellent *in vivo* targeting of PC3 xenografts with ^{89}Zr - and ^{111}In -hRS7 IgG within 3 days. The slow clearance from the circulation results in low tumor-to-background ratios at earlier time points after i.v. injection. For earlier imaging, we explored a pretargeting approach using the bispecific monoclonal antibody (bsAb) TF12, a trivalent bsAb that consists of two anti-TROP-2 Fab fragments and one anti-histaminesuccinyl-glycine (HSG) Fab fragment [6]. In pretargeting, unlabeled TF12 is injected i.v., and when it has cleared from the

blood, an HSG-substituted radiolabeled hapten-peptide is injected. This hapten-peptide will be trapped in the tumor by the anti-HSG arm of the bsAb or is rapidly cleared from the body.

In this study, the characteristics and the potential for pretargeted radioimmunoimaging and radioimmunotherapy with TF12 and the radiolabeled di-HSG peptide, IMP288, in mice with human PC xenografts were investigated.

MATERIALS AND METHODS

The anti-TROP-2 x anti-HSG bsAb TF12 was produced using the dock-and-lock technology (DNL[®]) as described previously [7]. The production and characterization of the anti-TROP-2 mAb hRS7 have been described previously [3]. The DOTA-conjugated hapten-peptide IMP288 [DOTA-D-Tyr-D-Lys(HSG)-D-Glu-D-Lys(HSG)-NH₂] was prepared as described by McBride et al. [8].

Cell culture

The human PC cell line PC3 is an androgen-independent cell line, originally derived from a PC bone metastasis. Cells were obtained from American Type Culture Collection (CRL 1435, Manassas, VA, USA) and were grown in RPMI 1640 medium (GIBCO[®], Life Technologies Corporation, Carlsbad, CA, USA), supplemented with 10 % fetal calf serum (FCS, Life Technologies, Grand Island, NY, USA). Before s.c. inoculation of mice to induce PC3 xenografts, tumor cells were washed with 0.9 % NaCl, disaggregated with trypsin, and resuspended in 67 % complete RPMI 1640 medium and 33 % Matrigel (BD Biosciences, San Jose, CA, USA) to the appropriate concentration (3×10^6 cells/200 μ l).

Mouse model

All experiments were approved by the institutional Animal Welfare Committee of the Radboud University Medical Center Nijmegen and were conducted in accordance with the principles set forth by the Revised Dutch Act on Animal Experimentation.

Male BALB/c nude mice (Janvier SAS, Le Genest Saint Isle, France), 8–9 weeks old, were adapted to laboratory conditions for at least 1 week before experimental use. Mice were housed under non-sterile standard conditions in filtertopped cages (five mice per cage), with free access to animal chow (Sniff Voer[®]) and water. The mice were inoculated s.c. in the flank with 200 μ l of PC3 cell suspension (3×10^6 cells). The s.c. PC3 tumors grew to approximately 0.1 g in 10 days after tumor cell inoculation, as determined by caliper measurements in three dimensions using the formula $V = 4/3\pi$ (length/2 \times width/2 \times height/2), assuming that the density of tumor tissue is 1 g/cm³. The radiolabeled preparations (0.2 ml) were injected intravenously.

Radiolabeling of IMP288 and hRS7

The DOTA-conjugated IMP288 was radiolabeled with ^{111}In (Covidien, Petten, The Netherlands), ^{177}Lu (IDB Holland BV, Baarle-Nassau, The Netherlands), or with ^{68}Ga from a TiO_2 -based $^{68}\text{Ge}/^{68}\text{Ga}$ generator (Cyclotron Co, Ltd., Obninsk, Russian Federation). Radiolabeling was performed essentially as described previously by Schoffelen et al. [9]. For ^{68}Ga labeling, 84 MBq of $^{68}\text{GaCl}_3$ was added to 1 μg of IMP288 in 1 M HEPES buffer (50 μl , 4-(2-hydroxyethyl)-1-piperazineethanesulfonic acid, Sigma-Aldrich, St. Louis, MO, USA). After incubation at 95 °C for 20 min, 50 mM ethylenediaminetetraacetic acid (EDTA, Sigma-Aldrich, St. Louis, MO, USA) was added to a final concentration of 1 μM . The ^{68}Ga -IMP288 preparation was purified on an Oasis[®] HLB cartridge (Waters, Milford, MA, USA) and eluted with 1 ml of 25 % ethanol essentially as described previously [10]. Before i.v. injection, the preparation was diluted at least 2.5 times with 0.5 % bovine serum albumin (BSA, Sigma-Aldrich, St. Louis, MO, USA) in phosphate-buffered saline (PBS).

DTPA conjugation and subsequent labeling of hRS7 IgG with ^{177}Lu were performed essentially as described previously [3, 5]. The radiochemical purity (RCP) of the labeled IMP288 preparations was determined using instant thin-layer chromatography (ITLC) and reversed phase high-performance liquid chromatography (RP-HPLC), as described previously [9]. ITLC was performed to determine the fraction of unbound ^{111}In , ^{177}Lu , or ^{68}Ga (mobile phase 1:1 0.1 M ammonium acetate (Merck, Darmstadt, Germany) and 0.1 M EDTA) and the fraction of colloid (mobile phase 1:1 methanol (Merck, Darmstadt, Germany) and 0.25 M ammonium acetate, pH 5.5).

For RP-HPLC, the C18 column (Zorbax Rx-C18, 5 μm , 4.6 \times 250 mm, Agilent Technologies, Amstelveen, The Netherlands) was eluted with a mixture of 97 % of a 0.1 % trifluoroacetic acid in H_2O solution (TFA, Labscan, Analytical Sciences, Brussels, Belgium) with 3 % of a 0.1 % TFA in acetonitrile solution (Lab-scan, Analytical Sciences, Brussels, Belgium) with a linear gradient to 100 % of the latter solution over 10 min at a flow rate of 1 ml/min. RCP of all labeled IMP288 preparations always exceeded 97 %; the RCP of ^{177}Lu -hRS7 exceeded 98 %.

Radiolabeling of TF12

The bsAb TF12 was radioiodinated with ^{125}I according to the iodogen method [11]. Twenty micrograms of TF12 and 3.7 MBq Na^{125}I (GE Healthcare Europe, Den Bosch, The Netherlands) in 50 mmol/L phosphate buffer, pH 7.4, were incubated in an Eppendorf vial coated with 50 μg of iodogen (1,3,4,6-tetrachloro-3,6-diphenylglycoluril; Pierce Biotechnology, Inc., Rockford, IL, USA) for 10 min at room temperature. ^{125}I -TF12 was purified on a PD-10 column (GE Healthcare, London, UK) eluted with PBS, 0.5 % BSA.

Immunoreactivity

The anti-TROP-2 reactivity of radiolabeled TF12 and hRS7 was determined using freshly trypsinized PC3 cells, as described by Lindmo et al. [12] with minor modifications. The bispecific immunoreactivity of TF12 was demonstrated by incubating PC3 cells with TF12 (10 µg/ml) and subsequent incubation with ¹¹¹In-IMP288 (200 Bq/ml). After 1 h at 37 °C, the total activity and the activity in the cell pellet were determined in a gamma counter. More than 70 % of the added hapten-peptide specifically bound to the PC3 cells.

Biodistribution studies

The effect of the TF12 dose on tumor uptake of a fixed amount (0.25 nmol=400 ng) of ¹¹¹In-labeled IMP288 in mice with s.c. PC3 tumors was determined by administering 1.25, 2.5, 5.0, and 12.5 nmol (231, 462, 924, and 2,310 µg) of TF12 i.v., and then 16 h later 0.4 MBq of ¹¹¹In-IMP288 was injected. Two hours later, mice were dissected and tissue uptake was determined (five mice/group). Subsequently, the optimal amount of IMP288 that can be given after administering a fixed dose of TF12 (2.5 nmol=462 µg) was determined. Four doses of IMP288 were examined: 25, 50, 100, and 200 nmol, each given 16 h after TF12. Two hours after injection of 0.4 MBq of ¹¹¹In-IMP288, mice were euthanized and necropsied (five mice/group). The optimal interval between TF12 and ¹¹¹In-IMP288 injection was assessed at the preselected optimal TF12 (2.5 nmol) and IMP288 doses (0.1 nmol). The following intervals were tested: 12, 14, 16, 18, 20, 24, and 36 h. Lastly, under optimized conditions (2.5 nmol TF12, 0.1 nmol IMP288, 16h interval), the retention of ¹¹¹In-IMP288 in the tumor was monitored over the course of 3 days.

Pretargeted immuno-PET

Groups of five mice with s.c. PC3 tumors were injected i.v. with 2.5 nmol of TF12 and 16 h later with 5 ± 2 MBq (0.1 nmol) of ⁶⁸Ga-IMP288. One hour after injection of ⁶⁸Ga-IMP288, mice were euthanized by O₂/CO₂ asphyxiation and PET/CT images were acquired with an Inveon® animal PET/CT scanner (Siemens Preclinical Solutions, Siemens Healthcare Molecular Imaging, Knoxville, TN, USA), having an intrinsic spatial resolution of 1.5 mm. The animals were placed in prone position. PET emission scans were acquired for 20 min, preceded by CT scans for anatomic reference (spatial resolution 113 µm, 80 kV, 500 µA, exposure time 300 ms). Scans were reconstructed using Inveon Acquisition Workplace software (version 1.2, Siemens Preclinical Solutions, Knoxville, TN, USA), with an ordered set expectation maximization-3D/maximum a posteriori (OSEM3D/MAP) algorithm with the following parameters: matrix 256×256×159, pixel size 0.43×0.43×0.8 mm³, and a beta value of 0.1. After imaging, tumors and organs were dissected, weighed, and counted in a gamma counter to determine the biodistribution of the radiolabel. The percentage injected dose per gram (% ID/g) tissue was calculated against an injection standard.

Pretargeted radioimmunotherapy

The potential of pretargeted radioimmunotherapy (PRIT) with TF12 and ^{177}Lu -IMP288 was assessed in a therapy experiment in mice with PC3 xenografts (ten mice/group). Mice were treated with TF12/ ^{177}Lu -IMP288 or ^{177}Lu -hRS7 IgG 9 days after PC3 cell inoculation, when tumors weighed approximately 0.1 g.

In the mice that were treated with PRIT, tumors were pretargeted with 2.5 nmol TF12 16 h before administration of the ^{177}Lu -IMP288. The next day, mice received the maximum ^{177}Lu activity dose that could be labeled to 0.1 nmol IMP288 (13.7 MBq). Another group was treated with the maximum tolerable dose of ^{177}Lu -hRS7 (11.1 MBq, 13.8 μg). One control group of PC3 tumor-bearing mice was injected i.v. with vehicle (200 μl PBS, 0.5 % BSA) twice instead of TF12 and IMP288. The other control group received vehicle instead of TF12 and was injected 16 h later with 13.7 MBq of ^{177}Lu -IMP288.

Tumor size was measured in three dimensions with a caliper and body weight was determined twice weekly starting 7 days after tumor cell inoculation. Blood samples of 0.1 ml of all mice were collected via submandibular bleeding before therapy and 14, 21, 35, 42, 56, 70, and 88 days after administration of the agents to determine hemoglobin levels and leukocyte and platelet counts. Blood creatinine and blood urea nitrogen (BUN) levels were determined before and 4 and 7 weeks after start of the therapy. When the humane endpoint was reached (tumor size $>2\text{ cm}^3$ or animal discomfort level >3), mice were euthanized by O_2/CO_2 asphyxiation and dissected. At dissection, the tumor and kidneys were excised and weighed. The experiment was terminated 120 days after injection of the radiolabeled compounds and the remaining mice were euthanized and dissected.

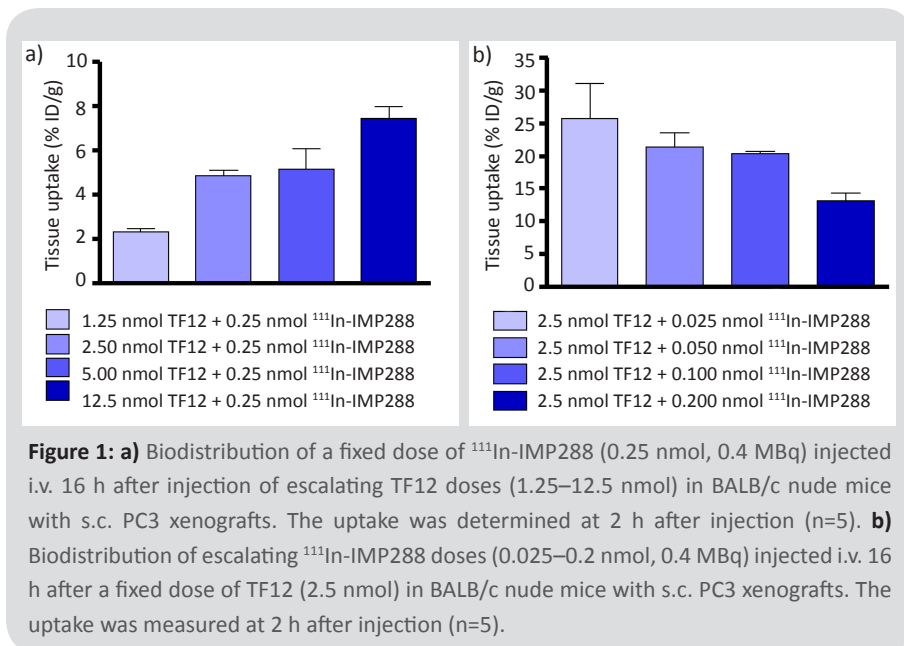
Statistical analysis

Statistical analysis was performed using GraphPad Prism version 5.00 for Windows. Survival curves were compared using the log-rank test. The level of significance was set at a p value of less than 0.05.

RESULTS

Biodistribution studies

The optimal TF12 protein dose to pretarget the PC3 tumors was determined in a protein dose escalation study. Tumor uptake of ^{111}In -IMP288 (0.25 nmol) 2 h after injection increased with increasing bsAb TF12 protein doses, as summarized in **figure 1a**. Highest uptake ($7.4 \pm 0.8\%$ ID/g) was obtained when the tumor was pretargeted by injection of 12.5 nmol of TF12. The optimal amount of TF12 was determined to be 2.5 nmol, since there was only minor improvement of tumor uptake (1.5-fold increase) at the highest bsAb dose (5-fold increase). Following



injection of increasing amounts of IMP288 at a fixed TF12 dose of 2.5 nmol, tumor uptake clearly decreased (**figure 1b**). Optimal uptake in the tumor (20–25% ID/g) was obtained at hapten-peptide doses ≤ 0.1 nmol IMP288. Based on these results, 0.1 nmol of IMP288 was used in further experiments, since this amount of IMP288 could be labeled with activity doses required for pretargeted immuno-PET imaging (^{68}Ga) and for pretargeted radionuclide therapy (^{177}Lu).

Recently, *in vitro* experiments have shown that TF12 is slowly internalized by the tumor cell after binding to TROP-2 [6]. To estimate the kinetics of internalization of TF12 *in vivo*, the biodistribution of bsAb TF12 labeled with ^{111}In and ^{125}I was studied in mice with s.c. PC3 tumors 16 h postinjection (p.i.). A clear and significant difference between uptake of $^{111}\text{In-TF12}$ ($4.9 \pm 0.6\%$ ID/g) and $^{125}\text{I-TF12}$ ($0.7 \pm 0.2\%$ ID/g, $p < 0.0001$) in the tumor was observed 16 h after injection of the radiolabeled TF12, which could be explained by the internalizing characteristics of TF12. The biodistribution of the ^{111}In -labeled TF12 indicated that the bsAb accumulated preferentially in the tumor ($4.9 \pm 0.6\%$ ID/g, 16 h p.i.), while the blood level at that time did not exceed $0.4 \pm 0.1\%$ ID/g. The optimal interval between injection of TF12 and $^{111}\text{In-IMP288}$ was assessed by examining seven intervals: 12, 14, 16, 18, 20, 24, and 36 h (three to five mice/group, **figure 2**). Extension of the time interval between injection of TF12 and injection of $^{111}\text{In-IMP288}$ from 16 to 36 h significantly decreased tumor uptake of the radiolabeled hapten, from $9.6 \pm 1.3\%$ ID/g to $1.0 \pm 0.5\%$ ID/g ($p < 0.0001$). Shortening the interval from 16 to 14 or 12 h did not improve

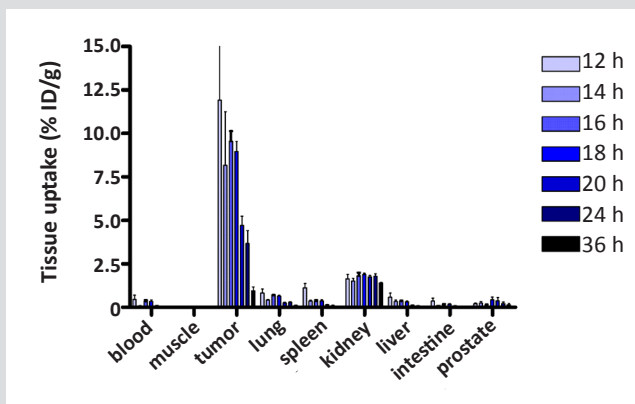


Figure 2: Biodistribution of ^{111}In -IMP288 (0.1 nmol, 0.4 MBq) in BALB/c nude mice with s.c. PC3 xenografts measured at 2 h after injection ($n=3-5$). Prior to injection of ^{111}In -IMP288, mice were injected i.v. with 2.5 nmol of TF12 at increasing time intervals (12, 14, 16, 18, 20, 24, and 36 h).

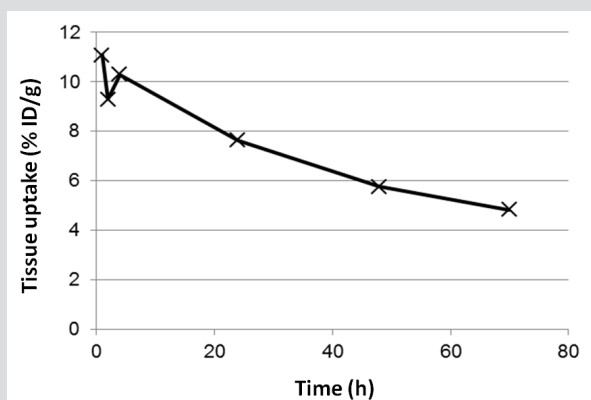


Figure 3: Tumor uptake at increasing time points (1, 2, 4, 24, 48, 70 h) after injection of TF12/ ^{111}In -IMP288 (2.5 nmol/0.1 nmol, 0.4 MBq, 16-h interval, $n=5$).

tumor uptake significantly ($p=0.81$ and $p=0.14$, respectively), while tumor-to-blood ratios were lower at the shorter intervals. Based on these observations an interval of 16 h between injection of TF12 and radiolabeled IMP288 was used. Retention of radiolabeled IMP288 in the tumor over time is particularly important in PRIT. Retention was determined at the optimal TF12 and ^{111}In -IMP288 dose (16-h interval) during 3 days p.i. (five mice/group). **Figure 3** shows that $>50\%$ of the ^{111}In label was still present in the tumor at 48 h after injection ($5.8 \pm 0.7\%$ ID/g, $t_{1/2}=50$ h).

At the optimized conditions determined in the experiments described above, ^{111}In -IMP288 showed a rapid and high uptake in the tumor ($20.4 \pm 0.6\%$ ID/g, 2 h p.i.), while concentrations in blood ($0.9 \pm 0.2\%$ ID/g) and normal tissues were low (**figure 4**). ^{111}In -IMP288 cleared very rapidly from the blood via the kidneys. The healthy organs with the highest uptake ($2.2 \pm 0.1\%$ ID/g) were the kidneys.

Pretargeted immuno-PET

With the same dosing schedule, similar results were obtained with TF12 and ^{68}Ga -IMP288, with slightly lower tumor uptake ($12.2 \pm 2.3\%$ ID/g). To determine the potential of pretargeted immuno-PET to detect TROP-2-expressing tumors, microPET imaging of ^{68}Ga -IMP288 was performed in nude mice with s.c. PC3 tumors of approximately 0.1 g. Images acquired as early as 1 h p.i. clearly showed the PC3 tumors (**figure 5**). No accumulation of radioactivity in the other normal organs was observed, except for the kidneys and the bladder.

Pretargeted radioimmunotherapy

The potential of PRIT using the bsAb TF12 and ^{177}Lu -labeled IMP288 was determined in a therapy experiment and compared to RIT with ^{177}Lu -hRS7 (11.1 MBq, 13.8 μg). PRIT with 2.5 nmol TF12 and 13.7 MBq ^{177}Lu -IMP288 significantly improved the median survival of mice with s.c. PC3 tumors from 67 to 90 days ($p < 0.0001$, **figure 6**). The control groups received either ^{177}Lu -IMP288 without TF12 or vehicle. Median survival of the mice in both control groups was similar, indicating that there is no effect of administration of a high activity dose of ^{177}Lu -IMP288

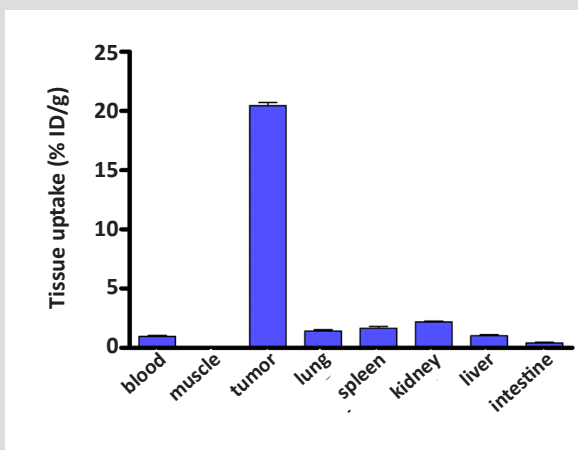


Figure 4: Biodistribution of ^{111}In -IMP288 (0.1 nmol, 0.4 MBq) injected i.v. 16 h after i.v. injection of TF12 (2.5 nmol) in BALB/c nude mice with s.c. PC3 xenografts at 2 h after injection (n=5).

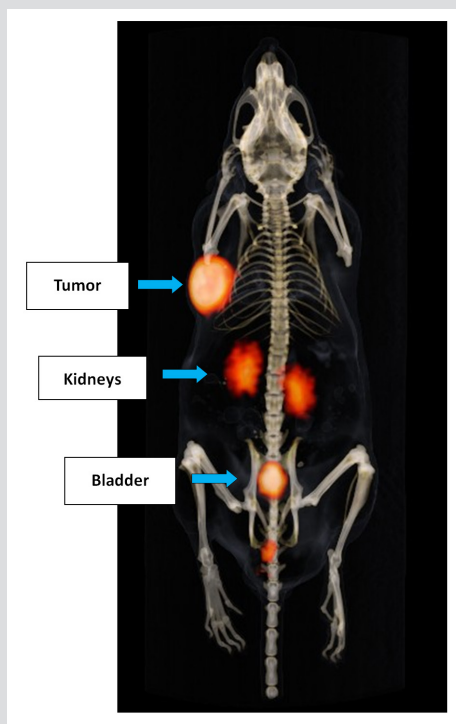


Figure 5: Anterior 3D volume-rendering projection of a microPET/CT scan of a BALB/c nude mouse with s.c. PC3 tumor on the shoulder injected with TF12 and ^{68}Ga -IMP288 (0.1 nmol, 5 MBq), acquired 1 h after injection.

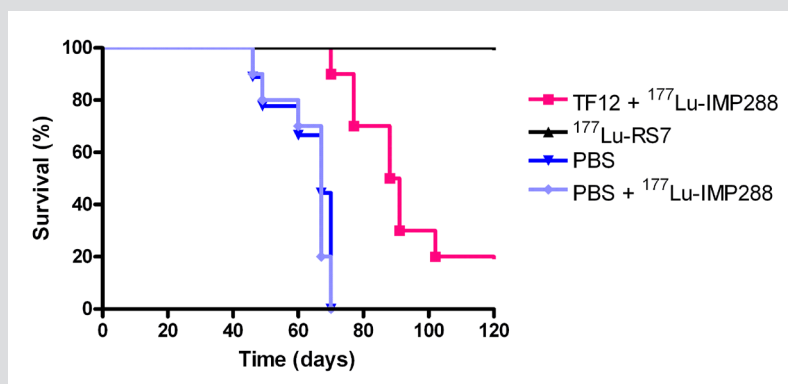


Figure 6: Survival of BALB/c nude mice with s.c. PC3 xenograft treated with TF12/ ^{177}Lu -IMP288 (2.5 nmol/11.1 MBq, 0.1 nmol), ^{177}Lu -hRS7 (13.7 MBq, 30 μg), ^{177}Lu -IMP288 without pretargeting (11.1 MBq, 0.1 nmol), or vehicle (n=10).

alone. At the end of the experiment (120 days), all mice treated with ^{177}Lu -hRS7 IgG were still alive. However, this increase in survival (median survival >120 days) was accompanied by a significant decrease in platelets (from $1,110 \pm 230 \times 10^9/\text{L}$ at $t=-3$ days to $430 \pm 250 \times 10^9/\text{L}$ at $t=14$ days, $p=0.0005$) and leukocytes (from $3.2 \pm 0.8 \times 10^9/\text{L}$ at $t=-3$ days to $0.6 \pm 0.3 \times 10^9/\text{L}$ at $t=14$ days, $p<0.0001$), which was not observed in the mice treated with PRIT. Thus, treatment with ^{177}Lu -hRS7 IgG appeared to be more effective, but also clearly more toxic.

In PRIT, the kidney could also be the organ at risk. Therefore, creatinine and urea levels were examined in the experimental groups and the kidneys were examined histologically after completion of the experiment (120 days). Creatinine and urea levels, and histological analysis of the kidneys compared to age-matched control mice, did not show any indication of renal toxicity.

DISCUSSION

The present study shows the potential of pretargeted immuno-PET and PRIT of PC with the bsAb TF12 and the radiolabeled hapten-peptide IMP288. The dose optimization studies in mice with s.c. PC3 tumors revealed that the highest uptake of the radiolabeled hapten-peptide in the tumor was obtained at bsAb doses of ≥ 2.5 nmol and at lower IMP288 doses (≤ 0.1 nmol). The optimal time interval between injection of TF12 and ^{111}In -IMP288 was 16 h. Most importantly, these experiments showed that internalization does not disqualify bsAbs for pretargeting as long as the dosage interval is carefully tuned, as shown previously by Sharkey et al. [6]. Retention of the radiolabel in the tumor was high: more than 50 % of the radiolabel that was present in the tumor at 1 h p.i. was still present after 48 h. In the TF2/IMP288 pretargeting system using the non internalizing anti-CEA x anti-HSG bsAb in mice with LS174T tumors only 32 % of the radiolabeled IMP288 was retained in the tumor [9], suggesting that the internalizing characteristics of TF12 could cause better retention of the radiolabel in the tumor due to internalization of the TF12-IMP288 complex by the tumor cells.

Retention in the tumor and rapid clearance from the blood enabled clear visualization of the tumor with PET as early as 1 h after injection. Some ^{68}Ga activity in the kidneys and bladder was observed, due to the renal clearance of IMP288. Renal clearance might be a disadvantage when imaging PC, since physiological uptake in the urinary tract might conceal pathological uptake in the lower abdomen. However, renal clearance of radiolabeled IMP288 is very efficient, which may enable the distinction between physiological and pathological uptake.

The PRIT experiment showed that TF12/ ^{177}Lu -IMP288 significantly improved the median survival of mice with s.c. PC3 tumors without significant hematological or renal toxicity. The improved median survival in the group of mice treated with ^{177}Lu -hRS7 IgG was achieved at the expense of severe hematological toxicity.

In the therapy experiments, the maximum activity dose of ^{177}Lu -IMP288 was used, which necessarily was below the maximum tolerated dose (MTD), due to the limited specific activity of the ^{177}Lu -chloride used for labeling of the peptide. Currently, carrier-free ^{177}Lu -chloride has become available with improved specific activity. In future studies, we will determine the safety and efficacy of PRIT with higher activity doses of ^{177}Lu -IMP288 and of multiple cycles of TF12/ ^{177}Lu / ^{90}Y -IMP288, as accomplished by Schoffelen et al. with anti-CEA x anti-HSG bsAb TF2 [13].

CONCLUSION

The dosing of the pretargeting agents TF12 and IMP288 was optimized in mice with s.c. PC3 tumors. At optimized conditions, TROP-2-expressing PC3 tumors could be targeted efficiently and very rapidly with the radiolabeled hapten-peptide IMP288. This pretargeting system allows rapid and sensitive PET imaging of PC using ^{68}Ga -labeled hapten-peptide. TF12 together with ^{177}Lu -labeled IMP288 could also be promising candidates for PRIT of TROP-2-expressing prostate tumors. Further PRIT studies at MTD with higher activity doses and/or multiple dosing are necessary to determine its application in the future.

REFERENCES

- (1) Beheshti M, Langsteger W, Fogelman I. Prostate cancer: role of SPECT and PET in imaging bone metastases. *Semin Nucl Med.* 2009; 39(6):396–407
- (2) Ravizzini G, Turkbey B, Kurdziel K, Choyke PL. New horizons in prostate cancer imaging. *Eur J Radiol.* 2009; 70(2):212–226
- (3) Basu A, Goldenberg DM, Stein R. The epithelial/carcinoma antigen EGP-1, recognized by monoclonal antibody RS7-3G11, is phosphorylated on serine 303. *Int J Cancer.* 1995; 62(4):472–479
- (4) Stein R, Basu A, Chen S, Shih LB, Goldenberg DM. Specificity and properties of MAb RS7-3G11 and the antigen defined by this pancarcinoma monoclonal antibody. *Int J Cancer.* 1993; 55(6):938–946
- (5) van Rij CM, Sharkey RM, Goldenberg DM, Frielink C, Molkenboer JD, Franssen GM, et al. Imaging of prostate cancer with immuno-PET and immuno-SPECT using a radiolabeled anti-EGP-1 monoclonal antibody. *J Nucl Med.* 2011; 52(10):1601–1607
- (6) Sharkey RM, van Rij CM, Karacay H, Rossi EA, Frielink C, Regino C, et al. A new Tri Fab bispecific antibody for pretargeting Trop-2-expressing epithelial cancers. *J Nucl Med.* 2012; 53(10):1625–1632
- (7) Rossi EA, Goldenberg DM, Cardillo TM, McBride WJ, Sharkey RM, Chang CH. Stably tethered multifunctional structures of defined composition made by the dock and lock method for use in cancer targeting. *Proc Natl Acad Sci U S A.* 2006; 103(18):6841–6846
- (8) McBride WJ, Zanzonico P, Sharkey RM, Norén C, Karacay H, Rossi EA, et al. Bispecific antibody pretargeting PET (immunoPET) with an ¹²⁴I-labeled hapten-peptide. *J Nucl Med.* 2006; 47(10):1678–1688
- (9) Schoffelen R, Sharkey RM, Goldenberg DM, Franssen G, McBride WJ, Rossi EA, et al. Pretargeted immuno-positron emission tomography imaging of carcinoembryonic antigen-expressing tumors with a bispecific antibody and a ⁶⁸Ga- and ¹⁸F-labeled hapten peptide in mice with human tumor xenografts. *Mol Cancer Ther.* 2010; 9(4):1019–1027
- (10) Brom M, Joosten L, Oyen WJ, Gotthardt M, Boerman OC. Improved labeling of DTPA- and DOTA-conjugated peptides and antibodies with ¹¹¹In in HEPES and MES buffer. *EJNMMI Res.* 2012; 2:4
- (11) Fraker PJ, Speck Jr JC. Protein and cell membrane iodinations with a sparingly soluble chloroamide, 1,3,4,6-tetrachloro-3 α ,6 α -diphrenylglycoluril. *Biochem Biophys Res Commun.* 1978; 80(4):849–57
- (12) Lindmo T, Boven E, Cuttitta F, Fedorko J, Bunn Jr PA. Determination of the immunoreactive fraction of radiolabeled monoclonal antibodies by linear extrapolation to binding at infinite antigen excess. *J Immunol Methods.* 1984; 72(1):77–89
- (13) Schoffelen R, van der Graaf WT, Franssen G, Sharkey RM, Goldenberg DM, McBride WJ, et al. Pretargeted ¹⁷⁷Lu radioimmunotherapy of carcinoembryonic antigen-expressing human colonic tumors in mice. *J Nucl Med.* 2010; 51(11):1780–1787

2.4

Anti-CEA antibody fragments labeled with [^{18}F]AIF for PET imaging of CEA-expressing tumors

Susanne Lütje¹
Gerben M. Franssen¹
Robert M. Sharkey²
Peter Laverman¹
Edmund A. Rossi²
David M. Goldenberg²
Wim J.G. Oyen¹
Otto C. Boerman¹
William J. McBride²

¹Department of Radiology and Nuclear Medicine,
Radboud University Medical Center, Nijmegen, Netherlands

²Immunomedics, Inc., Morris Plains, New Jersey, United States

Adapted from: Bioconjug Chem 2014; 25(2):335-41

ABSTRACT

Background

A facile and rapid method to label peptides with ^{18}F based on chelation of ^{18}F AIF has been developed recently. Since this method requires heating to 100 °C, it cannot be used to label heat-sensitive proteins. Here, we used a two-step procedure to prepare ^{18}F -labeled heat-labile proteins using the ^{18}F AIF method based on hot maleimide conjugation.

Methods

1,4,7-Triazacyclononane-1,4-diacetate (NODA) containing a methyl phenylacetic acid group (MPA) functionalized with N-(2-aminoethyl)maleimide (EM) was used as a ligand which was labeled with ^{18}F AIF and then conjugated to the humanized anti-CEA antibody derivatives hMN-14 Fab', hMN-14-(scFv)₂ (diabody) and a Dock-and-Lock engineered dimeric fragment hMN-14 Fab-AD2 at room temperature. The *in vivo* tumor targeting characteristics of the ^{18}F -labeled antibody derivatives were determined by PET imaging of mice with s.c. xenografts.

Results

NODA-MPAEM was radiolabeled with ^{18}F AIF at a specific activity of 29-39 MBq/nmol and a labeling efficiency of $94 \pm 2\%$. The labeling efficiencies of the maleimide conjugation ranged from 70% to 77%, resulting in ^{18}F AIF-labeled hMN14-Fab', hMN14-Fab-AD2, or hMN14-diabody with a specific activity of 15-17 MBq/nmol. The radiolabeled conjugates were purified by gel filtration. For biodistribution and microPET imaging, antibody fragments were injected intravenously into BALB/c nude mice with s.c. CEA-expressing LS174T xenografts (right flank) and CEA-negative SK-RC-52 xenografts (left flank). All ^{18}F AIF-labeled conjugates showed specific uptake in the LS174T xenografts with a maximal tumor uptake of 4.73 % ID/g at 4 h after injection. Uptake in CEA-negative SK-RC-52 xenografts was significantly lower. Tumors were clearly visualized on microPET images.

Conclusion

Using a ^{18}F AIF-labeled maleimide functionalized chelator, antibody fragments could be radiofluorinated within 4 h at high specific activity. Here, we translated this method to preclinical PET imaging studies and showed feasibility of ^{18}F AIF-fluorinated hMN-14-Fab', ^{18}F AIF-hMN-14-Fab-AD2, and ^{18}F AIF-hMN-14-diabody for microPET imaging of CEA-expressing colonic cancer.

INTRODUCTION

Positron emission tomography (PET) has evolved as a prominent molecular imaging modality in oncology, since it allows high sensitivity, quantitative imaging of cellular features and processes [1]. ¹⁸F is an ideal radionuclide for PET imaging, because of its low positron energy, the lack of other emissions, and its half-life of 109.8 minutes. The most commonly used tracer for PET imaging of tumors is 2-[¹⁸F]fluoro-2-deoxyglucose ([¹⁸F]FDG), which exploits the increased glucose metabolism of tumor cells.

Previously, ¹⁸F-radiolabeling of peptides was a time-consuming and inefficient multistep process. By exploiting the strong bond between [¹⁸F]-fluoride and Al³⁺, ¹⁸F-radiolabeling can be performed efficiently in one step by chelating [¹⁸F]AIF [2]. This method could only be applied to peptides and heat-stable proteins, because 100 °C is the optimal labeling temperature. By separating the chelation of [¹⁸F]AIF (at 100 °C) from the conjugation to the targeting molecule (at room temperature), the labeling approach can now also be applied to label heat-sensitive proteins with ¹⁸F [3]. In this approach, the [¹⁸F]AIF-chelating moiety 1,4,7-triazacyclononane-1,4-diacetate (NODA) with a methyl phenylacetic acid group (MPA) functionalized with N-(2-aminoethyl)maleimide (EM) is used. NODA-MPAEM can be labeled efficiently with ¹⁸F (at 100-110 °C) and subsequently be conjugated with the heat-sensitive protein at room temperature via a maleimide-thiol reaction.

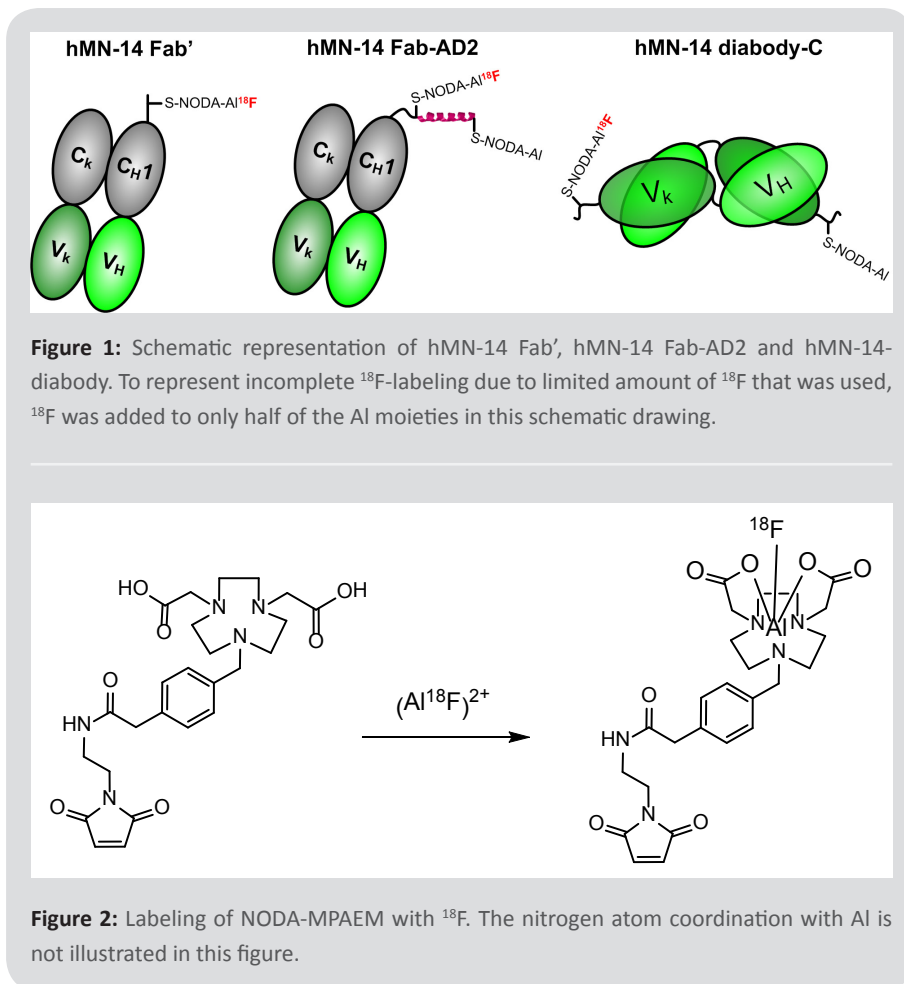
Although intact antibodies are not suitable for imaging of cancer with ¹⁸F because their accumulation in tumors generally takes several days, smaller antibody fragments such as Fab', F(ab')₂, and scFv, allow imaging of tumor lesions within several hours after injection, which is compatible with the half-life of ¹⁸F. Since Fab' fragments bind monovalently to target regions, which might have a negative impact on the tumor uptake and retention, we included the divalent (scFv)₂ diabody format of hMN-14 in our studies, which may provide more avid binding to the target.

In this study, we applied the 2-step method to prepare [¹⁸F]-AIF-fluorinated NODA-MPAEM-hMN-14-Fab', NODA-MPAEM-hMN-14-Fab-AD2, and NODA-MPAEM-hMN-14-diabody and evaluated the *in vitro* characteristics and the *in vivo* tumor targeting capacities of these tracers in nude mice with CEA-expressing LS174T human colon carcinoma xenografts.

MATERIALS AND METHODS

Antibody derivatives

The monoclonal antibody hMN-14 (labetuzumab) and hMN-14-Fab', hMN-14-Fab-AD2, and hMN-14-diabody (**figure 1**) were obtained from Immunomedics, Inc. (Morris Plains, NJ, USA).



Synthesis of NODA-MPAEM

NODA-MPAEM (methyl phenyl acetamido ethyl maleimide, **figure 2**) was synthesized as described by McBride et al. [2]. Briefly, (tBu)₂NODA-MPAA NHS ester (128.3 mg, 0.213 mmol) in CH_2Cl_2 (5 ml) was added to a solution of N-(2-aminoethyl) maleimide trifluoroacetate salt (52.6 mg, 0.207 mmol) in 250 μl dimethylformamide (DMF) and 20 μl N,N-diisopropylethylamine (DIEA). After three hours of incubation, the conjugation was evaporated and treated with 2 ml trifluoroacetic acid (TFA). In the following, the product was diluted with water and purified by preparative RP-HPLC using Waters PrepLC 4000 system with Sunfire Prep C18 optimal bed density (OBD) reverse-phase column (150 \times 30 mm, 5 μm), using a linear gradient of 100% A (0.1% TFA) to 15% B (90% acetonitrile, 10% water, 0.1% TFA) over 80 min at a flow rate of 45 mL/min (absorbance 220 nm).

¹⁸F radiolabeling of NODA-MPAEM

¹⁸F dissolved in water (BV Cyclotron VU, Amsterdam, The Netherlands) was passed through a SepPak CM cartridge (Waters, Etten-Leur, The Netherlands) and Sep-Pak QMA cartridge (Waters, Etten-Leur, The Netherlands), that were both preconditioned with 10 ml metal-free water. After removing the CM cartridge, ¹⁸F was eluted from the QMA cartridge with 0.9% NaCl. Subsequently, 75 μ L eluate (1.94 - 2.05 GBq) was mixed with AlCl₃ (40 nmol in 30 μ L 2 mM NaAc (pH 4.2)) and dissolved in 1.0 M NaAc (pH 4.2). After 10 min incubation at room temperature, acetonitrile (300 μ L) and NODA-MPAEM ligand (40 nmol), dissolved in 2 mM NaAc (pH 4.2) were added and incubated for 20 min at 106 °C. After incubation, the labeling mixture was evaporated to dryness and 100 μ L PBS was added. Labeling efficiency was determined by RP-HPLC (Agilent 1200 Series, Amstelveen, Netherlands) on a C18 Onyx monolithic column (4.6 x 100 mm, Phenomenex, Torrance, USA) in a gradient from H₂O/0.1 % TFA to acetonitrile/0.1 % TFA.

Conjugation of [¹⁸F]AIF-NODA-MPAEM to anti-CEA antibody fragments

[¹⁸F]AIF-NODA-MPAEM (22-23 nmol, 538-625 MBq) was conjugated to humanized anti-CEA antibody fragments, hMN-14 Fab' (20 nmol), hMN-14-Fab-AD2 (20 nmol), and hMN-14-diabody (20 nmol) in 100 μ L PBS, 2 mM EDTA. After incubating for 20 min at room temperature, labeling efficiency was determined by instant thin-layer chromatography, with 0.1 mol/L citrate buffer (pH 6.0), as the mobile phase. The reaction mixture was purified on a PD-10 column (GE Healthcare, Little Chalfont, United Kingdom) eluted with PBS, 0.5% bovine serum albumin (BSA). In all experiments, the labeling efficiency of the ¹⁸F-labeled antibody preparations was determined by instant thin layer chromatography and exceeded 95%. Radiochemical purity of the [¹⁸F]AIF fluorinated antibody fragments was determined by FPLC analysis using an ÄKTApurifier UPC-10 FPLC system (GE Healthcare Life Sciences, Little Chalfont, UK) with BioSEP SEC s3000 column (300 x 7.8 mm, Phenomenex, Torrance, California, USA) using PBS as eluent at a flow rate of 1 ml/min. For all [¹⁸F]AIF fluorinated antibody fragments, single peaks have been observed on FPLC analysis.

Cell culture

The human colorectal carcinoma cell line LS174T (CEA-positive) and the renal cell carcinoma cell line, SK-RC-52 (CEA-negative), were used. Both cell lines were cultured in RPMI 1640 medium, supplemented with 10% fetal calf serum (Life technologies, Bleiswijk, The Netherlands) and 2mM glutamine.

Immunoreactivity and IC₅₀

The immunoreactive fractions of the ¹⁸F-labeled antibody preparations were determined using freshly trypsinized LS174T cells, as described by Lindmo et al. [4]

with minor modifications: after 1 hour of incubation at 37 °C, the activity in the vials and after washing with 500 µL of binding buffer in the cell pellet, was determined in the γ -counter (Wizard2 Automatic Gamma Counter, PerkinElmer, Waltham, MA). The IC₅₀ of hMN-14 IgG, hMN-14-Fab', hMN-14-Fab-AD2, and hMN-14-diabody was determined in a competitive binding assay on LS174T cells that were grown to confluency in six-well plates. Cells were incubated on ice for 2.5 h in 1 mL of binding buffer with 1 kBq of the ¹¹¹In-labeled hMN-14 IgG. A concentration range from 0.1 – 300 nM of hMN-14 IgG, hMN-14-Fab', hMN-14-Fab-AD2, or hMN-14-diabody was added immediately before addition of ¹¹¹In-labeled hMN-14 IgG. After incubation, cells were washed with binding buffer and cell-associated activity was measured in a γ -counter. IC₅₀ values were calculated using GraphPad Prism software, version 5.03 (GraphPad, La Jolla, USA).

Mouse model

Female BALB/c nude mice (Janvier, Le Genest Saint Isle, France), 8-9 weeks old, were housed in IVC cages (5 mice per cage) under nonsterile standard conditions with free access to standard animal chow and water. After one week of adaption to laboratory conditions, mice were inoculated subcutaneously with 1 x 10⁶ CEA-expressing LS174T cells (right flank) and with 3 x 10⁶ CEA-negative SK-RC-52 cells (left flank), both suspended in 200 µL of complete RPMI 1640 medium. SK-RC-52 cells were inoculated 10 days prior to LS174T cells. Both tumors grew to approximately 0.1 g in 21 and 11 days after tumor cell inoculation, respectively. All experiments were approved by the institutional Animal Welfare Committee of the Radboud University, and were conducted in accordance to the principles set forth by the Revised Dutch Act on Animal Experimentation.

Biodistribution studies

To evaluate the *in vivo* tumor targeting characteristics and perform microPET imaging of the [¹⁸F]AIF-labeled antibody preparations, 1 nmol of [¹⁸F]AIF-hMN-14-Fab' (14 MBq/mouse, n = 5), [¹⁸F]AIF-hMN-14-Fab-AD2 (17 MBq/mouse, n = 5), and [¹⁸F]AIF-hMN-14-diabody (15 MBq/mouse, n = 4) were injected i.v. into mice bearing LS174T tumors and SK-RC-52 xenografts. One additional group of 4 mice received [¹⁸F]FDG (15.0 MBq/mouse) intravenously.

In addition, for all antibody fragment preparations, separate groups of 3-5 mice received an excess of unlabeled hMN-14 IgG (3.2 nmol/mouse) three days before injection of the [¹⁸F]AIF-labeled antibody preparation. Mice were euthanized by CO₂/O₂ asphyxiation and the biodistribution of the antibody preparations was determined 4 h after injection. Blood samples were obtained by cardiac puncture and tissues were dissected, weighed, and the radioactivity measured in a γ -counter. For calculation of the uptake of radioactivity in each tissue as a fraction of the injected dose, an aliquot of the injection dose was counted simultaneously.

MicroPET imaging

The above described groups of female BALB/c nude mice were imaged on an Inveon microPET/CT scanner (Siemens Preclinical Solutions, Knoxville, TN) at 4 h after injection. MicroPET images were acquired under general anesthesia (isoflurane/O₂) for 20 min. After the scanning procedure, mice were euthanized by CO₂/O₂ asphyxiation and the biodistribution of the radiolabel was determined. Activity concentrations in the tissues (percentage of the injected dose per gram; % ID/g) were determined as described above. The microPET scans were reconstructed with Inveon Acquisition Workplace software (version 1.5; Siemens Preclinical Solutions), using a 3-dimensional fast maximum a posteriori algorithm with the following parameters: matrix, 256 x 256 x 161; pixel size, 0.4 x 0.4 x 0.8 mm; and β -value of 1.5 mm resolution with uniform variance.

Statistical analysis

Statistical analyses were performed with Graphpad Prism, version 5.03 (GraphPad, La Jolla, CA). Results are presented as mean \pm standard deviation (SD). Differences in tumor uptake of the antibody preparations were tested for significance using the statistical tests as indicated in the results section. A p-value below 0.05 was considered significant.

RESULTS

Radiolabeling

The NODA-MPAEM ligand could be labeled rapidly (<60 min) and efficiently at a specific activity of 29-39 MBq/nmol with a labeling efficiency of 94 ± 2 %. The efficiencies of the maleimide conjugation were 70% ([¹⁸F]AIF-hMN-14-Fab'), 77% ([¹⁸F]AIF-hMN-14-Fab-AD2), and 77% ([¹⁸F]AIF-hMN-14-diabodies), respectively, resulting in [¹⁸F]AIF-labeled hMN-14 antibody fragment derivatives with a specific activity of 15-17 MBq/nmol (**table 1**). Radiochemical purity exceeded 95%.

Immunoreactivity and IC₅₀

The immunoreactive fractions of [¹⁸F]AIF-hMN-14-Fab', [¹⁸F]AIF-hMN-14-Fab-AD2, and [¹⁸F]AIF-hMN-14-diabodies as determined *in vitro* exceeded 60%. The IC₅₀ of hMN-14 IgG, which was included as a reference, was 8.3 ± 1.5 nM. The IC₅₀ values of hMN-14-Fab' (11.2 ± 1.3 nM), and hMN-14-diabody (7.9 ± 1.2 nM) were comparable to that of hMN-14 IgG, while the IC₅₀ of hMN14-Fab-AD2 (IC₅₀ 26.9 ± 1.3 nM) was slightly higher (**table 1**).

	[¹⁸ F]AIF-hMN14- Fab'	[¹⁸ F]AIF-hMN14- Fab-AD2	[¹⁸ F]AIF-hMN14- diabody
Specific activity (MBq/nmol)	18	23	20
Overall labeling efficiency (%)	66	71	71
Yield after purification (%)	49	59	66
Immunoreactive fraction	> 60	> 60	> 60
IC₅₀ value (nM)	11.2 ± 1.3	26.9 ± 1.3	7.9 ± 1.2

Table 1: Summary of the results of radiolabeling of [¹⁸F]AIF-NODA-MPAEM and hot conjugation with the hMN14 antibody fragments Fab', Fab-AD2, and diabody. The IC₅₀ of hMN14-IgG was 8.3 ± 1.5 nM and serves as a reference for the antibody fragments.

MicroPET imaging

3D-rendered microPET images of all [¹⁸F]AIF-labeled antibody formats in mice with tumors are displayed in **figure 3**. At 4 h after injection specific uptake of the antibody formats was observed in the CEA⁺ LS174T tumors (right flank). Tumors were imaged clearly with all three [¹⁸F]AIF-fluorinated antibody formats. However, based on visual non-quantitative analysis, clearest visualization of the CEA⁺ tumors with specific contrast to background tissue has been obtained with the [¹⁸F]AIF-hMN-14-Fab' and [¹⁸F]AIF-hMN-14-Fab-AD2 formats which is in concordance to the observed higher tumor-to-blood ratios of these formats. In addition, for all three antibody formats, high kidney and liver uptake was observed. The uptake in the CEA⁻ SK-RC-52 xenografts (left flank) remained low for all antibody formats and could not be visualized with microPET imaging.

Biodistribution studies

The results of the biodistribution studies with [¹⁸F]AIF-hMN-14-Fab', [¹⁸F]AIF-hMN-14-Fab-AD2, and [¹⁸F]AIF-hMN-14-diabodies in nude mice with s.c. CEA⁺ LS174T xenografts (right flank) and CEA⁻ SK-RC-52 xenografts (left flank) after dissection are summarized in **figure 4**. The biodistribution of [¹⁸F]FDG was determined in the same model as a reference. At 4 h after injection, all antibody preparations showed preferential accumulation in the CEA⁺ LS174T tumors, reaching 1.85 ± 0.36% ID/g, 2.10 ± 0.46% ID/g, and 4.61 ± 0.67% ID/g for [¹⁸F]AIF-hMN-14-Fab', [¹⁸F]AIF-hMN-14-Fab-AD2, and [¹⁸F]AIF-hMN-14-diabody (**figure 4**). Uptake in the negative control tumors remained significantly lower for all antibody formats, indicating the specific targeting of the antibody formats to CEA-expressing tumor. For all fragments, tumor uptake could be blocked by injection of an excess of unlabeled hMN14 IgG, resulting in non-CEA-mediated uptake of 0.59 ± 0.12% ID/g, 0.68 ± 0.13% ID/g, and 1.37 ± 0.04% ID/g for [¹⁸F]AIF-hMN-14-Fab', [¹⁸F]AIF-hMN-14-Fab-AD2, and [¹⁸F]AIF-hMN-14-diabody, respectively, at 4 h after injection.

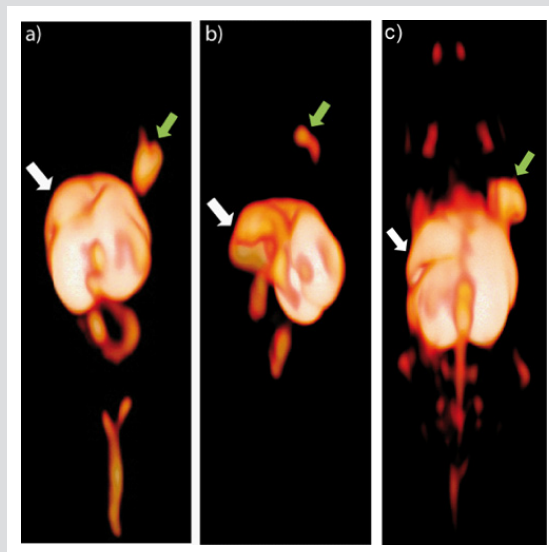
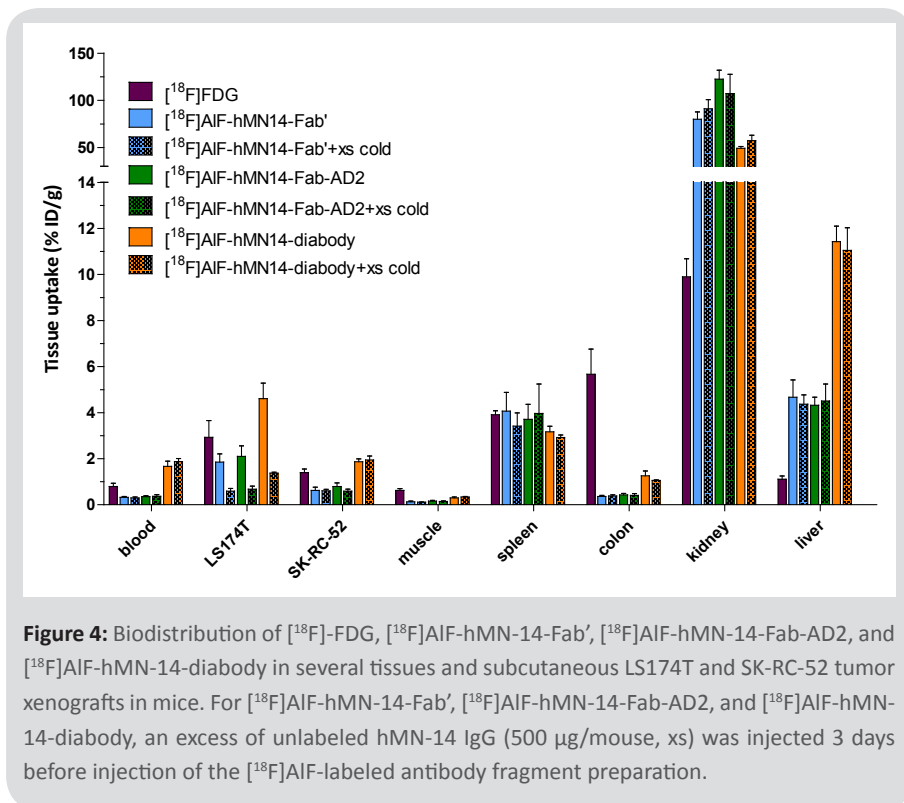


Figure 3: 3D-rendered microPET scans of **a)** [¹⁸F]AIF-NODA-MPAEM-hMN-14-Fab', **b)** [¹⁸F]AIF-NODA-MPAEM-hMN-14-Fab-AD2, and **c)** [¹⁸F]AIF-NODA-MPAEM-hMN-14-diabody in mice with s.c. LS174T (right flank, green arrows) and SK-RC-52 (left flank) xenografts. The white arrows indicate the liver.

Tumor-to-blood ratios at 4 h after injection were significantly higher for [¹⁸F]AIF-hMN-14-Fab' and [¹⁸F]AIF-hMN-14-Fab-AD2 compared to the [¹⁸F]AIF-hMN-14-diabody format, reaching 5.87 ± 0.93 ($p < 0.005$), 6.15 ± 1.58 ($p = 0.01$), and 2.75 ± 0.18 , respectively. Tumor-to-blood ratios of [¹⁸F]FDG were 3.70 ± 0.38 , which is significantly lower compared to those of [¹⁸F]AIF-hMN-14-Fab' ($p < 0.005$) and [¹⁸F]AIF-hMN-14-Fab-AD2 ($p < 0.05$).

CEA⁺-to-CEA⁻ tumor uptake ratios (localization index) for [¹⁸F]AIF-hMN-14-Fab', [¹⁸F]AIF-hMN-14-Fab-AD2, [¹⁸F]AIF-hMN-14-diabody, and [¹⁸F]FDG, were 3.1 ± 0.9 , 2.7 ± 0.7 , 2.5 ± 0.3 , and 2.1 ± 0.4 , respectively (**figure 5**). Tumor-to-muscle ratios obtained with the [¹⁸F]AIF-hMN-14-diabody format, [¹⁸F]AIF-hMN-14-Fab' and [¹⁸F]AIF-hMN-14-Fab-AD2 were comparable with 15.5 ± 2.3 , 14.3 ± 3.9 , and 14.0 ± 5.3 , respectively.

All antibody preparations showed high kidney retention. Renal accumulation was highest for [¹⁸F]AIF-hMN-14-Fab-AD2 ($122.6 \pm 9.4\%$ ID/g), while kidney uptake of [¹⁸F]AIF-hMN-14-Fab' was lower ($90.7 \pm 7.0\%$ ID/g) ($p < 0.005$). Lowest renal accumulation was observed for the [¹⁸F]AIF-hMN-14-diabody format ($57.4 \pm 5.5\%$ ID/g) ($p < 0.01$).



All [^{18}F]-AIF-labeled antibody derivatives showed high hepatic uptake. Liver uptake of [^{18}F]-AIF-hMN-14-Fab' ($4.36 \pm 0.57\%$ ID/g) and [^{18}F]-AIF-hMN-14-Fab-AD2 ($4.32 \pm 0.35\%$ ID/g) was significantly lower compared to the liver uptake of the [^{18}F]-AIF-hMN-14-diabody format ($11.1 \pm 1.0\%$ ID/g) ($p < 0.05$).

DISCUSSION

In this study, we applied a 2-step method to prepare [^{18}F]-AIF-fluorinated NODA-MPAEM-hMN-14-Fab', NODA-MPAEM-hMN-14-Fab-AD2, and NODA-MPAEM-hMN-14-diabody, and evaluated the *in vitro* characteristics and the *in vivo* tumor targeting capacities of these tracers in nude mice with CEA-expressing LS174T human colon carcinoma xenografts in order to show the applicability of [^{18}F]-AIF-fluorination for heat-sensitive biomolecules and to characterize the optimal antibody formats to image CEA-expressing colorectal cancer.

The immunoreactivity of the [^{18}F]-AIF-fluorinated antibody formats was preserved during the labeling procedure. The IC_{50} analyses indicated that the

affinities of hMN-14-Fab' and hMN-14-diabodies for CEA were comparable to that of hMN-14 IgG while the affinity of hMN-14-Fab-AD2 to CEA was slightly lower. Theoretically, the combination of [¹⁸F]AIF and the diabody formats is particularly promising because the diabody fragment might benefit from bivalent binding.

In vivo, preferential localization of all [¹⁸F]AIF-fluorinated antibody formats in the CEA⁺ xenografts was observed, demonstrating feasibility of these [¹⁸F]AIF-fluorinated antibody derivatives for imaging of CEA-expressing tumors. For hMN-14-Fab' and [¹⁸F]AIF-hMN-14-Fab-AD2, tumor-to-blood ratios were significantly higher compared to those of [¹⁸F]AIF-hMN-14-diabody.

Liver uptake of both [¹⁸F]AIF-hMN-14-Fab' and [¹⁸F]AIF-hMN-14-Fab-AD2 fragments was significantly lower compared to that of the diabody. Apparently, the diabody cleared partly via the hepatobiliary route. Consequently, visualization of liver metastases or tumors located in the liver can be obscured. Therefore, future studies will have to focus on decreasing the hepatic uptake of [¹⁸F]AIF-fluorinated antibody formats.

In contrast, renal accumulation of the [¹⁸F]AIF-hMN14-diabody derivative was significantly lower compared to that of the [¹⁸F]AIF-hMN-14-Fab' and [¹⁸F]AIF-hMN-14-Fab-AD2 fragments. The high accumulation in the kidneys most likely is a consequence of tubular reabsorption after glomerular filtration of the [¹⁸F]AIF-fluorinated antibody formats. This renal retention of [¹⁸F]AIF-fluorinated antibody derivatives might hamper the visualization of tumors located in the vicinity of the

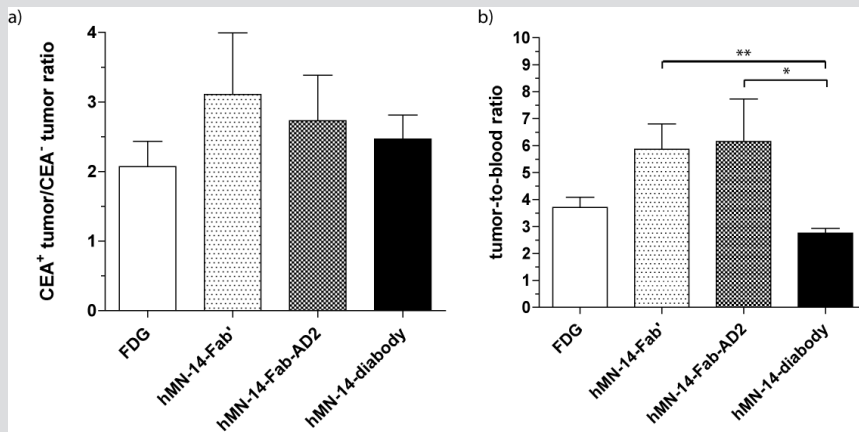


Figure 5: a) CEA⁺-to-CEA⁻ tumor, and b) tumor-to-blood ratios of [¹⁸F]-FDG, [¹⁸F]AIF-hMN-14-Fab', [¹⁸F]AIF-hMN-14-Fab-AD2, and [¹⁸F]AIF-hMN-14-diabody (t-test: * p=0.0032, ** p=0.0132).

kidneys. The lower renal accumulation of the [^{18}F]AIF-hMN14-diabody derivative is most likely due to the bivalency of the derivative leading to slower clearance from the blood which consequences in lower renal accumulation at early time points after injection.

With the development of new molecular imaging agents, the number of applications for diagnostic PET imaging continues to increase. Several positron-emitting radionuclides are used for PET imaging, such as ^{64}Cu , ^{68}Ga , ^{124}I , ^{86}Y , and ^{89}Zr . Labeling of Fab', F(ab')₂, and scFv antibody fragments as well as mini- and diabodies with these radioisotopes has been described by several groups [5-8]. Smith-Jones et al. chelated ^{68}Ga to DOTA-conjugated F(ab')₂ fragments of the anti-HER2 antibody Herceptin (trastuzumab) (^{68}Ga -DCHF) to demonstrate that ^{68}Ga -DCHF can be used to serially image HER2 expression in breast cancer xenografts [9].

Eder et al. [7] evaluated the role of several recombinant anti-EpCAM scFv antibody fragments and diabodies for imaging of EpCAM-expressing tumors with ^{68}Ga . They demonstrated that PET imaging of solid tumors with a ^{68}Ga -labeled anti-EpCAM diabody format is feasible using N,N'-bis[2-hydroxy-5-(carboxyethyl)benzyl] ethylenediamine-N,N'-diacetic acid (HBED-CC) as a chelate.

Wu and colleagues [10] evaluated the tumor targeting capacity of the anti-CEA minibody based on the T84.66 antibody labeled with ^{64}Cu , using DOTA as a chelate, in mice with s.c. LS174T tumors, and showed feasibility of this format to image colorectal cancer with PET, although hepatic uptake was relatively high. However, the half-life of ^{64}Cu (12.7 hours) might be too long for certain *in vivo* imaging studies. Sundaresan et al. [11] compared the tumor targeting capacity of the ^{124}I -labeled anti-CEA T84.66 minibody to that of the ^{124}I -labeled T84.66 diabody in the same model, and demonstrated specific visualization of the CEA⁺ xenografts with PET imaging with both ^{124}I -labeled formats.

The most widely used radionuclide for PET is ^{18}F . ^{18}F has ideal properties for PET due to its low positron energy of 635 keV that reveals optimal spatial resolution of PET images [12]. In addition, the lack of other emissions and wide availability of the cyclotron-produced ^{18}F are advantageous for PET. Moreover, the half-life of 109.8 minutes permits more complex and time-consuming synthetic manipulations and biological studies. However, in general the labeling of biomolecules of ^{18}F is cumbersome. Labeling procedures for ^{68}Ga in contrast are relatively straight-forward, because ^{68}Ga can be chelated with macrocyclic chelates such as DOTA or NOTA. In addition, ^{68}Ga is generated by a $^{68}\text{Ge}/^{68}\text{Ga}$ generator, allowing ^{68}Ga generation on-demand without the need for an on-site cyclotron. However, $^{68}\text{Ge}/^{68}\text{Ga}$ generators are not widely available and the relatively short half-life of 67.6 minutes restricts the use of ^{68}Ga . Additionally, ^{68}Ga has higher positron energy than ^{18}F , which limits the resolution of the PET images.

Despite these limitations, ^{68}Ga has been used in *in vivo* studies with antibodies and antibody fragments more frequently than ^{18}F , because of the more complex ^{18}F -labeling process, requiring labeling of a prosthetic group, deprotection and

subsequent conjugation to a protein [13]. The most widely used approaches for ¹⁸F-labeling of biomolecules are based on the use of N-succinimidyl-4-[¹⁸F]fluorobenzoate (SFB) [14] or [¹⁸F]fluorobenzaldehyde [15].

The [¹⁸F]AIF labeling method developed by McBride et al. [2] provides a promising alternative to previous ¹⁸F radiolabeling methods, as it can be efficiently performed in one step. However, this method requires a heating step to 100 °C to chelate [¹⁸F]AIF. This step limited the procedure to heat-stable peptides and molecules that tolerate high temperatures. Recently, McBride et al. showed that the method can be used to label heat-sensitive biomolecules using a two-step method [3]. In this method, the NODA-MPAEM ligand is labeled with [¹⁸F]AIF first, followed by conjugation to the biomolecule via its thiol group at room temperature. Here, we demonstrated feasibility of this two-step method to label heat-sensitive biomolecules with ¹⁸F *in vitro* and *in vivo*.

Taken together, all three [¹⁸F]AIF-fluorinated antibody derivatives show high tumor-to-background ratios, allowing microPET imaging of CEA-expressing tumors. While CEA⁺/CEA⁻ tumor ratios of all three antibody formats were comparable, significantly higher tumor-to-blood ratios were reached with the [¹⁸F]AIF-hMN-14-Fab' and [¹⁸F]AIF-hMN-14-Fab-AD2 fragments, which resulted in slightly clearer visualization of CEA-expressing tumors with [¹⁸F]AIF-hMN-14-Fab' and [¹⁸F]AIF-hMN-14-Fab-AD2. In addition, the lower hepatic uptake of [¹⁸F]AIF-hMN-14-Fab' and [¹⁸F]AIF-hMN-14-Fab-AD2, compared to the [¹⁸F]AIF-hMN-14-diabody format, might be advantageous for *in vivo* imaging of liver lesions. However, further research is needed to further decrease hepatic uptake of [¹⁸F]AIF-fluorinated antibody fragments.

CONCLUSION

We demonstrated an efficient two-step method to label heat-sensitive biomolecules with ¹⁸F and translated this method to preclinical PET imaging studies. *In vitro* and *in vivo* tumor targeting characteristics of [¹⁸F]AIF-fluorinated hMN-14-Fab', [¹⁸F]AIF-hMN-14-Fab-AD2, and [¹⁸F]AIF-hMN-14-diabody showed that all three antibody formats are promising candidates for PET imaging of CEA-expressing colorectal cancer.

REFERENCES

- (1) Volkow ND, Mullani NA, Bendriem B. Positron emission tomography instrumentation: an overview. *Am J Physiol Imaging*. 1988; 3(3):142-153
- (2) McBride WJ, Sharkey RM, Karacay H, D'Souza CA, Rossi EA, Laverman P, Chang CH, Boerman OC, Goldenberg DM. A novel method of ^{18}F radiolabeling for PET. *J Nucl Med*. 2009; 50(6):991-998
- (3) McBride WJ, D'Souza CA, Sharkey RM, Goldenberg DM. The radiolabeling of proteins by the [^{18}F]AIF method. *Appl Radiat Isot*. 2012; 70(1):200-204
- (4) Lindmo T, Boven E, Cuttitta F, Fedorko J, Bunn PA Jr. Determination of the immunoreactive fraction of radiolabeled monoclonal antibodies by linear extrapolation to binding at infinite antigen excess. *J Immunol Methods*. 1984; 72(1):77-89
- (5) Anderson CJ, Connett JM, Schwarz SW, Rocque PA, Guo LW, Philpott GW, Zinn KR, Meares CF, Welch MJ. Copper-64-labeled antibodies for PET imaging. *J Nucl Med*. 1992; 33(9):1685-1691
- (6) Cai W, Chen K, He L, Cao Q, Koong A, Chen X. Quantitative PET of EGFR expression in xenograft-bearing mice using ^{64}Cu -labeled cetuximab, a chimeric anti-EGFR monoclonal antibody. *Eur J Nucl Med Mol Imaging*. 2007; 34(6):850-858
- (7) Eder M, Knackmuss S, Le Gall F, Reusch U, Rybin V, Little M, Haberkorn U, Mier W, Eisenhut M. ^{68}Ga -labeled recombinant antibody variants for immuno-PET imaging of solid tumours. *Eur J Nucl Med Mol Imaging*. 2010; 37(7):1397-1407
- (8) Robinson MK, Doss M, Shaller C, Narayanan D, Marks JD, Adler LP, González Trotter DE, Adams GP. Quantitative immuno-positron emission tomography imaging of HER2-positive tumor xenografts with an iodine-124 labeled anti-HER2 diabody. *Cancer Res*. 2005; 65(4):1471-1478
- (9) Smith-Jones PM, Solit DB, Akhurst T, Afroze F, Rosen N, Larson SM. Imaging the pharmacodynamics of HER2 degradation in response to Hsp90 inhibitors. *Nat Biotechnol*. 2004; 22(6):701-706
- (10) Wu AM, Yazaki PJ, Tsai Sw, Nguyen K, Anderson AL, McCarthy DW, Welch MJ, Shively JE, Williams LE, Raubitschek AA, Wong JY, Toyokuni T, Phelps ME, Gambhir SS. High-resolution microPET imaging of carcinoembryonic antigen-positive xenografts by using a copper-64-labeled engineered antibody fragment. *Proc Natl Acad Sci U S A*. 2000; 97(15):8495-8500
- (11) Sundaresan G, Yazaki PJ, Shively JE, Finn RD, Larson SM, Raubitschek AA, Williams LE, Chatziioannou AF, Gambhir SS, Wu AM. ^{124}I -labeled engineered anti-CEA minibodies and diabodies allow high-contrast, antigen-specific small-animal PET imaging of xenografts in athymic mice. *J Nucl Med*. 2003; 44(12):1962-1969
- (12) Visser EP, Disselhorst JA, Brom M, Laverman P, Gotthardt M, Oyen WJ, Boerman OC. Spatial resolution and sensitivity of the Inveon small-animal PET scanner. *J Nucl Med*. 2009; 50(1):139-147
- (13) Miller PW, Long NJ, Vilar R, Gee AD. Synthesis of ^{11}C , ^{18}F , ^{15}O , and ^{13}N radiolabels for positron emission tomography. *Angew Chem Int Ed Engl*. 2008; 47(47):8998-9033

- (14) Lang L, Eckelman WC. One-step synthesis of ¹⁸F labeled [¹⁸F]-N-succinimidyl 4-(fluoromethyl)benzoate for protein labeling. *Appl Radiat Isot.* 1994; 45(12):1155-1163
- (15) Poethko T, Schottelius M, Thumshirn G, Hersel U, Herz M, Henriksen G, Kessler H, Schwaiger M, Wester HJ. Two-step methodology for high-yield routine radiohalogenation of peptides: ¹⁸F-labeled RGD and octreotide analogs. *J Nucl Med.* 2004; 45(5):892-902

Chapter 3.1

Targeted dual-modality NIRF and radionuclide imaging of cancer: preclinical status and clinical applications

Chapter 3.2

Dual-modality image-guided surgery of prostate cancer with a radiolabeled fluorescent anti-PSMA monoclonal antibody

Chapter 3.3

Pretargeted dual-modality immuno-SPECT and near-infrared fluorescence imaging for image-guided surgery of prostate cancer

Dual-modality imaging of prostate cancer



3.1

Targeted radionuclide and fluorescence dual-modality imaging of cancer: Preclinical advances and clinical translation

Susanne Lütje¹
Mark Rijpkema¹
Wijnand Helfrich²
Wim J.G. Oyen¹
Otto C. Boerman¹

¹Department of Radiology and Nuclear Medicine,
Radboud University Medical Center, Nijmegen, The Netherlands

²Department of Surgery, University Medical Centre Groningen,
Groningen, The Netherlands

Adapted from: Mol Imaging Biol. 2014 May 22 (in press)

ABSTRACT

In oncology, sensitive and reliable detection tumor tissue is crucial to prevent recurrences and to improve surgical outcome. Currently, extensive research is focused on the use of radionuclides as well as fluorophores to provide real-time guidance during surgery to aid the surgeon in the identification of malignant tissue. Particularly, dual-modality approaches combining radionuclide and near-infrared fluorescence (NIRF) imaging have shown promising results in preclinical studies. Radionuclide imaging allows sensitive intra-operative localization of tumor lesions using a gamma probe, whereas NIRF imaging allows more accurate real-time visualization of tumor delineation. Consequently, both radionuclide and NIRF imaging might complement each other and dual-modality image-guided surgery may overcome limitations of the currently used single-modality imaging techniques.

In this review, a comprehensive overview on recent preclinical advances in tumor-targeted radionuclide and fluorescence dual-modality imaging is provided. Subsequently, the clinical applicability of dual modality image-guided surgery is discussed.

INTRODUCTION

Cancer is the leading cause of death worldwide accounting for 7.6 million cases in 2008 [1]. Despite tremendous improvements in molecular imaging strategies, the detection of small tumor lesions remains challenging. Small cancer foci, micro-metastases, and tumor cell-containing resection margins, in particular, often remain undetected, leading to understaging and undertreatment, which may result in disease progression and/or recurrence.

Currently, the most commonly used imaging modalities to detect tumor lesions are computed tomography (CT), magnetic resonance imaging (MRI), positron emission tomography (PET), and single photon emission computed tomography (SPECT). While CT and MRI imaging provide high anatomical resolution of bony and soft tissue, respectively, PET and SPECT allow highly sensitive and specific visualization of tumor tissue. Since each technique has its specific advantages and limitations, the combination of imaging modalities could have additional value.

In addition to the need for sensitive and specific imaging methods for diagnostic purposes, accurate localization of tumor tissue during surgery may aid to optimize tumor resection. For surgery, radical tumor resection is of utmost importance for treatment outcome and patient survival [2, 3]. Therefore, the visualization of micro-metastases and tumor cell-containing resection margins is pivotal to prevent recurrence of the disease. Nuclear imaging performed prior to surgery can provide information on the spread of the malignant manifestations and may aid the surgeon in localizing (and complete resection of) small tumor lesions. The intra-operative discrimination between malignant and healthy tissue is currently still largely based on visual inspection and palpation by the surgeon. With the development of gamma probes, intra-operative nuclear imaging and radio-guided surgery have become available and provide the possibility to map tumor lesions within the surgical field. Since its introduction, radio-guided surgery has tremendously expanded and has evolved into what is now considered an established discipline in the operating theater, revolutionizing the surgical management of several types of malignancies [4]. Radio-guided surgery has significant impact on the surgical management of cancer as it provides real-time information on the location and extent of disease to the surgeon. Additionally, it allows minimization of the invasiveness of the surgical procedures, while maintaining maximum benefit to the cancer patient. Radio-guided surgery using gamma probe technology has been used for the detection of primary tumors and the location of sentinel lymph nodes [5]. However, gamma probes are not suited for accurate tumor delineation during surgery. For this purpose, intra-operative fluorescence-based imaging appears to be a better option as it allows exact delineation of tumor lesions during and following resection and can provide real-time visualization that is directly correlated to the surgical field.

Recently, extensive research has been focused on the development of probes

for dual-modality imaging. Dual-modality imaging can be performed either with agents that are dual-labeled with a fluorescent dye and a radionuclide or by co-injection of the radiotracer and the fluorescent probe, each conjugated to the same targeting molecule [6]. One limitation of the co-injection approach for dual-modality imaging is the fact that the biodistribution pattern of the probe might be altered when fluorescent dyes are conjugated to that molecule [7]. Thus, the radio signal and the fluorescent signal might not necessarily originate from the exact same location. Dual-labeled imaging agents, however, provide coherent imaging signals that originate from one and the same targeting molecule.

Two categories of dual-modality approaches can be distinguished: non-targeted and targeted approaches. While non-targeted approaches using dual-labeled probes have proven valuable for sentinel lymph node mapping, these agents are not tumor specific and therefore not suited for detection of tumor lesions and resection margins [8]. Targeted approaches, for instance using antibodies directed against tumor-associated cell surface antigens, can overcome these limitations. Here, we provide a comprehensive review on the preclinical advances and analyze the applicability for clinical translation of image-guided surgery in the rapidly evolving field of targeted dual-modality near-infrared fluorescence (NIRF) and radionuclide imaging of cancer.

INTRA-OPERATIVE RADIONUCLIDE IMAGING

PET and SPECT radionuclide imaging is based on detection of highly penetrating γ -photons (25 – 511 keV) produced during radioactive decay. Consequently, imaging with radionuclides is usually not hindered by limited penetration depth and is generally considered to be highly sensitive. However, application of radionuclide imaging is restricted by the inherited dangers of ionizing radiation, the relatively low spatial resolution, and the lack of anatomical references. In addition, a given radioisotope needs to match the intended clinical procedure as the half-life of commonly used radioisotopes for imaging ranges from minutes to months.

While pre-operative radionuclide imaging is highly useful for diagnostic purposes, the intra-operative use of radionuclide imaging is limited to specific applications. The hand-held gamma probe is one of the most frequently used devices for intra-operative radionuclide detection and radio-guided surgery. Since its introduction, radio-guided surgery has improved the surgical management of various malignancies and evolved into an established discipline in the operating theater. Radio-guided surgery provides real-time information on the location and the extent of disease. While this technique was originally used for the evaluation of primary tumors, radio-guided surgery using gamma probes is currently mainly applied for sentinel lymph node detection in various cancer, including breast cancer [9], cervical cancer [10], head and neck cancer [11], melanoma [12], and prostate cancer [13].

Major limitation of the hand-held gamma probe is the fact that this technique solely provides an acoustic signal which could guide the surgeon to the malignant lesion without providing an image of its exact localization. Therefore, its capacity for accurate tumor delineation is relatively low.

INTRA-OPERATIVE NIRF IMAGING

In contrast to radionuclide imaging, fluorescence imaging provides the possibility for more precise delineation of tumor lesions during surgery. Fluorescent tracers can be excited by absorption of light of a specific wavelength. When falling to its ground state, the fluorophore emits light of higher wavelength. In principle, fluorophores have extended half-lives and can be repeatedly activated. Furthermore, fluorescence imaging is a relatively low-cost imaging modality with high sensitivity and resolution [14]. However, due to limited tissue penetration depth caused by tissue absorption and scattering of photons, fluorescence imaging is limited to specific applications. The penetration depth of fluorescent light is improved when fluorophores are applied that emit light in the near-infrared (NIR) region (650 – 900 nm). Photons in the NIR region show higher tissue penetration than photons in the visible light range (400 – 600 nm) [15], resulting in a tissue penetration depth limited to the centimeter range [16].

So far, only a few fluorescent agents such as methylene blue (MB) and indocyanine green (ICG), which are both non-target specific, are approved for clinical use by the Food and Drug Administration (FDA). Whereas the far-red emitter MB has mainly been used to stain sentinel lymph nodes for dissection [17] and to identify colon polyps [18], the fluorophore ICG (emission peak at 830 nm) [19] has been used for intra-operative purposes such as mapping of blood vessel patency or tumor-draining lymph nodes [20].

A new approach to deal with one of the major challenges of NIRF imaging, the limited tissue penetration of light, is the combination of this technique with radionuclide imaging. Dual-modality approaches using both a radiolabel and a fluorescent dye can be applied for different approaches. First, the radionuclide aids the surgeon to intra-operatively localize the tumor using a gamma probe. Second, the fluorescent label may be used to detect micro-metastases and precisely evaluate resection margins during surgery.

NON-TARGETED DUAL-MODALITY RADIONUCLIDE AND NIRF IMAGING

The first clinical proof-of-concept studies of dual-modality imaging were provided

using dual-modality nanocolloids to identify the tumor draining lymph nodes in several malignancies, such as prostate cancer [21, 22], breast cancer [23], melanoma [24], and head and neck cancer [25]. For these purposes, ICG is combined with radiotracers into so-called nanocolloids that are injected in or near the primary tumors to assess lymph vasculature. However, several limitations of ICG restrict its use as a fluorescent agent, such as insufficient photostability in buffer and physiological conditions, small Stokes shift, the formation of aggregates in aqueous media, and the lack of a functional group to conjugate targeting moieties [26]. Obviously, the use of non-targeted imaging to assess resection margins for residual tumor tissue is far from ideal. For this purpose, targeted dual-modality imaging approaches have shown promising preclinical results.

TARGETED DUAL-MODALITY RADIONUCLIDE AND NIRF IMAGING

The development of NIRF dyes containing functional groups that are suitable for established chemical conjugation to biomolecules represent a promising opportunity for the design of target-specific fluorescent probes for molecular imaging. Many targeted optical probes have been developed which target cell surface and hormone receptors, metabolic pathways, or apoptotic markers [27]. When developing a dual-modality targeting agent, the following issues should be addressed: 1. which targeting agent, 2. which fluorophore, and 3. which type of coupling chemistry can be used.

1. Targeting molecules

Effective targeting molecules need to fulfill several criteria: First, the targeting agent has to reach its target in an efficient way, which is determined by the specific properties of the probe and the affinity of the targeting agent for its target. Second, the target needs to be present in sufficient amounts and non-specific binding of the targeting molecule should be low. In addition, the pharmacokinetics of the imaging agent and its excretion route should be taken into account.

At present, various targeting molecules are available for preclinical and clinical imaging purposes, such as antibodies or peptides [19]. Intact monoclonal antibodies such as bevacizumab, cetuximab, or trastuzumab as well as antibody fragments represent excellent candidates for targeted dual-modality imaging due to their high target-specificity, the abundance of suitable reactive amino acid residues for conjugation purposes, and the availability of clinical-approved antibodies [26]. Other promising candidates for dual-modality imaging are peptide ligands that bind with high affinity to the corresponding receptors on tumor cells, such as somatostatin analogues (SSTR), gastrin-releasing peptide receptor (GRPR) ligands, folate analogues, PSMA ligands, or matrix metalloproteinases (MMP). Peptide ligands usually are

chemically more robust than proteins and are easier to produce as clinical agents [26].

2. NIRF dyes

The ideal NIRF dye should have specific characteristics [28]. First, the Stokes shift should be large to gain a minimum of interference between excitation and emission wavelengths. In addition, the molar absorption coefficient and the quantum yield should be high enough to acquire a fluorescent signal. Moreover, the agent should be water soluble to avoid dye aggregation in aqueous solutions and it should be chemically and photo-stable in biological solutions [28]. In addition, as mentioned above, suitable functional groups need to be present to allow conjugation to targeting molecules. At present, two main categories of NIR fluorophores can be distinguished, inorganic and organic NIR dyes [28]. While inorganic NIRF dyes are mainly associated with quantum dots and other nanoparticles, organic NIRF dyes can be covalently or noncovalently conjugated with various molecules such as oligonucleotides, peptides, or antibodies [28].

3. Conjugation reactions

The fluorescent dye and the targeting molecule are usually coupled via a linker, which can be an alkyl chain with a functional group on each side. One of the most commonly used strategies to develop imaging probes is amide bond formation between a primary amino group (NH₂) and a carboxylic acid (COOH), as these groups are found in various fluorophores and in various targeting molecules [14]. To allow amide formation, N-acetylation between N-hydroxysuccinimide (NHS) activated carboxylic acid and a primary amino group is a commonly used approach [14]. Many of the NIRF dyes that are commercially available can be purchased as NHS esters, such as Cy5.5-NHS, Cy7-NHS, or IRDye800CW-NHS. Another conjugation reaction is the maleimide reaction with thiol groups. In this reaction, maleimides react with cysteine residues at neutral pH to generate a stable thioether bond.

One essential challenge in coupling fluorophores to targeting molecules is the lipophilicity of the fluorophores. It has been observed that the *in vivo* behavior of targeting agents can be affected by the conjugation of a fluorescent dye. In a study performed by Cohen et al., a substitution ratio of more than one molecule of IRDye800CW to one molecule of the antibody caused alterations in the pharmacokinetics of the targeting molecule, especially enhancing the liver uptake of the conjugate [7]. One explanation for this effect might be the lipophilicity of IRDye800CW. High accumulation of tracer in the liver can obscure small tumor nodules and metastases located in or in the vicinity of the liver. In addition, rapid and high tracer accumulation in the liver can reduce tumor uptake. Reduced hepatic uptake may be achieved by limiting the substitution ratio to one fluorescent dye per targeting molecule [7].

Preclinical studies using co-injection strategies

As described earlier, targeted dual-modality radionuclide and NIRF imaging can be performed either by co-injection strategies or by dual-label strategies. In co-injection strategies, the same targeting molecule, e.g. an anti-tumor antibody, is labeled with either a fluorescent dye or a radionuclide and these tagged antibodies are co-administered as a mixture. At first glance, co-injection of two single-labeled compounds seems to be simpler compared to dual-labeling strategies, where one targeting molecule is labeled with both a fluorescent dye and a radionuclide. Most NIR fluorophores are organic molecules with molecular weight of approximately 1,000 Da, while chelated radionuclides usually are polar molecules of a size of around 300-400 Da [26]. As a consequence, conjugation of a targeting molecule to different tracer dyes or chelators can cause alterations in pharmacokinetics, binding affinities, and biodistributions [7]. As a result, radio-signal and fluorescent signal may not necessarily originate from the same location.

Terwisscha van Scheltinga et al. compared optical imaging with PET in mice that received a co-injection of the anti-VEGF antibody bevacizumab labeled with ^{89}Zr and bevacizumab conjugated with IRDye800CW and reported specific VEGF-tumor targeting and tumor visualization with both the radiolabeled and fluorescent-labeled antibody [6]. Moreover, IRDye800CW-trastuzumab was used for intra-operative guidance during surgical removal of subcutaneous SK-Br-3 tumor lesions from tumor bearing mice [6]. For both IRDye800CW-trastuzumab and IRDye800CW-bevacizumab, even submillimeter intraperitoneal tumor lesions could be distinguished intra-operatively by the emission of fluorescent signal and could be removed from the peritoneum based on the fluorescent signal [6].

In another study, optical and radionuclide imaging was performed in mice that received either trastuzumab dual-labeled with both ^{111}In and ICG or co-injection of a mixture of ^{111}In -trastuzumab and ICG-trastuzumab [34]. Both approaches, revealed specific tumor visualization with fluorescence imaging.

Preclinical studies using dual-label targeting molecules

In contrast to co-injection strategies, dual-labeled imaging conjugates allow for coherent visualization of both imaging signals which originate from the same targeting molecule. For this purpose, the targeting molecule needs to be labeled with both the NIRF dye and a radionuclide. Several dual-labeled targeting molecules have been studied so far, with encouraging results.

1. Dual-labeled bevacizumab for imaging of VEGF-A expressing cancers

A promising target that has been studied for imaging of cancer is the vascular endothelial growth factor (VEGF) as it plays a pivotal role in the formation of blood vessels (neoangiogenesis). Bevacizumab (Avastin®) is a humanized anti-VEGF monoclonal antibody approved for treatment of colorectal cancer,

renal cell cancer, and glioblastoma [29].

Cohen et al. described the coupling of IRDye800CW to ^{89}Zr -labeled bevacizumab and cetuximab (anti-EGFR) to evaluate its behavior *in vivo* in mice bearing A431 or FaDu xenografts [7]. In this study, antibody-desferal conjugates were first labeled with ^{89}Zr , followed by conjugation to IRDye800CW. Excellent tumor targeting was achieved with dual-labeled antibodies at low substitution ratios of antibody molecule and IRDye800CW. The relatively long half-life of ^{89}Zr (78.4 hours) offers the opportunity to perform serial PET imaging with ^{89}Zr -labeled antibodies during a period of several days.

The use of radionuclides with a shorter half-life, such as ^{64}Cu (12.7 hours), allows imaging studies in which repeated injections of the labeled conjugate are required. Recently, bevacizumab was labeled with both ^{64}Cu and IRDye800CW for serial PET and NIRF imaging of mice with subcutaneous U87MG glioblastoma xenografts [30]. In this study, 0.8 IRDye800CW molecules were substituted to each bevacizumab molecule. Persistent and VEGF-specific uptake of ^{64}Cu -NOTA-bevacizumab-800CW in the U87MG xenografts was demonstrated, reaching a tumor uptake of $20.7 \pm 3.7\%$ ID/g at 72 h post injection.

2. Dual-labeled trastuzumab for imaging of HER-expressing cancers

The intracellular signaling pathways regulating cellular growth and differentiation of many cancer types are regulated by members of the human epidermal growth factor receptor (HER) family, which consists of several transmembrane receptor tyrosine kinases. One of these kinases, HER2, is of particular interest for cancer research as it is associated with aggressive tumor progression of breast and ovarian cancer [31]. Trastuzumab (Herceptin[®]) is a humanized anti-HER2 antibody approved for HER-2-overexpressing breast and metastatic gastric or gastroesophageal junction adenocarcinoma.

During the last decade, trastuzumab has been labeled with several radionuclides and fluorophores to develop dual-labeling strategies for dual-modality imaging of cancer. The FDA-approved fluorophore ICG was considered a promising fluorophore for this purpose. Ogawa et al. co-injected a cocktail of ICG-trastuzumab and ^{111}In -trastuzumab into mice with subcutaneous A431 and 3T3/HER2 tumors and compared the nuclear and optical imaging characteristics with dual-labeled trastuzumab with ^{111}In and ICG [32]. With both methods, they observed tumor uptake in the 3T3/HER2 tumors on nuclear and NIRF images. In addition, high uptake in the liver was observed, even though the average number of ICG molecules per antibody was kept below 1. This might be due to dissociation of ICG from the antibody after administration which might consequence in binding of the water-soluble ICG to albumin in plasma. Subsequently, the ICG-albumin complex is taken up by hepatocytes and cleared from the body through the hepatic route [32, 33].

With the development of the next generation NIR fluorophore IRDye800CW,

which can be functionalized with either NHS or maleimide, a broad variety of targeting molecules could be conjugated with IRDye800CW. In 2007, Sampath et al. labeled trastuzumab with ^{111}In and IRDye800CW for sequential NIRF and SPECT/CT imaging. They validated this dual-label agent in a subcutaneous HER2-positive human breast cancer mouse model showing specific tumor targeting of the agent *in vivo* [34].

In a subsequent study, Sampath et al. demonstrated the ability to detect HER2-expressing metastases with (^{64}Cu -DOTA)-trastuzumab-(IRDye800) using PET and NIRF imaging in mice with orthotopic 4T1.2neu/R tumors in the mammary fat pad [35]. In addition, comparison with ^{18}F FDG-PET imaging was performed. It was shown that PET with (^{64}Cu -DOTA)-trastuzumab-(IRDye800) as a tracer has greater sensitivity in detecting HER2 expressing metastases than FDG. In addition, non-specific liver uptake was observed which was attributed to the interaction of the Fc portion of the antibody with hepatocytes [35]. In this study, the average substitution ratio was 2.2.

3. Dual-labeled TRC105 for imaging of CD105-expressing cancers

CD105 is almost exclusively expressed on proliferating endothelial tumor cells [36] and overexpression of CD105 is strongly related to poor prognosis in more than 10 cancer types [37]. Therefore, CD105 represents a promising marker for tumor-related angiogenesis.

TRC105 is a chimeric human/murine IgG1 mAb with high affinity for human and murine CD105 [38]. Recently, this antibody was dual-labeled with ^{89}Zr using desferal as a chelator and IRDye800CW as a fluorophore for dual-modality PET/NIRF imaging of CD105 expression in a subcutaneous 4T1 breast cancer xenografts [39]. In this study, Df-TRC105 was substituted with 0.7 800CW-NHS moieties per antibody molecule. Such a mild substitution ratio might not only be favorable for low hepatic uptake, but might also avoid self-quenching due to close proximity of IRDye800CW molecules to each other, as fluorescence resonance energy transfer only occurs when two IRDye800CW fluorophores are located within 10 nm, which is about the size of an antibody molecule [39]. In this study, tumor uptake of ^{89}Zr -Df-TRC105-800CW reached approximately 12% ID/g. In a similar study from the same group, the same dual-label tracer ^{89}Zr -Df-TRC105-800CW was tested in a lung metastasis mouse model of breast cancer [40]. While significant uptake of ^{89}Zr -Df-TRC105-800CW in the lung metastases was observed with PET imaging as early as 24 h after injection, it was not possible to delineate the tumors with NIRF imaging *in vivo* due to the limited penetration depth of NIRF imaging due to the deep location of the lung metastases in the thoracic cavity. However, *ex vivo* imaging was used to validate the PET images. In addition, Hong et al. performed image-guided resection of subcutaneous 4T1 breast tumors in mice subjected to NIRF imaging at 4 h and 24 h after intravenous injection of ^{89}Zr -Df-TRC105-800CW. It was demonstrated that image-guided tumor removal was possible [40].

Very recently, Zhang et al. [41] conjugated TRC105 to NOTA and subsequently coupled IRDye800CW to NOTA-TRC105 and labeled it with ^{64}Cu to synthesize ^{64}Cu -NOTA-TRC105-800CW. In this study, on average 0.9 IRDye800CW moieties were conjugated per molecule of TRC105. Biodistribution studies and *ex vivo* PET/NIRF imaging with this ^{64}Cu -NOTA-TRC105-800CW dual-labeled conjugate showed rapid and persistent CD105-specific uptake of ^{64}Cu -NOTA-TRC105-800CW in fLuc-4T1 BC metastatic lung tumor nodules, reaching $13.9 \pm 3.9\%$ ID/g at 24 h after injection. In addition, proof-of-principle for image-guided surgery with optical imaging using NOTA-TRC105-800CW was provided in this study in a subcutaneous 4T1 tumor model in nude mice [41].

4. Dual-labeling strategies for imaging of EpCAM-expressing cancers

The epithelial cell adhesion molecule (EpCAM) also known as CD326, EGP-2, ESA, and TROP-1, is a type I transmembrane glycoprotein that is overexpressed in many cancers and therefore represents a promising target for imaging. EpCAM is overexpressed in 87% of the prostate cancers [42]. Recently, the anti-EpCAM antibody MAB9601 was conjugated with DOTA and was dual-labeled with ^{64}Cu and IRDye800CW in order to develop a multimodality-imaging agent for the detection of lymph node metastases in a preclinical animal model of human metastatic prostate cancer [43]. In this study, the substitution ratio of MAB9601 with IRDye800CW was 2.3 dye molecules per antibody molecule. Hall et al. performed NIRF and PET/CT as well as DsRed imaging on mice with orthotopically implanted PC3 cells expressing the fluorescent gene reporter DsRed. In this study, PC3-DsRed lymph node metastases developed at 10–12 weeks after implantation. The detection rates by NIRF and PET/CT imaging were similar, indicating the multimodality imaging capability of the dual-labeled agent for the detection of lymph node metastases in prostate cancer.

To evaluate the effect of binding affinity and the pharmacodynamics of antibody-based probes and to increase the accuracy for the detection of cancerous foci, a subsequent study was performed. In this study, the potential of several newly synthesized dual-labeled antibodies was evaluated [44]. The ^{64}Cu and IRDye800CW dual-labeled antibody MAB9601 was compared to a few other anti-EpCAM antibodies regarding their accuracy for the detection of cancer cell containing lymph nodes with NIRF and PET/CT imaging in an orthotopic mouse model of prostate cancer [44]. Hall et al. demonstrated that the in-house produced murine IgG1 monoclonal antibodies 7 (KD 2.3 nM) and 153 (KD 0.54 nM) had superior affinity for EpCAM compared to MAB9601 (KD 15.4 nM) and the accuracy in the detection of cancer cell containing lymph nodes for mAb 7 was higher compared to that of MAB9601 on NIRF as well as on PET/CT imaging. The authors concluded that antibodies with affinities in the low nanomolar range represent promising candidates for dual-modality PET/NIRF imaging.

5. Dual-labeling strategies for imaging of PSMA-expressing cancers

Prostate-specific membrane antigen (PSMA) is selectively overexpressed in prostate cancer in all stages of the disease and as such represents an excellent target for prostate cancer imaging [45]. The type II integral membrane glycoprotein PSMA is an enzyme of which the natural ligand is still unknown. For imaging purposes, various high affinity ligands for PSMA have been developed [46]. Recently, Banerjee et al. synthesized the first dual-modality SPECT/NIRF imaging agent with affinity for PSMA, based on glutamate urea compound conjugated with both DOTA and IRDye800CW for targeting PSMA-expressing prostate cancer in mice with s.c. PC3-PIP tumors [47]. They observed radiotracer uptake *ex vivo* and clear visualization of the tracer in the PSMA-expressing subcutaneous PC3-PIP prostate cancer xenografts ($16.4 \pm 3.7\%$ ID/g, 5 h p.i.), while uptake in the PSMA-negative PC3-flu control tumors was low ($1.9 \pm 0.2\%$ ID/g, 5 h p.i.). In addition, intense radiotracer uptake was observed the kidneys, which the authors contribute to the tracer's route of excretion and to its specific uptake due to expression of PSMA in kidneys [48].

6. Dual-labeling strategies for targeting CD20

CD20 is a phosphoglycoprotein expressed on the surface of B cells. At present, anti-CD20 mAbs are clinically used for treatment of non-Hodgkin's lymphomas and rheumatoid arthritis. Paudyal et al. [49] used the murine anti-CD20 mAb NuB2 for targeting CD20-positive tumors and labeled it via DOTA with ^{64}Cu along with the fluorophore Alexa Fluor 750. They performed *ex vivo* biodistribution and *in vivo* PET/NIRF imaging and demonstrated that ^{64}Cu -DOTA-NuB2-Alexa Fluor 750 specifically binds to CD20-expressing tumor xenografts ($16.34 \pm 2.75\%$ ID/g, 48 h p.i.).

Clinical translation

Image-guided surgery using tumor-targeting dual-label agents could potentially facilitate surgical resection of tumors. Complete resection of tumors and metastases may be improved in particular when tumor tissue cannot be easily discriminated from normal tissue, when scar tissue obscures the discrimination between normal and tumor tissue, or when multiple small metastases need to be removed.

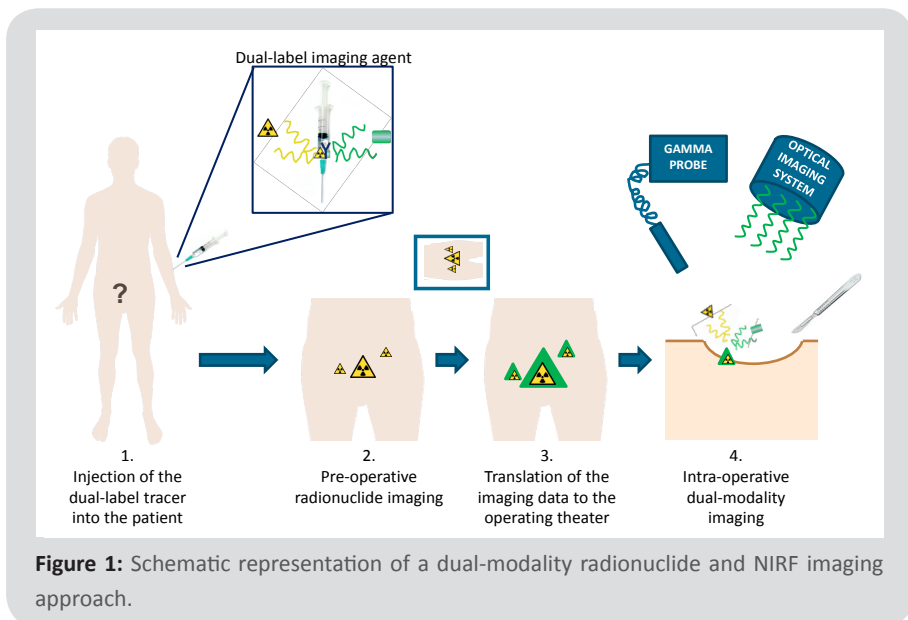
So far, a considerable number of preclinical studies has focused on the development of dual-labeled radionuclide and fluorescent targeting agents for dual-modality imaging. However, until now, no targeted dual-modality imaging approaches have been introduced into the clinic. To the best of our knowledge, so far, only one targeted fluorescence imaging approach has been translated to a clinical study. Van Dam et al. conjugated folate with fluorescein isothiocyanate (folate-FITC) for targeting the folate receptor- α with a real-time multispectral intra-operative fluorescence imaging system [50]. In this study, the first clinical results of intra-operative tumor-specific fluorescence imaging for real-time surgical visualization

of tumor tissue in ovarian cancer patients during laparotomy were described in a series of 10 patients intra-operative tumor-specific fluorescence imaging of folate-FITC, that was administered systemically, provided specific and sensitive detection of tumor tissue in real-time settings during surgery in patients with folate receptor- α -expressing ovarian cancer.

Recently, the first clinical trial using a fluorescently tagged anti-VEGF antibody (clinicaltrials.gov, NCT01508572) was started, aiming to show the feasibility of intra-operative NIRF imaging in breast tumor patients.

While the first targeted fluorescence imaging studies show promising results, the next step would be to introduce targeted dual-label approaches into the clinic. Using this approach, three major applications could be combined within one single approach and improve oncological surgery: The targeted radionuclide activity could be used to pre-operatively visualize tumor tissue (first) and intra-operatively localize tumor nodules with a gamma probe (second). Third, after surgical resection of tissue layers that may cover the tumor tissue, the fluorescent component of the dual-modality probe could aid the surgeon in the precise delineation and resection of tumor lesions. A schematic representation of how this dual-modality approach could be performed is provided in **figure 1**.

Clinical applications of these dual-modality approaches are looming, but a few hurdles have to be overcome. Particularly, the preparation of fluorescently labeled targeting molecules needs to be further standardized and validated [7]. Once these fluorescent agents are found to be safe, they can be conjugated to the radiolabeled dual-label targeting agent and should then be synthesized according



to GMP standards. In addition, it has to be determined, if open laparotomy or laparoscopic surgical procedures in which a laparoscope is equipped with an optical imaging system, is more sensitive for dual-modality radionuclide and NIRF imaging. In particular, the role of dual-label constructs for image-guidance during surgery needs further evaluation regarding sensitivity and specificity in the detection of small lesions or positive resection margins.

An important challenge in oncological surgery is to completely resect invasive tumor strands to obtain tumor cell negative resection margins [8]. To detect invasive tumor strands, NIRF imaging systems are required that have a high sensitivity and enable detection of tumor strands in resection margins. While, as mentioned earlier, it has been shown that both IRDye800CW-trastuzumab and IRDye800CW-bevacizumab are feasible for detection of tumor lesions in the millimeter range in intra-operative settings and that these intraperitoneal lesions could be resected completely based on the fluorescent signal preclinically [6], the value of such dual-modality approaches for the evaluation of resection margins still needs to be assessed. Subsequently, this finding needs to be confirmed in a clinical setting to evaluate the sensitivity and specificity of dual-label targeting agents for small amounts of tumor tissue. Another challenge that needs to be addressed in future studies is tumor heterogeneity. Tumors consist of various cell types that may display variable phenotypes [8]. To establish the dual-modality imaging approach, preferably a target antigen should be chosen that is homogeneously expressed throughout the whole tumor. In addition, dual-modality image-guided surgery needs to be correlated to the gold standard histology for margin assessment and the additional value of dual-modality NIRF and radionuclide imaging needs to be evaluated.

CONCLUSION

With the emergence of dual-labeling strategies and hybrid NIRF and radionuclide tracers, the first steps have been made for the combination of these powerful imaging techniques which might complement each other and improve the intra-operative detection and surgical removal of cancer tissue. So far, several preclinical studies demonstrated the potential value of combining these imaging modalities for image-guidance during surgery. However, further studies are needed to correlate dual-modality image-guided surgery to histology and to further evaluate the additional value of this dual-modality approach for overall survival. First clinical studies that aim to determine the value of NIR fluorescently labeled targeting molecules for diagnostic imaging are looming.

REFERENCES

- (1) Jemal A, Bray F, Center MM, Ferlay J, Ward E, Forman D. Global cancer statistics. *CA Cancer J Clin.* 2011; 61(2):69-90
- (2) Bristow RE, Puri I, Chi DS. Cytoreductive surgery for recurrent ovarian cancer: a meta-analysis. *Gynecol Oncol.* 2009; 112(1):265-274
- (3) Cao C, Yan TD, Black D, Morris DL. A systematic review and meta-analysis of cytoreductive surgery with perioperative intraperitoneal chemotherapy for peritoneal carcinomatosis of colorectal origin. *Ann Surg Oncol.* 2009; 16(8):2152-2165
- (4) Povoski SP, Neff RL, Mojzisek CM, O'Malley DM, Hinkle GH, Hall NC, Murrey DA Jr, Knopp MV, Martin EW Jr (2009). A comprehensive overview of radioguided surgery using gamma detection probe technology. *World J Surg Oncol* 7:11
- (5) Vermeeren L, Klop WM, van den Brekel MW, Balm AJ, Nieweg OE, Valdés Olmos RA. Sentinel node detection in head and neck malignancies: innovations in radioguided surgery. *J Oncol.* 2009; 681746
- (6) Terwisscha van Scheltinga AG, van Dam GM, Nagengast WB, Ntziachristos V, Hollema H, Herek JL, Schröder CP, Kosterink JG, Lub-de Hoog MN, de Vries EG. Intraoperative near-infrared fluorescence tumor imaging with vascular endothelial growth factor and human epidermal growth factor receptor 2 targeting antibodies. *J Nucl Med.* 2011; 52(11):1778-1785
- (7) Cohen R, Stammes MA, de Roos HC, Stigter-van Walsum M, Visser GWM, van Dongen GAMS. Inert Coupling of IRDye800CW to monoclonal antibodies for Clinical Imaging of Tumor Targets. *EJNMMI Research* 2011, 1:31
- (8) Keereweer S, Van Driel PB, Snoeks TJ, Kerrebijn JD, Baatenburg de Jong RJ, Vahrmeijer AL, Sterenborg HJ, Löwik CW. Optical image-guided cancer surgery: challenges and limitations. *Clin Cancer Res.* 2013; 19(14):3745-3754
- (9) Somasundaram SK, Chicken DW, Keshtgar MR. Detection of the sentinel lymph node in breast cancer. *Br Med Bull.* 2007; 84:117-131
- (10) van de Lande J, Torrenga B, Raijmakers PG, Hoekstra OS, van Baal MW, Brölmann HA, Verheijen RH. Sentinel lymph node detection in early stage uterine cervix carcinoma: a systematic review. *Gynecol Oncol.* 2007; 106(3):604-613
- (11) Côté V, Kost K, Payne RJ, Hier MP. Sentinel lymph node biopsy in squamous cell carcinoma of the head and neck: where we stand now, and where we are going. *J Otolaryngol.* 2007; 36(6):344-349
- (12) Harlow SP, Krag DN, Ashikaga T, Weaver DL, Meijer SJ, Loggie BW, Tanabe KK, Whitworth P Jr, Kuhn J, Kusminsky R, Carp NZ, Gadd M, Rawlings M Jr, Slingluff CL Jr. Gamma probe guided biopsy of the sentinel node in malignant melanoma: a multicentre study. *Melanoma Res.* 2001; 11(1):45-55
- (13) Fortuin A, Rooij Md, Zamecnik P, Haberkorn U, Barentsz J. Molecular and functional imaging for detection of lymph node metastases in prostate cancer. *Int J Mol Sci.* 2013; 14(7):13842-13875
- (14) Bai M, Bornhop DJ. Recent advances in receptor-targeted fluorescent probes for in vivo cancer imaging. *Curr Med Chem.* 2012; 19(28):4742-4758

- (15) Patterson MS, Chance B, Wilson BC. Time resolved reflectance and transmittance for the non-invasive measurement of tissue optical properties. *Appl Opt.* 1989; 28(12):2331-2336
- (16) Fomina N, McFearin CL, Sermsakdi M, Morachis JM, Almutairi A. Low power, biologically benign NIR light triggers polymer disassembly. *Macromolecules.* 2011; 44(21):8590-8597
- (17) East JM, Valentine CS, Kanchev E, Blake GO. Sentinel lymph node biopsy for breast cancer using methylene blue dye manifests a short learning curve among experienced surgeons: a prospective tabular cumulative sum (CUSUM) analysis. *BMC Surg.* 2009; 9:2
- (18) Kiesslich R, Fritsch J, Holtmann M, Koehler HH, Stolte M, Kanzler S, Nafe B, Jung M, Galle PR, Neurath MF. Methylene blue-aided chromoendoscopy for the detection of intraepithelial neoplasia and colon cancer in ulcerative colitis. *Gastroenterology.* 2003 Apr;124(4):880-888
- (19) Keereweer S, Kerrebijn JD, van Driel PB, Xie B, Kaijzel EL, Snoeks TJ, Que I, Hutteman M, van der Vorst JR, Mieog JS, Vahrmeijer AL, van de Velde CJ, Baatenburg de Jong RJ, Löwik CW. Optical image-guided surgery--where do we stand? *Mol Imaging Biol.* 2011; 13(2):199-207
- (20) Polom K, Murawa D, Rho YS, Nowaczyk P, Hünerbein M, Murawa P. Current trends and emerging future of indocyanine green usage in surgery and oncology: a literature review. *Cancer.* 2011; 117(21):4812-4822
- (21) van der Poel HG, Buckle T, Brouwer OR, Valdés Olmos RA, van Leeuwen FW. Intraoperative laparoscopic fluorescence guidance to the sentinel lymph node in prostate cancer patients: clinical proof of concept of an integrated functional imaging approach using a multimodal tracer. *Eur Urol.* 2011; 60(4):826-833
- (22) van den Berg NS, Valdés-Olmos RA, van der Poel HG, van Leeuwen FW. Sentinel lymph node biopsy for prostate cancer: a hybrid approach. *J Nucl Med.* 2013; 54(4):493-496
- (23) Schaafsma BE, Verbeek FP, Rietbergen DD, van der Hiel B, van der Vorst JR, Liefers GJ, Frangioni JV, van de Velde CJ, van Leeuwen FW, Vahrmeijer AL. Clinical trial of combined radio- and fluorescence-guided sentinel lymph node biopsy in breast cancer. *Br J Surg.* 2013; 100(8):1037-1044
- (24) Brouwer OR, Klop WM, Buckle T, Vermeeren L, van den Brekel MW, Balm AJ, Nieweg OE, Valdés Olmos RA, van Leeuwen FW. Feasibility of sentinel node biopsy in head and neck melanoma using a hybrid radioactive and fluorescent tracer. *Ann Surg Oncol.* 2012; 19(6):1988-1994
- (25) van den Berg NS, Brouwer OR, Klop WM, Karakullukcu B, Zuur CL, Tan IB, Balm AJ, van den Brekel MW, Valdés Olmos RA, van Leeuwen FW. Concomitant radio- and fluorescence-guided sentinel lymph node biopsy in squamous cell carcinoma of the oral cavity using ICG-(99m)Tc-nanocolloid. *Eur J Nucl Med Mol Imaging.* 2012; 39(7):1128-1136
- (26) Azhdarinia A, Ghosh P, Ghosh S, Wilganowski N, Sevic-Muraca EM. Dual-labeling strategies for nuclear and fluorescence molecular imaging: a review and analysis. *Mol Imaging Biol.* 2012; 14(3):261-276
- (27) Kelloff GJ, Krohn KA, Larson SM, Weissleder R, Mankoff DA, Hoffman JM, Link JM, Guyton KZ, Eckelman WC, Scher HI, O'Shaughnessy J, Cheson BD, Sigman CC, Tatum

- JL, Mills GQ, Sullivan DC, Woodcock J. The progress and promise of molecular imaging probes in oncologic drug development. *Clin Cancer Res.* 2005; 11(22):7967-7985
- (28) Luo S, Zhang E, Su Y, Cheng T, Shi C. A review of NIR dyes in cancer targeting and imaging. *Biomaterials.* 2011; 32(29):7127-7138
- (29) Meadows KL, Hurwitz HI. Anti-VEGF therapies in the clinic. *Cold Spring Harb Perspect Med.* 2012; 2(10)
- (30) Zhang Y, Hong H, Engle JW, Yang Y, Barnhart TE, Cai W. Positron Emission Tomography and Near-Infrared Fluorescence Imaging of Vascular Endothelial Growth Factor with Dual-Labeled Bevacizumab. *Am J Nucl Med Mol Imaging.* 2012; 2(1):1-13
- (31) Yarden Y. Biology of HER2 and its importance in breast cancer. *Oncology.* 2001;61 Suppl 2:1-13
- (32) Ogawa M, Regino CA, Seidel J, Green MV, Xi W, Williams M, Kosaka N, Choyke PL, Kobayashi H. Dual-modality molecular imaging using antibodies labeled with activatable fluorescence and a radionuclide for specific and quantitative targeted cancer detection. *Bioconjug Chem.* 2009; 20(11):2177-2184
- (33) Faybik P, Hetz H. Plasma disappearance rate of indocyanine green in liver dysfunction. *Transplant Proc.* 2006; 38(3):801-802
- (34) Sampath L, Kwon S, Ke S, Wang W, Schiff R, Mawad ME, Sevick-Muraca EM. Dual-labeled trastuzumab-based imaging agent for the detection of human epidermal growth factor receptor 2 overexpression in breast cancer. *J Nucl Med.* 2007; 48(9):1501-1510
- (35) Sampath L, Kwon S, Hall MA, Price RE, Sevick-Muraca EM. Detection of Cancer Metastases with a Dual-labeled Near-Infrared/Positron Emission Tomography Imaging Agent. *Transl Oncol.* 2010; 3(5):307-217
- (36) Fonsatti E, Nicolay HJ, Altomonte M, Covre A, Maio M. Targeting cancer vasculature via endoglin/CD105: a novel antibody-based diagnostic and therapeutic strategy in solid tumours. *Cardiovasc Res.* 2010; 86(1):12-19
- (37) Dallas NA, Samuel S, Xia L, Fan F, Gray MJ, Lim SJ, Ellis LM. Endoglin (CD105): a marker of tumor vasculature and potential target for therapy. *Clin Cancer Res.* 2008; 14(7):1931-1937
- (38) Seon BK, Haba A, Matsuno F, Takahashi N, Tsujie M, She X, Harada N, Uneda S, Tsujie T, Toi H, Tsai H, Haruta Y. Endoglin-targeted cancer therapy. *Curr Drug Deliv.* 2011; 8(1):135-143
- (39) Zhang Y, Hong H, Severin GW, Engle JW, Yang Y, Goel S, Nathanson AJ, Liu G, Nickles RJ, Leigh BR, Barnhart TE, Cai W. ImmunoPET and near-infrared fluorescence imaging of CD105 expression using a monoclonal antibody dual-labeled with (⁸⁹Zr and IRDye 800CW. *Am J Transl Res.* 2012; 4(3):333-346
- (40) Hong H, Zhang Y, Severin GW, Yang Y, Engle JW, Niu G, Nickles RJ, Chen X, Leigh BR, Barnhart TE, Cai W. Multimodality Imaging of Breast Cancer Experimental Lung Metastasis with Bioluminescence and a Monoclonal Antibody Dual-Labeled with (⁸⁹Zr and IRDye 800CW. *Mol Pharm.* 2012; 9(8):2339-2349
- (41) Zhang Y, Hong H, Nayak TR, Valdovinos HF, Myklejord DV, Theuer CP, Barnhart TE, Cai W. Imaging tumor angiogenesis in breast cancer experimental lung metastasis with positron emission tomography, near-infrared fluorescence, and bioluminescence. *Angiogenesis.* 2013; 16(3):663-674

- (42) Went P, Vasei M, Bubendorf L, Terracciano L, Tornillo L, Riede U, Kononen J, Simon R, Sauter G, Baeuerle PA. Frequent high-level expression of the immunotherapeutic target Ep-CAM in colon, stomach, prostate and lung cancers. *Br J Cancer*. 2006; 94(1):128-135
- (43) Hall MA, Kwon S, Robinson H, Lachance PA, Azhdarinia A, Ranganathan R, Price RE, Chan W, Sevick-Muraca EM. Imaging prostate cancer lymph node metastases with a multimodality contrast agent. *Prostate*. 2012; 72(2):129-146
- (44) Hall MA, Pinkston KL, Wilganowski N, Robinson H, Ghosh P, Azhdarinia A, Vazquez-Arreguin K, Kolonin AM, Harvey BR, Sevick-Muraca EM. Comparison of mAbs targeting epithelial cell adhesion molecule for the detection of prostate cancer lymph node metastases with multimodal contrast agents: quantitative small-animal PET/CT and NIRF. *J Nucl Med*. 2012; 53(9):1427-1437
- (45) Schülke N, Varlamova OA, Donovan GP, Ma D, Gardner JP, Morrissey DM, Arrigale RR, Zhan C, Chodera AJ, Surowitz KG, Maddon PJ, Heston WD, Olson WC. The homodimer of prostate-specific membrane antigen is a functional target for cancer therapy. *Proc Natl Acad Sci U S A*. 2003; 100(22):12590-12595
- (46) Malik N, Machulla HJ, Solbach C, Winter G, Reske SN, Zlatopolskiy B. Radiosynthesis of a new PSMA targeting ligand ([¹⁸F]FPy-DUPA-Pep). *Appl Radiat Isot*. 2011; 69(7):1014-1018
- (47) Banerjee SR, Pullambhatla M, Byun Y, et al. Sequential SPECT and optical imaging of experimental models of prostate cancer with a dual modality inhibitor of the prostate-specific membrane antigen. *Angew Chem Int Ed Engl*. 2011; 50:9167-9170
- (48) Silver DA, Pellicer I, Fair WR, Heston WD, Cordon-Cardo C. Prostate-specific membrane antigen expression in normal and malignant human tissues. *Clin Cancer Res*. 1997; 3(1):81-85
- (49) Paudyal P, Paudyal B, Iida Y, Oriuchi N, Hanaoka H, Tominaga H, Ishikita T, Yoshioka H, Higuchi T, Endo K. Dual functional molecular imaging probe targeting CD20 with PET and optical imaging. *Oncol Rep*. 2009; 22(1):115-119
- (50) van Dam GM, Themelis G, Crane LM, Harlaar NJ, Pleijhuis RG, Kelder W, Sarantopoulos A, de Jong JS, Arts HJ, van der Zee AG, Bart J, Low PS, Ntziachristos V. Intraoperative tumor-specific fluorescence imaging in ovarian cancer by folate receptor- α targeting: first in-human results. *Nat Med*. 2011; 17(10):1315-1319

3.2

Dual-modality image-guided surgery of prostate cancer with a radio- labeled fluorescent anti-PSMA monoclonal antibody

Susanne Lütje¹

Mark Rijpkema¹

Gerben M. Franssen¹

Giulio Fracasso²

Wijnand Helfrich³

Annemarie Eek¹

Wim J.G. Oyen¹

Marco Colombatti²

Otto C. Boerman¹

¹ Department of Radiology and Nuclear Medicine,
Radboud University Medical Center, Nijmegen, The Netherlands

² Department of Pathology and Diagnostics, University of Verona, Italy

³ Department of Surgery, University Medical Centre Groningen,
Groningen, The Netherlands

ABSTRACT

Background

Both radionuclide imaging and near-infrared fluorescence (NIRF) imaging have a high sensitivity to detect tumor lesions *in vivo*. The combination of these modalities using dual-labeled antibodies may allow both pre- and intra-operative tumor localization and could be used in image-guided surgery to ensure complete resection of tumor tissue. Here, we evaluated the potential of dual-modality imaging of prostate cancer with the monoclonal antibody D2B, directed against an extracellular domain of prostate-specific membrane antigen (PSMA). For these studies, D2B was labeled both with ^{111}In and the near-infrared fluorescent dye IRDye800CW.

Methods

D2B was conjugated with NHS-IRDye800CW and ITC-DTPA and subsequently radiolabeled with ^{111}In . For biodistribution and NIRF imaging, ^{111}In -DTPA-D2B-IRDye800CW (2 μg , 0.55 MBq/mouse) was injected intravenously into BALB/c nude mice with subcutaneous (s.c.) PSMA-expressing LNCaP tumors (right flank) and PSMA-negative PC3 tumors (left flank). The biodistribution was determined at 1, 2, 3, and 7 days after injection. In addition, microSPECT/CT and NIRF imaging with ^{111}In -DTPA-D2B-IRDye800CW (3 μg , 8.5 MBq/mouse) was performed in mice with intraperitoneally growing LS174T-PSMA tumor nodules.

Results

^{111}In -DTPA-D2B-IRDye800CW specifically accumulated in s.c. xenografted PSMA-positive LNCaP tumors ($45.8 \pm 8.0\%$ ID/g at 168 h p.i.), whereas uptake in s.c. PSMA-negative PC3 tumors was significantly lower ($6.6 \pm 1.3\%$ ID/g at 168 h p.i.). Intraperitoneal (i.p.) LS174T-PSMA tumors could be visualized specifically with both microSPECT/CT and NIRF imaging at 2 days p.i., and the feasibility of image-guided resection of i.p. tumors was demonstrated in this model.

Conclusion

Dual-label ^{111}In -DTPA-D2B-IRDye800CW enables specific and sensitive detection of prostate cancer lesions *in vivo* with microSPECT/CT and NIRF imaging. In addition to pre-operative microSPECT/CT imaging to detect tumor lesions, NIRF imaging enables image-guided surgical resection. These preclinical findings warrant clinical studies with ^{111}In -DTPA-D2B-IRDye800CW to improve tumor detection and resection in prostate cancer patients.

INTRODUCTION

Despite improvements in diagnostic and therapeutic approaches, prostate cancer remains one of the leading causes of cancer-related death in men in the Western world. For patients with low- and intermediate-risk localized prostate cancer and selected patients with high-risk localized disease, surgical removal of the cancerous foci is currently regarded as the treatment option of choice [1]. In radical prostatectomy tissue specimens obtained after surgical removal of localized prostate cancer, positive surgical margins are reported in 11 – 48% of the cases [2-4]. While the role of positive surgical margins on cancer-specific mortality remains controversial, positive surgical margins are recognized as a risk factor for prostate-specific antigen (PSA)-defined biochemical recurrence [5], which is associated with need for secondary therapy and may have considerable impact on patient's quality of life.

At present, several methods are clinically used to identify malignant tissues during surgery: First, cancerous tissue can be distinguished from benign structures visually based on color, texture and morphology. In addition, tactile palpation can aid the surgeon in the detection of tumor tissue due to differences in elasticity or plasticity [6]. However, the detection of tumor cells in resection margins and micro-metastases remains extremely challenging. Therefore, imaging techniques that can aid the identification of small cancer foci are needed.

Recently, progress has been made in the field of intra-operative detection of malignant tissue with fluorescence imaging, a sensitive technique that could improve visualization of positive surgical margins during surgery using fluorescent dyes which accumulate in tumor tissues. Van Dam et al [7]. reported the first-in-human use of intra-operative tumor-specific fluorescence imaging for real-time visualization of tumor tissue in patients with ovarian cancer. In this study, ovarian cancer overexpressing the folate receptor is targeted and visualized with folate conjugated to the fluorescent dye fluorescein isothiocyanate (FITC).

However, a shortcoming of fluorescence imaging is the limited penetration depth of emitted light in tissue. When tumor nodules are covered by other tissue, the fluorescent signal might not be visible and tumors may be missed. The use of near-infrared fluorescent (NIRF) dyes, which emit light in the near-infrared region (650 – 900 nm), can improve the tissue penetration depth to several millimeters [8]. Recently, the first clinical trial using the antibody bevacizumab tagged to the NIRF dye IRDye800CW (clinicaltrials.gov, NCT01508572) has started, aiming to show the feasibility of intra-operative fluorescence imaging in breast cancer patients.

A new approach to deal with the limited tissue penetration of NIRF imaging is the combination of this technique with radionuclide detection. Both radionuclide and NIRF imaging are highly sensitive in the detection of cancer lesions. A dual-label targeting agent with both a radionuclide and a fluorescent moiety could be used for three purposes: First, the radionuclide allows pre-operative assessment of the tumor

burden by SPECT or PET imaging. Secondly, the radionuclide could aid the surgeon to intra-operatively localize the tumor using a gamma probe. Finally, the optical label could be used to precisely evaluate resection margins during surgery and detect micro-metastases once the surgical field is exposed to the surface.

As the prostate-specific membrane antigen (PSMA) is selectively overexpressed on the surface of prostate cancer cells, it represents an attractive target for antibody-guided targeting of cancer cells with radionuclides and fluorophores [9]. In the present study, we applied this new imaging strategy and evaluated the tumor imaging characteristics of the newly developed anti-PSMA monoclonal antibody (mAb) D2B labeled with both ^{111}In and IRDye800CW to provide proof-of-principle for the use of the described dual-label imaging approach in mice with subcutaneous prostate cancer xenografts. In addition, we evaluated whether this dual-labeled D2B antibody preparation can be used to improve intra-operative visualization and to perform image-guided resection of tumor lesions in mice with intraperitoneally growing, PSMA-expressing tumor nodules.

MATERIALS AND METHODS

The anti-PSMA monoclonal antibody D2B (IgG1) [10] was purified from hybridoma culture supernatant by Protein A affinity chromatography. The antibody secreting cells were obtained according to the hybridoma technology from mice that were immunized with a cell lysate of membranes of LNCaP cells. Mice were injected three times (day 0, day 14 and day 28) i.p. with 800 μg of lysate and Freund's adjuvant (Sigma-Aldrich, St. Louis, MO, USA). The last three days before the spleen of the mice was harvested, mice were boosted with 10 μg of recombinant PSMA protein (Novagen, Milan, Italy) intravenously.

Mouse tumor models

Male BALB/c nude mice (Janvier, Le Genest Saint Isle, France), 7-8 weeks old, were housed in filter-topped cages (5 mice per cage) under nonsterile standard conditions with free access to standard animal chow and water. After one week of adaptation to laboratory conditions, 3×10^6 PSMA-expressing LNCaP cells were suspended in 200 μL of 33% complete RPMI 1640 medium with 67% Matrigel (BD Biosciences, Franklin Lakes, NJ) and injected subcutaneously (right flank). PSMA-negative PC3 cells were suspended in 200 μL of 67% complete RPMI 1640 medium with 33% Matrigel. LNCaP cells were inoculated 7 days prior to PC3 cells and tumors grew to approximately 0.1 g in 14 and 7 days, respectively. Both cell lines were grown in RPMI 1640 medium, supplemented with 10% fetal calf serum (Life technologies, Carlsbad, CA) and 2 mM glutamine.

For the intraperitoneal tumor model, LS174T colon carcinoma cells were transfected with human PSMA, using the plasmid pcDNA3.1-hPSMA [11]. Cells were transfected using X-tremeGENE 9 DNA transfection reagent (Roche Applied Science, Mannheim, Germany). After transfection, single clones stably expressing PSMA were selected and grown in the presence of 0.3 mg/ml G418. PSMA expression of LS174T-PSMA cells was confirmed by FACS analysis. LS174T-PSMA cells were grown in RPMI 1640 medium, supplemented with 10% fetal calf serum and glutamine in the presence of 0.3 mg/ml G418. 1×10^6 LS174T-PSMA cells were injected intraperitoneally in 200 μ L of complete RPMI 1640 medium and grew for 21 days after tumor cell inoculation.

For FACS analysis, stably transfected LS174T-PSMA cells (150,000 cells per well in a V-bottom 96 well plate) were washed twice and incubated on ice for 30 minutes with 25 μ L of either PBS, 0.5 %, an isotype control (mouse IgG (H+L) (5 μ g/ml) purified (Jackson ImmunoResearch Europe Ltd., Suffolk, UK), or the D2B antibody at 5 μ g/ml in PBS, 0.5 % BSA. Untransfected LS174T cells were included as a negative control and the PSMA expressing prostate cancer cell line LNCaP was included as a positive control for PSMA expression. After incubation, cells were washed three times and incubated on ice for 30 minutes under light-protected conditions with 25 μ L of secondary fluorescently labeled antibody (goat-anti-mouse-IgG(H+L)-Alexa488, 2.5 μ g/ml (Life Technologies)), in PBS, 0.5 % BSA. Cells were washed again three times and measured on a FACS-Calibur system with CELLQuest software (both from Beckton Dickinson Immunocytometry Systems, San Diego, CA).

All experiments were approved by the institutional Animal Welfare Committee of the Radboud University Medical Center and were conducted in accordance to the principles set forth by the Revised Dutch Act on Animal Experimentation.

Synthesis of DTPA-D2B-IRDye800CW

The murine mAb D2B IgG (5 mg) was conjugated with N-hydroxysuccinimide (NHS)-IRDye800CW (Li-Cor, Biosciences, Lincoln, NB) in 2 ml 0.1 M NaHCO_3 , pH 8.5, with a 16-fold molar excess of NHS-IRDye800CW (620 μ g). After 2 h of incubation at room temperature on an orbital shaker in the dark, IRDye800CW-D2B was purified by gel filtration on a PD10 column eluted with 0.1 M NaHCO_3 , pH 8.5. The conjugation ratio of the purified conjugate was determined on a Ultrospec 2000 spectrophotometer (Pharmacia Biotech) at wavelengths 280 nm and 774 nm and the substitution ratio was calculated using the formula: substitution ratio = $0.875 \cdot E_{774} / (E_{280} - (0.03 \cdot E_{774}))$. The substitution ratio of the conjugate used in these studies was 1.2. Subsequently, p-isothiocyanatobenzyl-diethylene-triamine-penta-acetic acid (ITC-DTPA) (Macrocylics, Dallas, USA) was added to the conjugate in 0.1 M NaHCO_3 , pH 9.5 (2.5 ml), in a 27-fold molar excess (4.1 mg IRDye800CW-D2B with 481 μ g ITC-DTPA). After 1 h of incubation at room temperature on an orbital shaker in the dark, the reaction mixture was dialyzed for 3 days in a Slide-A-Lyzer (10-kDa cutoff, Pierce) against 0.25 M NH_4Ac , pH 5.4.

Radiolabeling of DTPA-D2B-IRDye800CW

For biodistribution studies, IRDye800CW-D2B-DTPA (100 μg) was radiolabeled with 32 MBq ^{111}In (Covidien, Petten, the Netherlands) in 0.1 M MES buffer pH 5.4 (three times the volume of ^{111}In -chloride) and incubated during 30 min at room temperature under metal-free conditions. For SPECT/CT studies, IRDye800CW-D2B-DTPA (35 μg) was incubated with 280 MBq of ^{111}In in 0.1 M MES buffer pH 5.4. Following incubation, 50 mM EDTA was added to the final concentration of 5 mM to chelate unincorporated ^{111}In .

The labeling efficiency was determined by instant thin layer chromatography (ITLC) using 0.15 M citrate buffer, pH 6.0, as the mobile phase. The labeling efficiency was 85% for the biodistribution studies and 36% for the microSPECT/CT study. ^{111}In -DTPA-D2B-IRDye800CW was purified by gel filtration on a PD-10 column, and the radiochemical purity of the final dual label tracer was $\geq 97\%$, which was determined by ITLC.

Immunoreactivity

The immunoreactive fraction of the dual-labeled ^{111}In -DTPA-D2B-IRDye800CW was compared to that of ^{111}In -DTPA-D2B using freshly trypsinized LNCaP cells, essentially as described by Lindmo et al. [12, 13]. Briefly, a serial dilution of LNCaP cells (6.3×10^5 to 1.0×10^6 cells/ml) in 0.5 ml RPMI medium containing 0.5% BSA was incubated at 37 °C for 1 h with 0.002 pmol ^{111}In -DTPA-D2B-IRDye800CW (350 Bq). To determine nonspecific binding, an excess of unlabeled DTPA-D2B-IRDye800CW (160 pmol) was added to a duplicate of the lowest cell concentration. After incubation, cells were centrifuged and washed with 500 μL RPMI medium containing 0.5% BSA. The activity in the vials and in the cell pellet was determined in the gamma counter (Wizard 3rd 1480, LKB-Wallac, Oy, Finland). The inverse of the specific cell bound activity was plotted against the inverse of the cell concentration, and the immunoreactive fraction was calculated from the y-axis intercept using GraphPad Prism software (version 5.03 for Windows; GraphPad Software, La Jolla, USA).

Competitive binding assay

The IC_{50} of D2B IgG was determined in a competitive binding assay on LNCaP cells using ^{111}In -labeled D2B as a tracer. LNCaP cells were grown to confluency in six-well plates, and incubated on ice for 2 h in 1 mL of binding buffer with 1.85 kBq of ^{111}In -labeled D2B IgG and increasing concentrations (0.005-300 nM) of unlabeled D2B IgG. Cells were washed with binding buffer after incubation and the cell-associated activity was measured in a gamma counter. IC_{50} values were calculated using GraphPad Prism software, version 5.03.

Biodistribution and NIRF imaging in mice with subcutaneous tumors

For biodistribution studies, four groups of male BALB/c nude mice bearing LNCaP

(right flank) and PC3 (left flank) xenografts were intravenously injected into the tail vein with the dual-label conjugate ^{111}In -DTPA-D2B-IRDye800CW (0.55 MBq, 2.0 μg /mouse). Three additional mice (control group) were co-injected intravenously with an excess of unlabeled D2B IgG (300 μg /mouse) to determine nonspecific uptake of ^{111}In -DTPA-D2B-IRDye800CW.

At 24, 48, 72 and 168 h after injection, four mice per time point (5 mice at 168 h p.i.) were euthanized with CO_2/O_2 asphyxiation and tissues of interest (LNCaP and PC3 tumors, muscle, lung, spleen, kidney, liver, pancreas, stomach, duodenum, and prostate) were dissected, weighed and the radioactivity was measured in a gamma counter. Blood samples were obtained by heart puncture. For calculation of the uptake of radioactivity in each tissue as a fraction of the injected dose, an aliquot of the injection dose was counted simultaneously.

The mice that were scheduled for biodistribution at 48 h after injection were imaged with an IVIS imaging system (Xenogen VivoVision IVIS Lumina II, Caliper Life Sciences, Lincolnshire, United Kingdom; acquisition time 5 min) prior to dissection. The control group of mice that received an excess of unlabeled D2B IgG in addition to intravenously injected ^{111}In -DTPA-D2B-IRDye800CW was euthanized and dissected as described above at 72 h after injection.

Dual-modality microSPECT/CT and NIRF imaging and image-guided surgery

Four male BALB/c nude mice with intraperitoneally growing LS174T-PSMA tumor nodules were intravenously injected with the dual-labeled ^{111}In -DTPA-D2B-IRDye800CW (8.5 MBq and 3.0 μg /mouse) and imaged at 48 h after injection on both the IVIS imaging system (acquisition time 5 min) and a small-animal microSPECT/CT scanner (U-SPECT II, MILabs, Utrecht, Netherlands) with a 1.0 mm diameter pinhole collimator tube (acquisition time 30 min). MicroSPECT/CT scans were performed pre-operatively, followed by NIRF imaging of the mice in supine position after surgical relocation of skin, abdominal muscle layers, and peritoneum. After IVIS image acquisition, the visualized tumor lesions were resected, followed by NIRF imaging to control whether residual tumor tissue and positive surgical margins are in situ. In addition, microSPECT/CT scans were performed after resection of the tumor lesions using the same scanning parameters that were used for pre-operative evaluation. Scans were reconstructed with MILabs reconstruction software, which uses an ordered-subset expectation maximalization algorithm.

Statistical analysis

Statistical analyses were performed with Graphpad Prism, version 5.03 (GraphPad, La Jolla, CA). Results are presented as mean \pm standard deviation (SD).

RESULTS

In vitro characterization

The immunoreactive fractions of ^{111}In -DTPA-D2B-IRDye800CW and ^{111}In -DTPA-D2B were 75% and 84%, respectively, indicating that the immunoreactivity of the D2B antibody was largely preserved during the two conjugation procedures.

The IC_{50} value of D2B IgG was 3.7 nM (95% confidence interval (CI): 2.8 – 4.8 nM).

Biodistribution studies and imaging of subcutaneous tumors

^{111}In -DTPA-D2B-IRDye800CW specifically accumulated in the s.c. PSMA-positive LNCaP tumors reaching $12.5 \pm 4.9\%$ ID/g (n=4) at 24 h p.i., $26.1 \pm 7.4\%$ ID/g (n=4) at 48 h p.i., $40.2 \pm 4.0\%$ ID/g (n=4) at 72 h p.i., and $45.8 \pm 8.0\%$ ID/g (n=5) at 168 h after injection (**figure 1a**). Tumor uptake in PSMA-negative PC3 xenografts was significantly lower at 48, 72, and 168 h after injection, reaching $9.8 \pm 2.8\%$ ID/g (n=4) at 24 h p.i. ($p = 0.3768$), $10.6 \pm 2.3\%$ ID/g (n=4) at 48 h p.i. ($p = 0.0071$), $10.4 \pm 1.2\%$ ID/g (n=4) at 72 h p.i. ($p < 0.0001$), and $6.6 \pm 1.3\%$ ID/g (n=5) at 168 h p.i. ($p < 0.0001$).

The uptake of ^{111}In -DTPA-D2B-IRDye800CW remained low in most normal tissues, uptake in the liver ranged from $25.6 \pm 7.2\%$ ID/g at 24 h p.i. to $6.8 \pm 1.3\%$ ID/g at 168 h after injection (**figure 1a**).

Tumor-to-blood ratios of PSMA⁺ LNCaP xenografts were 1.3 ± 0.3 (24 h p.i.), 2.9 ± 0.9 (48 h p.i.), 5.3 ± 0.8 (72 h p.i.), and 9.4 ± 1.5 (168 h p.i.). Tumor-to-blood ratios of the PSMA⁻ PC3 xenografts were significantly lower at 48, 72, and 168 h after injection ($p < 0.0001$), reaching 1.0 ± 0.1 (24 h p.i.), 1.1 ± 0.1 (48 h p.i.), 1.4 ± 0.2 (72 h p.i.), and 1.4 ± 0.3 (168 h p.i.) (**figure 1b**). PSMA⁺-to-PSMA⁻ tumor ratios were 1.2 ± 0.2 (24 h p.i.), 2.5 ± 0.7 (48 h p.i.), 3.9 ± 0.7 (72 h p.i.), and 7.2 ± 2.0 (168 h p.i.). At 48 h after injection, accumulation of ^{111}In -DTPA-D2B-IRDye800CW could be visualized in subcutaneous PSMA-positive LNCaP tumors using the IVIS fluorescence imager, while PSMA-negative tumors showed no fluorescent signal (**figure 1c**).

Tumor uptake of ^{111}In -DTPA-D2B-IRDye800CW could be blocked by coinjection of an excess of 300 μg of unlabeled D2B IgG, resulting in nonspecific (non-PSMA-mediated) uptake of $11.0 \pm 1.41\%$ ID/g (n=3) and $9.5 \pm 2.9\%$ ID/g (n=3) at 72 h p.i. in LNCaP and PC3 xenografts, respectively. This further confirms the specific uptake of ^{111}In -DTPA-D2B-IRDye800CW in the PSMA-expressing tumor.

Dual-modality microSPECT/CT and NIRF imaging in mice with i.p. tumors

Five BALB/c nude mice with intraperitoneal LS174T-PSMA tumors were imaged with both the IVIS fluorescence scanner and the microSPECT/CT small animal scanner at 48 h after injection of dual-label ^{111}In -DTPA-D2B-IRDye800CW. A typical microSPECT/CT acquisition with corresponding fluorescence image in supine

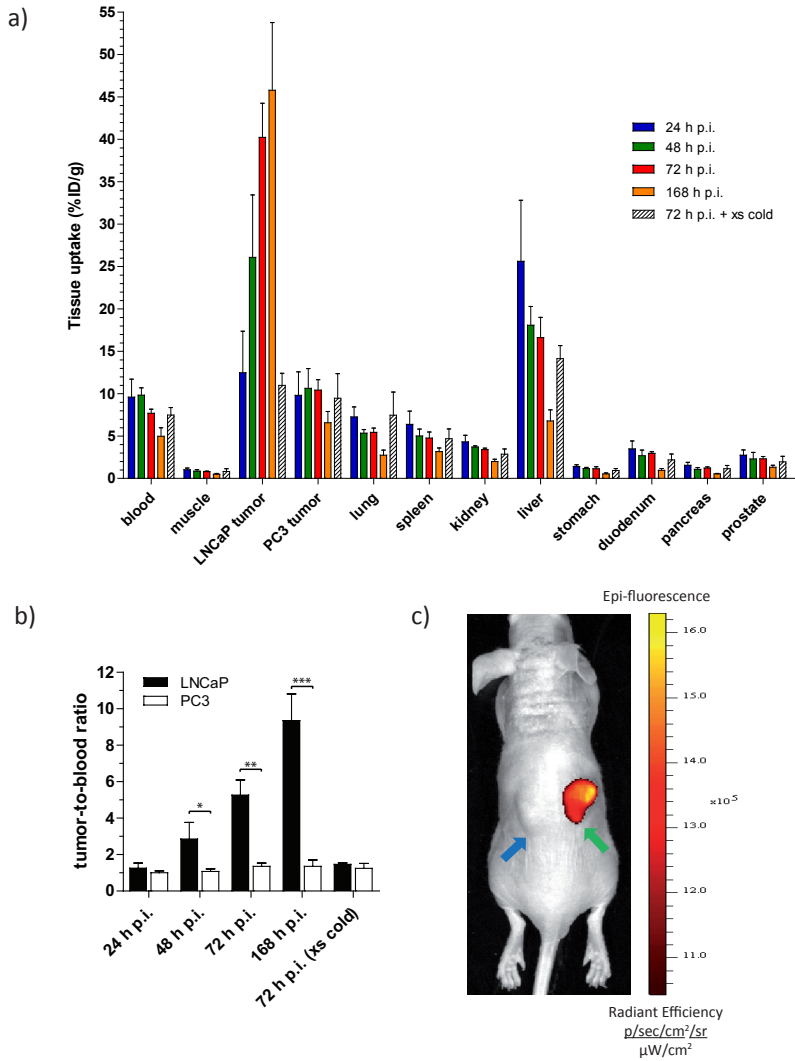
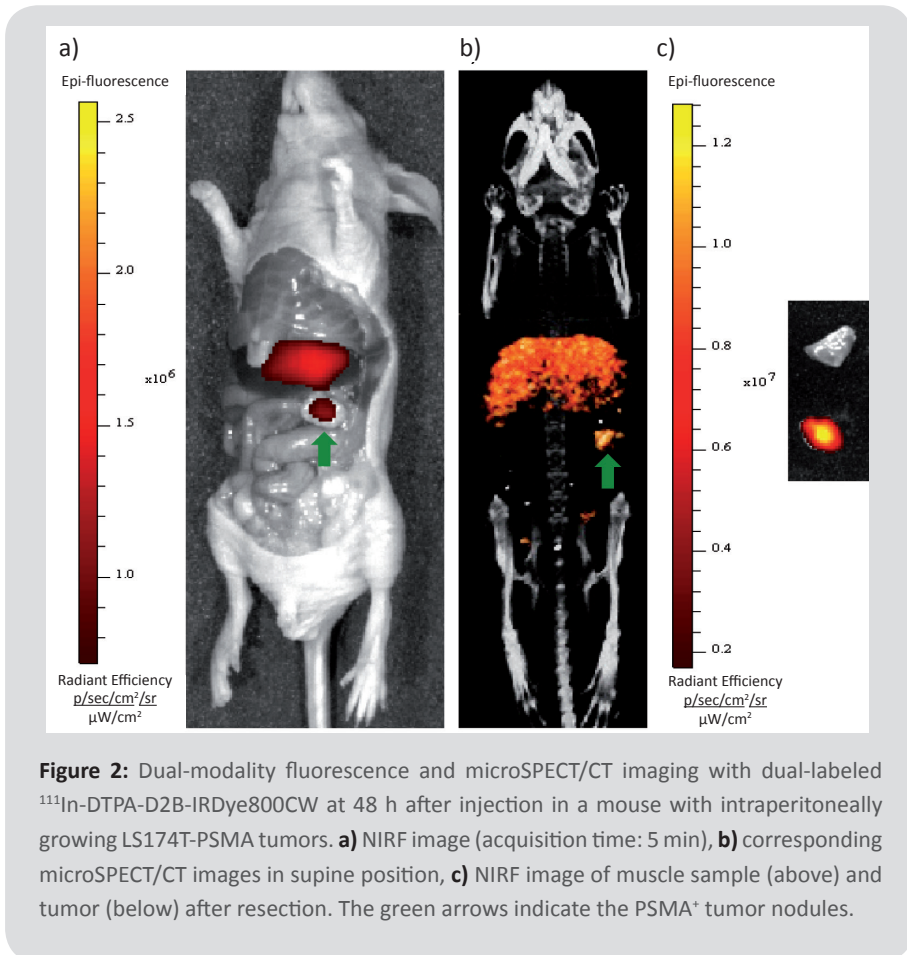


Figure 1: **a)** Biodistribution of ^{111}In -DTPA-D2B-IRDye800CW (0.55 MBq, 2.0 $\mu\text{g}/\text{mouse}$) in mice with subcutaneous PSMA⁺ LNCaP and PSMA⁻ PC3 xenografts at several time points after injection. An excess of unlabeled D2B IgG (300 $\mu\text{g}/\text{mouse}$) was coinjected in one group of mice as a negative control. LNCaP-to-PC3 tumor ratios at 48 h p.i. were 2.5 ± 0.7 . **b)** PSMA⁺ and PSMA⁻ tumor-to-blood ratios at several time points after injection of ^{111}In -DTPA-D2B-IRDye800CW, t test: * $p < 0.0001$, ** $p < 0.0001$, *** $p < 0.0001$. **c)** For illustration purposes, a NIRF image of a mouse bearing a PSMA⁺ LNCaP tumor on the right flank (green arrow) and a PSMA⁻ PC3 tumor on the left flank (blue arrow) at 48 h after i.v. injection of dual-labeled ^{111}In -DTPA-D2B-IRDye800CW.

position is shown in **figure 2**. LS174T-PSMA tumor lesions were specifically visualized by both imaging modalities. In case tumor nodules were located deeper in the peritoneal cavity, the fluorescent signals detected were less intense or even absent due to tissue absorption of the emitted photons (**figure 3**).

Image-guided resection of intraperitoneal tumor nodules

After pre-operative evaluation of tumor lesions by microSPECT/CT, image-guided surgery of the tumor lesions was performed in mice with intraperitoneally growing LS174T-PSMA nodules. First, the exact tumor location was identified by NIRF imaging. Subsequently, all detected tumors were resected and additional NIRF and microSPECT/CT imaging was performed to ensure radical surgical resection. In **figure 4**, the applicability of the dual-modality probe for intra-operative image-guided resection of the intraperitoneal tumor nodules is shown.



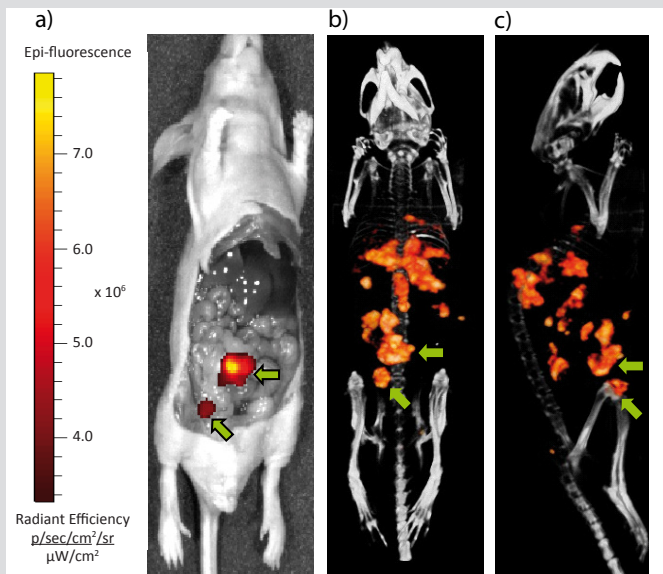


Figure 3: Dual-modality fluorescence and microSPECT/CT imaging with dual-labeled ^{111}In -DTPA-D2B-IRDye800CW of a mouse with several intraperitoneal LS174T-PSMA tumor nodules located at different depth in the peritoneal cavity performed at 48 h after injection. **a)** NIRF image (acquisition time: 5 min), **b)** and **c)** corresponding microSPECT/CT images in supine and left lateral position, showing the limited penetrations depth of NIRF imaging. The arrows indicate two tumor nodules that are located superficial enough to be visualized with fluorescence imaging. Tumors located deeper inside the peritoneal cavity are not visualized with fluorescence imaging.

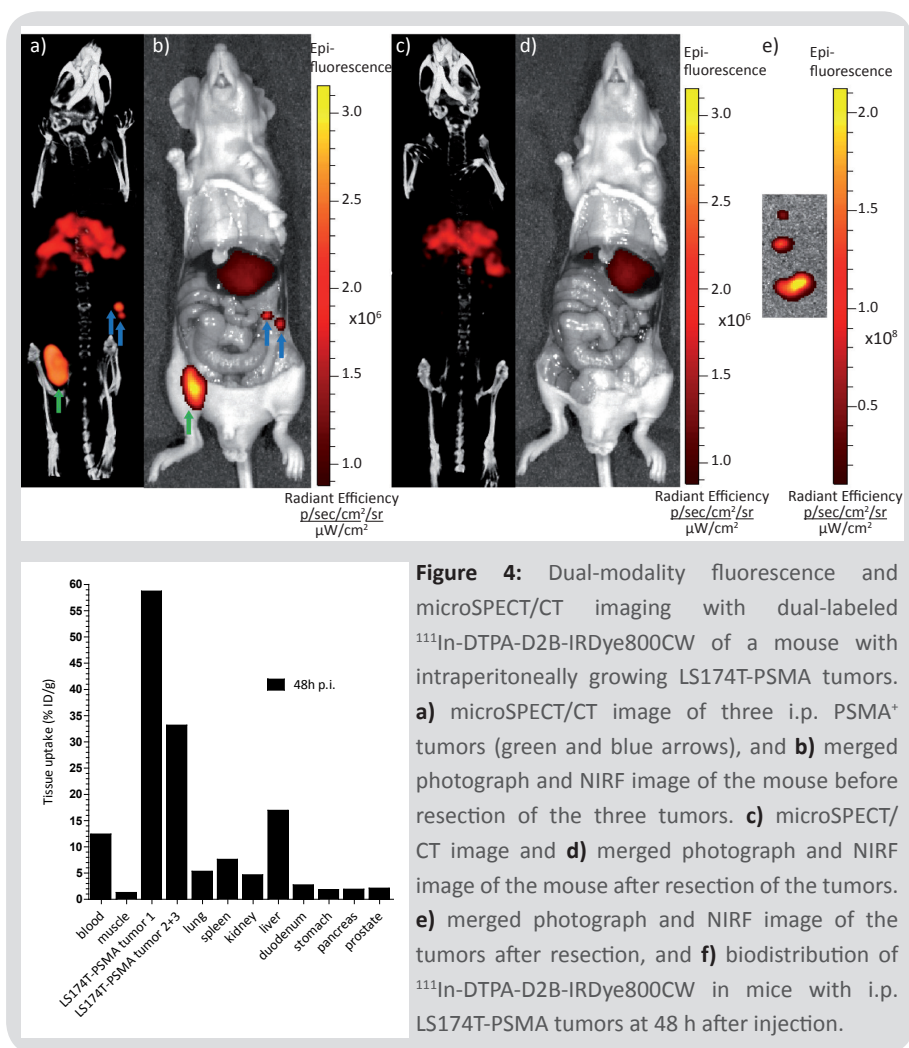
DISCUSSION

This study provides proof-of-principle for targeting PSMA-expressing prostate cancer *in vivo* with the dual-labeled ^{111}In -DTPA-D2B-IRDye800CW in a prostate cancer model with subcutaneous and intraperitoneal tumor lesions. In addition, dual-modality image-guided surgery based on this dual-labeled conjugate was performed.

During surgery, detection of small cancer foci or positive surgical margins remains challenging and may be enhanced by NIRF imaging, which allows real-time intra-operative visualization of malignant tissues [7]. Non-targeted NIRF imaging based on the use of fluorescent nanoparticles is frequently used for sentinel lymph node detection in patients with various malignancies [14]. The first clinical proof-of-concept studies using this sentinel lymph node mapping technique with dual-modality nanocolloids show promising results in prostate cancer [15]. However, non-targeted agents are not tumor selective and hence cannot be used for real

time visualization of tumor cells in resection margins. The use of targeted imaging approaches could allow more sensitive and real-time detection of cancerous foci and positive surgical margins in the submillimeter range and would permit patient-tailored surgical interventions. Several groups so far have reported the use of fluorophores conjugated to monoclonal antibodies that target receptors such as the epidermal growth factor (EGF) receptor [16], HER2/neu receptor [17] or the vascular endothelial growth factor (VEGF) [18].

Targeted NIRF imaging to identify prostate cancer cells in intra-operative settings using PSMA as a target was introduced by Liu et al. [19], who conjugated the low molecular weight PSMA ligand CTT-54.2 with Cy5.5 and demonstrated the tumor-binding potential of the Cy5.5-CTT-54.2 conjugate *in vitro*. Recently, the humanized



anti-PSMA mAb J591 has been conjugated with an ICG derivative by Nakajima and colleagues. This conjugate showed specific targeting of the s.c. PSMA-expressing tumors in mice [20]. Chen et al. [21] conjugated the anti-PSMA monoclonal antibody YC-27 with IRDye800CW. In mice with s.c. PC3-PIP tumors, tumor-to-nontarget ratios of 10 were obtained. Recently, Banerjee et al. synthesized the first dual-modality SPECT/NIRF imaging agent with affinity for the center of PSMA based on glutamate urea compound conjugated with both DOTA and IRDye800CW for targeting PSMA-expressing prostate cancer in a subcutaneous mouse model [22].

In the present study, we show that NIRF-SPECT dual-modality imaging allows specific visualization of both subcutaneous and intraperitoneal prostate cancer tumors and provide proof-of-principle for image-guided surgery with ^{111}In -DTPA-D2B-IRDye800CW in mice with intraperitoneally growing, PSMA-expressing tumor nodules.

Specific accumulation of ^{111}In -DTPA-D2B-IRDye800CW in the PSMA-expressing s.c. and i.p. tumor lesions was observed, while uptake in the other tissues remained low, except for the liver. Enhanced hepatic uptake of IRDye800CW-conjugated antibodies has been reported in previous studies. Cohen et al. [23] reported enhanced liver uptake of the dual-labeled antibodies ^{89}Zr -cetuximab-IRDye800CW and ^{89}Zr -bevacizumab-IRDye800CW *in vivo*, which was attributed to the lipophilicity and charge of the antibody conjugate. In this study, a substitution ratio of <2 was found to be optimal to prevent enhanced blood clearance and hepatic liver uptake.

All s.c. and i.p. PSMA-expressing tumor lesions were clearly visualized with microSPECT/CT. On the corresponding IVIS fluorescence scans in an intra-operative setting, all intraperitoneal tumor nodules that were located superficially could be visualized. However, tumor nodules which are located deeper inside the peritoneal cavity may not be visualized, due to absorption of the emitted fluorescent light in tissues. Although the absorption coefficient of biological tissue is relatively low in the near-infrared region (700-900 nm), light of this wavelength can only penetrate up to a few millimeters in tissue [24]. Therefore, in addition to pre-operative tumor localization, dual-labeled NIRF and radionuclide targeting agents allow intra-operative mapping of deeper laying malignant tissue with a gamma probe. Subsequently, the exact position can be determined with NIRF imaging, indicating the additive value of dual-modality imaging for detection of tumor lesions, their resection and real-time *in vivo* margin assessment.

Taken together, we showed that PSMA-expressing prostate cancer can be visualized sensitively and specifically with dual-modality microSPECT/CT and NIRF imaging with the newly developed ^{111}In -DTPA-D2B-IRDye800CW conjugate in mice with s.c. and i.p. prostate cancer xenografts. For translation of dual-modality imaging of ^{111}In -DTPA-D2B-IRDye800CW into the clinic, this antibody construct has to be considered as a new medicinal product, which has to be studied extensively regarding toxicological aspects before it can be tested.

Major advantage for clinical use is the integration of both SPECT/CT and NIRF imaging modalities in intra-operative settings to improve image-guided surgery, which could be applied for both for open laparotomy as well as for endoscopic procedures.

CONCLUSION

Here, we demonstrate the feasibility of targeting PSMA-expressing prostate cancer with the dual-labeled ^{111}In -DTPA-D2B-IRDye800CW imaging agent and provide proof-of-principle that dual-modality image-guided surgery using this conjugate is feasible. Prostate cancer lesions were specifically and sensitively detected *in vivo* in a mouse model with intraperitoneal PSMA-expressing tumor nodules. In this setting, radionuclide imaging may allow pre-operative detection and intra-operative localization of tumor lesions, while NIRF imaging enables subsequent accurate delineation of tumor lesions and real-time assessment of resection margins. These preclinical findings encourage future clinical studies with targeted dual-label imaging probes for pre- and intra-operative guidance of prostate tumor resection, to achieve radical tumor resection.

REFERENCES

- (1) Heidenreich A, Bellmunt J, Bolla M, et al. European Association of Urology. EAU guidelines on prostate cancer. Part 1: screening, diagnosis, and treatment of clinically localised disease. *Eur Urol*. 2011; 59:61-71
- (2) Eastham JA, Kuroiwa K, Ohori M, Serio AM, Gorbonos A, Maru N, Vickers AJ, Slawin KM, Wheeler TM, Reuter VE, Scardino PT. Prognostic significance of location of positive margins in radical prostatectomy specimens. *Urology*. 2007; 70:965-969
- (3) Eastham JA, Kattan MW, Riedel E, Begg CB, Wheeler TM, Gerigk C, Gonen M, Reuter V, Scardino PT. Variations among individual surgeons in the rate of positive surgical margins in radical prostatectomy specimens. *J Urol*. 2003; 170:2292-2295
- (4) Yossepowitch O, Briganti A, Eastham JA, Epstein J, Graefen M, Montironi R, Touijer K. Positive Surgical Margins After Radical Prostatectomy: A Systematic Review and Contemporary Update. *Eur Urol*. 2014; 65(2):303-313
- (5) Stephenson AJ, Eggener SE, Hernandez AV, Klein EA, Kattan MW, Wood DP Jr, Rabah DM, Eastham JA, Scardino PT. Do Margins Matter? The Influence of Positive Surgical Margins on Prostate Cancer-Specific Mortality. *Eur Urol*. 2014; 65(4):675-680
- (6) Kelderhouse LE, Chelvam V, Wayua C, Mahalingam S, Poh S, Kularatne SA, Low PS. Development of tumor-targeted near infrared probes for fluorescence guided surgery. *Bioconjug Chem*. 2013; 24:1075-1080
- (7) van Dam GM, Themelis G, Crane LM, Harlaar NJ, Pleijhuis RG, Kelder W, Sarantopoulos A, de Jong JS, Arts HJ, van der Zee AG, Bart J, Low PS, Ntziachristos V. Intraoperative tumor-specific fluorescence imaging in ovarian cancer by folate receptor- α targeting: first in-human results. *Nat Med*. 2011; 17:1315-1319
- (8) Fomina N, McFearin CL, Sermsakdi M, Morachis JM, Almutairi A. Low power, biologically benign NIR light triggers polymer disassembly. *Macromolecules*. 2011; 44:8590-8597
- (9) Ross JS, Sheehan CE, Fisher HA, Kaufman RP Jr, Kaur P, Gray K, Webb I, Gray GS, Mosher R, Kallakury BV. Correlation of primary tumor prostate-specific membrane antigen expression with disease recurrence in prostate cancer. *Clin Cancer Res*. 2003; 9:6357-6362
- (10) Colombatti M. Isolated monoclonal antibody or fragment thereof binding Prostate Specific Membrane Antigen, conjugates and uses thereof. WO 2009/130575 A2 International Patent Application (PCT/IB2009/005326)
- (11) Castelletti D, Fracasso G, Alfalah M, Cingarlini S, Colombatti M, Naim HY. Apical transport and folding of prostate-specific membrane antigen occurs independent of glycan processing. *J Biol Chem*. 2006; 281:3505-3512
- (12) Lindmo T, Boven E, Cuttitta F, Fedorko J, Bunn PA Jr. Determination of the immunoreactive fraction of radiolabeled monoclonal antibodies by linear extrapolation to binding at infinite antigen excess. *J Immunol Methods*. 1984; 72:77-89
- (13) Heskamp S, van Laarhoven HW, Molkenboer-Kuennen JD, Franssen GM, Versleijen-Jonkers YM, Oyen WJ, van der Graaf WT, Boerman OC. ImmunoSPECT and immunoPET of IGF-1R expression with the radiolabeled antibody R1507 in a triple-negative breast cancer model. *J Nucl Med*. 2010; 51:1565-1572

- (14) van den Berg NS, Valdés-Olmos RA, van der Poel HG, van Leeuwen FW. Sentinel lymph node biopsy for prostate cancer: a hybrid approach. *J Nucl Med.* 2013; 54:493-496
- (15) van der Poel HG, Buckle T, Brouwer OR, Valdés Olmos RA, van Leeuwen FW. Intraoperative laparoscopic fluorescence guidance to the sentinel lymph node in prostate cancer patients: clinical proof of concept of an integrated functional imaging approach using a multimodal tracer. *Eur Urol.* 2011; 60:826-833
- (16) Gleysteen JP, Duncan RD, Magnuson JS, Skipper JB, Zinn K, Rosenthal EL. Fluorescently labeled cetuximab to evaluate head and neck cancer response to treatment. *Cancer Biol Ther.* 2007; 8:1181-1185
- (17) Lee SB, Hassan M, Fisher R, Chertov O, Chernomordik V, Kramer-Marek G, Gandjbakhche A, Capala J. Affibody molecules for in vivo characterization of HER2-positive tumors by near-infrared imaging. *Clin Cancer Res.* 2008; 14:3840-3849
- (18) Withrow KP, Newman JR, Skipper JB, Gleysteen JP, Magnuson JS, Zinn K, Rosenthal EL. Assessment of bevacizumab conjugated to Cy5.5 for detection of head and neck cancer xenografts. *Technol Cancer Res Treat.* 2008; 7:61-66
- (19) Liu T, Wu LY, Hopkins MR, Choi JK, Berkman CE. A targeted low molecular weight near-infrared fluorescent probe for prostate cancer. *Bioorg Med Chem Lett.* 2010; 20:7124-7126
- (20) Nakajima T, Mitsunaga M, Bander NH, Heston WD, Choyke PL, Kobayashi H. Targeted, activatable, in vivo fluorescence imaging of prostate-specific membrane antigen (PSMA) positive tumors using the quenched humanized J591 antibody-indocyanine green (ICG) conjugate. *Bioconjug Chem.* 2011; 22:1700-1705
- (21) Chen Y, Dhara S, Banerjee SR, Byun Y, Pullambhatla M, Mease RC, Pomper MG. A low molecular weight PSMA-based fluorescent imaging agent for cancer. *Biochem Biophys Res Commun.* 2009; 390:624-629
- (22) Banerjee SR, Pullambhatla M, Byun Y, Nimmagadda S, Foss CA, Green G, Fox JJ, Lupold SE, Mease RC, Pomper MG. Sequential SPECT and optical imaging of experimental models of prostate cancer with a dual modality inhibitor of the prostate-specific membrane antigen. *Angew Chem Int Ed Engl.* 2011; 50:9167-9170

3.3

Pretargeted dual-modality immuno-SPECT and near-infrared fluorescence imaging for image-guided surgery of prostate cancer

Susanne Lütje¹

Mark Rijpkema¹

David M. Goldenberg²

Catharina M. van Rij¹

Robert Sharkey²

William J. McBride²

Gerben M. Franssen¹

Cathelijne Frielink¹

Wijnand Helfrich³

Wim J.G. Oyen¹

Otto C. Boerman¹

¹ Department of Radiology and Nuclear Medicine, Radboud University Medical Center, Nijmegen, The Netherlands

² Immunomedics Inc., Morris Plains, NJ, USA

³ Department of Surgery, University Medical Centre Groningen, Groningen, The Netherlands

ABSTRACT

Background

Radical removal of malignant lesions may be improved using tumor targeted dual-modality probes that contain both a radiotracer and a fluorescent label, to allow for enhanced intra-operative delineation of tumor resection margins. Since pretargeting strategies yield high signal-to-background ratios, we evaluated the feasibility of a pretargeting strategy for intra-operative imaging in prostate cancer using an anti-TROP-2 x anti-HSG bispecific antibody (TF12), in conjunction with the dual-labeled diHSG peptide (RDC018) equipped with both a DOTA chelate for radiolabeling purposes and a fluorophore (IRdye800CW) to allow near-infrared optical imaging.

Methods

Nude mice implanted s.c. with TROP-2-expressing PC3 human prostate tumor cells or with PC3 metastases in the scapular and suprarenal region were injected i.v. with 1 mg of TF12 and, after 16h of tumor accumulation and blood clearance, were subsequently injected with 10 MBq, 0.2 nmol/mouse of either ^{111}In -RDC018 or ^{111}In -IMP288 as a control. Two hours post injection, both microSPECT/CT and fluorescence images were acquired, both before and after resection of the tumor nodules. After image acquisition, the biodistribution of ^{111}In -RDC018 and ^{111}In -IMP288 was determined and tumors were analyzed immunohistochemically.

Results

The biodistribution of the dual-label RDC018 showed specific accumulation in the TROP-2 expressing PC3 tumors ($12.4 \pm 3.7\%$ ID/g at 2h p.i.), comparable to ^{111}In -IMP288 ($9.1 \pm 2.8\%$ ID/g at 2h p.i.). MicroSPECT/CT and near-infrared fluorescence (NIRF) imaging confirmed this TROP-2-specific uptake of the dual-label ^{111}In -RDC018 in both the s.c. and metastatic growing tumor model. In addition, PC3 metastases could be visualized preoperatively with SPECT/CT and could subsequently be resected by image-guided surgery using intra-operative NIRF imaging.

Conclusion

We provide preclinical feasibility of a novel pretargeted dual-modality imaging approach in prostate cancer that allows for image-guided resection of TROP-2-expressing tumors.

INTRODUCTION

Despite advances in diagnostic procedures and clinical management prostate cancer remains associated with significant morbidity and is the second leading cause of cancer-related deaths in men in the Western world.

At present, extensive research is focused on the development of new molecular imaging techniques to improve detection and staging of this disease. In this regard, radiolabeled antibodies that target prostate cancer-associated cell surface antigens appear to be particularly promising. This is supported by the clinical application of the PSMA-directed antibody capromab pendetide, also known as ProstaScint® (7E11-C53), or the antibody J591 [1]. However, antibodies typically show slow clearance from the circulation ($t_{1/2} = 2\text{-}3$ days), which requires a relatively long interval between time of injection of the radiolabeled antibody and subsequent image acquisition in order to achieve adequate contrast. In addition, the slow blood clearance results in limited target-to-background ratios. To overcome these limitations and to improve targeting of tumors, various pretargeting techniques have been developed. Previously, we reported a study in which we evaluated a pretargeting approach that targets TROP-2-expressing prostate cancer [2]. TROP-2, also known as EGP-1 (epithelial glycoprotein-1), is a 46-kDa transmembrane glycoprotein expressed on diverse carcinomas, such as of the lung, bladder, breast, cervix, ovary, stomach and prostate [3]. We previously applied the trivalent bispecific antibody (bsAb) TF12, which consists of two anti-TROP-2 Fab fragments and one anti-HSG (histamine-succinyl-glycine) Fab fragment. In this strategy, an unlabeled bsAb with affinity for both the tumor cell and a radiolabeled diHSG peptide was injected. After TF12 had accumulated in the tumor and was cleared from the blood, the ^{111}In -labeled diHSG peptide IMP288 was administered, which was rapidly and selectively trapped at the tumor. This method allowed for imaging within 1-2 h after injection of the radiolabeled peptide while yielding high target-to-background ratios.

At present, surgical removal of prostate cancer lesions is the treatment of choice for patients with low- and intermediate-risk localized disease, and in selected patients with high-risk localized disease [4]. The use of intra-operative imaging might guide the surgeon in the detection of malignant tissue which might improve the outcome, and reduce morbidity and treatment-related side effects. However, the application of nuclear imaging-based pretargeting strategies appears to be limited for intra-operative imaging purposes as tumor tissue cannot be delineated precisely by radionuclide detection in the intra-operative setting.

Near-infrared fluorescence (NIRF) imaging with fluorophores conjugated to tumor targeting agents is rapidly emerging as a new sensitive intra-operative imaging technique for improved and real-time detection of malignant lesions during surgery. However, the penetration depth of both excitation and emission light in tissues is usually limited to several millimeters [5]. One strategy to deal with this limited

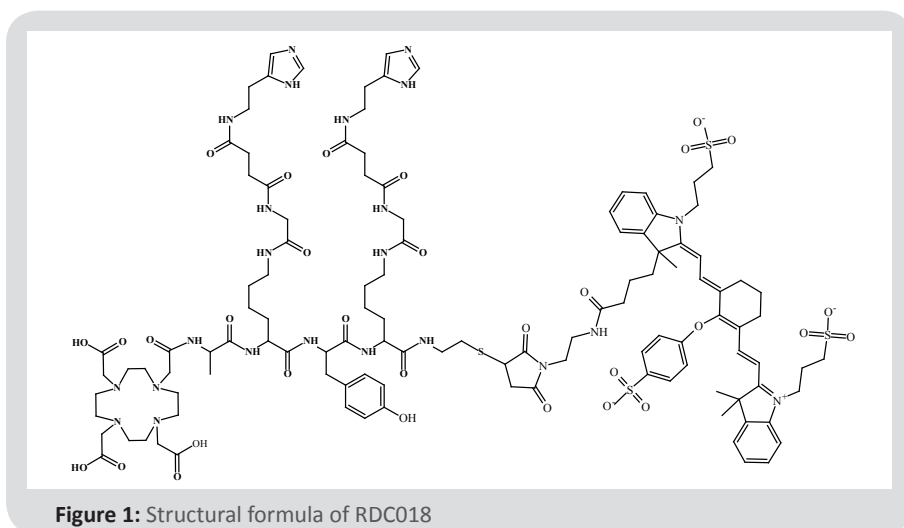
penetration depth is combining NIRF and radionuclide imaging techniques. With this dual-modality approach, the burden of the disease could be assessed pre-operatively, followed by localization of the tumor lesions intra-operatively using a gamma probe, and subsequent intra-operative guidance for surgical removal of the tumor lesions based on the fluorescent component of the dual-label agent.

Here, we evaluated a bispecific antibody-based pretargeting strategy for prostate cancer preclinically, using a novel hapten, designated RDC018, which was equipped with both a 1,4,7,10-tetraazacyclododecane-1,4,7,10-tetraacetic acid (DOTA) chelate for radiolabeling and the fluorophore IRDye800CW for NIRF imaging. The DOTA chelate of RDC018 was labeled with ^{111}In . The pretargeting characteristics of the TF12/RDC018 approach were evaluated in a mouse tumor model bearing TROP-2-expressing prostate cancer metastases. In addition, the feasibility of this dual-label pretargeting strategy for image-guided surgery based on microSPECT/CT and NIRF imaging was investigated.

MATERIALS AND METHODS

Pretargeting reagents TF12 and RDC018

BsAb TF12, having both TROP-2- and HSG-binding specificities, was produced using the Dock-and-Lock[®] technology as described previously by Rossi et al. [6]. The NIR fluorescent peptide RDC018 is a peptide-hapten derived from IMP288, a 1,4,7,10-tetraazacyclododecane-1,4,7,10-tetraacetic acid (DOTA)-conjugated D-Tyr-D-Lys-D-Glu-D-Lys tetrapeptide, in which both lysine residues are substituted with an HSG moiety. In addition to the DOTA chelator for radiolabeling, RDC018 also contains a NIR fluorescent IRDye800CW moiety (**figure 1**).



Cell Culture

The TROP-2-expressing human prostate cancer cell line PC3, originally derived from a prostate cancer bone metastasis was obtained from American Type Culture Collection (CRL 1435, Manassas, VA, USA). Cells were cultured in RPMI 1640 medium, supplemented with 10% fetal calf serum (Life technologies, Carlsbad, CA) and 2 mM glutamine.

Mouse Models

Male BALB/c nude mice (Janvier, Le Genest Saint Isle, France), 8-9 weeks old, housed in individual ventilated cages (5 mice per cage) under nonsterile standard conditions with free access to standard animal chow and water, were adapted to laboratory conditions for one week before experimental use. Mice were subcutaneously inoculated with 3×10^6 PC3 cells (right flank) suspended in 200 μ L of 67% complete RPMI 1640 medium with 33% matrigel (BD Biosciences, Franklin Lakes, NJ). PC3 xenografts grew to approximately 0.1 g in 7 days after tumor cell inoculation. To induce metastatic prostate cancer growth, mice were anesthetized with isoflurane and 5×10^5 PC3 cells in 50 μ L of PBS were inoculated with a 30-gauge needle through the diaphragm into the left cardiac ventricle after midline incision [7]. PC3 metastases were allowed to grow for 10 - 12 weeks after tumor cell inoculation.

All experiments have been approved by the institutional Animal Welfare Committee of the Radboud University Medical Center and were conducted in accordance to the guidelines of the Revised Dutch Act on Animal Experimentation.

Radiolabeling of IMP288 and RDC018

IMP288 was labeled with ^{111}In (Covidien, Petten, The Netherlands) at a specific activity of 60.5 MBq/nmol under strict metal-free conditions. Briefly, 60 MBq of ^{111}In was added to 2.4 μ g of IMP288 in 0.1 M MES buffer pH 5.4 (three times the volume of ^{111}In -chloride) during 20 min of incubation at 95°C. Following incubation, 50 mM ethylenediaminetetraacetic acid (EDTA) was added to the labeling reaction to a final concentration of 1mM EDTA to chelate unincorporated ^{111}In . The labeling efficiency, determined by instant thin layer chromatography on silicagel strips (ITLC-SG; Gelman Sciences, Ann Arbor, MI, USA) using 0.1 M ammonium acetate (NH₄Ac) buffer with 0.1 M EDTA (pH 5.5) as the mobile phase, reached 97%.

RDC018 was radiolabeled under metal-free conditions at a specific activity of 25.5 MBq/nmol. For this reaction, 127 MBq of ^{111}In was added to 7.2 μ g of RDC018 in 0.1 M MES buffer pH 5.4 (three times the volume of ^{111}In -chloride) for 20 min of incubation at 95°C. For imaging and image-guided surgery, 2.5 μ g of RDC018 was radiolabeled with 32 MBq (specific activity 18.5 MBq/nmol). After incubation, 50 mM ethylenediaminetetraacetic acid (EDTA) was added to the labeling reaction to a final concentration of 1mM EDTA. The labeling efficiency for the RDC018 labeling reaction ranged between 87 and 97%.

Immunoreactivity

To demonstrate bispecific immunoreactivity of TF12, a serial dilution of PC3 cells in RPMI medium containing 0.5% BSA (1.6×10^6 to 2.6×10^7 cells in 0.5 ml) was incubated with TF12 (50 $\mu\text{g}/\text{ml}$) for 30 min at 37°C. Cells were washed twice in RPMI medium containing 0.5% BSA followed by incubation with ^{111}In -RDC018 (250 Bq). To determine nonspecific binding, a duplicate of the lowest cell concentration was incubated without TF12. After incubation, cells were centrifuged and washed with 500 μl RPMI medium containing 0.5% BSA. The activity in the vials and in the cell pellet was determined in a gamma counter (Wizard 3" 1480, LKB-Wallac, Oy, Finland).

Immunohistochemical analysis of TROP-2-expressing tumors

Expression of TROP-2 in subcutaneous PC3 tumors was determined immunohistochemically on 5- μm frozen tissue sections. The tissue sections were fixed with acetone (100%) for 10 min at -20°C. After overnight drying, the sections were blocked with 20% normal goat serum (Bodinco) for 30 minutes and stained with the anti-TROP-2 humanized monoclonal antibody hRS7 (4 $\mu\text{g}/\text{ml}$ antibody in PBS 1% BSA) for 1 hour at room temperature under light-protected conditions. Subsequently, the tissue sections were washed in PBS and stained with a secondary goat-anti-human HRP (Abcam, Cambridge, UK) at a dilution of 1:100 in PBS, 1% BSA, for 30 min at room temperature. After incubation, the tissue sections were washed with PBS three times. Finally, tumor sections were incubated with 0.019 g of 3,3-diaminobenzidine tetrahydro-chloride (DAB) substrate (Bright DAB, Immunologic, Duiven, Netherlands) in 25 ml PBS and 62.5 μl H_2O_2 for 10 min for development, followed by a hematoxylin counterstaining. Immunohistochemical analysis of the resected s.c. PC3 tumors revealed TROP-2 expression in all tumors (not shown).

Pretargeted immuno-SPECT/CT and NIRF imaging

In the first experiment, male BALB/c nude mice ($n=4$) with subcutaneous PC3 xenografts in the right flank were intravenously injected into the tail vein with 1 mg of TF12 (6.4 nmol) in 200 μl of PBS followed by i.v. injections of either ^{111}In -RDC018 (10 MBq, 0.6 μg (0.2 nmol)) or ^{111}In -IMP288 (10 MBq, 0.4 μg (0.2 nmol)) 16 h later. Two additional groups of mice ($n=2$) did not receive TF12 prior to injection of the radiolabeled peptide to determine the non-TF12-mediated localization of the peptide. One of these groups received only ^{111}In -RDC018 (10 MBq, 0.6 $\mu\text{g}/\text{mouse}$) and one group received only ^{111}In -IMP288 (10 MBq, 0.4 $\mu\text{g}/\text{mouse}$).

Two hours after injection of ^{111}In -RDC018, mice were anesthetized with isoflurane and imaged on a small-animal microSPECT/CT scanner (U-SPECT II, MILabs, Utrecht, Netherlands) with a 1.0 mm diameter pinhole collimator tube (acquisition time 30 min) in prone position. After microSPECT/CT imaging, the mice were euthanized by O_2/CO_2 asphyxiation and NIRF images were acquired on an IVIS imaging system (Xenogen VivoVision IVIS Lumina II, Caliper Life Sciences, Lincolnshire,

United Kingdom; acquisition time 5 min, binning: medium, Fstop: 2, excitation: 745 nm, excitation autofluorescence: 675 nm, emission: ICG, lamp level: high, FOV: D). MicroSPECT/CT scans were reconstructed with MILabs reconstruction software, which uses an ordered-subset expectation maximalization algorithm.

Biodistribution of pretargeted ^{111}In -RDC018 and ^{111}In -IMP288

Subsequently, the biodistribution in mice ($n=4$) with s.c. PC3 tumors of ^{111}In -RDC018 was compared to that of ^{111}In -IMP288. Tissues of interest (tumor, muscle, lung, spleen, kidney, liver, pancreas, stomach, duodenum and prostate) were dissected, weighed and the radioactivity was measured in a gamma counter to determine the biodistribution of ^{111}In -IMP288 and ^{111}In -RDC018. Blood samples were obtained by heart puncture. For calculation of the uptake of radioactivity in each tissue as a fraction of the injected dose, an aliquot of the injection dose was counted simultaneously.

Dual-modality microSPECT/CT and NIRF image-guided surgery

In the second experiment, male BALB/c nude mice ($n=20$) with PC3 metastases in the submandibular, shoulder, and adrenal gland region that developed after injection of PC3 cells into the right cardiac ventricle were injected intravenously with the bsAb TF12 (1 mg/mouse), followed by i.v. injection of ^{111}In -RDC018 (0.6 μg /mouse, 20 MBq/ μg) at 16 h after injection of TF12. Mice were imaged 2 hours later on both the IVIS imaging system and a small-animal microSPECT/CT scanner with the same settings as in the first experiment. MicroSPECT/CT scans were performed pre-operatively, followed by NIRF imaging of the mice in the supine position after surgical removal of skin, abdominal muscle layers, and peritoneum. After NIRF image acquisition, the visualized tumor lesions were resected, followed by NIRF imaging to check whether residual tumor tissue was left in situ. In addition, microSPECT/CT scans were performed after resection of the tumor lesions, using the same scanning parameters that were used for pre-operative evaluation.

Statistical analyses

Statistical analyses were performed with Graphpad Prism, version 5.03 (GraphPad, La Jolla, CA, USA). Results are presented as mean \pm standard deviation (SD). To determine statistical differences, unpaired t -tests were used.

RESULTS

***In vitro* characterization**

Analysis of the bispecific immunoreactivity of TF12 revealed that in the *in vitro* assay up to 82% of the added peptide specifically bound to the PC3 cells (results not shown).

Tumor growth and development of metastases

Subcutaneous PC3 tumors in the right flank reached a tumor size of approximately 0.1 g at 7 days after tumor cell inoculation. To induce metastases, mice (n=20) received injections of PC3 cells into the left cardiac ventricle. The mice were dissected after 10-12 weeks and soft-tissue PC3 metastases were most frequently found in the submandibular, shoulder, and adrenal gland region. In addition, several PC3 metastases were found in the rectovesical pouch. Besides the formation of soft-tissue PC3 metastases at different anatomical sites, microCT imaging showed the development of PC3 bone metastases in the vertebral column (n=3) and in the ribs (n=2) of the mice.

Biodistribution of $^{111}\text{In-RDC018}$ and $^{111}\text{In-IMP288}$

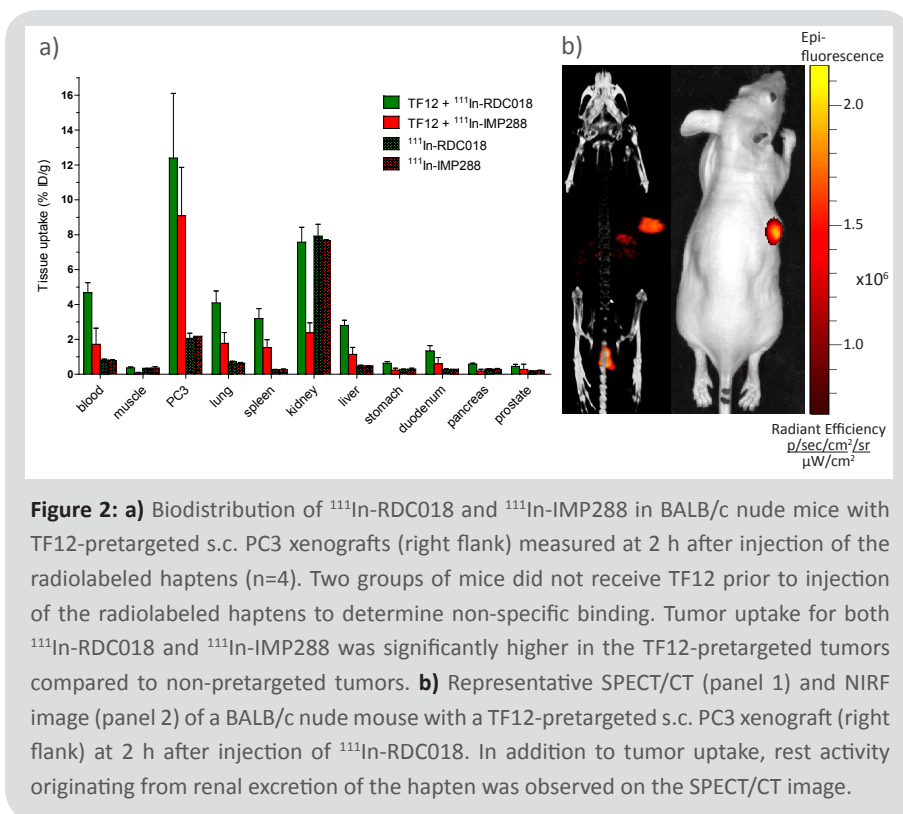
$^{111}\text{In-RDC018}$ and $^{111}\text{In-IMP288}$ specifically accumulated in the s.c. TF12-pretargeted TROP-2-expressing PC3 tumors (right flank). Uptake of $^{111}\text{In-RDC018}$ and $^{111}\text{In-IMP288}$ in the PC3 tumor was comparable at 2 h after injection ($12.4 \pm 3.7\%$ ID/g (n=4) and $9.1 \pm 2.8\%$ ID/g (n=4), respectively), **figure 2a**. Tumor uptake of $^{111}\text{In-RDC018}$ and $^{111}\text{In-IMP288}$ in non-pretargeted tumors was significantly lower, reaching $2.1 \pm 0.3\%$ ID/g ($p=0.020$) and $2.2 \pm 0.0\%$ ID/g ($p=0.029$) for $^{111}\text{In-RDC018}$ and $^{111}\text{In-IMP288}$, respectively. Overall, the biodistribution profiles of $^{111}\text{In-RDC018}$ and $^{111}\text{In-IMP288}$ show similar patterns (**figure 2a**). One essential difference in the biodistribution profiles of $^{111}\text{In-RDC018}$ and $^{111}\text{In-IMP288}$ after pretargeting with TF12 is renal accumulation. While the accumulation of $^{111}\text{In-IMP288}$ in the kidneys was relatively low ($2.4 \pm 0.6\%$ ID/g), renal uptake of $^{111}\text{In-RDC018}$ was significantly higher, reaching $7.6 \pm 0.9\%$ ID/g at 2 h after injection ($p<0.0001$). In addition, blood levels of $^{111}\text{In-RDC018}$ were significantly higher compared to $^{111}\text{In-IMP288}$ ($4.7 \pm 0.6\%$ ID/g and $1.7 \pm 0.9\%$ ID/g ($p=0.0016$), respectively), indicating slower blood clearance. Moreover, liver uptake of $^{111}\text{In-RDC018}$ and $^{111}\text{In-IMP288}$ differed significantly, reaching $2.8 \pm 0.3\%$ ID/g for $^{111}\text{In-RDC018}$ and $1.1 \pm 0.4\%$ ID/g for $^{111}\text{In-IMP288}$ ($p=0.0006$). Tumor-to-blood ratios of $^{111}\text{In-RDC018}$ and $^{111}\text{In-IMP288}$ in the TF12-pretargeted tumors were 2.6 ± 0.7 and 5.9 ± 2.0 ($p=0.021$), respectively.

Pretargeted immuno-SPECT/CT and NIRF imaging

Five BALB/c nude mice with s.c. TROP-2-expressing PC3 tumors (right flank) were imaged by both fluorescence imaging and microSPECT/CT at 2 h after injection of $^{111}\text{In-RDC018}$ (18 h after pretargeting with TF12). A typical microSPECT/CT image with the corresponding fluorescence image of a mouse in prone position is shown in **figure 2b**. The PC3 xenograft was clearly and specifically visualized with both imaging modalities.

Dual-modality microSPECT/CT and NIRF image-guided surgery

BALB/c nude mice with PC3 metastases were imaged by both fluorescence imaging



and microSPECT/CT at 2 h after injection of radiolabeled RCD018. A typical example of a microSPECT/CT image with corresponding NIRF image of a mouse with two bone metastases in the vertebral column is shown in **figure 3**. Another example of dual-modality microSPECT/CT and NIRF imaging of a mouse with TF12-pretargeted bone metastases originating from the ribs is depicted in **figure 4**.

After pre-operative evaluation of tumor lesions by microSPECT/CT, image-guided surgery of the tumor lesions was performed. First, the exact tumor location was identified by NIRF imaging. Subsequently, these tumor lesions were resected and NIRF and microSPECT/CT imaging was repeated to ensure radical surgical resection. In **figure 5**, the feasibility of the dual-modality probe for intra-operative image-guided surgical resection of the metastatic tumor nodules is shown.

DISCUSSION

In the present preclinical study, the *in vivo* tumor targeting characteristics of the dual-modality fluorescent ^{111}In -labeled hapten RDC018 in TROP-2-expressing prostate

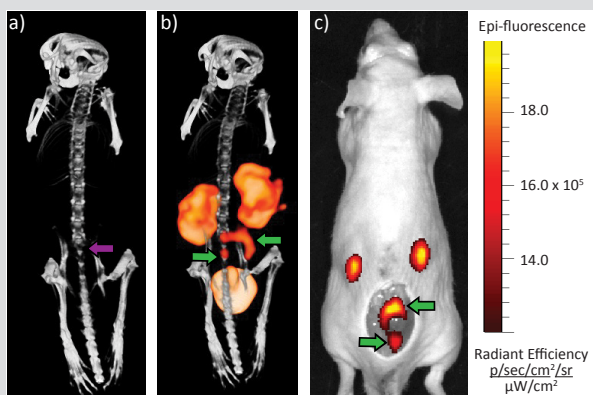


Figure 3: Sequentially acquired dual-modality microSPECT/CT and NIRF image with ^{111}In -RDC018 in a mouse with two TF12-pretargeted tumors. PC3 bone metastases located in 2 vertebrae with soft tissue outgrowth were visualized 2 h after injection of ^{111}In -RDC018. **a)** CT scan illustrating the alterations in bone structure in the two vertebrae, **b)** microSPECT/CT scan showing uptake in the bone metastases with soft tissue outgrowth, as well as accumulation in kidneys and bladder due to renal excretion of ^{111}In -RDC018 **c)** corresponding NIRF image showing specific uptake in both PC3 metastases and kidneys.

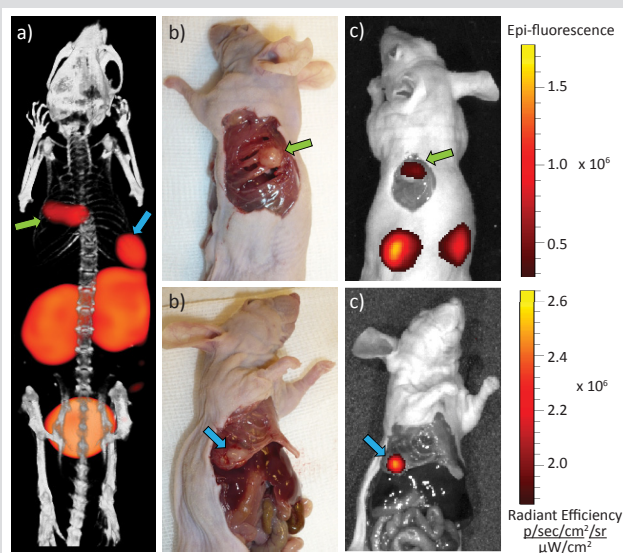
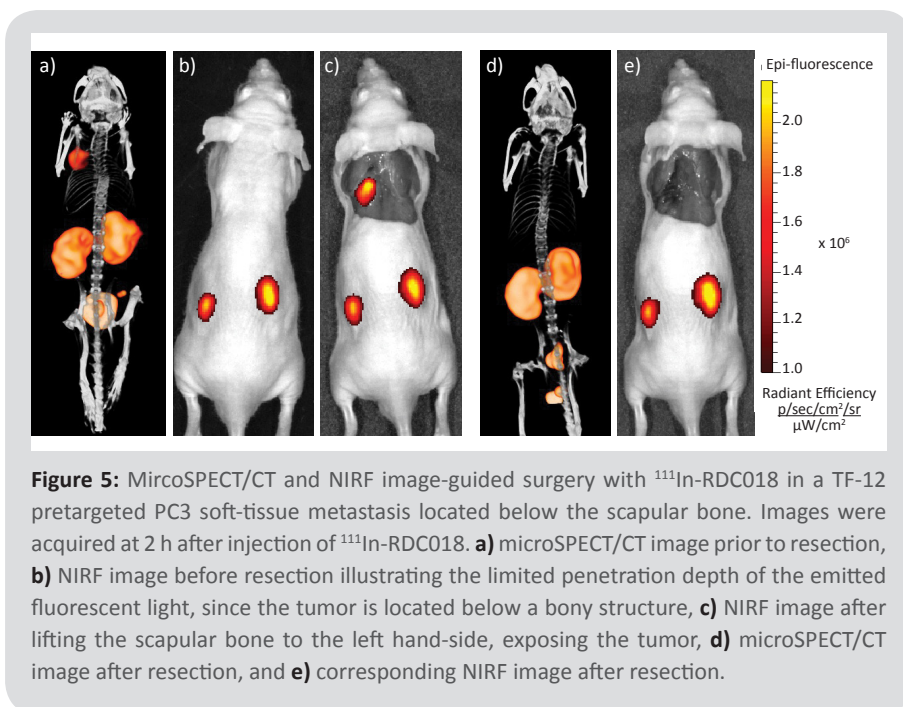


Figure 4: Sequentially acquired dual-modality microSPECT/CT and NIRF image with ^{111}In -RDC018 (12 MBq, 0.5 μg /mouse) in a mouse with two TF12-pretargeted PC3 bone metastases originating from the ribs. Images were acquired 2 h after injection of ^{111}In -RDC018. **a)** MicroSPECT/CT scan showing kidneys, bladder and two tumor manifestations (green and blue arrow), **b)** photographs of exposed metastases, and **c)** corresponding NIRF images showing specific uptake of ^{111}In -RDC018 in both PC3 metastases.



cancer pretargeted with the trivalent bsAb TF12 were evaluated. The feasibility of this approach for image-guided surgery was demonstrated in mice bearing TROP-2-expressing metastases. In a previous study, the potential for imaging pretargeted prostate cancer with the bsAb TF12 and the radiolabeled hapten IMP288 was evaluated [2]. It was shown in mice with s.c. PC3 tumors that this pretargeting approach allows for rapid and sensitive imaging of TROP-2-expressing prostate cancer. For intra-operative imaging purposes, radionuclide detection can be used to localize tumor nodules with a gamma probe; however, precise delineation of tumor lesions or assessment of tumor cell-containing surgical margins remains challenging with this modality. NIRF imaging is a sensitive technique that may be exploited to improve visualization of small to microscopic malignant lesions and potentially of positive resection margins during surgery.

So far, several preclinical studies have evaluated methods to intra-operatively visualize tumor tissue and resection margins in prostate cancer [8-10]. Targeted approaches using antibodies or peptides are particularly promising to apply dual-modality imaging. Very recently, the first clinical trial using the anti-VEGF antibody bevacizumab tagged with the NIRF dye IRDye800CW (clinicaltrials.gov, NCT01508572) has begun, with the aim to show the feasibility of tumor-targeted intra-operative fluorescence imaging in breast cancer patients. Since the penetration depth of emitted light in tissue is limited to several millimeters, the combination with

a radiolabel would allow intra-operative probe-guided tumor detection and image-guided surgery.

In the present study, analysis of biodistribution of ^{111}In -RDC018 and ^{111}In -IMP288 showed that the addition of the IRDye800CW fluorophore to the IMP288 diHSG peptide hapten only slightly affected the *in vivo* behavior of the molecule. The overall biodistribution profile of both peptides was similar, however, RDC018 showed enhanced hepatic uptake. Previously, this has also been observed for IRDye800CW conjugated antibodies [11] and may be due to the increased lipophilicity of RDC018 compared to IMP288.

Biodistribution studies demonstrated high and specific PC3 tumor targeting for both ^{111}In -RDC018 as well as ^{111}In -IMP288. Using this subcutaneous tumor model, we provide proof-of-principle that ^{111}In -RDC018 can be used for rapid dual-modality imaging of TROP-2-expressing tumors. As early as 2 hours after injection, high tumor-to-background ratios were achieved. With both imaging modalities, the fluorescent ^{111}In -labeled hapten-peptide RDC018 accumulated specifically in the TROP-2-expressing PC3 tumors, whereas no specific tumor targeting with ^{111}In -RDC018 was observed in mice with subcutaneous tumors that were not pretargeted with TF12. Accordingly, the non-pretargeted PC3 tumors were not visualized by NIRF imaging. These results clearly demonstrate that the accumulation of ^{111}In -RDC018 is TF12-mediated. While the uptake of ^{111}In -RDC018 in other tissues remained low, intermediate accumulation in the kidneys was observed, which is most likely caused by renal clearance of the peptide. The enhanced renal retention of RDC018 compared to that of IMP288 suggests increased tubular reabsorption of the dual-labeled peptide in the kidneys. High accumulation of small-sized fluorescent tracers has been observed previously. Banerjee and colleagues synthesized a dual-label PSMA ligand (based on glutamate urea) which was tagged with both ^{111}In and IRDye800CW for targeting PSMA-expressing prostate cancer in mice with subcutaneous xenografts [12]. In this study, high tumor uptake in the PSMA-expressing PC3-PIP xenografts was observed, while uptake in the PSMA-negative PC3-FLU tumors remained low. Both tumor cell lines were derived from PC3 human prostate cancer cells and only differ in their expression of PSMA (PIP: PSMA⁺, FLU: PSMA⁻). PSMA-expressing tumors could be visualized specifically on both SPECT/CT and NIRF imaging. However, intense radiotracer uptake was observed in the kidneys, which was attributed to the tracer's route of excretion and specific uptake by PSMA expressed in the kidneys.

In addition to biodistribution and NIRF imaging experiments, we performed sequential dual-modality microSPECT/CT and NIRF imaging to demonstrate the feasibility of this pretargeting approach using the bsAb TF12 and the dual-label fluorescent hapten-peptide ^{111}In -RDC018. Preferential accumulation of the dual-label hapten-peptide ^{111}In -RDC018 was confirmed with both NIRF and microSPECT/CT imaging in TROP-2-expressing soft-tissue and bone metastases. PC3 metastases could be visualized clearly with both microSPECT/CT and NIRF imaging, showing

accurate conformity of single tumor lesions by both imaging modalities. In addition, image-guided surgery based on microSPECT/CT and NIRF images was performed to provide proof-of-principle for feasibility of using this pretargeting approach for intra-operative detection of tumor lesions. It was shown that metastases imaged by microSPECT/CT and NIRF prior to surgery could be resected with image-guidance using this pretargeting approach. Moreover, NIRF imaging could be performed intra-operatively to ensure that the tumor tissue was resected completely without leaving visible tumor-cell containing resection margins in situ. MicroSPECT/CT imaging, which was performed after surgery to exclude false negative observations from intra-operatively conducted NIRF imaging, confirmed complete resection of all metastatic tumor lesions.

In summary, we showed that TF12-pretargeted TROP-2-expressing prostate cancer can be visualized with both microSPECT/CT and NIRF imaging using the dual-label near-fluorescent ^{111}In -labeled hapten-peptide RDC018. In addition, proof-of-principle was provided that this dual-label pretargeting approach can be used for image-guided surgery of TROP-2-expressing metastatic prostate cancer lesions. To translate this dual-modality pretargeting approach to the clinic, the safety, feasibility, and validity of this approach need to be evaluated.

CONCLUSION

Compared to targeting approaches using dual-labeled antibodies, pretargeting strategies may yield better signal-to-background ratios. Here, we show feasibility of the ^{111}In -labeled near-infrared fluorescent hapten-peptide RDC018 for dual-modality detection of prostate cancer metastases in a mouse model of TROP-2-expressing soft-tissue and bony prostate cancer metastases pretargeted with the bsAb TF12. Both soft-tissue as well as bony prostate cancer lesions were specifically and sensitively detected *in vivo*. While radionuclide imaging may allow pre-operative detection and intra-operative localization of tumor lesions, NIRF imaging enables subsequent accurate delineation of tumors and real-time assessment of resection margins. In addition, proof-of-principle for image-guided resection of metastatic lesions using this dual-modality pretargeting approach was provided.

REFERENCES

- (1) Ravizzini G, Turkbey B, Kurdziel K, Choyke PL. New horizons in prostate cancer imaging. *Eur J Radiol.* 2009; 70(2):212-226
- (2) van Rij CM, Lütje S, Frielink C, Sharkey RM, Goldenberg DM, Franssen GM, et al. Pretargeted immuno-PET and radioimmunotherapy of prostate cancer with an anti-TROP-2 x anti-HSG bispecific antibody. *Eur J Nucl Med Mol Imaging.* 2013; 40(9):1377-1383
- (3) Basu A, Goldenberg DM, Stein R. The epithelial/carcinoma antigen EGP-1, recognized by monoclonal antibody RS7-3G11, is phosphorylated on serine 303. *Int J Cancer.* 1995; 62(4):472-479
- (4) Heidenreich A, Bellmunt J, Bolla M, et al. European Association of Urology. EAU guidelines on prostate cancer. Part 1: screening, diagnosis, and treatment of clinically localised disease. *Eur Urol.* 2011; 59:61-71
- (5) Keereweer S, Van Driel PB, Snoeks TJ, Kerrebijn JD, Baatenburg de Jong RJ, Vahrmeijer AL, et al. Optical image-guided cancer surgery: challenges and limitations. *Clin Cancer Res.* 2013; 19(14):3745-3754
- (6) Rossi EA, Goldenberg DM, Cardillo TM, McBride WJ, Sharkey RM, Chang CH. Stably tethered multifunctional structures of defined composition made by the dock and lock method for use in cancer targeting. *Proc Natl Acad Sci U S A.* 2006; 103(18):6841-6846
- (7) Brown JM. In vivo models of human prostate cancer bone metastasis. *Methods Mol Med.* 2003; 81:149-162
- (8) Lütje S, Rijpkema M, Franssen GM, Fracasso G, Helfrich W, Eek A, et al. Dual-modality image-guided surgery of prostate cancer with a radiolabeled fluorescent anti-PSMA monoclonal antibody. *J Nuc Med.* 2014; 55(6):995-1001
- (9) Chen Y, Dhara S, Banerjee SR, Byun Y, Pullambhatla M, Mease RC, et al. A low molecular weight PSMA-based fluorescent imaging agent for cancer. *Biochem Biophys Res Commun.* 2009; 390:624-629
- (10) Nakajima T, Mitsunaga M, Bander NH, Heston WD, Choyke PL, Kobayashi H. Targeted, activatable, in vivo fluorescence imaging of prostate-specific membrane antigen (PSMA) positive tumors using the quenched humanized J591 antibody-indocyanine green (ICG) conjugate. *Bioconjug Chem.* 2011; 22:1700-1705
- (11) Cohen R, Stammes MA, de Roos HC, Stigter-van Walsum M, Visser GWM, van Dongen GAMS. Inert Coupling of IRDye800CW to monoclonal antibodies for Clinical Imaging of Tumor Targets. *EJNMMI Research.* 2011, 1:31
- (12) Banerjee SR, Pullambhatla M, Byun Y, Nimmagadda S, Foss CA, Green G, et al. Sequential SPECT and optical imaging of experimental models of prostate cancer with a dual modality inhibitor of the prostate-specific membrane antigen. *Angew Chem Int Ed Engl.* 2011; 50:9167-9170

General Discussion

Summary

Samenvatting

Zusammenfassung

List of Publications

Curriculum Vitae

Epilogue

4

GENERAL DISCUSSION

GENERAL DISCUSSION

Prostate cancer is one of the most common causes for morbidity and mortality in men worldwide. One of the major reasons for the high mortality is the difficulty to detect prostate cancer in an early and potentially curable stage. The timely detection of prostate cancer requires reliable and highly sensitive imaging techniques. Currently, the most commonly used imaging technique for prostate cancer is transrectal ultrasound (TRUS), which is also used to perform image-guided biopsies. However, TRUS has only limited sensitivity and is unable to differentiate benign processes, such as benign prostatic hyperplasia (BPH), atrophy and inflammation, from malignant disease in the prostate gland. In case of negative biopsies, but persisting clinical suspicion for malignant involvement of the prostate, computed tomography (CT) and magnetic resonance imaging (MRI) may be applied [1]. While CT can be used for the detection of metastatic spread to lymph nodes, organs, and bones, MRI provides more accurate visualization of the prostate, which allows more reliable detection of malignant lesions. Currently, extensive research has been focused on magnetic resonance (MR)-guided biopsies to improve the sensitivity in the detection of cancer lesions compared to TRUS. Other innovative imaging techniques such as diffusion weighted MRI (DWI), MR spectroscopy (MRS), and dynamic contrast-enhanced MRI (DCE-MRI) allow functional assessment of the disease, which results in more precise staging and follow-up. With DWI, the restricted diffusion of water molecules in malignant tissue can be visualized. As prostate cancer usually has relatively tight glandular elements with increased cellular density and decreased extracellular space, high signal intensity foci on DWI can be obtained. However, differentiation between benign and malignant lesions remains challenging as benign lesions can show low water diffusion as well [2]. With DCE-MRI, tumor vascularization can be visualized by quantitative kinetic parameters that reflect blood flow and vascular permeability. However, visualization of small tumors in particular remains a challenge as angiogenesis might not be prominent in early stages. An advanced approach to detect malignant involvement of lymph nodes is high resolution MRI combined with lymphotropic superparamagnetic (ultra) small particles of iron oxide, (U)SPIO, which relies on visualization of macrophage activity. However, the clinical use of USPIO-MRI is limited by several disadvantages, in particular the limited sensitivity of USPIO-MRI in small lymph nodes (<5 mm) [3], but also by the requirement for specific expertise and its rather time consuming nature.

Positron Emission Tomography (PET) is another imaging technique that allows for visualization of cellular and molecular processes that are associated with biological features of tumors. The standard functional imaging agent for PET in oncology is ^{18}F -FDG, which visualizes the enhanced glucose demand of malignant cells. Unfortunately, ^{18}F -FDG based PET is not suitable for imaging of prostate cancer in early stages as a large fraction of prostate cancers show only a limited

¹⁸F-FDG uptake [4]. Another tracer for PET imaging is choline which can be labeled with ¹¹C or ¹⁸F. The use of choline relies on the fact that it is a key precursor in the biosynthesis of phosphatidylcholine, a major component of the cell membrane. Eschmann et al. [5] compared ¹¹C-choline PET/CT with conventional whole-body MRI and reported a better overall diagnostic performance with ¹¹C-choline PET/CT with a higher detection rate of lymph node metastases. However, ¹¹C- or ¹⁸F-choline PET/CT still has limited sensitivity and strongly depends on tumor configuration [6]. In addition, the specificity of this tracer in differentiation of prostate cancer tissue from benign pathologies is limited [7].

Therefore, other approaches need to be identified that are more suitable for the detection of prostate cancer lesions. Extensive research has focused on targeting prostate cancer with alternative radiolabeled metabolite tracers, receptor binding ligands, or antibodies against prostate cancer-associated cell surface antigens.

Several promising targets for prostate cancer imaging have been identified, such as the prostate stem cell antigen (PSCA) or the gastrin releasing peptide receptor (GRPR). One of the first radiolabeled bombesin analogs which target GRPR, Cu-64-DOTA-8-amino-octanoicacid-bombesin, was introduced by Rogers et al. [8]. In this study, specific tumor localization of ⁶⁴Cu-labeled bombesin in mice with PC-3 prostate cancer xenografts was demonstrated by microPET imaging and biodistribution studies. However, clinical implementation was prevented by the high uptake of ⁶⁴Cu-labeled bombesin in normal tissues. So far, several bombesin agonists such as PESIN or AMBA and antagonists such as Demobesin-1 have been developed for targeting GRPR-expressing prostate cancer [9].

Another promising target for prostate cancer imaging is the prostate specific membrane antigen (PSMA) which is of particular interest due to its selective overexpression in prostate cancer in nearly all stages of the disease. Initial validation of PSMA as an *in vivo* target came from imaging trials with the ¹¹¹In-labeled monoclonal antibody (mAb) capromab pendetide (7E11/CYT-356, ProstaScint®) [10], which is an FDA approved agent for diagnostic imaging in patients with biopsy-proven prostate cancer who are at high risk for pelvic lymph node metastases [11]. However, capromab pendetide appears to be a suboptimal imaging agent for prostate cancer, as it is directed against an epitope on the intracellular domain of PSMA [12]. It has been postulated that capromab pendetide may only bind to dying or necrotic cells with cellular membranes that are permeable to the antibody. Our results confirm that capromab pendetide indeed binds to the intracellular domain of PSMA. Recently, new anti-PSMA monoclonal antibodies have been generated that bind to an extracellular domain of PSMA, including the mAb D2B. Our results demonstrate that mAb D2B binds to viable tumor cells without the need for internalization. This indicates that clinical application of D2B for imaging of prostate cancer is feasible.

Previous studies indicated that tumor targeting can be further optimized by the use of antibody fragments instead of intact IgG antibodies [13, 14]. Intact antibodies clear relatively slowly from the circulation and usually reach maximum tumor uptake 3 - 7 days after injection. The slow accumulation of intact antibodies has been attributed to the presence of various physiological barriers between antibodies in the circulation and the tumor cell surface [15]. Antibody fragments such as F(ab')₂ and Fab fragments are cleared more rapidly from the circulation, which on the one hand leads to lower uptake in the tumor compared to intact IgG molecules. On the other hand, high tumor-to-background ratios can be reached, because antibody fragments diffuse more rapidly in the interstitial fluid compared to intact antibodies and clear more rapidly from the nontarget tissues. In this thesis, we have shown that these principles apply for imaging of PSMA-expressing prostate cancer. The use of ¹¹¹In-F(ab')₂ and ¹¹¹In-Fab fragments derived from of D2B IgG might be advantageous in settings where imaging is required early after injection. Intact D2B IgG in contrast has a higher absolute uptake in the tumor, which may be desirable in diagnostic settings where detection of small lesions depends on high absolute tumor uptake.

Recently, several PSMA-targeting peptides have been developed that might further improve prostate cancer imaging, as these small-sized peptides are cleared from the circulation even faster compared to antibody fragments. So far, several high-affinity small-molecule inhibitors of PSMA have been developed that might be suitable for prostate cancer imaging, such as ¹²³I-MIP-1072 or ¹²³I-MIP-1095, which were first tested in the clinic in 2008 [16]. Feasibility of these molecules to detect tumor lesions in soft-tissue, bone and the prostate gland as early as 1-4 h after injection was demonstrated in patients with metastatic prostate cancer [17]. More recently, PSMA ligands/inhibitors labeled with other radionuclides have been developed and are now tested for prostate cancer imaging. The feasibility of ^{99m}Tc-MIP-1404 to detect the disease is being evaluated in an international phase 2 study in men scheduled for prostatectomy using histopathology as the gold standard (ClinicalTrials.gov Identifier NCT01667536). Another candidate for prostate cancer imaging is the PSMA ligand Glu-NH-CO-NH-Lys-(Ahx)-[⁶⁸Ga(HBED-CC)]. First clinical results have shown excellent visualization of suspicious prostate cancer lesions with high overall detection rates [18]. One of the limitations of this technique however, is renal clearance which might conceal cancer lesions.

Another very promising approach to improve tumor-to-background ratios in prostate cancer radionuclide imaging is pretargeting using bispecific antibodies and corresponding radiolabeled peptides. The value of this pretargeting system has been shown previously for colon cancer [19]. In this thesis, it was demonstrated that the pretargeting strategy using the anti-TROP2 x anti-HSG bispecific antibody TF12 in combination with the ¹¹¹In-labeled peptide IMP288 is feasible for imaging

of prostate cancer, especially at time points early after injection. This makes this imaging approach particularly suitable for PET imaging with radionuclides that have a relatively short half-life, such as ^{18}F and ^{68}Ga .

In radionuclide imaging, the choice of the most suitable radionuclide is pivotal. For PET imaging, the most commonly used radionuclide is ^{18}F as it has ideal properties such as a low positron energy (635 keV), which provides optimal spatial resolution to PET images [20]. Moreover, cyclotron-produced ^{18}F is currently widely available. Another advantage of the use of ^{18}F is its favorable half-life of 109.8 minutes, which permits more complex and time-consuming synthetic manipulations and imaging studies. However, so far, the labeling procedure of most biomolecules with ^{18}F has been cumbersome and was restricted to heat-stable biomolecules as most labeling procedures require heating up to 100 °C. Recently, a two-step procedure to prepare ^{18}F -labeled heat-labile proteins using the [^{18}F]AIF method based on hot maleimide conjugation was introduced. In this thesis, the feasibility of this approach to label heat-sensitive anti-CEA Fab', (scFv)₂ (diabody) and Fab-AD2 fragments with ^{18}F and their ability to target CEA-expressing tumors is demonstrated.

While the timing of diagnosis of prostate cancer represents one of the major issues that determine prostate cancer mortality, the choice of appropriate treatment is essential, too. Currently, nerve sparing radical prostatectomy, involving the removal of the entire prostate gland, seminal vesicles and sufficient surrounding tissue to obtain negative resection margins is the surgical treatment strategy of choice for localized prostate cancer. However, positive surgical margins in radical prostatectomy tissue specimens obtained after surgical removal of localized prostate cancer, are reported in 10 – 48% of the cases [21]. While the role of positive surgical margins on prostate cancer-specific mortality remains controversial, positive surgical margins are recognized as a risk factor for prostate-specific antigen (PSA)-defined biochemical recurrence [22-24], which is associated with the need for secondary therapy and may have considerable impact on patient's quality of life.

To improve the achievement of negative resection margins, highly sensitive intra-operative imaging methods are needed to provide the surgeon with real-time visual information of resection margins. With the development of handheld gamma probes, antibody-based radionuclide imaging became available for intra-operative purposes. However, a major limitation of the use of gamma probes is the associated lack of visual information on the tumor location. In contrast, near-infrared fluorescence (NIRF) imaging does provide visual information on tumor lesions intra-operatively, albeit with rather limited tissue penetration. These limitations may be overcome in an approach where intra-operative radionuclide detection is combined with near-infrared fluorescence imaging. In such a dual-modality approach the acoustic signal produced by the gamma probe and detailed image information obtained from the fluorescent dye typically originate from the same tracer molecule and as such may

complement each other to improve intra-operative detection and resection of tumor tissue.

In this thesis, the feasibility of dual-modality imaging and image-guided surgery of prostate cancer was shown in two approaches, first using a dual-labeled antibody and second, using a dual-label peptide in TF12-pretargeted prostate cancer xenografts. We demonstrated that tumor-selective targeting was achieved with both approaches and provided proof-of-principle that these approaches might be used for image-guided surgery of prostate cancer.

So far, no targeted dual-modality imaging approaches have been introduced into the clinic, but the first clinical studies are looming. To translate the results described in this thesis to the clinic, several aspects have to be considered. In particular, the preparation of fluorescently labeled targeting agents needs to be standardized and validated [25]. Once these fluorescent agents are found to be safe, they can be conjugated to radiolabeled dual-label targeting agents according to GMP standards. Furthermore, the role of dual-label agents for image-guided surgery requires further evaluation in terms of detection sensitivity and specificity of small lesions and accurate tumor margin assessment. In addition, dual-modality image-guided surgery needs to be compared to bench mark histology for margin assessment and the added value of dual-modality NIRF and radionuclide imaging needs to be evaluated in greater detail. Moreover, it has to be determined whether or not dual-modality imaging approaches can be used in laparoscopic surgical procedures in which a laparoscope is equipped with an optical imaging system.

The aim of the studies described in this thesis was to investigate approaches to improve prostate cancer imaging. Our preclinical results suggest that prostate cancer imaging might be improved by the use of antibody fragments and pretargeting using bispecific antibodies and corresponding peptides. In addition, it was demonstrated that dual-modality radionuclide and near-infrared fluorescence imaging approaches can improve both tumor detection and image-guided surgery of prostate cancer. Using these novel sensitive and specific imaging techniques, prostate cancer may be detected more accurately and in earlier stages of the disease, which may help to select patients that are still eligible for curative treatment. These preclinical findings warrant clinical studies to further investigate the added value of dual-modality imaging approaches in prostate cancer patients. However, as these imaging strategies have their specific advantages and limitations, it should be carefully evaluated which strategy is optimal in particular cases. In this respect, the newly developed imaging methods for sensitive and accurate detection of prostate cancer are aligned seamlessly with the concept of personalized medicine.

REFERENCES

- (1) Heidenreich A, Bastian PJ, Bellmunt J, Bolla M4, Joniau S, van der Kwast T, Mason M, Matveev V, Wiegel T, Zattoni F, Mottet N. EAU Guidelines on Prostate Cancer. Part II: Treatment of Advanced, Relapsing, and Castration-Resistant Prostate Cancer. *Eur Urol.* 2014; 65(2):467-479
- (2) Turkbey B, Pinto PA, Choyke PL. Imaging techniques for prostate cancer: Implications for focal therapy. *Nat Rev Urol.* 2009; 6(4):191–203
- (3) Harisinghani MG, Barentsz J, Hahn PF, Deserno WM, Tabatabaei S, van de Kaa CH, de la Rosette J, Weissleder R. Noninvasive detection of clinically occult lymph-node metastases in prostate cancer. *N Engl J Med.* 2003; 349(10):1010
- (4) Jana S, Blafox MD. Nuclear medicine studies of the prostate, testes, and bladder. *Semin Nucl Med.* 2006; 36(1):51–72
- (5) Eschmann SM, Pfannenberger AC, Rieger A, Aschoff P, Müller M, Paulsen F, Anastasiadis A, Claussen CD, Bares R, Schlemmer HP. Comparison of ¹¹C-choline-PET/CT and whole body-MRI for staging of prostate cancer. *Nuklearmedizin.* 2007; 46(5):161–168
- (6) Souvatzoglou M, Weirich G, Schwarzenboeck S, Maurer T, Schuster T, Bundschuh RA, Eiber M, Herrmann K, Kuebler H, Wester HJ, Hoefler H, Gschwend J, Schwaiger M, Treiber U, Krause BJ. The sensitivity of [¹¹C]choline PET/CT to localize prostate cancer depends on the tumor configuration. *Clin Cancer Res.* 2011; 17(11):3751-3759
- (7) Schwarzenböck S, Souvatzoglou M, Krause BJ. Choline PET and PET/CT in Primary Diagnosis and Staging of Prostate Cancer. *Theranostics.* 2012; 2(3):318-330
- (8) Rogers BE, Bigott HM, McCarthy DW, Della Manna D, Kim J, Sharp TL, Welch MJ. MicroPET imaging of a gastrin-releasing peptide receptor-positive tumor in a mouse model of human prostate cancer using a ⁶⁴Cu-labeled bombesin analogue. *Bioconjug Chem.* 2003; 14(4):756–763
- (9) Schröder RP, Müller C, Reneman S, Melis ML, Breeman WA, de Blois E, Bangma CH, Krenning EP, van Weerden WM, de Jong M. A standardised study to compare prostate cancer targeting efficacy of five radiolabelled bombesin analogues. *Eur J Nucl Med Mol Imaging.* 2010; 37(7):1386–1396
- (10) Ross JS, Sheehan CE, Fisher HA, Kaufman RP, Jr, Kaur P, Gray K, Webb I, Gray GS, Mosher R, Kallakury BV. Correlation of primary tumor prostate-specific membrane antigen expression with disease recurrence in prostate cancer. *Clin Cancer Res.* 2003; 9(17):6357-6362
- (11) FDA CapromabPendetide Product Approval Information; <http://www.fda.gov/Drugs/DevelopmentApprovalProcess/HowDrugsareDevelopedandApproved/ApprovalApplications/TherapeuticBiologicApplications/ucm080734.htm>
- (12) Barren RJ 3rd, Holmes EH, Boynton AL, Misrock SL, Murphy GP. Monoclonal antibody 7E11.C5 staining of viable LNCaP cells. *Prostate.* 1997; 30(1):65-68
- (13) Heskamp S, van Laarhoven HW, Molkenboer-Kuenen JD, Bouwman WH, van der Graaf WT, Oyen WJ, Boerman OC. Optimization of IGF-1R SPECT/CT Imaging Using ¹¹¹In-Labeled F(ab')₂ and Fab Fragments of the Monoclonal Antibody R1507. *Mol Pharm.* 2012; 9(8):2314-2321

- (14) Fleuren ED, Versleijen-Jonkers YM, Heskamp S, Roeffen MH, Bouwman WH, Molkenboer-Kuening JD, van Laarhoven HW, Oyen WJ, Boerman OC, van der Graaf WT. The strength of small: improved targeting of insulin-like growth factor-1 receptor (IGF-1R) with F(ab')₂-R1507 fragments in Ewing sarcomas. *Eur J Cancer*. 2013; 49(13):2851-2858
- (15) Jain RK. Physiological Barriers to Delivery of Monoclonal Antibodies and Other Macromolecules in Tumors. *Cancer Res*. 1990; 50(3 Suppl):814s-819s
- (16) Eder M, Eisenhut M, Babich J, Haberkorn U. PSMA as a target for radiolabelled small molecules. *Eur J Nucl Med Mol Imaging*. 2013; 40(6): 819–823
- (17) Barrett JA, Coleman RE, Goldsmith SJ, Vallabhajosula S, Petry NA, Cho S, Armor T, Stubbs JB, Maresca KP, Stabin MG, Joyal JL, Eckelman WC, Babich JW. First-in-man evaluation of 2 high-affinity PSMA-avid small molecules for imaging prostate cancer. *J Nucl Med*. 2013; 54(3):380-387
- (18) Afshar-Oromieh A, Malcher A, Eder M, Eisenhut M, Linhart HG, Hadaschik BA, Holland-Letz T, Giesel FL, Kratochwil C, Haufe S, Haberkorn U, Zechmann CM. PET imaging with a [⁶⁸Ga]gallium-labelled PSMA ligand for the diagnosis of prostate cancer: biodistribution in humans and first evaluation of tumour lesions. *Eur J Nucl Med Mol Imaging*. 2013; 40(4):486-495
- (19) Schoffelen R, van der Graaf WT, Sharkey RM, Franssen GM, McBride WJ, Chang CH, Laverman P, Goldenberg DM, Oyen WJ, Boerman OC. Pretargeted immuno-PET of CEA-expressing intraperitoneal human colonic tumor xenografts: a new sensitive detection method. *EJNMMI Res*. 2012; 2:5
- (20) Visser EP, Disselhorst JA, Brom M, Laverman P, Gotthardt M, Oyen WJ, Boerman OC. Spatial resolution and sensitivity of the Inveon small-animal PET scanner. *J Nucl Med*. 2009; 50(1):139-147
- (21) Stephenson AJ, Eggener SE, Hernandez AV, Klein EA, Kattan MW, Wood DP Jr, Rabah DM, Eastham JA, Scardino PT. Do Margins Matter? The Influence of Positive Surgical Margins on Prostate Cancer-Specific Mortality. *Eur Urol*. 2014; 65(4):675-680
- (22) Rouanne M, Rode J, Campeggi A, Allory Y, Vordos D, Hoznek A, Abbou CC, La Taille AD, Salomon L. Long-term impact of positive surgical margins on biochemical recurrence after radical prostatectomy: Ten years of follow-up. *Scand J Urol*. 2014 Apr;48(2):131-137
- (23) Lee JW, Ryu JH, Kim YB, Yang SO, Lee JK, Jung TY. Do positive surgical margins predict biochemical recurrence in all patients without adjuvant therapy after radical prostatectomy? *Korean J Urol*. 2013; 54(8):510-515
- (24) Choo MS, Cho SY, Ko K, Jeong CW, Lee SB, Ku JH, Hong SK, Byun SS, Kwak C, Kim HH, Lee SE, Jeong H. Impact of positive surgical margins and their locations after radical prostatectomy: comparison of biochemical recurrence according to risk stratification and surgical modality. *World J Urol*. 2013 Dec 21. [Epub ahead of print]
- (25) Cohen R, Stammes MA, de Roos HC, Stigter-van Walsum M, Visser GWM, van Dongen GAMS. Inert Coupling of IRDye800CW to monoclonal antibodies for Clinical Imaging of Tumor Targets. *EJNMMI Research*. 2011, 1:31

SUMMARY

SUMMARY

The aim of the studies described in this thesis was to optimize antibody-based targeting strategies of prostate cancer and to develop dual-modality fluorescence and radionuclide-based imaging approaches to improve the detection and surgical resection of prostate cancer.

In **section 1** of this thesis, an introduction to prostate cancer is provided. In addition, the basic principles of radionuclide and fluorescence imaging are described together with the most commonly used imaging approaches.

In **section 2** of this thesis, several strategies for the optimization of antibody-based radionuclide imaging of cancer are described. First, in **chapter 2.1**, the currently used imaging techniques for prostate cancer are reviewed. At present, the most commonly used imaging technique for prostate cancer is transrectal ultrasound (TRUS) which can be used for imaging-guided biopsy. Major limitations of TRUS are limited sensitivity and the fact that differentiation between benign processes such as benign prostatic hyperplasia (BPH), atrophy, or inflammation in the prostate gland cannot be distinguished from malignant disease. Other techniques, such as computed tomography (CT) or magnetic resonance imaging (MRI) have higher sensitivity in the detection of lesions. However, differentiation between malignancies and benign disease processes remains challenging. To overcome this limitation, radionuclide imaging modalities such as positron emission tomography (PET) or single photon emission tomography (SPECT) are suitable imaging modalities as they can be used to image tumor-specific processes or antigens with various tracers such as radiolabeled metabolite tracers, androgen receptor binding ligands, gastrin-releasing peptide receptor binding ligands, choline, amino acids, or antibodies against prostate cancer-associated antigens.

An attractive target for antibody-based imaging of prostate cancer is the prostate-specific membrane antigen (PSMA). Due to its selective overexpression in prostate cancer, PSMA is an excellent target for imaging purposes. In **chapter 2.2**, the potential of the ^{111}In -labeled anti-PSMA monoclonal antibody D2B for targeting of PSMA-expressing prostate cancer was evaluated in mice with subcutaneous PSMA-expressing prostate cancer xenografts and compared to the targeting characteristics of ^{111}In -labeled F(ab')_2 and Fab fragments of this antibody. In addition, the tumor targeting characteristics of D2B IgG, which binds to an extracellular domain of PSMA were compared with those of the clinically approved antibody capromab pendetide, which is directed against an intracellular epitope.

It was demonstrated that all ^{111}In -labeled antibody formats specifically accumulate in the PSMA-expressing tumors. Highest uptake was observed for ^{111}In -

D2B IgG and ^{111}In -capromab pendetide at 168 h p.i. ($94.8 \pm 19.2\%$ ID/g and $16.7 \pm 2.2\%$ ID/g, respectively).

Uptake of ^{111}In -D2B F(ab')_2 and ^{111}In -Fab fragments peaked at 24 h p.i. ($12.1 \pm 3.0\%$ ID/g and $15.1 \pm 2.9\%$ ID/g, respectively). Maximum tumor-to-blood ratios were 13.0 ± 2.3 (168 h p.i.), 6.2 ± 0.7 (24 h p.i.), 23.0 ± 4.0 (24 h p.i.), and 4.5 ± 0.6 (168 h p.i.) for ^{111}In -D2B IgG, ^{111}In - F(ab')_2 , ^{111}In -Fab, and ^{111}In -capromab pendetide, respectively. The PSMA-expressing tumors were clearly visualized with microSPECT with all antibody formats.

Overall, the new monoclonal antibody D2B IgG had excellent *in vivo* tumor targeting characteristics. Due to renal accumulation of F(ab')_2 and Fab fragments visualization of malignant tissue located in the vicinity of the kidneys might be hampered. However, especially in settings where multiple images within a short time interval are required, ^{111}In -D2B F(ab')_2 and Fab fragments can be used.

In **chapter 2.3**, a pretargeting strategy was used to improve antibody-based imaging of prostate cancer. TF12 is a trivalent bispecific antibody which consists of two anti-TROP-2 Fab fragments and one anti-histaminesuccinyl-glycine (HSG) Fab fragment. TROP-2 is an antigen which is found in many epithelial cancers, including prostate cancer. As TF12 targets TROP-2, this bispecific antibody could be suitable for pretargeting of prostate cancer with the aim to reach high tumor-to-background ratios. In this chapter, the potential for pretargeted radioimmunodiagnosis and radioimmunotherapy with TF12 and the radiolabeled diHSG peptide IMP288 in mice with subcutaneous TROP-2-expressing prostate cancer xenografts was investigated. It was demonstrated that TF12 and ^{111}In - or ^{68}Ga -labeled IMP288 show high and fast accumulation in tumor tissue. One disadvantage of this pretargeting strategy might be the renal clearance of the diHSG peptide IMP288, as physiological uptake in the urinary tract might conceal pathological uptake in the lower abdomen. However, renal clearance of radiolabeled IMP288 is very efficient, which may enable the distinction between physiological and pathological uptake.

In addition, the feasibility of pretargeted radioimmunotherapy was investigated in mice with s.c. PC3 tumors. One treatment cycle with TF12 and ^{177}Lu -labeled IMP288 showed significant improvement of survival compared to treatment with ^{177}Lu -IMP288 alone (90 vs. 67 days, $p < 0.0001$), without renal or hematological toxicity. We concluded that TROP-2-expressing prostate cancer can be pretargeted efficiently with TF12, with very rapid uptake of the radiolabeled hapten-peptide, IMP288, sensitive immuno-PET, and effective therapy.

Chapter 2.4 describes the application of a new labeling method that allows ^{18}F radiofluorination to heat sensitive molecules such as antibody fragments with the AIF method. Previously, ^{18}F radiofluorination was restricted to heat-stable molecules since this method requires heating to $100\text{ }^\circ\text{C}$. Recently, a two-step procedure to prepare ^{18}F -labeled heat-labile proteins using the [^{18}F]AIF method combined with a hot maleimide conjugation was introduced. In this chapter, the two step method was

applied to label heat sensitive anti-CEA Fab', (scFv)₂ (diabody) and Fab-AD2 fragments. Subsequently, the tumor targeting characteristics of these ¹⁸F-fluorinated antibody derivatives were evaluated in mice with subcutaneous colorectal cancer xenografts.

Biodistribution studies revealed that all [¹⁸F]AIF-labeled antibody conjugates specifically accumulated in the CEA-expressing xenografts. At 4 h, tracer uptake in the CEA-expressing tumors reached $1.85 \pm 0.36\%$ ID/g, $2.10 \pm 0.46\%$ ID/g, and $4.61 \pm 0.67\%$ ID/g for [¹⁸F]AIF-hMN-14-Fab', [¹⁸F]AIF-hMN-14-Fab-AD2, and [¹⁸F]AIF-hMN-14-diabody, respectively. Tumor-to-muscle ratios were 15.5 ± 2.3 , 14.3 ± 3.9 , and 14.0 ± 5.3 for [¹⁸F]AIF-hMN-14-diabody, [¹⁸F]AIF-hMN-14-Fab' and [¹⁸F]AIF-hMN-14-Fab-AD2, respectively.

All antibody preparations showed high kidney retention. However, renal accumulation for the [¹⁸F]AIF-hMN-14-diabody format ($57.4 \pm 5.5\%$ ID/g) ($p < 0.01$) was significantly lower compared to that of [¹⁸F]AIF-hMN-14-Fab' and [¹⁸F]AIF-hMN-14-Fab-AD2. In addition, all ¹⁸F-fluorinated antibody derivatives showed high hepatic uptake. However liver uptake of [¹⁸F]AIF-hMN-14-Fab' ($4.36 \pm 0.57\%$ ID/g) and [¹⁸F]AIF-hMN-14-Fab-AD2 ($4.32 \pm 0.35\%$ ID/g) was significantly lower compared to that of the [¹⁸F]AIF-hMN-14-diabody format ($11.1 \pm 1.0\%$ ID/g) ($p < 0.05$).

CEA-expressing tumors were clearly visualized on microPET images with all ¹⁸F-labeled antibody derivatives. Overall, based on the *in vitro* and *in vivo* tumor targeting characteristics of [¹⁸F]AIF-fluorinated hMN-14-Fab', [¹⁸F]AIF-hMN-14-Fab-AD2, and [¹⁸F]AIF-hMN-14-diabody, all three ¹⁸F-labeled antibody formats are promising candidates for PET imaging of CEA-expressing colorectal cancer.

Section 3 of this thesis focuses on the development and characterization of dual-modality imaging approaches for prostate cancer. In addition, the feasibility of these techniques for image-guided surgery was evaluated. At present, surgery represents the treatment option of choice for various malignancies. For curative intentions, complete removal and the achievement of negative resection margins is pivotal.

In **chapter 3.1**, a comprehensive overview on recent preclinical advances in receptor-targeted radionuclide and near-infrared fluorescence (NIRF) dual-modality imaging of cancer is provided and their applicability for image-guided surgery in a clinical setting is described. Nuclear imaging can be performed prior to surgery and could provide information on the spread of the malignant manifestations. In addition it can aid the surgeon in localizing tumor lesions. However, the translation of pre-operatively acquired nuclear images to the surgical field may be challenging, particularly, when multiple small tumor nodules are present. With the development of gamma probes, intra-operative radio-guided surgery has become feasible. The impact of radio-guided surgery on the surgical management of cancer patients includes providing real-time information to the surgeon on the location and extent of disease. However, gamma probes cannot be used for accurate tumor delineation during surgery.

Intra-operative imaging using near-infrared fluorescence represents a suitable option for this purpose as it allows precise delineation of tumor margins during and following resection and could provide real-time visualization directly correlated to the surgical field. This technique however is restricted by limited penetration depth of light in biological tissue.

With the emergence of dual-modality imaging agents that are labeled with both a fluorescent dye and a radionuclide, these powerful imaging techniques that complement each other in the detection and surgical removal of cancer tissue are combined. So far, several preclinical studies have demonstrated the potential value of merging these imaging modalities. However, further studies are needed to evaluate sensitivity and specificity of this dual-modality approach. At present, first clinical studies are looming that aim to determine the value of NIR fluorescently labeled targeting molecules for diagnostic and therapeutic approaches. In **chapter 3.2** of this thesis, both radionuclide and NIRF imaging were combined by dual-labeling the anti-PSMA antibody D2B to ^{111}In and the NIR fluorophore IRDye800CW. In this chapter, the potential of dual-modality SPECT/CT and NIRF imaging of prostate cancer using ^{111}In -DTPA-D2B-IRDye800CW was evaluated in mice with subcutaneous and metastatic PSMA-expressing tumor lesions.

Biodistribution studies revealed specific accumulation of ^{111}In -DTPA-D2B-IRDye800CW in s.c. tumor lesions, reaching a tumor uptake level of 45.8 ± 8.0 %ID/g at 7 days after injection. While uptake in most other tissues remained low, the dual-labeled antibody showed enhanced hepatic uptake. This could be due to the increased lipophilicity of the fluorophore-conjugated antibody, which consequences in hepatic accumulation. To avoid this, mild substitution ratios of approximately 1 IRDye800CW per antibody molecule are recommended.

Both s.c. as well as intraperitoneal xenografts could be visualized specifically with both microSPECT/CT and NIRF imaging at 2 days after injection. In addition, the feasibility of image-guided resection of i.p. tumors was demonstrated in this model. Taken together, preclinical findings on the dual-modality targeting agent ^{111}In -DTPA-D2B-IRDye800CW for imaging of prostate cancer encourage clinical studies with targeted dual-label imaging probes for intra-operative guidance of prostate tumor resection, to achieve radical tumor resection.

Finally, **Chapter 3.3** describes a dual-modality imaging approach using a pretargeting system. In this study, the feasibility of a pretargeting system for intra-operative imaging of prostate cancer using an anti-TROP-2 x anti-HSG bispecific antibody (TF12), together with a newly developed dual-label diHSG peptide (RDC018) with a DOTA chelate for radiolabeling and a fluorophore (IRDye800CW) for optical imaging is evaluated.

The biodistribution of the dual-label diHSG peptide ^{111}In -RDC018 and the single-label peptide ^{111}In -IMP288 (control) showed specific accumulation in the TROP-2 expressing xenografts ($12.4 \pm 3.7\%$ ID/g at 2 h p.i. and $9.1 \pm 2.8\%$ ID/g at 2 h

p.i., respectively). While uptake in most other organs remained low, significant radiotracer uptake was observed in the kidneys, which probably is due to enhanced tubular reabsorption of this peptide as compared to IMP288.

MicroSPECT/CT and near-infrared fluorescence (NIRF) imaging showed specific uptake of the dual-label ^{111}In -RDC018 in both s.c. and metastatic bony and soft tissue TROP-2-expressing tumor lesions. In addition, proof-of-principle was provided for image-guided resection of TROP-2 expressing metastases using intra-operative NIRF imaging.

The studies described in this thesis have added to the knowledge of antibody-based PET and SPECT imaging of prostate cancer. In addition, development and preclinical application of two different dual-modality NIRF and radionuclide imaging approaches have led to proof-of-principle that image-guided surgery of prostate cancer is feasible using either a dual-label antibody or a pretargeting strategy with a dual-label peptide. These preclinical findings encourage future clinical studies to further elucidate the added value of dual-modality imaging in prostate cancer patients.

SAMENVATTING

SAMENVATTING

Het doel van de studies beschreven in dit proefschrift was het optimaliseren van antilichaam targeting strategieën van prostaatkanker. Daarnaast zijn gecombineerde fluorescentie/radionuclide imaging methoden ontwikkeld om de detectie en de resectie van prostaatkanker te verbeteren.

In **sectie 1** van dit proefschrift worden de basisprincipes van radionuclide en fluorescentie imaging beschreven.

Sectie 2 van dit proefschrift richt zich op de optimalisatie van radioimmunoimaging van kanker. **Hoofdstuk 2.1** geeft een overzicht van de beschikbare imaging methoden voor prostaatkanker. De meest gebruikte imaging techniek voor prostaatkanker op dit moment is transrectal ultrasound (TRUS), dat ook gebruikt kan worden voor echogeleide biopsie. Het gebruik van TRUS wordt echter beperkt door de relatief lage sensitiviteit en het feit dat differentiatie tussen benigne veranderingen zoals benigne prostaathyperplasie (BPH), atrofie of ontstekingen in de prostaat en maligniteiten van de prostaat moeilijk is. Andere technieken zoals computed tomography (CT) of magnetic resonance imaging (MRI) hebben een hogere sensitiviteit voor de detectie van tumor laesies. Echter, de differentiatie tussen maligne en benigne aandoeningen met MRI blijft moeilijk. Radionuclide imaging technieken zoals positron emission tomography (PET) of single photon emission tomography (SPECT) kunnen bijdragen tot een betere diagnose van prostaatkanker, omdat met behulp van deze technieken tumor-specifieke processen in beeld kunnen worden gebracht. Voor detectie van prostaatkanker met radionuclide imaging kunnen verschillende tracers worden gebruikt, zoals radioactief gelabelde liganden van GRPR (gastrin releasing peptide receptor), androgeen receptor bindende liganden, choline, aminozuren of antilichamen gericht tegen prostaatkanker geassocieerde antigenen.

Een veelbelovend target voor antilichaam-gebaseerd imaging van prostaatkanker is het prostate-specific membrane antigen (PSMA). De selectieve overexpressie van PSMA in prostaatkanker maakt dit eiwit een zeer geschikt target voor imaging doeleinden. In **hoofdstuk 2.2** van dit proefschrift wordt de mogelijkheid onderzocht om PSMA-expresserende prostaattumoren in beeld te brengen met behulp van het ¹¹¹In-gelabeld anti-PSMA antilichaam D2B in muizen met subcutane prostaatkanker xenograften. De tumor targeting eigenschappen van D2B IgG werden vergeleken met die van ¹¹¹In-gelabelde F(ab')₂ en Fab fragmenten van dit antilichaam. Bovendien werden de targeting karakteristieken van D2B IgG, dat gericht is tegen een epitoom op het extracellulaire domein van PSMA, vergeleken met de eigenschappen van het klinisch gebruikte antilichaam capromab pendetide, dat gericht is tegen een intracellulair epitoom. Alle ¹¹¹In-gelabelde antilichaam vormen accumuleerden

specifiek in de PSMA-expresserende tumoren. De hoogste tumor opname werd gevonden met ^{111}In -D2B en ^{111}In -capromab pendetide (respectievelijk $94.8 \pm 19.2\%$ ID/g en $16.7 \pm 2.2\%$ ID/g, 7 dagen na injectie). De opname van ^{111}In -D2B $\text{F}(\text{ab}')_2$ en ^{111}In -Fab fragmenten in de tumor was het hoogst 24 h na injectie (respectievelijk $12.1 \pm 3.0\%$ ID/g en $15.1 \pm 2.9\%$ ID/g). De tumor/bloed opname ratio's waren 13.0 ± 2.3 (168 h p.i.), 6.2 ± 0.7 (24 h p.i.), 23.0 ± 4.0 (24 h p.i.) en 4.5 ± 0.6 (168 h p.i.), respectievelijk voor ^{111}In -D2B IgG, ^{111}In - $\text{F}(\text{ab}')_2$, ^{111}In -Fab, en ^{111}In -capromab pendetide. De PSMA-expresserende tumoren konden duidelijk worden afgebeeld met microSPECT met alle antilichaam formaten. Overall heeft het nieuwe monoclonale antilichaam D2B zeer goede *in vivo* tumor targeting eigenschappen. Als gevolg van hoge opname van $\text{F}(\text{ab}')_2$ en Fab fragmenten in de nieren kunnen maligne laesies in (de buurt van) de nieren moeilijk zichtbaar gemaakt worden. Echter, in gevallen waar meerdere images binnen korte tijd gemaakt moeten worden, kunnen ^{111}In -D2B $\text{F}(\text{ab}')_2$ en Fab fragmenten juist uitstekend worden toegepast.

In **hoofdstuk 2.3** werd een pretargeting strategie getest voor het afbeelden van prostaatkanker. TF12 is een trivalent bispecifiek antilichaam dat bestaat uit twee anti-TROP-2 Fab fragmenten en één anti-histaminesuccinylglycine (HSG) Fab fragment. TROP-2 is een antigeen dat tot expressie komt op verschillende carcinomen, waaronder prostaatkanker. Aangezien TF12 gericht is tegen TROP-2, zou dit bispecifiek antilichaam geschikt kunnen zijn voor pretargeting van prostaatkanker, met het doel om een hoge opname in de tumor te bereiken en tegelijkertijd een snelle klaring uit normale weefsels en bloed. In dit hoofdstuk werd de potentie van pretargeted radioimmunoimaging en radioimmunotherapie met TF12 en het radioactief gelabelde diHSG peptide IMP288 onderzocht in muizen met subcutane TROP-2-expresserende prostaat tumoren. Er werd aangetoond dat TF12 en ^{111}In - of ^{68}Ga -gelabeld IMP288 snel en efficiënt in de tumor accumuleerden. Een nadeel van deze pretargeting strategie zou de renale klaring van het diHSG peptide IMP288 kunnen zijn, omdat fysiologische opname in de urinewegen de detectie van laesies in het abdomen zou kunnen bemoeilijken. De klaring van radioactief gelabeld IMP288 verloopt echter zeer snel en compleet, wat uiteindelijk de differentiatie tussen fysiologische en pathologische opname toch mogelijk zou kunnen maken.

Verder werd in dit hoofdstuk de mogelijkheid van pretargeted radioimmunotherapie onderzocht in muizen met s.c. PC3 tumoren. Eén behandelingscyclus met TF12 en ^{177}Lu -gelabeld IMP288 liet een significante verbetering van de overleving zien. De studie liet zien dat de pretargeting strategie met TF12 bij TROP-2 expresserende prostaatkanker effectief kan zijn, met snelle opname van het radioactief gelabelde IMP288 in de tumor.

Hoofdstuk 2.4 beschrijft de toepassing van een nieuwe labelingsmethode van hitte-sensitieve moleculen (bv. antilichaam fragmenten) met F-18, gebruik makend van de

AIF technologie. Tot voor kort kon ^{18}F -fluoridering alleen worden toegepast op hitte-stabiele moleculen, omdat de labeling werd uitgevoerd bij $100\text{ }^{\circ}\text{C}$. Recentelijk werd een twee-staps procedure ontwikkeld om hitte-labele eiwitten te kunnen labelen met ^{18}F . In dit hoofdstuk werd deze methode toegepast om anti-CEA Fab', (scFv)₂ (diabody) en Fab-AD2 fragmenten te labelen met ^{18}F . De tumor targeting eigenschappen van deze ^{18}F -gelabelde antilichaam fragmenten werden bepaald in muizen met subcutane tumoren.

De biodistributiestudies lieten zien dat alle [^{18}F]AIF-gelabelde antilichaam fragmenten specifiek accumuleerden in CEA-expresserende tumoren. Na 4 h was de concentratie in de CEA-expresserende tumoren $1.85 \pm 0.36\%$ ID/g, $2.10 \pm 0.46\%$ ID/g en $4.61 \pm 0.67\%$ ID/g van respectievelijk [^{18}F]AIF-hMN-14-Fab', [^{18}F]AIF-hMN-14-Fab-AD2 en [^{18}F]AIF-hMN-14-diabody. Alle F-18-gelabelde antilichaam vormen vertoonden hoge opname in de nieren. Echter, de opname in de nieren van het [^{18}F]AIF-hMN-14-diabody ($57.4 \pm 5.5\%$ ID/g) was significant lager dan dat van [^{18}F]AIF-hMN-14-Fab' en [^{18}F]AIF-hMN-14-Fab-AD2 ($p < 0.01$). Bovendien vertoonden alle ^{18}F -gelabelde antilichaam vormen relatief hoge opname in de lever. Echter, de lever opname van [^{18}F]AIF-hMN-14-Fab' ($4.36 \pm 0.57\%$ ID/g) en [^{18}F]AIF-hMN-14-Fab-AD2 ($4.32 \pm 0.35\%$ ID/g) was significant lager dan die van het [^{18}F]AIF-hMN-14-diabody ($11.1 \pm 1.0\%$ ID/g) ($p < 0.05$). De CEA-expresserende tumoren worden duidelijk afgebeeld met microPET met alle ^{18}F -gelabelde antilichaam vormen. Op basis van de *in vitro* en *in vivo* tumor targeting eigenschappen van [^{18}F]AIF-gelabelde hMN-14-Fab', [^{18}F]AIF-hMN-14-Fab-AD2 en [^{18}F]AIF-hMN-14-diabody kon worden geconcludeerd dat deze drie ^{18}F -gelabelde antilichaam formaten gebruikt kunnen worden voor PET imaging van tumoren die CEA expresseren, zoals bijvoorbeeld dikkedarmkanker.

In **Sectie 3** van dit proefschrift wordt de ontwikkeling en karakterisering van dual-modality imaging methoden voor prostaatkanker beschreven. Operatieve verwijdering van tumor laesies is voor diverse vormen van kanker de belangrijkste vorm van behandeling. Om volledige genezing te bereiken is complete verwijdering van de tumor essentieel. In **hoofdstuk 3.1** wordt een overzicht van de meest recente ontwikkelingen op het gebied van receptor-targeted radionuclide en near-infrared fluorescentie (NIRF) dual-modality imaging van kanker gegeven. Intra-operatieve dual modality imaging zou de volledige verwijdering van tumoren kunnen verbeteren. Met de ontwikkeling van gamma probes werd intra-operatieve radiodetectie-geleide resectie van tumoren mogelijk. Hierdoor kan een chirurg tumorlaesies tijdens de operatie beter opsporen. Echter, de gamma probes is niet geschikt voor het detecteren van tumorcellen in de snijranden. Intra-operatieve beeldvorming met near-infrared fluorescentie daarentegen is hiervoor mogelijk wel geschikt. Een nadeel van deze techniek is echter dat de penetratie van licht in weefsel zeer beperkt is (1-2 mm).

Met dual-modality imaging technieken die gebruik maken van tracers die gelabeld zijn met zowel een fluorescerende stof als met een radionuclide worden de

sterke eigenschappen van beide imaging technieken gecombineerd. In de afgelopen jaren hebben diverse studies in muizenmodellen de waarde van de combinatie van deze beide technieken laten zien.

In **hoofdstuk 3.2** van dit proefschrift werd radionuclide imaging en NIRF imaging gecombineerd door het anti-PSMA antilichaam D2B te labelen met ^{111}In en de fluorescerende stof IRDye800CW. In dit hoofdstuk werd de mogelijkheid van dual-modality SPECT/CT and NIRF imaging van prostaatkanker bestudeerd in muizen met PSMA-expresserende tumoren. Biodistributie studies van ^{111}In -DTPA-D2B-IRDye800CW in muizen lieten zien dat ^{111}In -DTPA-D2B-IRDye800CW specifiek accumuleerde in subcutane tumoren ($45.8 \pm 8.0\%$ ID/g, 7 dagen na injectie). Het dubbelgelabelde antilichaam toonde ook een verhoogde opname in de lever. Dit zou het gevolg kunnen zijn van de verhoogde lipofiliciteit van de antilichamen die geconjugeerd zijn met het IRDye800CW.

De tumoren konden zichtbaar gemaakt worden met microSPECT/CT en NIRF imaging 2 dagen na injectie van de tracer. De ^{111}In -DTPA-D2B-IRDye800CW tracer zou gebruikt kunnen worden voor de intra-operatieve detectie van prostaatkanker lesies.

In **hoofdstuk 3.3** wordt een dual-modality imaging techniek beschreven waarin gebruikt gemaakt wordt van een pretargeting strategie. In deze studie werd intra-operatieve beeldvorming van prostaatkanker met het anti-TROP-2 x anti-HSG bispecifieke antilichaam (TF12), in combinatie met het nieuwe dual-label diHSG peptide (RDC018) onderzocht.

In de biodistributie van het dual-label diHSG peptide ^{111}In -RDC018 en het single label peptide ^{111}In -IMP288 (controle) accumuleerden beiden specifiek in de TROP-2-expresserende tumoren (respectievelijk $12.4 \pm 3.7\%$ ID/g, 2 h p.i. en $9.1 \pm 2.8\%$ ID/g, 2 h p.i.). De concentratie van RDC018 in de nieren was significant hoger dan dat van IMP288. MicroSPECT/CT en NIRF imaging lieten specifieke opname van het dual-label ^{111}In -RDC018 in de TROP-2 expresserende tumoren in muizen zien. In deze studie werd proof-of-principle geleverd voor beeldgeleide resectie van TROP-2 expresserende tumor laesies met behulp van intra-operatieve NIRF imaging.

De studies beschreven in dit proefschrift hebben bijgedragen aan de kennis over radioimmunodetectie van prostaatkanker met PET en SPECT. Bovendien werden twee dual-modality imaging methoden voor prostaatkanker getest in muizenmodellen en werd getoond dat deze methoden mogelijk gebruikt kunnen worden voor beeldgeleide resectie van tumor laesies.

ZUSAMMENFASSUNG

ZUSAMMENFASSUNG

Ziel der in dieser Dissertation beschriebenen Studien ist die Optimierung von Antikörper-basierten Targeting Strategien für Malignome der Prostata und die Entwicklung von kombinierten Fluoreszenz und Radionuklid-basierten Methoden um die Detektion von Prostata Krebs zu verbessern.

In **Sektion 1** dieser Dissertation wurden die Basisprinzipien von Radionuklid und Fluoreszenz Imaging am Beispiel von Prostata Krebs beschrieben.

In **Sektion 2** wurden Strategien für die Optimierung von Antikörper-basiertem Radionuklidimaging von Prostatakarcinomen evaluiert. Zunächst wurden die derzeit gängigsten bildgebenden Techniken für Karzinome der Prostata beschrieben (**Kapitel 2.1**). Die derzeit am häufigsten verwendete Bildgebungsmethode bei Prostata Krebs ist der transrektale Ultraschall (TRUS) der Prostata, welcher auch zur bildgeleiteten Biopsie genutzt werden kann. Wesentliche Einschränkungen von TRUS sind begrenzte Sensitivität sowie die Tatsache, dass nur unzureichend zwischen gutartigen Prozessen der Prostata, wie benigner Prostatahyperplasie (BPH), Atrophie oder Entzündungen und Malignitäten unterschieden werden kann. Andere bildgebende Techniken wie Computertomographie (CT) oder Magnetresonanztomographie (MRT) weisen eine höhere Sensitivität im Nachweis von Tumorfäsonen auf. Jedoch ist der Wert dieser Techniken in der Differenzierung zwischen benignen und malignen Krankheitsprozessen verbesserungswürdig. Mithilfe von Radionuklid Imaging Modalitäten wie Positronen Emissions Tomographie (PET) oder Single Photon Emission Computed Tomography (SPECT) kann die Differenzierung zwischen benignen und malignen Läsionen erheblich verbessert werden, da sie zur Visualisierung von tumorspezifischen Prozessen oder Antigenen genutzt werden können.

Ein attraktives Target für Imaging von tumorspezifischen Antigenen, die assoziiert sind mit Prostata Krebs, ist das prostate-specific membrane Antigen (PSMA). Durch seine selektive Überexpression in Karzinomen der Prostata stellt PSMA ein exzellentes Target für Imaging Zwecke dar. In **Kapitel 2.2** wurde das Potential vom ^{111}In -gelabelten anti-PSMA monoklonalen Antikörper D2B evaluiert hinsichtlich dessen Fähigkeit spezifisch an PSMA-exprimierende Tumore der Prostata zu binden. Dies wurde in BALB/c Nacktmäusen mit subkutanen PSMA-exprimierenden Prostata Krebs Xenotransplantaten untersucht. Desweiteren wurden diese Eigenschaften verglichen mit den Targeting Eigenschaften von ^{111}In -gelabelten F(ab')_2 und Fab Fragmenten dieses Antikörpers. Da D2B IgG an ein extrazelluläres Epitop von PSMA bindet, wurden außerdem dessen Targeting Eigenschaften verglichen mit denen vom klinisch zugelassenen Antikörper Carpomab Pendetide, der gegen ein intrazelluläres Epitop gerichtet ist.

Es wurde gezeigt, dass alle ^{111}In -markierten Antikörperformate spezifisch im PSMA-exprimierenden Tumorgewebe akkumulierten. Die höchste Tracer Aufnahme im Tumor wurde für ^{111}In -D2B und ^{111}In -Carpomab Pendetide 168 h p.i. beobachtet, wohingegen die höchste Aufnahme von ^{111}In -D2B F(ab')_2 und ^{111}In -Fab Fragmenten nach 24 h erreicht wurde ($12.1 \pm 3.0\%$ ID/g und $15.1 \pm 2.9\%$ ID/g). Die maximalen Tumor-zu-Blut Verhältnisse waren 13.0 ± 2.3 (168 h p.i.), 6.2 ± 0.7 (24 h p.i.), 23.0 ± 4.0 (24 h p.i.), und 4.5 ± 0.6 (168 h p.i.) für ^{111}In -D2B IgG, ^{111}In - F(ab')_2 , ^{111}In -Fab, und ^{111}In -Capromab Pendetide. Desweiteren konnten die PSMA-expressierenden Tumore mithilfe aller Antikörperformate mit SPECT/CT deutlich visualisiert werden. Zusammenfassend wurde gezeigt, dass der monoklonale Antikörper D2B über exzellente *in vivo* Tumor Targeting Charakteristiken verfügt. Als Folge renaler Akkumulation der F(ab')_2 und Fab Fragmente kann die Bildgebung von malignem Gewebe, das sich in räumlicher Nähe zu den Nieren befindet, behindert werden. Dennoch sind ^{111}In -D2B F(ab')_2 und Fab Fragmente für Zwecke der Bildgebung geeignet, vor allem wenn die Untersuchung mehrfach in kurzen Zeitabständen wiederholt werden soll.

In **Kapitel 2.3** wurde eine Pretargeting Strategie zur Verbesserung von antikörperbasiertem Imaging von Prostata Krebs angewandt. TF12 ist ein trivalenter bispezifischer Antikörper bestehend aus zwei anti-TROP-2 Fab Fragmenten und einem anti-histaminesuccinyl-glycine (HSG) Fab Fragment. Das Antigen TROP-2 kommt in verschiedenen Malignomen zur Expression, worunter auch Karzinome der Prostata. Da TF12 gegen TROP-2 gerichtet ist, stellt dieser bispezifische Antikörper ein geeignetes Target für Pretargeting von Karzinomen der Prostata dar. In diesem Kapitel wurde das Potential der Pretargeted Radioimmunbildgebung mit TF12 und dem radioaktiv markierten diHSG Hapten-Peptid IMP288 in Mäusen mit subkutanen TROP-2-expressierenden Prostata Karzinomen untersucht. Sowohl ^{111}In als auch ^{68}Ga gelabeltes IMP288 akkumulierte spezifisch und schnell im Tumor Gewebe. Ein potentieller Nachteil dieser Pretargeting Strategie könnte allerdings die renale Ausscheidung vom diHSG Peptid IMP288 darstellen, da dessen physiologische Aufnahme in den Harnwegen eine pathologische Akkumulation im unteren Abdomen verdecken könnte. Da die renale Ausscheidung des radioaktiv markierten IMP288 jedoch sehr effektiv verläuft, könnte die Abgrenzung von physiologischem und pathologischen Uptake dennoch möglich sein. Desweiteren wurde in diesem Kapitel die Durchführbarkeit und Eignung von pretargeted Radioimmuntherapie in Mäusen mit subkutanen PC3 Tumoren evaluiert. Ein Behandlungszyklus mit TF12 und ^{177}Lu -gelabeltem IMP288 zeigte eine signifikante Verbesserung des Überlebens im Vergleich zur Behandlung mit ^{177}Lu -IMP288 ohne Gabe von TF12 (90 vs. 67 Tage, $p < 0.0001$). Darüberhinaus wurden weder renale noch hämatologische Toxizität beobachtet. Hieraus folgt, dass effizientes Pretargeting von TROP-2-expressierenden Prostata Karzinomen möglich ist bei schnellem Uptake des radioaktiv

gelabelten Hapten-Petides IMP288. Darüberhinaus könnte dieses Peptid zusammen mit TF12 eine effektive therapeutische Variante darstellen.

In **Kapitel 2.4** wurde die Anwendung von einer neuen Markierungsmethode beschrieben, welche die Radiofluorinierung von hitzesensitiven Molekülen wie Antikörper Fragmenten mit AIF ermöglicht. Bisher war die ^{18}F Radiofluorinierung auf hitzestabile Moleküle beschränkt, da für diese Labelingprozedur eine Erhitzung auf $100\text{ }^\circ\text{C}$ erforderlich war. Vor kurzem allerdings wurde eine Zwei-Schritt Methode zur ^{18}F Markierung entwickelt die auch für hitzelabile Moleküle geeignet ist und welche die ^{18}F AIF Methode mit einer heißen Maleimid Konjugation kombiniert. In diesem Kapitel wurde diese Zwei-Schritt Methode angewandt um hitzesensitive anti-CEA Fab', (scFv)₂ (diabody) und Fab-AD2 Fragmente zu mit ^{18}F zu markieren. Anschließend wurden die Tumor Targeting Eigenschaften von diesen ^{18}F -fluorinierten Antikörper Formaten in Mäusen mit subkutanen Xenotransplantaten einer kolorektalkarzinom-Zelllinie evaluiert.

Die Studien zur Biodistribution zeigten, dass alle ^{18}F AIF-gelabelten Antikörper Konjugate in spezifischer Weise an die CEA-expressierenden Xenotransplantate akkumulierten. Nach 4 h wurden Tracermengen in den CEA-expressierenden Tumoren von $1.85 \pm 0.36\%$ ID/g, $2.10 \pm 0.46\%$ ID/g, und $4.61 \pm 0.67\%$ ID/g für ^{18}F AIF-hMN-14-Fab', ^{18}F AIF-hMN-14-Fab-AD2, und ^{18}F AIF-hMN-14-diabody erreicht. Die Tumor-zu-Muskel Ratios waren 15.5 ± 2.3 , 14.3 ± 3.9 , und 14.0 ± 5.3 für ^{18}F AIF-hMN-14-diabody, ^{18}F AIF-hMN-14-Fab', beziehungsweise ^{18}F AIF-hMN-14-Fab-AD2.

Alle Antikörper Fragmente zeigten hohe Aufnahme in den Nieren. Jedoch war die renale Aufnahme für das ^{18}F AIF-hMN-14-diabody Format ($57.4 \pm 5.5\%$ ID/g) ($p < 0.01$) signifikant niedriger verglichen mit dem von den ^{18}F AIF-hMN-14-Fab' und ^{18}F AIF-hMN-14-Fab-AD2 Fragmenten. Darüberhinaus zeigten alle ^{18}F -fluorinierten Antikörper Derivate eine hohe Aufnahme in der Leber. Verglichen mit dem ^{18}F AIF-hMN-14-diabody Format ($11.1 \pm 1.0\%$ ID/g) zeigten jedoch sowohl ^{18}F AIF-hMN-14-Fab' ($4.36 \pm 0.57\%$ ID/g) als auch ^{18}F AIF-hMN-14-Fab-AD2 ($4.32 \pm 0.35\%$ ID/g) signifikant niedrigeren Uptake ($p < 0.05$).

Die CEA-exprimierenden Tumore konnten mit microPET mit allen ^{18}F -gelabelten Antikörper Derivaten deutlich visualisiert werden. Basierend auf den *in vitro* und *in vivo* Tumor Targeting Charakteristiken von ^{18}F AIF-fluoriertem hMN-14-Fab', ^{18}F AIF-hMN-14-Fab-AD2 und ^{18}F AIF-hMN-14-diabody wurde gezeigt, dass alle drei ^{18}F -gelabelten Antikörper Formate vielversprechende Kandidaten für PET Imaging von CEA-exprimierenden kolorektalen Karzinomen sind.

In **Sektion 3** dieser Dissertation wurde die Entwicklung und Charakterisierung von dualen Bildgebungsverfahren für Prostata Krebs behandelt. Zusätzlich wurde die Anwendbarkeit dieser Techniken für bildgeleitete Chirurgie bestimmt. Gegenwärtig repräsentiert die chirurgische Behandlung die Behandlungsoption der Wahl für

zahlreiche Malignitäten. Insbesondere bei kurativem Ansatz sind die komplette Entfernung jeglichen Tumorgewebes sowie das Erzielen negativer Resektionsgrenzen ausschlaggebend für den Therapieerfolg.

In **Kapitel 3.1** wurde eine Übersicht über die neuesten präklinischen Fortschritte in dualer, Rezeptor-targeted Radionuklid und near-infrared Fluoreszenz (NIRF) Bildgebung von Malignomen erstellt und deren Wert zur Verbesserung bildgestützter Chirurgie im klinischen Alltag bestimmt. Während Radionuklidimaging präoperativ durchgeführt werden und Informationen zum Ausbreitungsgrad der Krankheit liefern könnte, stellt sich die Übertragung von präoperativ aufgenommenen Szintigraphien auf das Operationsgebiet als Herausforderung dar, insbesondere bei multiplen kleinen Tumorkläsionen. Mit der Entwicklung von Gamma Sonden allerdings wurde die intraoperative radiogeleitete Chirurgie verfügbar, welche die Identifizierung von Tumorkläsionen in Echtzeit während der Operation ermöglicht. Gamma Sonden eignen sich allerdings nicht für eine akkurate Abgrenzung von Tumorgewebe. Desweiteren beruht die Nutzung von Gamma Sonden vor allem auf akustischen Signalen. Bildgebung im eigentlichen Sinne ist darum nicht gegeben. Für akkurate Abgrenzung von Tumorgewebe könnten intraoperative Bildgebungsverfahren die NIRF Imaging nutzen eine geeignetere Variante darstellen, da das operative Feld mithilfe dieser Technik visuell auf die Anwesenheit von Tumorgewebe überprüft werden könnte. Die Anwendung dieser Technik wird jedoch durch die eingeschränkte Penetrationstiefe von Licht in biologischem Gewebe limitiert.

Mit der Entwicklung von Molekülen, die mit sowohl einem fluoreszierenden als auch mit einem radioaktiven Stoff markiert werden können, ist es möglich Radionuklid und NIRF Imaging zu kombinieren und von den Vorteilen beider Techniken zu profitieren. Bisher konnte der potentielle Wert dieser Verbindung in ersten präklinischen Studien angezeigt werden. Gegenwärtig laufen erste klinische Studien an, die darauf zielen den Wert von fluoreszent markierten spezifischen Molekülen für diagnostische und therapeutische Zwecke einzuschätzen.

In **Kapitel 3.2** dieser Dissertation wurden Radionuklid und NIRF Imaging kombiniert durch Doppelmarkierung des anti-PSMA Antikörpers D2B mit sowohl ^{111}In als auch dem Fluorophor IRDye800CW. In dieser Studie wurde das Potential von dualer Bildgebung mit SPECT/CT und NIRF Imaging für Prostata Krebs mithilfe von ^{111}In -DTPA-D2B-IRDye800CW in Mäusen mit subkutanen und intraperitonealen PSMA-exprimierenden Tumorkläsionen charakterisiert. Studien zur Biodistribution zeigen spezifische Akkumulation von ^{111}In -DTPA-D2B-IRDye800CW in subkutanen Tumorkläsionen (Uptake: $45.8 \pm 8.0\%$ ID/g 168 h p.i.). Während der Tumor Uptake in den meisten Organen und Geweben niedrig blieb, verzeichnete der dual-gelabelte Antikörper erhöhten Leber Uptake. Dies könnte eine Folge der Lipophilie des fluoreszent markierten Antikörpers sein, die zu Akkumulation des Tracers in der Leber

führt. Um dies weitestgehend zu vermeiden wird ein niedriges Substitutionsverhältnis von ungefähr einem IRDye800CW per Antikörpermolekül empfohlen.

Sowohl die subkutanen als auch die intraperitonealen Xenotransplantate konnten in spezifischer Weise mit microSPECT/CT und NIRF Imaging visualisiert werden (2 d p.i.). Desweiteren wurde die Anwendbarkeit dieses doppelmarkierten Targeting Konstrukts für bildgestützte Chirurgie von intraperitonealen Tumoren evaluiert. Aus diesen präklinischen Ergebnissen ist zu schließen, dass sich dieser doppelmarkierte Antikörper für intraoperative Bildgebung und bildgeleitete Resektion von Prostata Karzinomen eignet.

Abschließend wurde in **Kapitel 3.3** ein Ansatz für duale Bildgebung beschrieben, für den ein Pretargeting System genutzt wurde. In dieser Studie wurde die Eignung der in **Kapitel 2.3** beschriebenen Pretargeting Strategie für intraoperatives Imaging von Prostata Karzinomen die den anti-TROP-2 x anti-HSG bispezifischen Antikörper TF12 nutzt. In diesem Kapitel wurde zusätzlich ein neu entwickeltes dual-label diHSG Hapten-Peptid (RDC018) genutzt, welches ein DOTA Chelat zur Radiolabeling und ein Fluorophor (IRDye800CW) besitzt für NIRF Imaging.

Die Bioverteilung des doppelt markierten Peptids ^{111}In -RDC018 und des einfach markierten Peptids ^{111}In -IMP288 (Kontrolle) zeigte spezifische Akkumulation in den TF12-vorakkumulierten (pretargeted) TROP-2-expressierenden Tumorkläsionen ($12.4 \pm 3.7\%$ ID/g bei 2 h p.i. und $9.1 \pm 2.8\%$ ID/g bei 2 h p.i.). Während die Traceraufnahme in den meisten Organen niedrig bleibt, wurde signifikante Akkumulation in den Nieren beobachtet, was wahrscheinlich eine Folge erhöhter tubulärer Reabsorption des Peptids ist im Vergleich mit IMP288.

MicroSPECT/CT und NIRF Imaging zeigten spezifische Aufnahme des dual-label Peptids ^{111}In -RDC018 in sowohl subkutanen Tumoren als Metastasen der Weichteile sowie des Skeletts. Desweiteren wurde der prinzipielle Beweis erbracht für die Anwendbarkeit von bildgestützter Resektion von TROP-2 exprimierenden Metastasen mithilfe von intraoperativem NIRF Imaging.

Die in dieser Dissertation beschriebenen Studien haben die Kenntnisse über Antikörper-basiertes PET und SPECT Imaging von Prostatakarzinomen deutlich erweitert. Darüberhinaus wurden zwei duale Radionuklid und NIRF Imaging Bildgebungsverfahren entwickelt, welche die bildgestützte Resektion von Prostatakarzinom Metastasen ermöglichen. Diese präklinischen Resultate stützen und stimulieren die Einleitung klinischer Studien um den Wert von dualen Bildgebungsverfahren bei Patienten mit Malignomen der Prostata weiter zu evaluieren.

LIST OF PUBLICATIONS

LIST OF PUBLICATIONS

Susanne Lütje, Jacky W. de Rooy, Sandra Croockewit, Emmeline Koedam, Wim J.G. Oyen, Reinier A. Raymakers. Role of radiography, MRI and FDG-PET/CT in diagnosing, staging and therapeutical evaluation of patients with multiple myeloma. *Annals of Hematology*. 2009; 88(12):1161-1168

Susanne Lütje, Otto C. Boerman, Catharina M. van Rij, Michiel Sedelaar, Wijnand Helfrich, Wim J.G. Oyen, Peter F. Mulders. Prospects in radionuclide imaging of prostate cancer. *The Prostate*. 2012; 72(11):1262-1272

Catharina M. van Rij, Susanne Lütje, Cathelijne Frielink, Robert M. Sharkey, David M. Goldenberg, Gerben M. Franssen, William J. McBride, Edward A. Rossi, Wim J.G. Oyen, Otto C. Boerman. Pretargeted immuno-PET and radioimmunotherapy of prostate cancer with an anti-TROP-2 x anti-HSG bispecific antibody. *European Journal of Nuclear Medicine and Molecular Imaging*. 2013; 40(9):1377-1383

Susanne Lütje, Gerben M. Franssen, Robert M. Sharkey, Peter Laverman, Edward A. Rossi, David M. Goldenberg, Wim J.G. Oyen, Otto C. Boerman, William J. McBride. Anti-CEA Antibody Fragments Labeled with [¹⁸F]AIF for PET Imaging of CEA-Expressing Tumors. *Bioconjugate Chemistry*. 2014; 25(2):335-341

Susanne Lütje, Catharina M. van Rij, Gerben M. Franssen, Giulio Fracasso, Wijnand Helfrich, Annemarie Eek, Wim J.G. Oyen, Marco Colombatti, Otto C. Boerman. Targeting human prostate cancer with ¹¹¹In-labeled D2B IgG, F(ab')₂ and Fab fragments in nude mice with PSMA-expressing xenografts. *Contrast Media and Molecular Imaging*. 2014. In press.

Susanne Lütje, Mark Rijpkema, Gerben M. Franssen, Giulio Fracasso, Wijnand Helfrich, Annemarie Eek, Wim J.G. Oyen, Marco Colombatti, Otto C. Boerman. Dual-modality image-guided surgery of prostate cancer with a radiolabeled fluorescent anti-PSMA monoclonal antibody. *Journal of Nuclear Medicine*. 2014; 55(6):995-1001

Susanne Lütje, Mark Rijpkema, Wijnand Helfrich, Wim J.G. Oyen, Otto C. Boerman. Targeted radionuclide and fluorescence dual-modality imaging of cancer: Preclinical advances and clinical translation. *Molecular Imaging and Biology*. 2014. In press.

Susanne Lütje, Mark Rijpkema, David M. Goldenberg, Catharina M. van Rij, Robert M. Sharkey, William J. McBride, Gerben M. Franssen, Cathelijne Frielink, Wijnand Helfrich, Wim J. G. Oyen, Otto C. Boerman. Pretargeted dual-modality immuno-SPECT and near-infrared fluorescence imaging for image-guided surgery of prostate cancer. Submitted for publication.

Catharina M. van Rij, Cathelijne Frielink, Robert M. Sharkey, Susanne Lütje, David M. Goldenberg, William J. McBride, Wim J.G. Oyen, Otto C. Boerman. Pretargeted radioimmunotherapy of prostate cancer with an anti-TROP-2 x anti-HSG bispecific antibody and a ¹⁷⁷Lu-labeled peptide. *Cancer Biotherapy and Radiopharmaceuticals*. 2014. In press.

Catharina M. van Rij, Cathelijne Frielink, David M. Goldenberg, Robert M. Sharkey, Gerben M. Franssen, Susanne Lütje, William J. McBride, Wim J.G. Oyen, Otto C. Boerman. Pretargeted ImmunoPET of prostate cancer with an anti-TROP-2 x anti-HSG bispecific antibody in mice with PC3 xenografts. *Molecular Imaging and Biology*. 2014. In press.

CURRICULUM VITAE

CURRICULUM VITAE

Susanne Lütje was born on January 31st 1986 in Duisburg, Germany. After qualification for university entrance, she started her Bachelor's in Biology at the faculty of Science of the Radboud University Nijmegen in the Netherlands. In 2008 she obtained her Bachelor's exam. Due to her interests in medical fields, she enrolled to medical school at the faculty of Medical Sciences at Radboud University Nijmegen, starting the Bachelor's program of Medicine in 2008. After several weeks of attending medical school, she enrolled to the Master's program 'Medical Biology' at the faculty of Science as well. During her 1st Master's internship of Medical Biology (2009) she evaluated the role of PET/CT in diagnosing, staging, and response monitoring of patients with multiple myeloma at the Department of Hematology at Radboud University Medical Center Nijmegen under supervision of Dr. Reinier Raymakers. Her 2nd Master's internship (2010) she performed at the Center for Infectious Medicine at the Karolinska Institute in Stockholm, Sweden, under the supervision of Prof. Hans-Gustaf Ljunggren and Prof. Karl-Johan Malmberg, where she worked on the characterization of molecular specificities of human NK cells and their role in donor selection to optimize NK cell-based immunotherapy against cancer. For her work she received the Nijbakker Morra Student Award 2010/2011. In 2010 she passed her Master's exam in Medical Biology cum laude and received the L.M. van Nieuwenhoven Award 2011. In the same year, she passed her Bachelor's exam in Medicine and started clinical rotations for the Master's program in Medicine. In 2011, she started working on her PhD project under supervision of Prof. Otto C. Boerman in parallel to the clinical rotations. She finished the clinical rotations in January 2013, receiving her Master's degree in Medicine. During her PhD project, she got nominated for the Marie Curie Award 2012 and the Best Poster Award of the Annual Meeting of the Center for Translational Molecular Medicine in 2013 and received the IC Medical Young Scientist Best Poster Award 2014 at the January Meeting of the Dutch Clinical Radiochemistry Society. In the same year, she received the Young Professionals Committee Award (3rd Place) of the Society of Nuclear Medicine and Molecular Imaging in the Basic Science Category. During her PhD project, she did a two-months internship on intravital-fluorescence microscopy at the Department of Radiology and Radiological Sciences at Johns Hopkins University in Baltimore, US, under supervision of Prof. Martin G. Pomper and Dr. Il Minn.



DANKWOORD

DANKWOORD

Toen ik 9 jaar geleden de beslissing nam om een tijdje in Nederland te gaan studeren, had ik een aantal dingen volstrekt niet verwacht:

1. Hoe lang ik zou blijven
2. Hoe gezellig die Nederlanders toch zijn
3. Hoeveel kansen ik zou krijgen
4. Hoe moeilijk het zou zijn, om dit allemaal achter te laten en uit Nederland te vertrekken

Dit boekje is nu een beetje het eindproduct van mijn tijd in Nederland geworden. Echter dit proefschrift was nooit tot stand gekomen, als er niet een aantal mensen waren geweest die een ontzettend grote bijdrage hieraan hebben geleverd en mij in bijzondere mate hebben gesteund. Graag wil ik hen bij deze gelegenheid in het bijzonder bedanken.

Prof. Dr. Boerman, beste Otto, je hebt dit al in veel boekjes gelezen, maar ik moet dit hier toch nog eens noemen: ook ik had het niet beter kunnen treffen dan met jou als mijn eerste promotor. Naast je wetenschappelijke kwaliteiten heb ik veel waardering voor je openheid en de oprechte interesse die je hebt voor alle leden van je onderzoeksgroep. Ik wil je bedanken voor je onvoorwaardelijke steun tijdens mijn promotietijd en je bereidheid om steeds individuele oplossingen mogelijk te maken, zoals in begin 2011, toen ik je vroeg om een klein bijbaantje op het lab, wat uiteindelijk leidde tot dit promotietraject. Lang niet elke professor is dusdanig open-minded, bedankt hiervoor! Bovendien wil ik bij deze gelegenheid nog eens mijn waardering uitspreken over hoe snel jij commentaar leverde op diverse manuscripten. Soms ontving ik je commentaar op een stuk zelfs twee keer op één dag!

Prof. Dr. Wim Oyen, beste Wim, door jou ben ik bij de afdeling Nucleaire Geneeskunde terecht gekomen. Hartelijk dank dat jij mij deze kans gaf. Je enthousiasme voor het vak was aanstekelijk! Bedankt ook voor je waardevolle inbreng en het richtinggevende commentaar bij het schrijven van artikelen.

Dr. Rijpkema, beste Mark, je bent een hartstikke goede copromotor. De vele besprekingen met jou heb ik als zeer waardevol ervaren. Hoe complex een onderwerp ook is, je hebt een talent om het duidelijk en met veel enthousiasme uit te leggen. Heel veel dank ook voor je altijd aanhoudende optimisme; vooral als de resultaten weer eens niet echt mee zaten hebben jouw optimisme en enthousiasme ertoe bijgedragen dat wij toch door bleven zoeken.

Dr. Helfrich, beste Wijnand, bedankt voor het meedenken en al je commentaar op onze artikelen. Vanuit een iets andere hoek heb jij altijd nog nieuwe aspecten kunnen leveren die onze manuscripten verder verbeterden. Bedankt hiervoor!

Prof. Dr. Gotthardt, lieber Martin, vielen Dank, dass Du mich in Deine Beta-Projekte hast reinschnuppert lassen, inspirierende Forschung in einer tollen Arbeitsgruppe!

Besten Dankauch für all Deinen (manchmal mehr, manchmal weniger ernstgemeinten) Kommentar zur der deutschen und niederländischen Arbeitsweise in der Klinik. Ich bin gespannt, was sich bewahrheitet!

Beste **Gerben**, heel erg bedankt voor de goede samenwerking de afgelopen jaren. Ik heb het als zeer fijn en gezellig ervaren om met jou samen te werken. Vooral in het begin hebben we veel samen op het lab gestaan en achter de scanner gezeten en heb jij mij de kunst van het labelen (en alle berekeningen :-) geleerd. Maar ook later stond je mij steeds met raad en daad terzijde. En wilden de labelingen toch een keer niet lukken, wist je altijd nog een trucje te bedenken!

Beste **Annemarie**, ik wil je bedanken voor de goede samenwerking, je hulp met het plannen en uitvoeren van experimenten, maar vooral ook je vriendschap en gezelligheid.

Bianca, Kitty, Iris, Henk en **Nicole**: dankzij jullie verstand en kundigheid in de omgang met proefdieren wordt zorgvuldig en verantwoord onderzoek mogelijk. Hartelijk dank voor de goede samenwerking, de vele overlegmomenten, jullie flexibiliteit in de planning van de experimenten en natuurlijk de gezellige kletspartijen. Ik heb het elke keer weer leuk gevonden om weer eens jullie kant op te komen.

Beste **Sandra**, je bent altijd een beetje mijn 'promovendus role model' geweest. Of het nou tips waren met het plannen van experimenten, het maken van wetenschappelijke posters/presentaties, of het schrijven/layouts van het proefschrift, je was altijd present en bereid om te helpen, ook al had je het druk met je eigen werk. Heel erg bedankt voor je hulp!

Beste **Katja**, bedankt voor het meewerken aan artikelen, posters en presentaties. Je wist altijd nog belangrijk commentaar te leveren.

Beste kantoorgenootjes **Sam, Floor, Mark** en **Peter**: Ik heb er hartstikke van genoten om met jullie een kantoor (en taart/snoep) te delen. Jullie zijn een supergezellige club, dit kantoorje zal ik missen!

Cathelijne, Janneke, Maarten, Tessa, Stefanie, Willem, Wietske, Inge, Selen, Charlotte, Stijn, Lieke, Desirée, Danny, Jurrian en alle andere medewerkers van de afdeling: mede door jullie is mijn tijd bij de Nucleaire Geneeskunde zo leuk geworden. Op het lab, of gewoon in de koffiekamer bij een stukje taart, het was altijd gezellig.

Wael: tack så mycket för svenska godis!

Marie-Louise en **Jacqueline**, ik ben al een redelijk groot aantal secretaresses tegengekomen, maar nog nooit heb ik er eentje ontmoet die zo competent en aardig was als jullie. Ondanks jullie hoge werkdruk kon ik altijd bij jullie terecht en wisten jullie steeds prima oplossingen te vinden, waar ik ook mee kwam. Bedankt hiervoor!

Prof. Dr. Pomper, dear Marty, thank you very much for giving me the opportunity to do a research internship in your laboratory. It was an enriching experience!

Dr. Minn, dear Il, thank you so much for teaching me all kinds of assays in the lab and introducing me to intravital fluorescence microscopy. It was inspiring to work with you and participate in your projects. I appreciate your enthusiasm. Thank you for showing me around in Baltimore and organizing social events.

Thanks to the members of Karl-Johan Malmbergs research group at the Center for Infectious Medicine at Karolinska Institute, especially **Kalle, Sandra, Mattias,** and **Monika**. The wonderful and inspiring time in such a great research environment actually awakened my passion for science.

Lieber **Hendrik**, vielen Dank für Deine Freundschaft. Seit 2005 haben wir viele tolle Dinge zusammen erlebt, sowohl an der Uni als auch privat. Die unzähligen geselligen Abende hab ich sehr genossen, Fortsetzung folgt natürlich!

Lieber **Jan**, vielen Dank für Deine Unterstützung. Du hattest immer ein offenes Ohr, an allen Höhen und Tiefen hast du Anteil genommen und warst einfach immer am Start. Danke dafür!

Zu guter Letzt geht mein besonderer Dank an meine **Eltern**. Ohne Eure tatkräftige Unterstützung wäre all das nicht möglich gewesen. Ihr habt mir während der langen Jahre des Studiums und der Promotion den Rücken immer frei gehalten und mir dadurch die Freiheit gegeben, meine Ambitionen zu verwirklichen, egal welche Hürden zu überwinden waren. Vielen Dank für alles!

ABOUT THE COVER

In oncology, the search for tumor lesions in the body of a patient can be compared to looking for the proverbial needle in a haystack. With a suitable detection technique, the search for this needle could be facilitated. On this cover, the magnet represents the detection technique, which in this case would be near-infrared fluorescence and radionuclide dual-modality imaging, each being represented by one pole of the magnet. With only one pole being active, the needle cannot be detected, however when both poles of the magnet are active, the needle, representing a small tumor lesion, can be found.

